Yasser Abdel-Fattah Abdel-Hadi

Development of optical concentrator systems for directly solar pumped laser systems

Technical University of Berlin
Institute of Optics
2005
D 83

Development of optical concentrator systems for directly solar pumped laser systems

von

Yasser Abdel-Fattah Abdel-Hadi, M.Sc.

aus Kairo, Ägypten

Fakultät II - Mathematik und Naturwissenschaften
der Technischen Universität Berlin
zur Verleihung des akademischen Grades
Doktor der Naturwissenschaften
Dr.rer.nat

genehmigte Dissertation

Berlin 2005
D 83

Tag der wissenschaftlichen Aussprache: 22.12.2005

Berichter: Prof. Dr. –Ing. Adalbert Ding
Berichter: Prof. Dr.-Ing. Hans Joachim Eichler
Vorsitzender: Prof. Dr. Erwin Sedlmayr

To the souls of my parents I present this work…

They wanted to be happy to see this work finished…

But they died before it…

I think they are now happy to see it finished…

I also present this work to my home country Egypt and to Germany…

Yasser

Abstract

Two new solar directly-pumped solid state laser systems were developed to avoid the disadvantages of the previously developed system.

Using the advantages of the Fresnel lenses, a small solar directly-pumped laser system was developed. This system consists of a rectangular Fresnel lens as a primary concentrator, a secondary concentrator and the laser cavity. A slab laser of the type of Nd:YAG laser was firstly used. For this laser, a collimator convex lens was used as a secondary concentrator. Another laser rod of the type of $Nd:YVO_4$ was used. For this laser, a new non-imaging concentrator of the type of Compound Spherical Concentrator (CSC) was used as a secondary concentrator. The system was constructed on an astronomical mount to track the sun during the day.

A medium-scale mirror-array concentrator using a system of 105 flat mirrors of the dimensions 15 cm × 15 cm was developed. The mirrors were organised in three rows. Each row had seven panels. Each panel carried five mirrors. Six electro-mechanical computer-controlled motors were used to let the system track the sun during the day. Three of these motors were responsible for the tracking in the vertical component (altitude of the sun). The other three motors were responsible for the tracking in the horizontal component (azimuth of the sun). The mirrors were contolled through these motors in order to result a single fixed reflected image of the whole system during the day. An additional Fresnel lens was used to increase the concentration ratio of the whole system.

The measurements of the both systems were taken in the Technical University of Berlin (Germany). These measurements showed promising results which can lead to substitute systems which use the large parabolic- or hyperbolic dish concentrators.

Abstract in German

Abstrakt

Neue optische Solarkonzentratoren zum Einsatz in Festkörper-Lasersysteme wurden entwickelt.

Unter Verwendung von großflächigen Fresnellinsen wurde ein kleines direkt-gepumptes Lasersystem entwickelt. Dieses System besteht aus einer Fresnellinse, einen Sekundärkonzentrator und einer Laserkavität.

Für das erste System wurde eine asphärische Linse als Sekundärkonzentrator verwendet, womit ein Nd:YAG Slab-Kristall gepumpt wurde.

Für das zweite System wurde ein monolithischer, nicht abbildender sphärischer Konzentrator (CSC) als Sekundärkonzentrator eingesetzt, der einen Nd:YVO$_4$ Stab, der in eine Keramikkavität eingesetzt war, transversal pumpte.

Für Lasersysteme mittlerer Leistung wurde ein System bestehend aus Primär- und Sekundär-Konzentratoren sowie Kavität entwickelt. Der Primärkonzentrator war ein Steuerbares Vielspiegelarraysystem bestehend aus 105 quadratische Spiegeln (15 cm × 15 cm). Die Spiegel sind in 3 von einander unabhängigen Gruppen unterteilt, die mit je 2 Motoren (für die vertikale und horizontale Bewegung der Gruppe) eingestellt werden können. Jede Gruppe besteht aus 7 Panelen mit je 5 vereingestellte Spiegeln. Die Spiegel wurden so justiert, dass die Sonnenstrahlung auf einen Fleck minimaler Dimensionen konzentriert wurde. Eine zusätzliche Fresnellinse wurde verwendet, um die Konzentration des System zu erhöhen.

Contents

List of figures

X

XII

List of tables

Chapter 1: Introduction

1.1 The inspiration of the issue

The potential of lasers for producing energy is evident and well-known. Listed here are some examples of applications: space communication, energy support in space, efficient energy transfer over large distances, efficient laser pumping for chemical reactions to mention just a few.

If the laser energy could be produced with an efficient conversion rate, it would be economically good. For some applications, direct solar pumping seems to be advantageous. Depending on conversion efficiency, complexity, reliability, or other conditions, it could be the preferable pump source for a laser and superior to all other methods, including electrical pumping by photo cells. This holds, for example, for an autark energy satellite, where the solar spectrum is split. The spectrally adapted part supplies the energy for the laser and the rest is used for driving solar cells that provide the energy for the peripheral systems.

It is possible that solar pumped lasers will become a cheap source for coherent and high power radiation. It is a dream of mankind to convert the sunlight, which is an incoherent, broadband radiation into laser radiation which is coherent and monochromatic [1].

Perhaps the first inspiration for producing a coherent monochromatic light from the sun was taken from the old Egyptian scripts. One icon shows the Pharaoh Akhenaton with his family praying to his god Aton, symbolized by the solar disc from which fine beams radiate to waiting hands as shown in Fig 1-1.

(a)   (b)
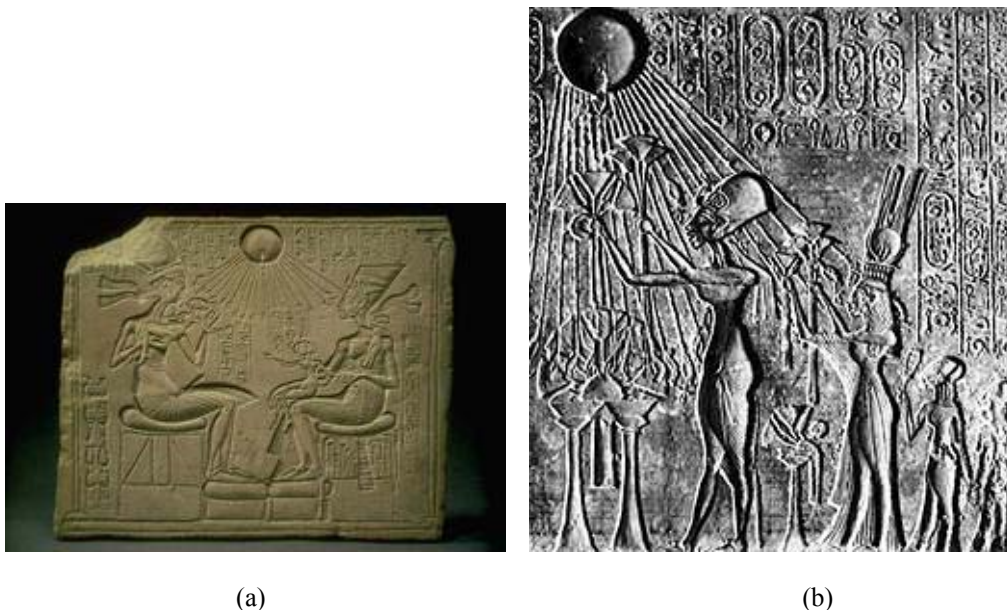
Fig. 1- 1 The Pharaoh Akhenaton praying to his god Aton (symbolized by the solar disc).

This dream began to be realized shortly after the invention of the laser. The scientists made progress in reducing the cost of production of lasers by reducing the pumping energy.

1.2 Why Solar Laser?

To stimulate a high threshold level solid state laser, a light source of high optical stimulating power is needed. In the classical laser systems, pulsed or cw- flashlamps, while in the modern ones diode lasers are used. Although the latter are very efficient, they are expensive. The total efficiency of the flashlamp-pumped lasers is less than 4 % (50 % efficiency of the flashlamp times 8 % efficiency of the optical laser system). The efficiency of the diode-pumped lasers lies between 35 % and 50 % depending on the electrical input power.

The use of the solar-pumped laser could be advantageous in the underdeveloped countries which have reliable intensive sun shine. The applications using the concentrated thermal solar radiation can reach a fraction of the sun surface temperature (< 6000 K). However, laser generation does not lie in the field of thermal application. In the solar laser field, the solar energy is converted into laser energy. With the well-established design of lasers, the beam quality, compared with a classical light source, has been significantly improved.

Time critical applications are almost based on the reserved and always available energy. With the help of the solar energy, that can be reached through the photovoltaic and photothermal generation and reserving the electrical power, with which the conventional laser and other required equipments operate. Typical values for the energy efficiency of the commercial photovoltaic cells lie nowadays between 12 % and 15 % for the cells alone. We have also to take into account the conversion loss and the aging of the cells, so that a net efficiency of 10 % - 13 % is realistic. If we combine these values with the above mentioned laser efficiencies, we can get maximal total efficiencies of 0.5 % for flashlamp-pumped systems and 1.5 % to 2 % for the diode-pumped ones. Those values could be increased to 8%, through direct pumping of the laser crystals using the sun's energy in which the conversion loss may be neglected.

Directly pumped solar lasers are only able to be applied if the processes are not time-critical. These applications could be welding, soldering, cutting and hardening, especially in the field of the micro-mechanics or for light stimulated chemical conversion processes. Nevertheless, the solar radiation must be high enough to reach the threshold level.

These solar pumped lasers could be interesting in the following fields of application:

- **On earth:**

    High power solar pumped lasers could be used for industrial applications (e.g. processing, laser welding, photochemistry etc.). This can be realized in a factory where one laser produces the radiation which is delivered via glass fibres to the

2

application sites. Another possible terrestrial application could be the pollutant control and analysis of samples with a mobile measuring system.

- **In space:**

They could be used as an energy source for transmission of energy to other satellites, for space communication and for telemetric purposes.

The part of the solar spectrum that can not be used by the laser could be converted to electrical energy by means of photovoltaic systems or a thermal engine.

In thinking about the substitution of the directly pumped solar laser instead of the electrically or chemically powered ones, one can see from Fig. 1-2 the amount of the energy lost during the operating of the electrically generated laser. Only 2.8 % of the supplied energy could be converted to the laser beam. The rest energy is lost.
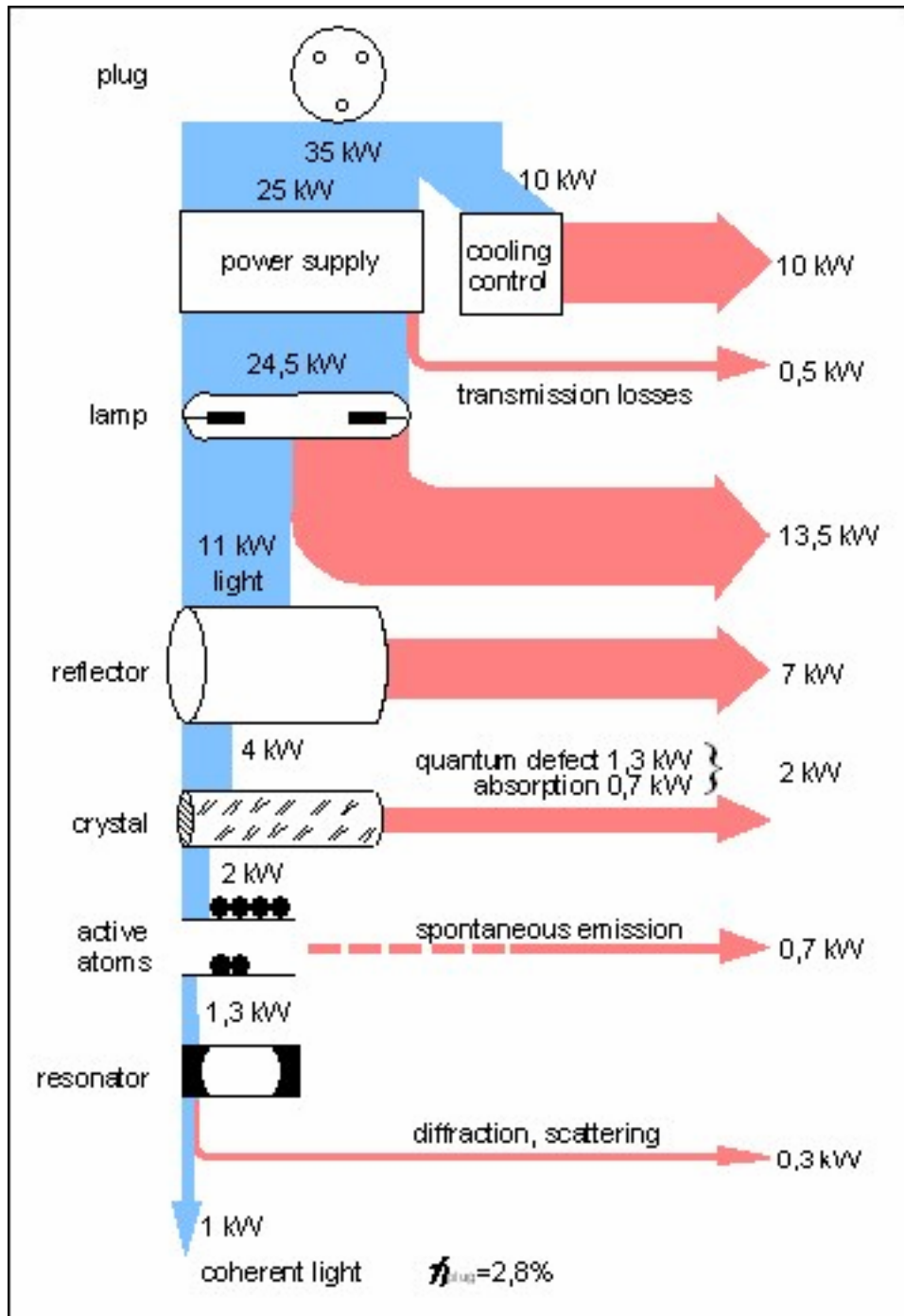
Fig. 1- 2 Energy loss during laser operation.

Among optically pumped lasers, the solid –state lasers are the most attractive for solar pumping because of their compactness, reliability and efficiency as well as long and good experience in many applications. There have been several publications on solar pumped solid state lasers operating at room temperature [1]. Since the thermal conductivity which is a limiting factor for many garnet crystals is increasing with decreasing temperature, it would be advantageous to cool the crystal to cryogenic temperatures. There would be less distortion inside the crystal and therefore a better beam quality can be expected [1].

1.3 Solar laser as a possible selection

The discovery of the laser provided a remarkable source for monochromatic and coherent light. The technique by which the laser radiation is generated is called pumping, and the ways by which this technique takes place are many: electrical, chemical and optical ways. Pumping is the excitation of the lower level atoms to meta-stable states via higher excited states. The lasing takes place in the meta-stable state.

A good idea for optical pumping is to expose the laser medium to a concentrated solar radiation; so producing a "*Solar Laser*".

Shortly after the invention of the laser, scientists began directly converting incoherent broadband sunlight into coherent monochromatic laser radiation. This was quickly realized, but the typical efficiencies of sun-pumped lasers have been less than one percent. The chief reason for the low performance is that lasers have high thresholds: the amplifying medium must have a high power density before any lasing can take place.

The idea of directly converting broad-band solar radiation into coherent and narrow-band laser radiation is almost as old as the laser itself. In principle, any laser material that can be optically pumped can also be used as a solar laser. If lasers are needed in remote locations where sunlight is abundant and other forms of energy are scarce, a solar laser would seem to be the best choice.

Non-imaging optics, a relatively new subdiscipline of optics, provides a means of concentrating light to intensities approaching the theoretical limit.

A solar-pumped laser requires a concentrating device that tracks the sun. The laser head and its associated optics are then placed near or at the focus of the collector. Between 10 and 50 sq.ft of collector area per 100 W of laser output power is required, depending on the type of laser material used. Compared to an electrically operated laser, a solar laser is simpler due to the complete elimination of the electrically powered pumping source. It is particularly attractive in applications where extended run times are required and where compactness, reliability and efficiency are critical [1].

Solar lasers have been proposed for space applications. A solar laser system could be sent into space to collect the solar radiation before its dispersion in the earth's atmosphere. This would require placing the solar laser system on a satellite and the laser output would be sent directly to the earth.

NASA has been pursuing the development of solar lasers mainly for space power transmission and propulsion. New potential applications of solar lasers in space are emerging, driven by NASA and DOD requirements. These include earth, ocean and atmospheric observation from space; detecting, illuminating and tracking hard targets in space; and deep space communications. Figs. 1-3 and 1-4 show the schematics for a solar-pumped laser power station [1].
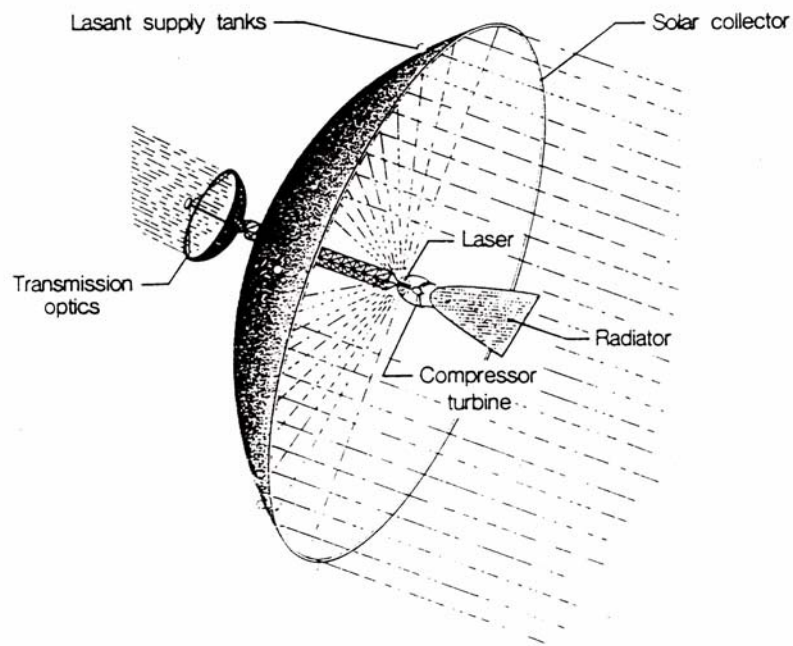
Fig. 1- 3 Schematic representation of the solar-pumped laser power station.
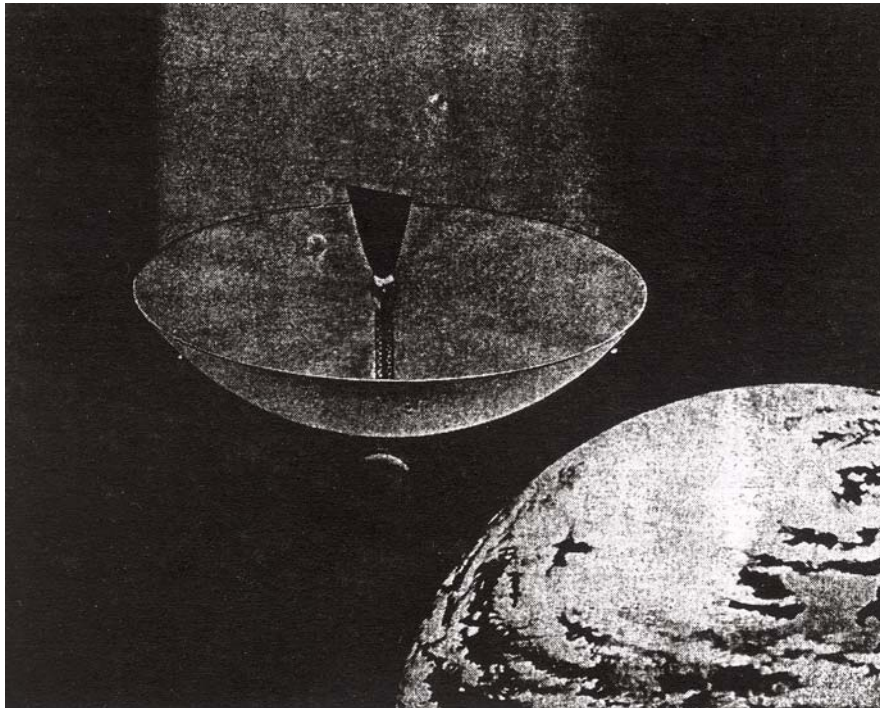
Fig. 1- 4 Solar-pumped laser power station in space.

Gas, liquids and solid state lasers have all been considered as candidates for solar lasers. Of these, the solid lasers appear to be most attractive because of their inherent high energy density and compactness, their relatively low pumping threshold and their potential for efficient solar-to-laser power conversion.

The device used to *concentrate* the solar radiation into the laser medium is called a *concentrator*. It is an optical device used to increase the amount of solar radiation intensity, i.e., the result is a beam of concentrated solar radiation which can reach high levels of optical and thermal insolation. Recently, an insolation level greater than that on the surface of the sun itself, has been obtained [1].

As we see, our problem is mainly an optical or thermal one. In the case of laser pumping or photovoltaic applications, the problem is mainly an optical one. The thermal side coming from the absorption of the concentrated solar radiation by the absorber (target) will be considered as waste energy and may damage the laser medium or the cell. One solution for solving this new problem is the use of cooling techniques. The thermal side is useful in the case of water heating or cooking.

1.4 Sun and solar radiation energy

1.4.1 The sun

The sun is a sphere of intensely hot gaseous matter with a diameter of 1.39×10^9 m and is, on average, 1.5×10^{11} m from the earth. As seen from the earth, the sun rotates on its axis about once every four weeks. However, it does not rotate uniformly as a solid body; the equator takes about 27 days and the polar regions take about 30 days for each rotation [2].

As viewed from earth, the sun has an effective blackbody temperature of 5777°K. The temperature in the central interior regions is estimated between 8×10^6 and 40×10^6 °K, and the density is estimated to be about 100 times that of water. The sun is, in effect, a continuous fusion reactor with its constituent gases as the "containing vessel" retained by gravitational forces. Several fusion reactions have been suggested as the suppliers of energy radiated by the sun. The one considered the most important is a process in which hydrogen (i.e., four protons) combines to form helium (i.e., one helium nucleus); the mass of the helium nucleus is less than that of the four protons, mass having been lost in the reaction and converted to energy [2].

The energy produced in the interior of the solar sphere, where temperatures of many millions of degrees, must be transferred to the surface and then be radiated into space. A succession of radiative and convective processes occur with successive emission, absorption, and re-radiation; the radiation in the sun's core is in the x-ray and gamma-ray regions of the spectrum, with the wavelengths of the radiation increasing as the temperature drops at larger radial distances [2].

1.4.2 The sun-earth geometry

Fig. 1-5 shows schematically the geometry of the sun-earth relationships. The eccentricity of the earth's orbit is such that the distance between the sun and the earth varies by 1.7%. At a distance of one astronomical unit, 1.495×10^{11} m, the mean earth-sun distance, the sun subtends an angle of 32′. The radiation emitted by the sun and its spatial relationship to the earth result in a nearly fixed intensity of solar radiation outside of the earth's atmosphere [2].
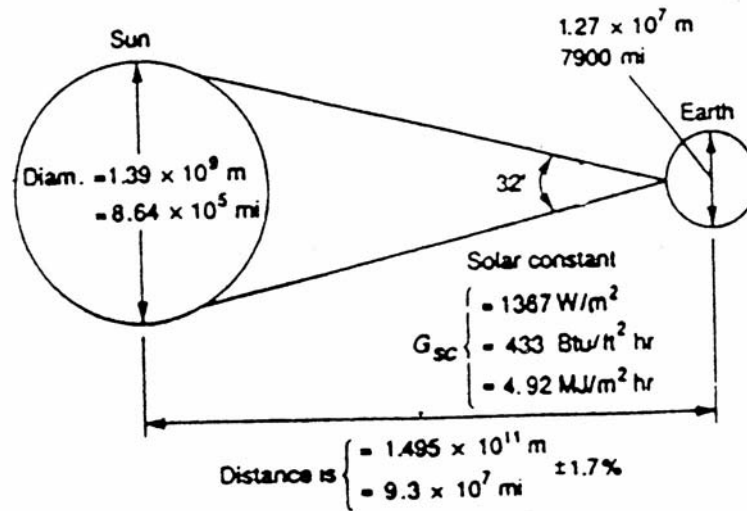
Fig. 1- 5 Sun-earth relationship.

1.5 Solar radiation outside the earth's atmosphere

1.5.1 The solar constant

Before rockets and spacecraft, estimates of the solar constant G_{SC} had to be made from ground-based measurements of solar radiation after it had been transmitted through the atmosphere and thus in part absorbed and scattered by components of the atmosphere. Extrapolations from the terrestrial measurements made from high mountains were based on estimates of atmospheric transmission in various portions of the solar spectrum. Pioneering studies were done by C. G. Abbot and his colleagues at the Smithsonian Institution. Abbot's value of the solar constant of 1322 W/m^2 was revised by Johnson to 1395 W/m^2 [2].

The availability of very-high-altitude aircraft, balloons and spacecraft has permitted direct measurements of solar radiation outside most or all of the earth's atmosphere. These measurements were made with a variety of instruments in nine separate experimental programmes. They resulted in a value for the solar constant of 1353 W/m^2 with an estimated error of ± 1.5%. This standard value was accepted by NASA and the American Society of Testing Materials [2].

Data from Nimbus and Mariner satellites have also been included in the analysis, and as of 1978, Frohlich recommends a new value of the solar constant of 1373 W/m^2, with a probable error of 1 to 2%. The World Radiation Center (WRC) has adopted a value of 1367 W/m^2, with an uncertainty of the order of 1% [3]. A value of the solar constant of 1367 W/m^2 (1.960 cal/cm^2 min, 432 Btu/ft^{2}hr) is the most commonly one in use [2].

8

1.5.2 Spectral distribution of extraterrestrial radiation

In addition to the total energy in the solar spectrum (i.e., the solar constant), it is useful to know the spectral distribution of the extraterrestrial radiation, i.e., the radiation that would be received in the absence of the atmosphere. A standard spectral irradiance curve has been compiled based on high altitude and space measurements. The WRC standard and a 5777° K blackbody spectrum are shown in Fig. 1-6. Table 1-1 provides the same information about the WRC spectrum in numerical form. The average energy $G_{sc,\lambda}$ (in W/m^2 μm) over small bandwidths centred at wavelength λ is given in the second column. The fraction $f_{0-\lambda}$ of the total energy in the spectrum that is between wavelengths 0 and λ is given in the third column. The table is in two parts, the first at regular intervals of wavelength and the second at even fractions $f_{0-\lambda}$. [2].

Fig. 1- 6 Spectral distribution of the extra-terrestrial solar radiation.

λ μm	$G_{sc,\lambda}$ W/m² μm	$f_{0-\lambda}$	λ μm	$G_{sc,\lambda}$ W/m² μm	$f_{0-\lambda}$	λ μm	$G_{sc,\lambda}$ W/m² μm	$f_{0-\lambda}$
0.250	13.8	0.002	0.520	1820.9	0.243	0.880	965.7	0.621
0.275	224.5	0.005	0.530	1873.4	0.257	0.900	911.9	0.635
0.300	542.3	0.012	0.540	1873.3	0.271	0.920	846.8	0.648
0.325	778.4	0.023	0.550	1875.0	0.284	0.940	803.8	0.660
0.340	912.0	0.033	0.560	1841.1	0.298	0.960	768.5	0.671
0.350	983.0	0.040	0.570	1843.2	0.311	0.980	763.5	0.683
0.360	967.0	0.047	0.580	1844.6	0.325	1.000	756.5	0.694
0.370	1130.8	0.056	0.590	1782.2	0.338	1.050	668.6	0.720
0.380	1070.3	0.064	0.600	1765.4	0.351	1.100	591.1	0.743
0.390	1029.5	0.071	0.620	1716.4	0.377	1.200	505.6	0.783
0.400	1476.9	0.079	0.640	1693.6	0.401	1.300	429.5	0.817
0.410	1698.0	0.092	0.660	1545.7	0.424	1.400	354.7	0.846
0.420	1726.2	0.104	0.680	1492.7	0.447	1.500	296.6	0.870
0.430	1591.1	0.117	0.700	1416.6	0.468	1.600	241.7	0.890
0.440	1837.6	0.129	0.720	1351.3	0.488	1.800	169.0	0.921
0.450	1995.2	0.143	0.740	1292.4	0.507	2.000	100.7	0.941
0.460	2042.6	0.158	0.760	1236.1	0.526	2.500	49.5	0.968
0.470	1996.0	0.173	0.780	1188.7	0.544	3.000	25.5	0.981
0.480	2028.8	0.187	0.800	1133.3	0.561	3.500	14.3	0.988
0.490	1892.4	0.201	0.820	1089.0	0.577	4.000	7.8	0.992
0.500	1918.3	0.216	0.840	1035.2	0.593	5.000	2.7	0.996
0.510	1926.1	0.230	0.860	967.1	0.607	8.000	0.8	0.999

ᵃ $G_{sc,\lambda}$ is the average solar irradiance over the interval from the middle of the preceeding wavelength interval to the middle of the following wavelenght interval. For example, at 0.600 μm, 1765.4 W/m² μm is the average value between 0.595 and 0.610 μm.

Table 1-1a Extraterrestrial Solar Irradiance (The WRC Spectrum) in Increments of Wavelength.

$f_{0-\lambda}$	λ	$f_{0-\lambda}$	λ
0.05	0.364	0.55	0.787
0.10	0.417	0.60	0.849
0.15	0.455	0.65	0.923
0.20	0.489	0.70	1.010
0.25	0.525	0.75	1.114
0.30	0.562	0.80	1.245
0.35	0.599	0.85	1.413
0.40	0.638	0.90	1.658
0.45	0.683	0.95	2.118
0.50	0.731	1.00	∞

Table 1-1b Extraterrestrial Solar Irradiance in Equal Increments of Energy.

1.5.3 Variation of extraterrestrial radiation

Measurements indicate that the energy flux received from the sun outside the earth's atmosphere is essentially constant. The *solar constant* G_{sc} is the rate at which energy is received from the sun on a unit area perpendicular to the rays of the sun at the mean distance of the earth from the sun.

The earth revolves around the sun in an elliptical orbit having a very small eccentricity, and with the sun at one of the foci. Consequently, the distance between the earth

10

and the sun varies a little through the year. Because of this variation, the extraterrestrial flux also varies. The value on any day can be calculated from the Eq. (1-1).

$$G'_{sc} = G_{sc}(1 + 0.033\cos\frac{360n}{365})$$ (1-1)

where n is the day of the year.

It is also useful to know the spectral distribution of extra-terrestrial solar radiation. Measurements of this distribution are plotted in Fig. 1-6 [2].
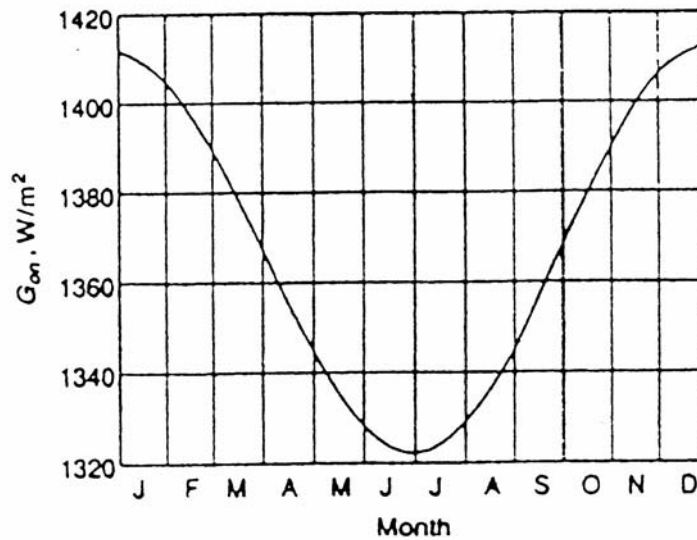
Fig. 1- 7 Variation of extraterrestrial solar radiation with time of year.

1.6 Solar radiation at the earth's surface

Solar radiation is received at the earth's surface after being subjected to the mechanisms of attenuation, reflection and scattering in the earth's atmosphere. The radiation received without change of direction is called *beam radiation*, while that received after its direction has been changed by scattering and reflection is called *diffuse radiation*. The sum of the beam and diffuse radiation flux is referred to as *total radiation* or *global radiation* [24].

There are also some indicators of the solar radiation measurements at the earth's surface that we have to define here; the *Clearness Index K_t* and the *Diffuse Fraction K_D*.

The Clearness Index K_t:

Energy flux $E_{G,hor}$ received from the sun at the horizontal surface of the earth over the energy flux $E_{o,hor}$ received at the top of atmosphere averaged over one day [3].

It can be calculated from the following Eq. (1-2).

$$K_t = \frac{\sum\limits_{h=1}^{24} \overline{E_{G,hor}(h)}}{\sum\limits_{h=1}^{24} \overline{E_{o,hor}(h)}} \tag{1-2}$$

The diffuse Fraction K_D:

Diffuse solar radiation $E_{D,hor}$ over the total (global) one $E_{o,hor}$ averaged over one day [3].

It can be calculated from the following Eq. (1-3).

$$K_D = \frac{\sum\limits_{h=1}^{24} \overline{E_{D,hor,h}(h)}}{\sum\limits_{h=1}^{24} \overline{E_{G,hor,h}(h)}} \tag{1-3}$$

1.7 Solar radiation over Egypt

Egypt is one of the countries in the world which receives extremely high amounts of solar radiation. The measurements indicate that the annual average of the global solar radiation is 5.21 kWh/m^2/day, direct solar radiation is 6.26 kWh/m^2/day, diffuse solar radiation is 1.86 kWh/m^2/day, the clearness index K_t is 0.61, and the diffuse fraction K_D is 0.37. If we use a system with an optical concentrator at this high level of insolation, we would expect a laser output of relatively high efficiency and accordingly high power [4].

Variability of solar radiation has created a basic problem for the engineering of solar energy systems. For some future solar energy applications, periodic reduction in solar energy on various time scale (days to years) may be important; such reduction occur naturally as a result of cloud variability and will continue into the future.

The Egyptian Solar Atlas shows the solar energy distribution over Egypt in simplified maps. The maps show the monthly and annual average global solar radiation over Egypt in

kWh/m^2/day. For example, Fig. 1-8 shows a regular increase of the global radiation from the north to the south of Egypt during all seasons, with the exception of a decrease in both Cairo and Eastern Owienat due to air pollution and sand storms in the deep desert respectively. The variation of global radiation from north to south in Egypt has a wide range (8 to 8.3 kWh/m^2/day) in summer. The transitional seasons have an intermediate range. The seasonal variation of global radiation over Egypt is clear. It varies from winter to summer in a wide range (3.7 to 8 kWh/m^2/day) in the north and in a narrow range (5 to 8.3 kWh/m^2/day) in the southern Egypt [4].

The measurements of Helwan solar radiation station (south of Cairo by 30 km of latitude 30° N and longitude 31° E) indicate that the annual average of the global solar radiation is 5.21 kWh/m^2/day, direct solar radiation is 6.26 kWh/m^2/day, diffuse solar radiation is 1.86 kWh/m^2/day, the clearness index K_t is 0.61 and the diffuse fraction K_D is 0.37 [4].
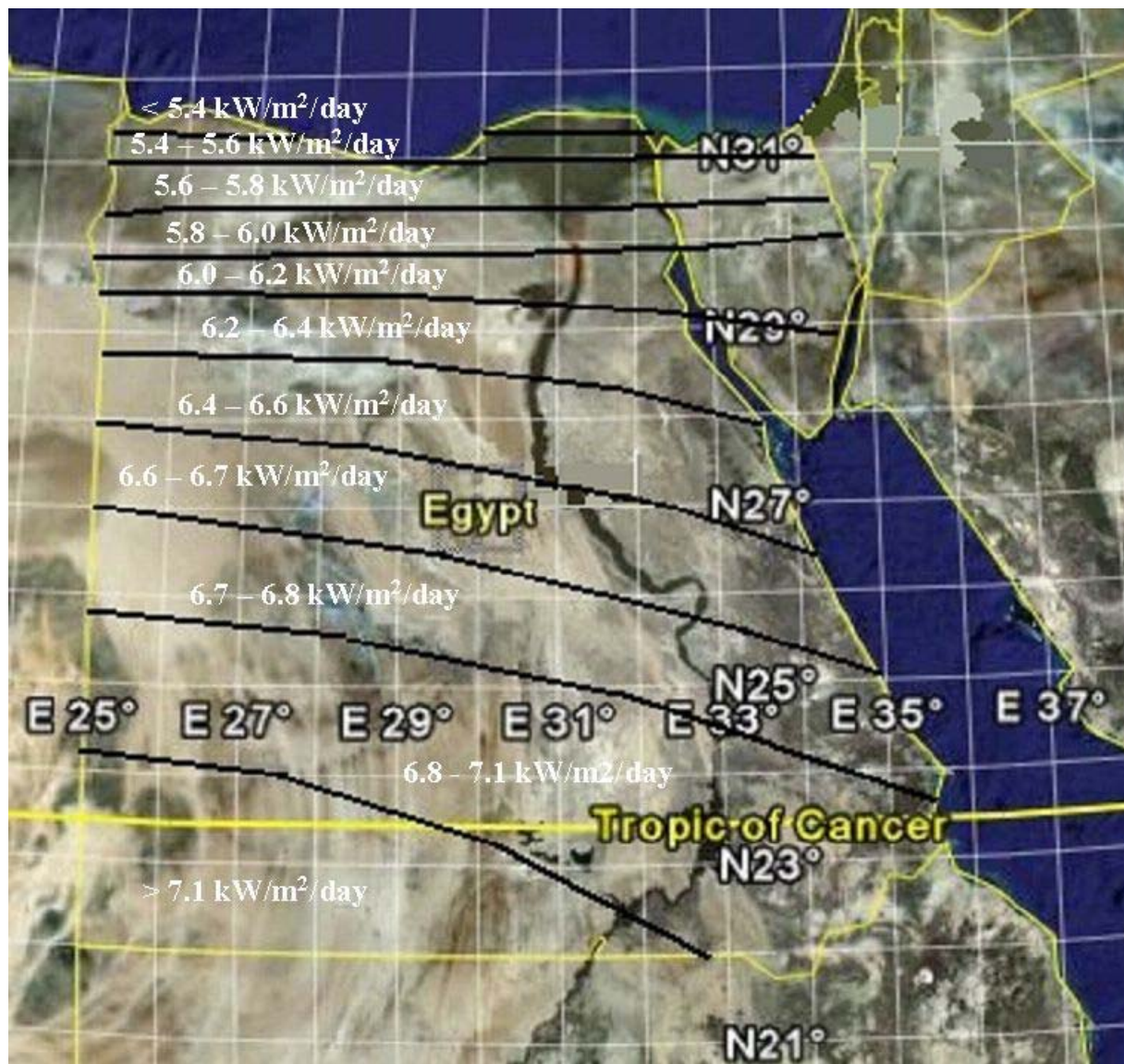
Fig. 1- 8 The annual average of global solar radiation over Egypt.

1.8 Solar laser techniques

The idea of the solar laser depends on concentrating the solar radiation in order to obtain a pumping intensity greater than the threshold level needed to generate the laser. For such purposes, optical concentration devices are used like the three-dimensional parabolic concentrator (paraboloidal concentrator (3D-PC)), spherical concentrator (SC), Fresnel lens (FL), solar towers, solar mirror arrays, etc. With the help of the two- or three-dimensional non-imaging concentrators e.g. compound parabolic concentrators, conical concentrator, V-trough concentrator, etc, one can increase the concentration level to a higher one to attain the approximately the theoretical energy level.

When thinking of laser power production, some points come immediately to mind:

1- The population inversion should be produced by a simple and cheap method.

2- The lasing medium should be a simple and cheap material.

3- The produced laser power should be applicable to the conversion processes.

Various applications have been proposed for solid-state lasers in space. As solar energy is the main continuous energy source in space, it can be used to pump solid-state lasers either directly or indirectly. In indirect pumping, the solar light can illuminate solar cells to produce electricity, which powers diode lasers. The emitted diode laser light can pump a solid-state laser. The technologies of the photovoltaic, diode lasers and diode laser-pumped solid-state lasers have separately attracted much attention in the past and achieved industrial maturity and efficiency. Direct solar pumping of the solid-state lasers saves two energy conversion steps, and thus is potentially more efficient, simpler and more reliable. However, much less attention has been devoted to direct solar-pumped lasers and thus the technology is currently much less mature. Solar lasers are reality now, but there is still a lot to be done to reach perfection.

The set-up for continuously operating high power laser systems using solar energy falls in two types:

(I) Indirect pumping

When a solar powered electrical generator is used to run a conventional electric discharge laser (EDL) which has an efficiencies of about 50%, or excimer laser which has an efficiency of about 15%, solid state laser or diode laser, the method would be called an indirect pumping method.

The system of this type consists of:

    1- Sun light collector.
    2- Adaptive optics.
    3- Electrical power generator.
    4- Laser medium.

Indirect pumping can also be produced by photovoltaic converter which converts solar radiation into electricity.

Table 1-1 shows a typical comparison between the different types of known indirect solar pumped lasers [5], [6].

Laser Type	Efficiency of the laser component	Total Efficiency of the whole system
Photovoltaic Generator	12 % (with loss at voltage change)	---
Lampe pumped Nd:YAG System	3 – 4 %	0.4 – 0.5 %
Diode pumped Nd:YAG System	15 – 20 %	1.8 – 2.4 %
Diode laser	40 %	5 %
CO_2-Laser	25 %	3 %

Table 1-2 Typical comparison between the different types of the known indirect solar pumped laser.

(II) Direct pumping

Large concentrators focus the image of the sun to a relatively small volume (image), where the laser cavity exists. In such a case, the sun (accordingly the concentrated solar radiation at the focus) is the source of the pumping light needed to generate the laser.

One of the most important parameters in solar pumped lasers of this type is the wavelength overlap. This parameter is the overlapping between the standard solar emission spectrum and the laser absorption one. It enters in the calculations and affects the output laser power attained from the system of solar laser. This is because not all wavelength regions of the already concentrated solar spectrum are absorbed by the laser to populate the laser levels. The efficiency of this type of pumping is between 2 and 3% until now.

1.9 Comparison between different pumped lasers

The main disadvantage of indirect pumping is the big size of the electric generators and the technology of several steps. On the other hand, the main disadvantage of direct pumping is the waste heat produced from the un-utilised wavelengths by absorption in the lasing medium. This could be overcomed by cooling or chopping.

Table 1-2 shows an overlook of the advantages and the disadvantages of the often used pumping types of lasers [5], [6].

Laser Type		Advantages	Disadvantages
Lamp pumped Laser		1- Standard technology. 2- Independent of the time of the day, the seasons, and the weather.	1- Expensive. 2- Many-step process.
Diode pumped laser		1- Simple. 2- Independent of the time of the day, the seasons, and the weather. 3- Higher efficiency.	1- Very Expensive. 2- Pulsive operation. 3- Big needs by the constructive design
Solar pumped laser	Indirect solar pumped laser	1- Construction from standard components. 2- No tracking of the sun needed. 3- Environment friendly.	1- More expensive construction. 2- Very low efficiency. 3- Dependent on the time of the day, the seasons, and the weather. 4- Many-step process.
	Direct solar pumped laser	1- Reasonable price. 2- One-step process. 3- Middle efficiency. 4- No damageable parts. 5- Environment friendly.	1- Tracking of the sun needed. 2- Complicated adjustment of the optical components. 3- Dependent on the time of the day, the seasons, and the weather.

Table 1-3 Overlook of the advantages and the disadvantages of the often used pumping types of lasers.

To imagine the expected output that one could get from a solar pumped laser system built on the surface of the earth, we can have a look on Fig. 1-9 that represents the loss in the solar radiation power through the earth's atmosphere until it reaches the earth's surface.
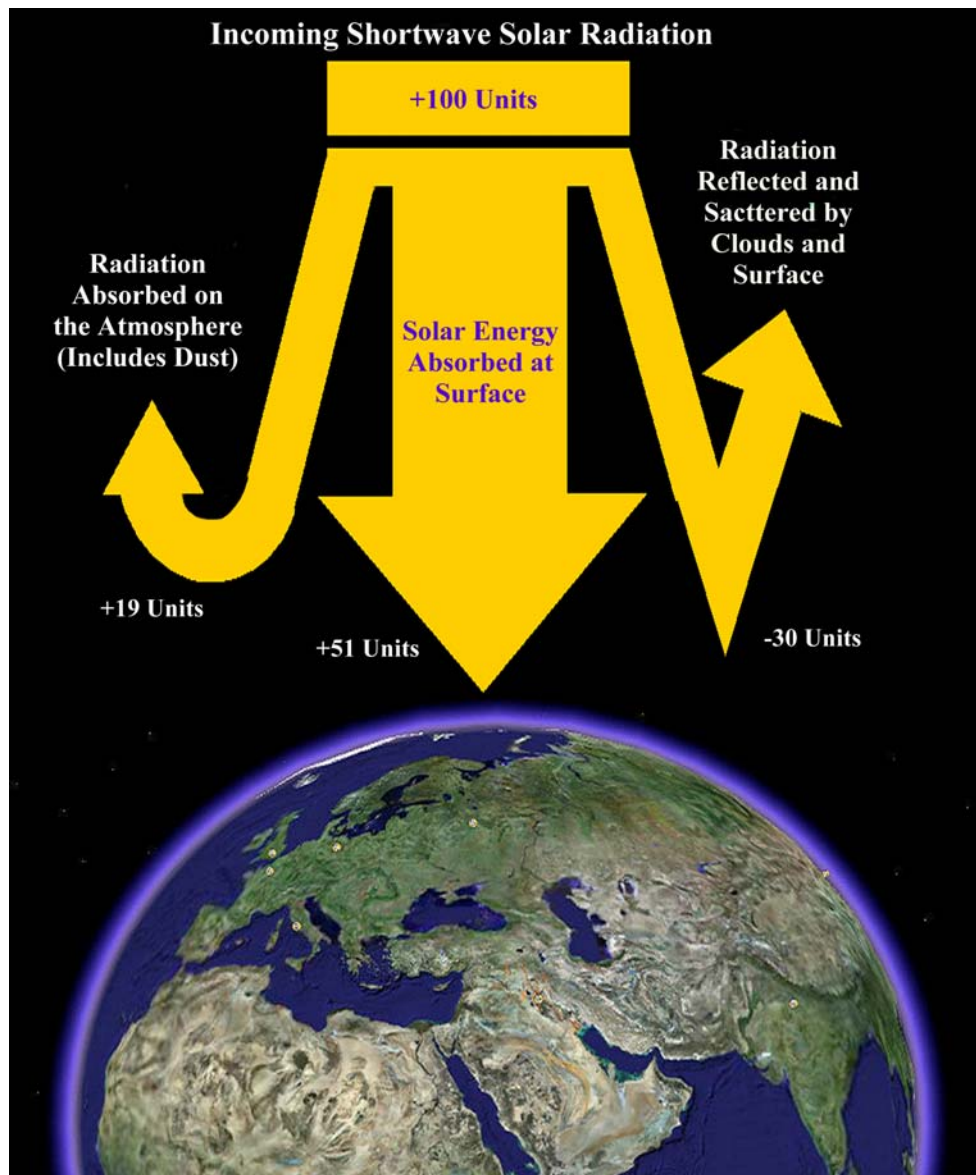
Fig. 1- 9 Solar radiation loss inside the earth atmosphere.

1.10 Types of direct solar laser pumping

In our research, we have used two techniques for solar pumping solid state lasers: side pumping and end pumping technique.

1- Side pumping:

In the side pumping technique, the concentrated solar radiation is inserted onto the side of a cylindrical laser rod. One can use a primary concentrator of the type of the parabolic or spherical dish or a Fresnel lens while the secondary one is of the type of the compound parabolic concentrator (CPC) or V-Trough Concentrator. This system can collect and concentrate the solar radiation onto the side of the previously mentioned laser rod. This laser rod is placed as an absorber of the secondary concentrator which is also in turn fixed in the

focus of the primary concentrator. Pumping will take place and the laser rays will be emitted. Fig. 1-10 shows a schematic design of a system generating the solar laser using the side pumping technique.

(a)

(b)
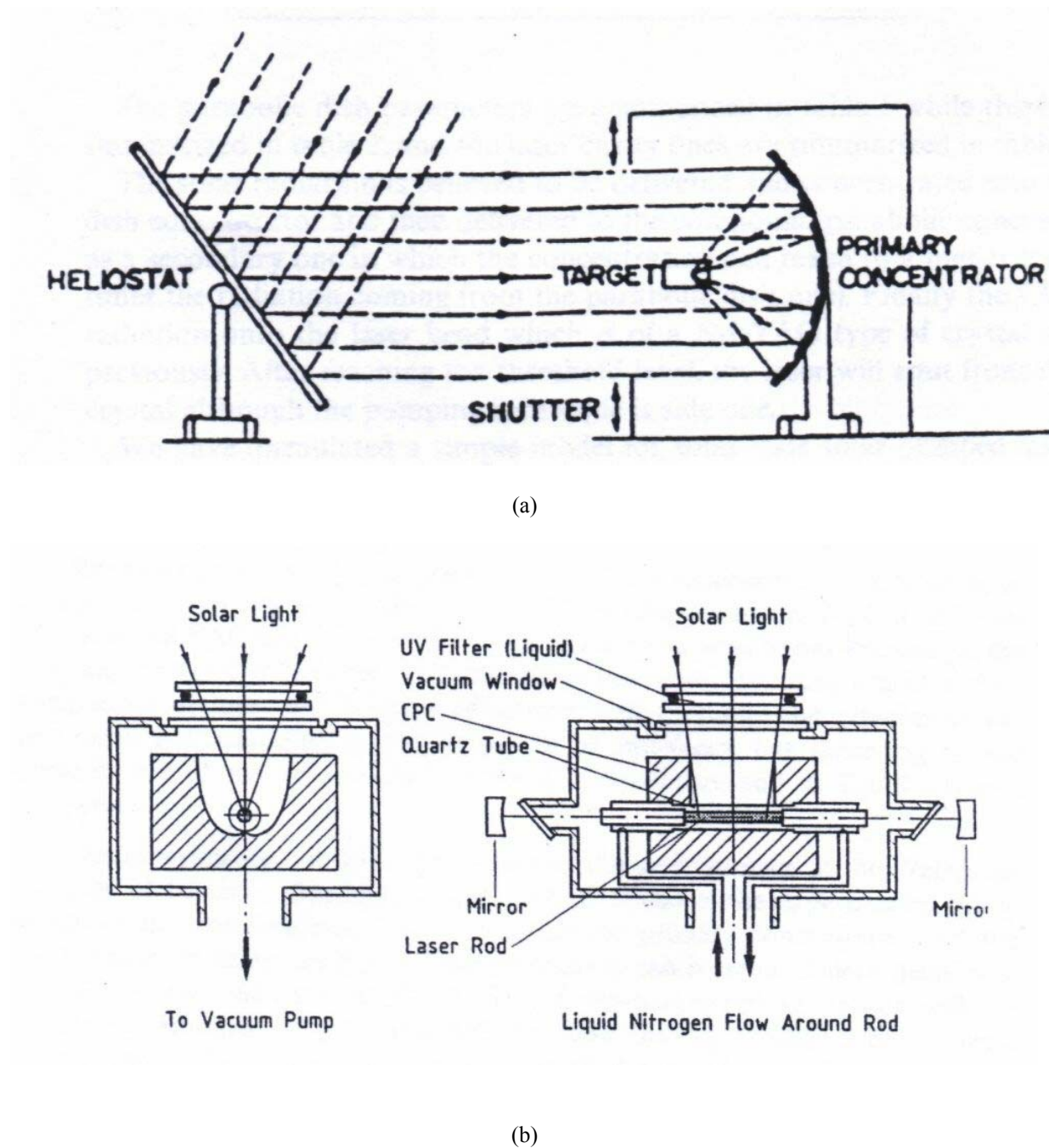
Fig. 1-10 Typical side pumping solar laser design.

2- End pumping:

In the end pumping technique, the concentrated solar radiation is applied onto one end of a laser rod. One can use a primary concentrator of the type of the parabolic or the spherical dish or the Fresnel lens, while the secondary one is of the type of the conical concentrator or

three-dimensional compound parabolic concentrator (3D-CPC). This system collects and concentrates the solar radiation onto one end of the laser rod which is placed as an absorber of the secondary concentrator. This laser rod is also in turn fixed in the focus of the primary concentrator and pumping again will take place and then the laser will be emitted. Fig. 1-11 shows a schematic design of a system generating the solar laser using the side pumping technique.
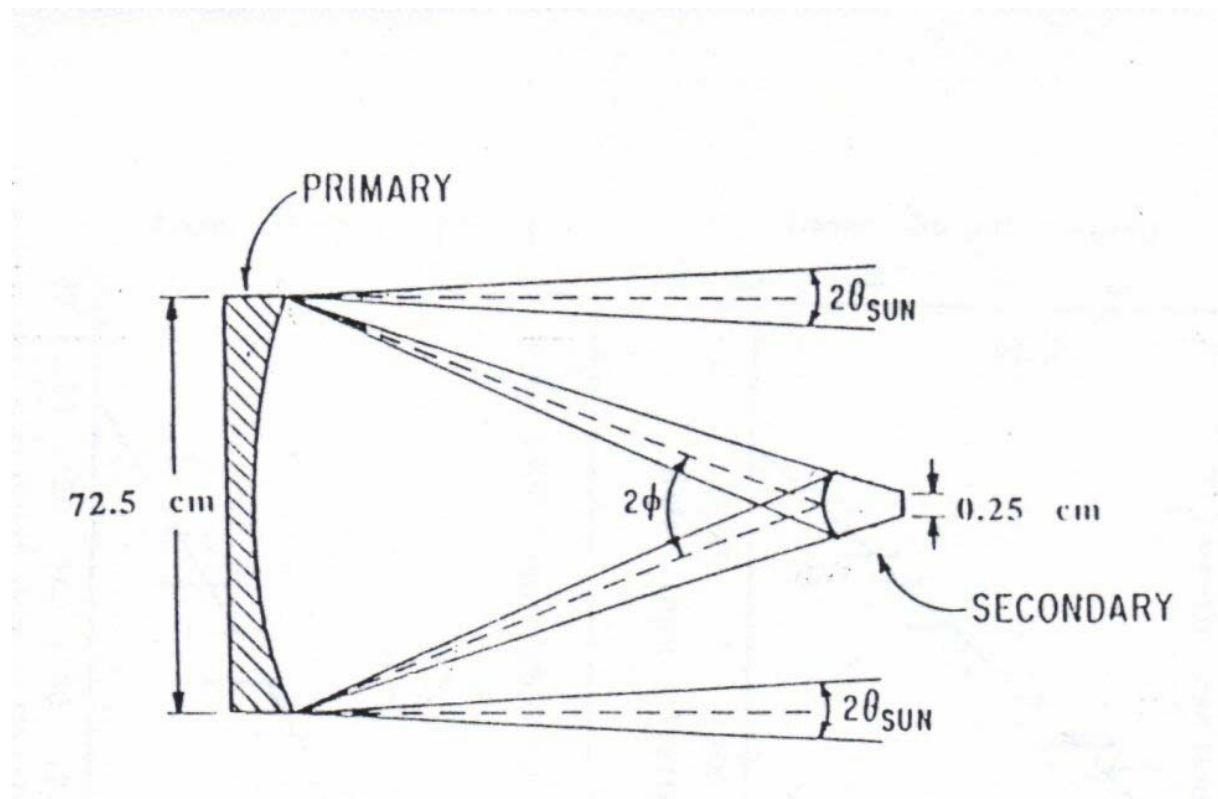
(a)
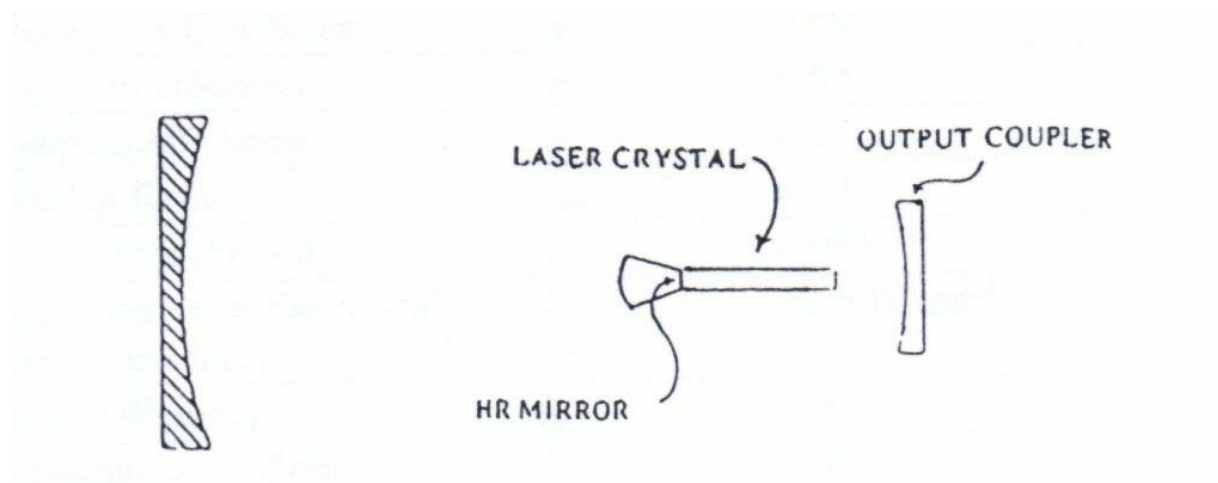
(b)

Fig. 1-11 Typical end pumping solar laser design.

1.11 Solar laser in space

The use of the solar laser in space was firstly enrolled in the research direction of generating laser radiation from the solar energy before doing it on the surface of the earth. In the outer space, one could use the whole solar energy avoiding the attenuation, the absorption and the reflection through the earth's atmosphere. Those physical actions decrease the useful part of the solar radiation needed to overcome the threshold pumping power of the laser medium. One also can say, in the outer space, we need smaller concentrators than on the earth's surface. This would decrease the costs of constructing huge instruments. But on the other hand, we have to remember the costs of pushing such devices into outer space and controlling them the whole time. For such a level of technology, a space shuttle is needed to push the system into the outer space until it orbits. It then has to be adjusted and directed to get the energy radiated from the sun. Fig. 1-12 shows a typical solar laser system used in the outer space [7].
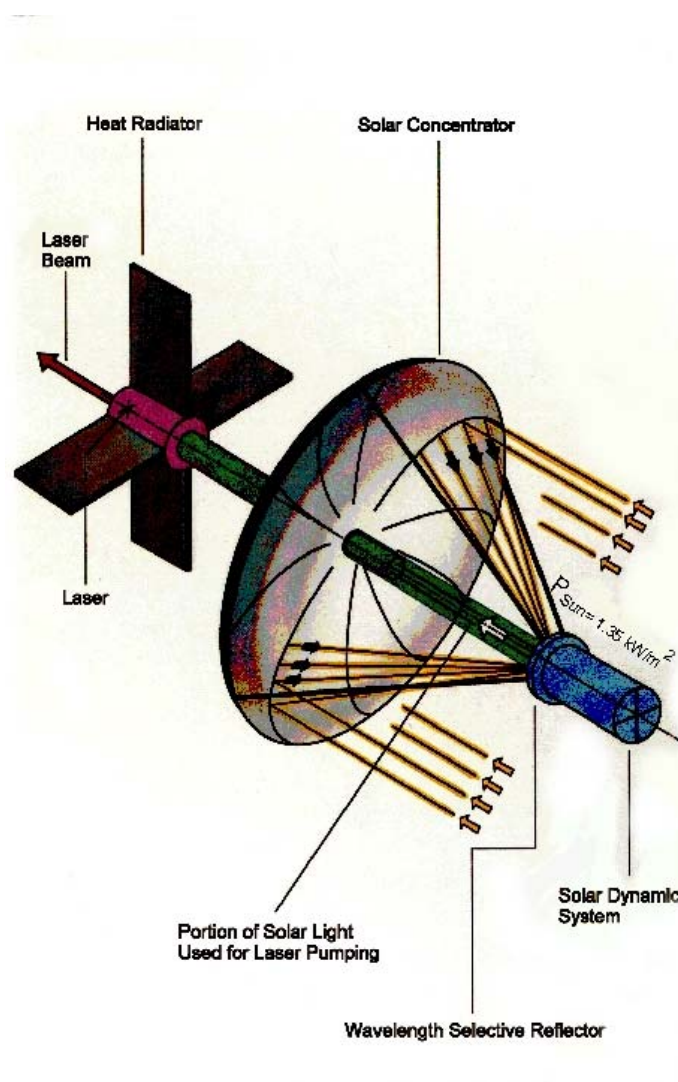
Fig. 1-12 Typical solar laser system used in the outer space.

Solar-pumped lasers are being developed for the direct conversion and transmission of solar power in space. Laser radiation is appropriate for power transmission in space because of the small divergence and the short wavelength of a laser beam compared to that generated by a microwave system. Applications of laser technology include:

1- Laser power transmission from space to Earth.
2- Laser propulsion of space-borne or air-borne vehicles.
3- Laser power transmission to remote spacecraft.
4- Deep-space communications.
5- Remote-sensing.
6- Materials-processing and manufacturing.

These applications are shown in Fig. 1-13.

Whilst conventional lasers powered by electrical energy could be used to transmit solar energy in space, direct solar-pumped lasers offer the advantage of eliminating the need for electrical power-generating plant. However, a laser system operating in space has a number of requirements imposed upon it including:

1- A gas or liquid-phase lasant for continuous cooling and recharging for operation at power levels greater than 1MW.

2- A high temperature operation to reduce cooling requirements.

3- A chemical reversibility to renew the lasant in space.

4- A broadband pumping to make efficient use of the available solar spectrum.
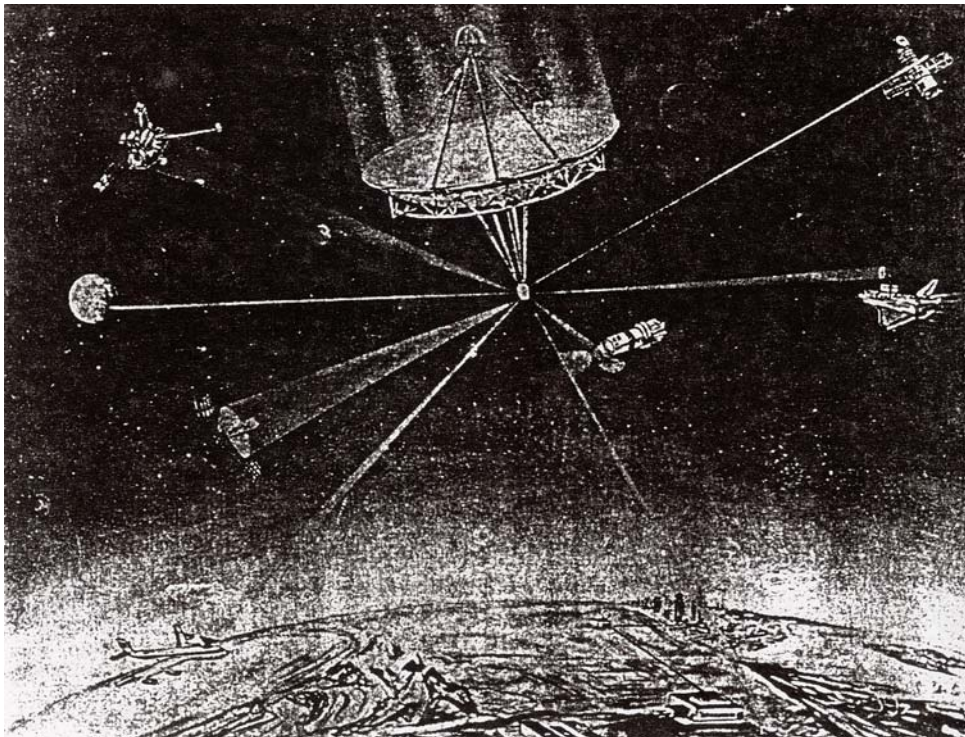
Fig. 1-13 Solar pumped laser applications.

"Solar pumping" in this context means that solar radiation directly and immediately makes the lasant material lase. The power output of solid state lasers is limited by the rate at which the laser rod can be cooled. Gas-dynamic solar-powered lasers (GDLs) use solar radiation to heat the lasant gas rather than make it lase directly. Consequently, equipment is required for the heating and recirculation of the lasant gas which makes GDL systems heavier and more complex than equivalent direct solar-pumped laser systems. The gas is stationary in a direct solar-pumped laser: solar radiation photodissociates the lasant gas to form excited atoms which emit coherent radiation upon de-excitation [8].

Recent researches have been directed towards the identification and assessment of lasant materials with pumping thresholds which are low enough to allow the use of parabolic trough concentrators (PTC). Such concentrators allow unrestricted laser gain length, are relatively simple to construct and enlarge and are thus being proposed for large-scale solar power systems in space [8].

The relative merits of parabolic dish, parabolic trough and conical concentrators for solar-pumped laser applications are summarized in Table 1-3.

Concentrator	Advantages	Disadvantages
Parabolic Dish	High concentration of solar radiation (~ 20,000)	• High tracking accuracies along two axes. • Concentrates over small volume and short length. • Difficult to enlarge. • Expensive, Complex.
Parabolic Trough	• Tracking accuracy required along one axis only. • Can be of unrestricted length. • Easy to enlarge. • Allow long laser gain length. • Simple to construct, Inexpensive.	Low concentration (~ 200 Solar Constants).
Conical	• Simple to construct. • Laser can be placed within cone. • Higher concentration than trough.	• Requires tracking accuracy along two axes. • Difficult to ensure even concentration of radiation along lasant. • Difficult to enlarge. • Finite length.

Table 1-4 Relative merits of concentrators for Space-based solar-pumped laser systems.

The advantages of the parabolic trough concentrator for use in solar-pumped lasers include its simplicity, as stated, and its low mass. It may be possible to use the Inflatable Space Rigidised Structure technology (ISRS) to create large low-mass concentrators for such systems. The disadvantage is that lasants with low thresholds which can be pumped by this

type of concentrator do not utilize a significant proportion of the solar spectrum and, consequently large concentrators will be required for such systems. Conversely, the optical-fibre solar-pumped laser system would require complex, high-mass concentrator arrays. However, the high concentration ratios which such systems may produce would allow the use of high-threshold lasants which make better use of available solar spectrum and will, consequently require less collector area than a parabolic trough system of equivalent output [8].

1.12 Previous work

In our research, we have used two techniques of solar pumping solid state laser; side pumping and end pumping ones. In the end pumping technique, we used a Fresnel lens as a primary concentrator to concentrate the solar radiation onto a crystal of the type Nd:YAG laser (Slab Laser). With the help of a collimator lens, we increased the concentration ratio applied to the laser crystal. In the side pumping technique, we used the same primary concentrator with a secondary glass concentrator of the type of compound cylindrical concentrator (CSC) to concentrate the solar radiation on a laser rod of the type $Nd:YVO_4$.

(a) Side pumping trend

For the side pumping trend, R. Winston and W. T. Welford [9] showed how paraboloidal mirrors of short focal ratio and similar systems can have their flux concentration enhanced to near the thermodynamic limit by the addition of nonimaging compound elliptical concentrators.

M. Weksler and J. Shwartz [10] obtained very interesting results in their experimental work. They scanned the focal plane of the primary concentrator to estimate the best position for fixing the absorber. Also, they constructed a complete system for side pumping technique for a solar laser system using a laser rod of the Nd:YAG type. This system was also provided with a cooling system which is a Pyrex cooling sleeve using a 1% solution of potassium chromate in water. The obtained performance curves showed that more than 60 Watts of output power was readily obtained from this solar-pumped Nd:YAG rod with a slope efficiency exceeding 2%.

U. Brauch et al. [11] carried out a comparison of solar pumped laser oscillators made of Nd:YAG and Nd:Cr:GSGG rods at 77 and 300 K. The comparison included the power achieved at various output coupling mirrors and a study of the beam divergence. The study showed that good quality beams, about four times the diffraction limit, can be extracted from a rod of 5 mm diameter and 62 mm exposed length. Maximal slope efficiency was 3.4 %. The power was 30 percent higher in the GSGG case than in the YAG case. The two cold runs showed 3 times higher power than the 300 K runs. The results established a sound base for the design of a high continuous wave power cold laser.

R. M. J. Benmair et al. [12] used Er, Tm, Ho:YAG to generate a solar pumped laser. They used the same system M. Weksler and J. Schwartz [10] used for the operation of Nd:YAG and Nd:Cr:GSGG. Slope efficiency values between 2.18 % and 3.28 % corresponding to output coupling values between 5 % and 30 % respectively for 5 msec and 20 % duty cycle exposures were attained.

K. H. Kim et al. [13] studied thermal effects on cavity stability of chromium- and neodymium-doped gadolinium scandium gallium garnet laser under solar simulator pumping. Only at low solar simulator beam intensities of up to 1500 solar constants (203 W/cm^2) was the laser operation lasting longer than 10 min achieved. For higher pump beam intensities of up to 2500 solar constants (338 W/cm^2), a quasi-cw-laser operation was obtained with continuously chopped pumping, with a duty cycle of 0.5 and a repetition rate of 13 Hz. The experimental results were compared with a calculated stability condition of the laser resonator for various pump powers and showed that the thermal focusing of the Cr:Nd:GSGG is 8-15 times greater than that of the neodymium-doped yttrium aluminium garnet (Nd:YAG) laser for the pump beam intensities from 1000 to 3000 solar constants.

I. H. Heon and J. H. Lee [14] studied the efficiency and threshold pump intensity of cw solar-pumped solid-state lasers. They worked on the Nd:YAG, Cr:Nd:GSGG, alexandrite and ruby lasers. For all laser materials the slope efficiency did not vary so much at the output mirror reflectances below 0.8, except for the 100 cm long laser rod. The dependence of the slope efficiency on the output mirror reflectances over 0.9 is, however, very strong; thus the slope efficiency reduces very rapidly with the increase of the reflectance. The threshold pump intensity decreases as the output mirror reflectance increases for all of the laser materials used in this work. It unexpectedly depends on the length of the laser rod, but does not at the reflectance near unity. The maximum achievable efficiency of Nd:YAG is estimated to be about 5 % with a 1 cm diameter laser rod when the pumping source is an air-mass-zero (AM0) solar radiation. Cr:Nd:GSGG crystal shows the maximum efficiency of about 12 % when the diameter laser crystal is 1 cm and when the threshold pump intensity at the output mirror reflectance of 99 % is about 100 AM0 s.c. The ruby crystal shows about 3 % slope efficiency but this crystal seems to have no practical worth due to its high threshold pump intensity. Alexandrite has a similar slope efficiency to Cr:Nd:GSGG; however, the threshold pump intensity depends very strongly on the output mirror reflectance so that the achievable effieciency is less than 10 % in the practical range for pump intensity. For all the laser materials used, the dominant deciding factor for the threshold pump intensity is the loss coefficient for a long laser rod.

U. Brauch et al. [15] constructed a side pumping solar laser system to compare between different laser types. Nd:YAG and Nd:Cr:GSGG laser types were selected according to their laser and physical properties. This comparison indicated that solar pumped solid state lasers, especially the Nd:Cr:GSGG laser, are the best choice for space-power transmission, while depending on the conditions, Nd:YAG lasers may also be useful. They have demonstrated that the thermal problems, associated with high power CW solid state lasers can be reduced dramatically by cooling. Their experiments with direct solar pumped Nd:Cr:GSGG and Nd:YAG lasers at 77 K and 300 K showed that cooling the laser crystals to temperatures much lower than 300 K reduces thermal problems, increases efficiency and improves beam quality. They have also shown that the overall system efficiency can be increased by splitting the solar spectrum into different parts for conversion to laser power and to electrical power. The estimated values were 17 % for a laser/photovoltaic system and 27 % for a laser/solar dynamic system.

U. Brauch et al. [16] constructed a similar system with different dimensions and studied experimentally the effect of the operating temperature on a number of physical quantities like the power, divergence and stress-induced birefringence. The coolant used was either room temperature water or pressurized liquid nitrogen. They also used two types of solid state laser rods, namely Nd:YAG and Nd:Cr:GSGG (neodymium- and chromium-doped gadolinium scandium gallium garnet). They also compared between the two types of lasers.

24

Y. A. Abdel-Hadi et al. [1] developed a numerical simulation model for the side pumping technique for use in the weather of Cairo (Egypt). They calculated the optimum conditions of choosing the concentrators system dimensions. The model scenario was the concentration of the solar energy using a primary concentrator of the type of parabolic dish with a 9.69 m diameter and 5.896 m focal length onto a secondary one of the type of compound parabolic concentrator (CPC) of 1.743 times concentration ratio. A Nd:YAG laser rod of 7.5 cm long and 6.25 mm diameter was used. Recorded data from the area of Helwan (30 Km south of Cairo) were applied to this model. The system of concentrators was used for two conditions. The first one was with filling the secondary concentrator with nothing but the air which has a refractive index of unity. The second one was with filling the secondary concentrator with the sapphire which has a refractive index of 1.76. In the first case, the maximum output laser power for such a simple system was 136.763 W (4.459 MW/m^2) in the Winter, 137.001 W (4.466 MW/m^2) in the Spring, 199.858 W (6.514 MW/m^2) in the Summer and 169.971 W (5.54 MW/m^2) in the Autumn. These results gave an average maximum laser output power of 160.8925 W (5.2448 MW/m^2) during the year. In the second case, the maximum laser output power was 247.99 W (8.083 MW/m^2) in the Winter, 248.407 W (8.097 MW/m^2) in the Spring, 359.036 W (11.7 MW/m^2) in the Summer and 306.435 W (9.988 MW/m^2) in the Autumn. These results gave an average maximum laser output power of 290.467 W (9.467 MW/m^2) during the year. The slope efficiency of such a system was 2 %.

N. Naftali, I. Pe'er and A. Yogev [17] developed a lab simulation which demonstrates the power beaming concept based on a solar pumped laser and a photovoltaic cell. The simulation included a parabolic dish, a 3D-CPC, a 2D-CPC as a laser head for transmission and a photovoltaic cell for converting the laser light into electricity. A Nd:YAG laser rod was solar pumped using imaging systems producing 52 Watt laser at Sun flux of 830 Watt/m^2. The solar light concentration assembly contained a Fresnel heliostat field as an initial concentrator stage, a parabolic dish as a second concentration stage, a 3D-CPC as third concentration stage and a 2D-CPC as a fourth (final) concentrator stage. The solar cell of dimensions of 11 mm × 11 mm was exposed to a laser light using Nd:YAG and Alexandrite lasers respectively. The efficiencies achieved were 33 % laser to electricity efficiency for the Nd:YAG laser and ~ 40 % for the Alexandrite.

M. Lando et al. [18] reported on two visible solar-pumped lasers; a red alexandrite laser with a potential tunability range between 700 and 818 nm, and a frequency doubled Nd:YAG laser operating at 532 nm. Highly concentrated solar energy was obtained by a 3-stage concentrator (12 Fresnel parabolic heliostats of 52 m^2 in area, directing the solar radiation to the 12th floor of a solar tower as a first stage, a 3D-CPC as a second stage and a 2D-CPC as a final stage). An output power of up to 12 W was obtained from the alexandrite laser. The Q-switched Nd:YAG laser employed a type II KTP crystal for interactivity frequency doubling. Q-switching was obtained either passively or actively. In the passive Q-switching version, a water cooled Cr^{+4}:YAG crystal was introduced into a laser cavity acting as both a saturable absorber and a laser rear mirror, and enforced high repetition rate operation between 10 and 50 kHz. The average output power at 532 nm was 4.1 W. With an active acousto-optic modulator introduced between the laser rod and the high reflection rear mirror, the average output power at 532 nm and 7.3 kHz repetition rate was 8.7 W.

M. Lando et al. [19] studied the passive Q-switching of a solar-pumped Nd:YAG laser. They demonstrated the superior thermal characteristics and durability of Cr^{4+}:YAG single crystals as passive Q switches for lamp and diode-pumped high-power lasers. They also reported on an average power of 37 W and a switching efficiency of 80 % obtained when

using a solar-pumped Nd:YAG laser Q switched by a Cr^{4+}:YAG saturable absorber. They used a three-stage concentrator, composed of 12 heliostats, a 3D-CPC and a 2D-CPC. The water-cooled passive Q-switch also served as the laser rear mirror. Repetition rates of as much as 50 kHz, at pulse durations between 190 and 310 ns (FWHM) were achieved. The saturated single-pass power absorption of the Cr^{4+}:YAG device was estimated as 3 ± 1 %.

M. Lando et al. [20] reported on solar side-pumped Nd:YAG laser experiments, which included comprehensive beam quality measurements and demonstrated record collection efficiency and day long operation. A 5.75 m^2 segmented primary mirror was mounted on a commercial two-axis positioner and focused the solar radiation towards a stationary non-imaging-optics secondary concentrator, which illuminated a Nd:YAG laser rod. Solar side-pumped laser experiments were conducted in both the low and the high pumping density regimes. The low density system was composed of a 89 × 98-mm^2 aperture two-dimensional compound parabolic concentrator (CPC) and a 10 mm diameter, 130 mm long Nd:YAG laser rod. The laser emitted up to 46 W and operated continuously for 5 hours. The high density system was composed of a three-dimensional CPC with 98 mm entrance diameter and 24 mm exit diameter, followed by a two-dimensional CPC with a rectangular 24 × 33 mm^2 aperture. It pumped a 6-mm diameter 72 mm long Nd:YAG laser rod, which emitted up to 45 W. The results constituted a record collection efficiency of 6.7 W/m^2 of primary mirror. A scaled up design for a 400 W laser pumped by a solar collection area of 60 m^2, incorporating simultaneously high collection efficiency and high pumping density, was presented.

(b) End pumping trend

In the same way, for the side pumping trend, C. G. Young [21] generated a sun-pumped cw 1 W laser using a cassegrain sun-tracking telescope consisting of a 61 cm diameter *f/1.5* aluminized paraboloidal primary mirror, a water-cooled hyperbolic-cylindric secondary mirror, a hemicircular cylindric tertiary mirror as a primary concentrator and a silver reflecting cone as a secondary concentrator. The collector was mounted in an equatorial mount that included an adjustable polar axis angle, motor-driven right ascension drive, sighting telescope. Locks and vernier adjustments were on the right ascension and declination axes. The used lasers are of the type Nd:YAG crystal and Nd:Glass. It was found, that for the first type of laser crystal, while 0.8 W of laser output emerged from the transmitting end, 0.2 W was radiated from the opposite end. The sun-pumped laser was operated many times from June through October at a latitude of 42° N. Final adjustment and maximum output were obtained in late October. Operation over many hours was obtained with no evidence of reduction of output. Temporally, the output of the sun-pumped YAG was spike-free during continuous operation, although the output is spiked under flashlamp excitation. Spatially, assuming that the beam spread obtained from tungsten-lamp pumped YAG, it should be possible to reduce the output beam spread to a milliradian by the use of a 10 X afocal telescope having a 30-mm objective. For the neodymium-doped glass type of laser, the power output obtained was 1.25 W. With dielectric-end mirrors, rather than the silver used here, the output would probably be higher.

P. Gleckman [22] constructed an end pumping two-stage solar concentrator consisting of 40.6 cm diameter primary which forms a 0.98 cm diameter image and a nonimaging refracting secondary with index n = 1.53 (i.e. filled with oil). The types of lasers used are Nd:YAG and Nd:Cr:GSGG. The geometrical concentration ratio is 102,000 times. The highest irradiance value achieved was 4.4 ± 0.2 kW/cm^2, or 56,000 ± 5000 suns, relative to a solar insolation of 800 W/m^2. With this two-stage system, 55 W of sunlight was squeezed

into a spot 1.27 mm in diameter with a 55% efficiency. With this efficiency, two-stage end pumping of solid state laser rods had the potential for an improvement on the previous direct-pumped solar laser.

Also, R. Winston et al. [23] worked on the end pumping technique; they constructed a complete system of this trend also using the two types of laser rods previously mentioned. They plotted the performance curve and then they calculated the pumping and slope efficiencies for each type. They succeeded in using a system of two concentrators to reach a concentration level up to 84,000 times. Using a spphire concentrator with a refractive index n=1.76, the laser reached an incident intensity of 72 W/mm^2. Such a high intensity exceeds the intensity of light at the surface of the sun itself (63 W/mm^2).

G. Phillipps [24] developed a theoretical study of solar-pumped laser using an optical fibre to deliver the solar radiation to a lens or to a lens system constructed at the end of the crystal. This lens or lens system will concentrate the radiation and will direct it onto the laser medium. In the case of Nd:YAG, the system gave an output of 1.7 W with a collecting area of 0.41 m^2 from the input power of 200 W. The slope efficiency of that system was found to be 0.85. In the case of Nd:Cr:GSGG, the output power is 3.2 W with a collecting area of 0.41 m^2 from the input power of 200 W. The slope efficiency of that system was found to be 1.6%.

Y. A. Abdel-Hadi et al. [1] developed a numerical simulation model for the end pumping technique to use it in the Cairo (Egypt) weather. They calculated the optimum conditions for choosing the concentration system dimensions. The model scenario was the concentration of the solar energy using a primary concentrator of the type parabolic dish with a diameter of 0.807 m and a focal length of 0.49 m onto a secondary conical concentrator of 5.59 times concentration ratio. A Nd:YAG laser rod of 2 cm long and 2.5 mm diameter was used. Recorded data in the area of Helwan (30 Km south of Cairo) were applied to this model. The system of concentration was used for two conditions. The first one was with filling the secondary concentrator with nothing but air which has a refractive index of unity. The second one was with filling the secondary concentrator with sapphire which has a refractive index of 1.76. In the first case, the maximum laser output power for such a simple system was 0.515 W (0.1048 MW/m^2) in the Winter, 0.518 W (0.1055 MW/m^2) in the Spring, 1.398 W (0.2848 MW/m^2) in the Summer and 0.979 W (0.1995 MW/m^2) in the Autumn. These results gave an average maximum laser output power of 0.8528 W (0.17365 MW/m^2) during the year. In the second case, the maximum laser output power was 4.812 W (0.9802 MW/m^2) in the Winter, 4.822 W (0.9823 MW/m^2) in the Spring, 7.547 W (1.538 MW/m^2) in the Summer and 6.252 W (1.274 MW/m^2) in the Autumn. These results gave an average maximum output laser power of 5.5853 W (1.1936 MW/m^2) during the year. The slope efficiency of such system was 2.4 %.

I. Pe'er et al. [25] reported the design and experimental realization of a solar pumped dimmer gas-laser. The amplifying medium is Te_2 gas, which is capable of amplifying laser signals over a broad spectral range. They used a parabolic heliostat (sun tracking mirror) to illuminate a 1-m^2 segmented parabolic dish. The dish reflects the sunlight onto a three-dimensional compound parabolic concentrator (3D CPC) with a concentration ratio of 4.53. The light from the compound parabolic concentrator enters a light guide. A Te_2 quartz cell is place inside the light guide. Its central part is a cylindrical cell with Brewster windows surrounded by a double wall. Hot CO_2 flows in and out through the tubes and enables the experimenters to control the temperature of the cell. A gain of 42 ± 1 % was measured at a wavelength of 632.8 nm by passing a modulated 3-mW He-Ne laser beam through the Te_2 gas

medium and measuring its intensity with and without solar pumping. The measured power on the detector after the gain medium was 7.6 mW, of which 3.3 mW was solar contribution and 4.3 was the amplified laser intensity. They also presented studies of the material characteristics and a brief review of the study of other candidate materials for solar pumping.

1.13 The aim of the project

We can summarize our aim of this work in the following points:

1- Getting an alternative method for using solar energy.

2- Transformation of the solar energy directly to laser radiation without conversion to electrical energy.

3- Beginning of large scale projects for using the solar energy to generate the laser beam needed in different fields of recent technologies.

Chapter 2: Theory of Lasers

Overview

In this chapter, information about the laser as a special type of radiation device is discussed. Its properties are discussed in detail. Also, the equations of operation are derived and discussed. The parameters affecting its operation are also mentioned. More details about the types of laser used in our work (Nd:YAG and Nd:YVO$_4$ laser) are discussed. Some definitions used in our work are mentioned. Finally, the introducing of solar energy as a recommended solution for laser beam generation is mentioned.

2.1 Introduction

The word LASER is an acronym for **L**ight **A**mplification by **S**timulated **E**mission of **R**adiation. The history of this field began in 1917, when Albert Einstein showed that the process of stimulated emission existed. This was the beginning of proving a new type of emitted radiation existed [26].

During the twenties, thirties and forties of the last century, physicists were occupied with the new discoveries in quantum mechanics, particle physics and nuclear physics. For the most part, the possibility of laser action lay dormant, although the needs of science and technology for such a device grew for many fields like: telecommunications, engineering and ophthalmology, etc [26].

Experience gained in the development of radar during World War II and the continuation of such work at higher microwave frequencies prompted scientists to explore the conditions that are necessary for laser action to be achieved.

In the early fifties, a group at Colombia University, U.S.A headed by Charles. H. Townes operated a microwave device that amplified radiation by the stimulated emission process. The device was termed a MASER, an acronym for Microwave Amplification by Stimulated Emission of Radiation. During the remainder of the fifties, the maser principle was employed with many materials. In 1958, Townes and Arthur L. Schawlow published an important paper in which they discussed the extension of maser principles to the optical region of the electromagnetic spectrum [26].

By 1960, a number of groups were investigating systems that might serve as the basis for an optical maser, as it was called by some laser action at optical frequencies is given to T. H. Maiman of the Hughes Research Laboratories. His laser consisted of a pink ruby rod with silver end coatings acting as mirrors. This device was inserted into a helical coil of the photographic flashlamp.

Within six months of the invention of the ruby laser, laser action was obtained in a mixture of helium and neon gases.

The development of lasers since 1960 has been extremely rapid and although applications for lasers had a very slow start during their first decade, many new applications for laser radiation are being found now almost every day [26].

2.2 Emission and Absorption of radiation

When an electron in an atom undergoes transitions between two energy states or levels it either emits or absorbs a photon which can be described in terms of wave of frequency $\nu = \Delta E/h$, ΔE being the energy difference between the two levels concerned. Let us consider the electron transitions which may occur between the two energy levels of the hypothetical atomic system shown in Fig. 2-1. If the electron is in the lower level E_1 then in the presence of a photon of energy $(E_2 - E_1)$ it may be excited to the upper level E_2 by absorbing the photon. Alternatively if the electron is in the level E_2 it may return to the ground state with the emission of the photon. The emission process may occur in two distinct ways. These are:

(a) The spontaneous emission process:
In which the electron drops to the lower level in an entirely random way.

(b) The stimulated emission process:
In which the electron is 'triggered' to undergo the transition by the presence of photons of energy $(E_2 - E_1)$.
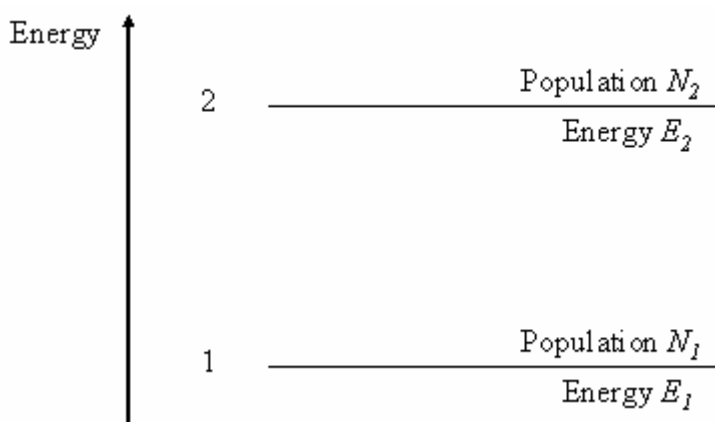
Fig. 2-1 Two level energy system.

The absorption and emission processes are illustrated in Figs. 3-2 (a), (b) and (c). Under normal circumstances we do not observe the stimulated process because the probability of the spontaneous process occurring is much higher. The average time the electron exists in the excited state before making a spontaneous transition is called the lifetime τ_{21} of the excited state. The '21' here indicates the energy levels involved. The probability that a particular atom will undergo spontaneous emission within a time interval dt is given by $A_{21}dt = dt/\tau_{21}$, where A_{21} is the spontaneous transition rate. Because the spontaneous radiation from any atom is emitted as random radiation, a large number of atoms clearly will be incoherent. In contrast to this the stimulated emission process results in coherent radiation as the waves associated with the stimulating and stimulated photons are identical in frequencies, phase and

polarization. This means that stimulated emission generates a light wave that grows as it passes through a collection of atoms. This is clearly an amplification process [26].

Initial State   Final State

Stimulated
Absorption

(a)

Spontaneous
Emission

(b)

Stimulated
Emission

(c)
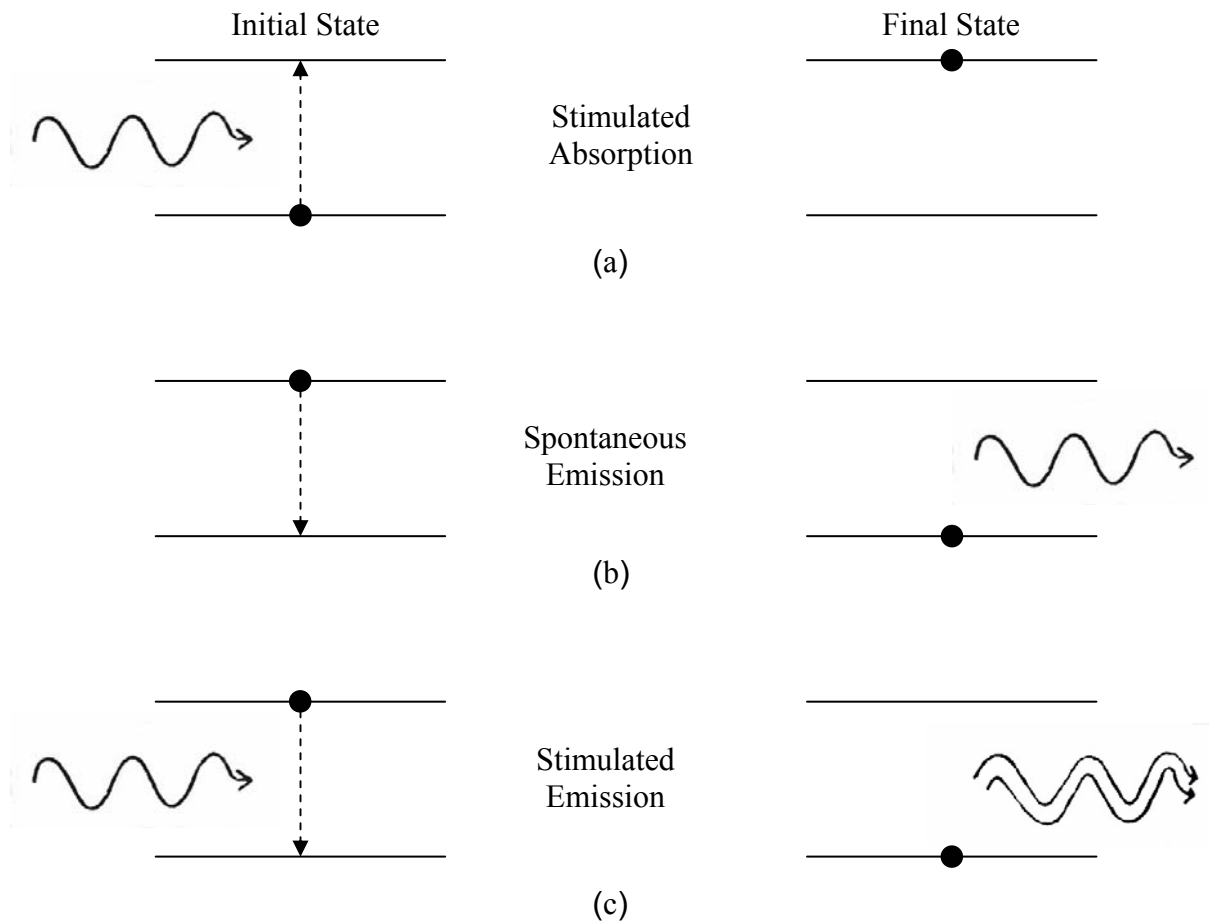
Fig. 2-2 Energy levels diagram illustrating (a) absorption, (b) spontaneous emission and (c) stimulated emission. The black dot indicates the state of the atom before and after the transition.

A quantum mechanical treament of the interaction between radiation and matter demonstrates that the stimulated emission is, in fact, completely indistinguishable from the stimulating radiation field. This means that the stimulated radiation has the same directional properties, same polarization, same phase, and same spectral characteristics as the stimulating emission. These facts are responsible for the extremely high degree of coherence which characterizes the emission from lasers. The fundamental nature of the induced or stimulated emission process was already described by A. Einstein and M. Planck [27].

In solid-state lasers, the energy levels and the associated transition frequencies result from the different quantum energy levels or allowed quantum states of the electrons orbiting about the nuclei of atoms. In addition to the electronic transitions, multi-atom molecules in gases exhibit energy levels that arise from the vibrational and rotational motions of the molecule as a whole [27].

2.3 The Einstein relations

Einstein showed that the parameters describing the above three processes are related through the requirement that for a system in thermal equilibrium the rate of upward transitions (from E_1 to E_2) must equal the rate of the downward transition processes [26].

If there are N_1 atoms per unit volume with energy E_1, then the upward transition or absorption rate will be proportional to both N_1 and to the number of photons available at the correct frequency. Now, the energy density ρ_ν at frequency ν, is given by:

$$\rho_\nu = nh\nu$$

where n is the number of photons per unit volume having frequency ν. Therefore we may write the upward transition rate as $N_1\rho_\nu B_{12}$, where B_{12} is a constant of the material. Similarly if there are N_2 atoms per unit volume in the collection with energy E_2 then the induced transition rate from level 2 to level 1 is $N_2\rho_\nu B_{21}$, where B_{21} is a constant. The total downward transition rate is the sum of the induced and spontaneous contributions, i.e.

$$N_2\rho_\nu B_{21} + N_1 A_{21}$$

A_{21}, B_{21} and B_{12} are called the *Einstein Coefficients*; the relationships between them can be established as follows.

For a system in equilibrium the upward and downward transition rates must be equal and hence we have

$$N_1\rho_\nu B_{12} = N_2\rho_\nu B_{21} + N_1 A_{21} \qquad (2\text{-}1)$$

thus:

$$\rho_\nu = \frac{N_2 A_{21}}{N_1 B_{12} - N_2 B_{21}}$$

or:

$$\rho_v = \frac{A_{21}/B_{21}}{\dfrac{B_{12}}{B_{21}}\dfrac{N_1}{N_2} - 1} \tag{2-2}$$

Now the populations of the various energy levels of a system in thermal equilibrium are given by Boltzmann statistics to be:

$$N_j = \frac{g_j N_o \exp(-E_j/kT)}{\sum\limits_i g_i \exp(-E_i/kT)} \tag{2-3}$$

where N_o is the total number of atoms and g_j is the degeneracy of the *jth* level. Hence

$$\frac{N_1}{N_2} = \frac{g_1}{g_2}\exp((E_2 - E_1)/kT) = \frac{g_1}{g_2}\exp(h\nu/kT) \tag{2-4}$$

Therefore, substituting Equation (3-4) into Equation (3-2) gives

$$\rho_v = \frac{A_{21}/B_{21}}{\left[\dfrac{g_1}{g_2}\dfrac{B_{12}}{B_{21}}\exp(h\nu/kT)\right] - 1} \tag{2-5}$$

We are considering the system being in thermal equilibrium. The collection of atoms must then give rise to radiation which is identical to blackbody radiation, the radiation density of which can be described by

$$\rho_v = \frac{8\pi h \nu^3}{C^3}\left(\frac{1}{\exp(h\nu/kT) - 1}\right) \tag{2-6}$$

Comparing Equations (3-5) and (3-6) for ρ_v we see that

$$g_1 B_{12} = g_2 B_{21} \tag{2-7}$$

and

$$\frac{A_{21}}{B_{21}} = \frac{8\pi h \nu^3}{c^3} \qquad (2\text{-}8)$$

Equation (2-7) and (2-8) are referred to as the *Einstein relations*. The second relation enables us to evaluate the ratio of the rate of spontaneous emission to the rate of stimulated emission for a given pair of energy levels. We see that this ratio is given by

$$R = \frac{A_{21}}{\rho_\nu B_{21}} \qquad (2\text{-}9)$$

which also can be written as

$$R = exp(h\nu/kT)\text{-}1$$

The above discussion indicates that the process of stimulated emission competes with the processes of spontaneous emission and absorption. Clearly if we wish to amplify a beam of light by stimulated emission then we must increase the rate of this process in relation to the other two processes. Consideration of Equation (2-1) indicates that to achieve this for a given pair of energy levels we must increase both the radiation density and the population density N_2 of the upper level in relation to the population density N_1 of the lower level. Indeed, we shall show that to produce laser action we must create a condition in which $N_2 > (g_2/g_2)N_1$ even though $E_2 > E_1$, that is we must create a so-called *population inversion*. Before describing this situation in detail it will be instructive to look more closely at the process of absorption [26].

2.4 Absorption and Stimulated Emission of radiation

Consider a collimated beam of perfectly monochromatic radiation of unit cross-sectional area passing through an absorbing medium. We assume for simplicity that there is only one relevant electron transition, which occurs between the energy levels E_1 and E_2. Then the change in irradiance of the beam as a function of distance is given by

$$\Delta I(x) = I(x + \Delta x) \text{ - } I(x)$$

For a homogeneous medium $\Delta I(x)$ is proportional both to the distance traveled Δx and $I(x)$. That is $\Delta I(x) = \text{-}\alpha I(x)\Delta x$, where the constant of proportionality, α is the *absorption coefficient*. The negative sign indicates the reduction in beam irradiance due to absorption as α is a positive quantity. Writing this expression as a differential equation we have:

$$\frac{dI(x)}{dx} = -\alpha I(x)$$

Integrating this equation gives:

$$I = I_O e^{-\alpha x} \qquad\qquad (2\text{-}10)$$

where I_O is the incident irradiance.

Consider the absorption coefficient in more detail. It is clear that the degree of absorption of the beam will depend on how many atoms N_1 there are with electrons in the lower energy state E_1 and on how many atoms N_2 there are in the upper energy state E_2. If N_2 were zero then absorption would be a maximum, while if all of the atoms were in the upper state the absorption would be zero and the probability of stimulated emission would be large.

We can write an expression for the net rate of loss of photons per unit volume, $-dN/dt$, from the beam, as it travels through a volume element of medium of thickness Δx and unit cross-sectional area (Fig. 2-3) as:

$$-dN/dt = N_1 \rho_v B_{12} - N_2 \rho_v B_{21}$$

or substituting from Equation (2-7)

$$-dN/dt = ((g_2/g_1)N_1 - N_2)\, \rho_v B_{21} \qquad\qquad (2\text{-}11)$$

In this discussion we have deliberately ignored photons generated by spontaneous emission as these are emitted randomly in all directions and do not therefore contribute to the collimated beam. Similarly we have ignored scattering losses [26].
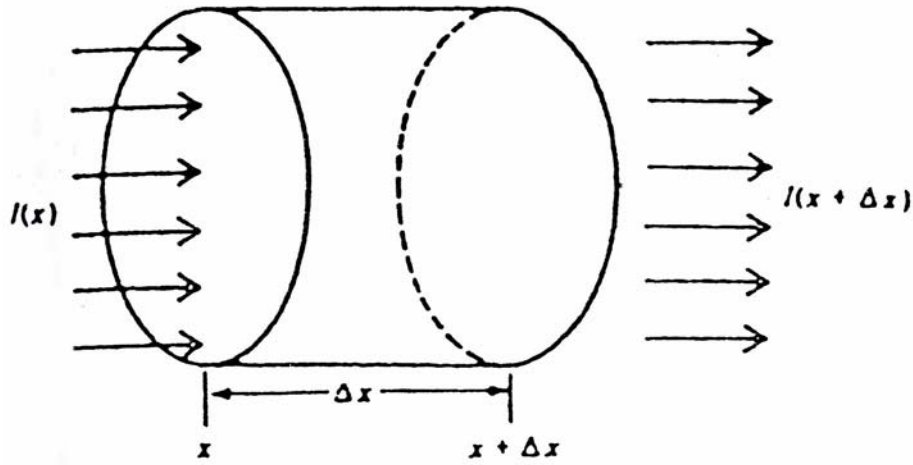
Fig. 2-3 Radiation passing through a volume element of length Δx and unit cross-sectional area.

We can now link Equation (2-11), which contains the difference in populations of the two energy levels, to the absorption coefficient α. We recall that the irradiance of the beam is the energy crossing unit area in unit time and therefore is given by the energy density ρ times the speed of light in the medium, that is $I = \rho c/n$. For photons of frequency ν

$$I_\nu = \rho_\nu \, c/n = N \, h\nu c/n$$

where c is the speed of light *in vacuum* and n is the refractive index of the medium. Hence the change in photon density within the beam between the boundaries x and $x + \Delta x$ of the volume element can be written as:

$$- dN(x) = [I(x) - I(x + \Delta x)](n/h \nu_{21} c)$$

If Δx is sufficiently small we can rewrite this equation as:

$$- dN(x) = -\frac{dI(x)}{dx} \frac{\Delta x n}{h\nu_{21} c}$$

Thus, the rate of decay of photon density in a time interval $dt \, (= \Delta x/c/n)$ is:

36

$$dN(x)/dt = \frac{dI(x)}{dx} \frac{1}{h\nu_{21}}$$

and substituting for dI/dx from Equation (2-10) gives:

$$dN(x)/dt = -\alpha I(x)(1/h\nu_{21}) = -\alpha\rho_v(c/n)(1/h\nu_{21}) \tag{2-12}$$

Hence comparing Equations (2-11) and (2-12) we have:

$$\alpha\rho_v \frac{c}{n} \frac{1}{h\nu_{21}} = \left(\frac{g_2}{g_1} N_1 - N_2\right)\rho_v B_{21}$$

Therefore the absorption coefficient α is given by:

$$\alpha = \left(\frac{g_2}{g_1} N_1 - N_2\right)\frac{B_{21}h\nu_{21}n}{c} \tag{2-13}$$

We see from Equation (2-13) that α, as we supposed earlier, depends on the difference in the populations of the two energy levels E_1 and E_2. For a collection of atoms in thermal equilibrium, since $E_2 > E_1$, $(g_2/g_1)N_1$ will always be greater than N_2 (Equation (2-4)) and hence α is positive. If, however, we can create a situation in which N_2 becomes greater than $(g_2/g_1)N_1$ then α is negative and the quantity $(-\alpha x)$ in the exponent of Equation (2-10) becomes positive. Thus the irradiance of the beam grows as it propagates through the medium in accordance with the equation:

$$I = I_0 e^{-kx} \tag{2-14}$$

where k is referred to as the *small signal gain coefficient* and is given by:

$$k = \left(N_2 - \frac{g_2}{g_1} N_1\right)\frac{B_{21}h\nu_{21}n}{c} \tag{2-15}$$

2.5 Population inversion

The population inversion condition required for light amplification is a non-equilibrium distribution of atoms among the various energy levels of the atomic system. The Boltzmann distribution which applies to a system in thermal equilibrium is given by Equation (2-3) and is illustrated in Fig. 2-4 (a); N_j is the number of atoms in the *jth* energy level and clearly as E_j increases N_j decreases for a constant temperature. We note that if the energy difference between E_1 and E_2 were nearly equal to kT ($\cong 0.0025$ eV at room temperature) then the population of the upper level would be *1/e* or 0.37 of the lower level. For an energy difference large enough to give visible radiation ($\cong 2.0$ eV), however, the population of the upper level at room temperature is almost negligible [26].

Clearly then, if we are to create a population inversion, illustrated in Fig. 2-4 (b), we must supply a large amount of energy to excite atoms into the upper level E_2. This excitation process is called *pumping* and much of the technology of lasers is concerned with how the pumping energy can be supplied to a given laser system. Pumping produces a non-thermal equilibrium situation; we shall now consider in general terms how pumping enables a population inversion to be achieved [26].
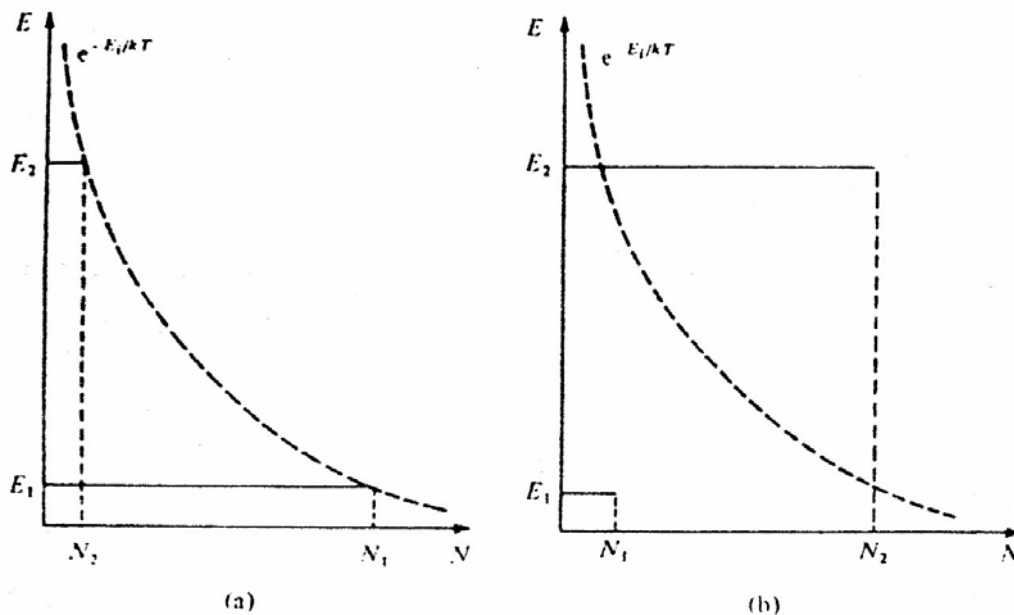
Fig. 2-4 Populations of a two level energy system: (a) in thermal equilibrium and (b) after a population inversion has been produced.

2.5.1 Attainment of a population inversion

One of the methods used for pumping is stimulated absorption that is the energy levels which one hopes to use for laser action are pumped by intense irradiation of the system. Now as B_{12} and B_{21} are equal (assuming $g_1 = g_2$), the probabilities of further stimulated absorption or emission are equal once atoms are excited into the upper level. Even with very intense

pumping the best that can be achieved with the two level system, considered hitherto, is equality of the populations of the two levels [26].

As a consequence we must look for materials with either three or four energy level system; this is not really a disadvantage as atomic systems generally have a large number of energy levels.

The three level system first proposed by Bloembegen is illustrated in Fig. 2-5. Initially the distribution obeys the Boltzmann law. If the collection of atoms is intensely illuminated the electrons can be excited (i.e. pumped) into the level E_2 from the ground state E_o. From E_2 the electrons decay by non-radiative processes to the level E_1 and a population inversion may be created between E_1 and E_o. Ideally the transition from level E_2 to E_1 should be very rapid, thereby ensuring that there are always vacant states at E_2, while that from E_1 to E_o should be very slow, that is E_1 should be a *metastable* state. This allows a large build-up in the number of atoms in level E_1, as the probability of spontaneous emission is relatively small. Eventually N_1 may become greater than N_o and then population inversion will have been achieved.

The level E_2 should preferably consist of a large number of closely spaced levels so that pumping uses as wide a part of the spectral range of the pumping radiation as possible, thereby increasing the pumping efficiency. Even so, three level lasers, for example ruby, require very high pump powers because the terminal level of the laser transition is the ground state. This means that rather more than half of the ground state atoms (this number is usually very nearly equal to the total number of atoms in the collection) have to be pumped to the upper state to achieve a population inversion.
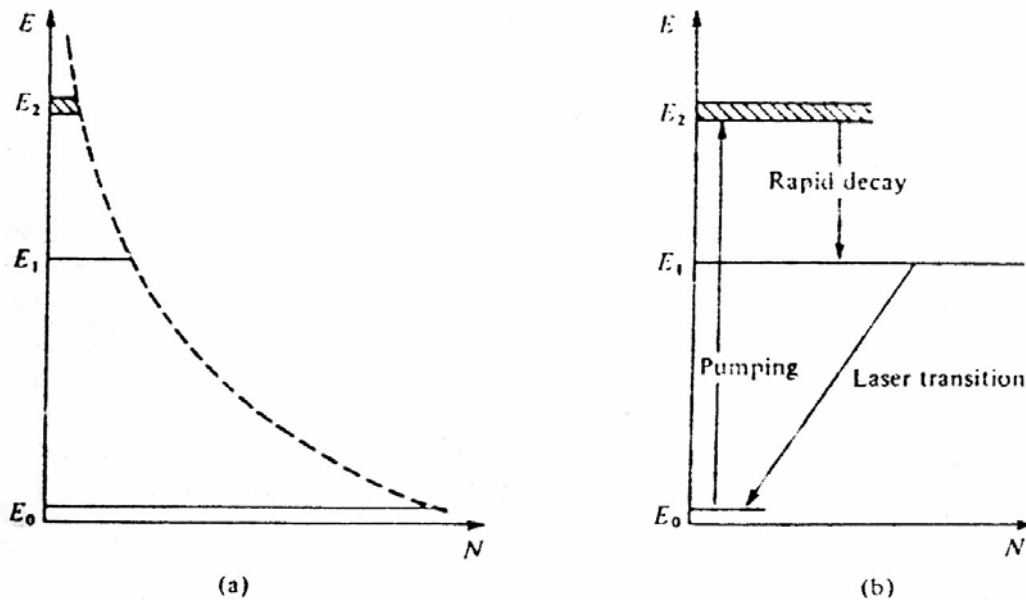
Fig. 2-5 Population of the energy levels by pumping in three-level system: (a) Boltzmann distribution before pumping and (b) distribution after pumping and the transitions involved.

The four-level system shown in Fig. 2-6 has much lower pumping requirements. If (E_2-E_o) is rather large compared to kT, the thermal energy at the temperature of operation,

then the populations of the levels E_1, E_2 and E_3 are all very small in conditions of thermal equilibrium. Thus, if atoms are pumped from the ground state to the level E_3 from which they decay very rapidly to the metastable level E_2 a population inversion is quickly created between levels E_2 and E_1.
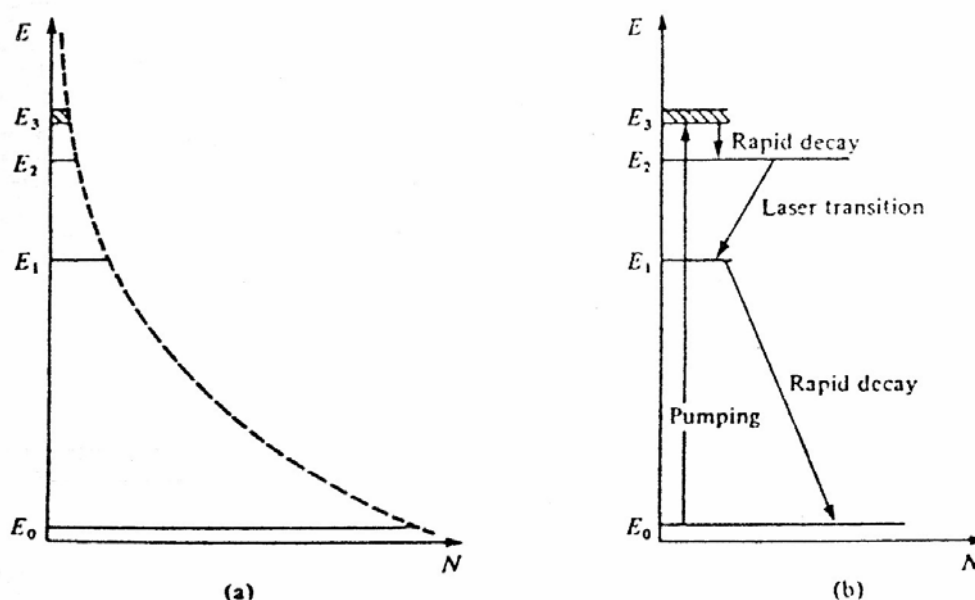
Fig. 2-6 Population of the energy levels in a four system: (a) before pumping and (b) after pumping.

Again the upper level E_3 should preferably consist of a large number of levels for greatest pumping efficiency. If the lifetimes of the transitions $E_3 \rightarrow E_2$ and $E_1 \rightarrow E_o$ are short the population inversion between E_2 and E_1 can be maintained with moderate pumping and continuous laser action can be achieved more readily. In the Nd:YAG laser, for example, $\tau_{21} \cong 0.5$ ms while $\tau_{10} \cong 30$ ns and, although there are many upper levels used for pumping, each has a lifetime of about 10^{-8} s (i.e. $\tau_{32} \cong 10^{-8}$ s). The details of the mechanisms used for pumping lasers can be quite complicated. In addition to optical pumping, pumping can also occur in an electrical discharge, or by electron bombardment, by the release of chemical energy, the passage of a current etc. The energy level schemes of the media used in lasers are often complex but they can usually be approximated by either three or four level schemes [26].

2.6 Optical feedback

The laser, despite its name, is more analogous to an oscillator than an amplifier. In an electronic oscillator an amplifier which is tuned to a particular frequency is provided with positive feedback and, when switched on, any electrical noise signal of the appropriate frequency appearing at the input will be amplified. The amplified output is fed back to the input and amplified yet again and so on. A stable output is quickly reached, however, since the amplifier saturates at high input voltages as it cannot produce a larger output than the supply voltage [26].

40

In the laser, positive feedback may be obtained by placing the gain medium between a pair of mirrors which form an optical cavity or Fabry-Perot resonator. The initial stimulus is provided by any spontaneous transitions between appropriate energy levels in which the emitted photon travels along the axis of the system. The signal is amplified as it passes through the medium and 'fed back' by the mirror. Saturation is reached when the gain provided by the medium exactly matches the losses incurred during a complete round trip [26].

The gain per unit length of most active media is so small that very little amplification of a beam of light results from a single pass through the media. In the multiple passes which a beam undergoes when the medium is placed within a cavity, however, the amplification may be substantial [26].

We have tacitly assumed that the radiation within the cavity propagates to and fro, between two plane-parallel mirrors in a well-collimated beam. Because of diffraction effects this cannot be as a perfectly collimated beam cannot be maintained with mirrors of finite extent; some radiation will spread out beyond the edges of the mirrors. Diffraction losses of this nature can be reduced by using concave mirrors. In practice a number of different mirror curvatures and configurations are used depending on the applications envisaged and the type of laser being used.

Using simple ray tracing techniques, however, it is quite easy to anticipate the results of such an analysis in that mirror configurations which retain a ray of light, initially inclined at a small angle to the axis, within the optical cavity after several reflections, are likely to be useful [26].

The commonly used mirror configurations are shown in Fig. 2-7; they all have various advantages and disadvantages. The plane-parallel configuration, for example, makes maximum use of the laser medium (i.e. we say that the *mode volume* is large) but it is difficult to align correctly, an accuracy of about 1 second of arc is required and the mirrors need to be flat to $\lambda/100$. On the other hand, the confocal arrangement is relatively easy to align (an accuracy of 1.5 minutes of arc is sufficient) but the use of the active medium is restricted (i.e. the mode volume is small). In gas lasers, if maximum power output is required we use a large radius resonator, while if uniphase operation, i.e. maximum beam coherence, is required we use the hemispherical system. The gain is usually very small so it is essential to minimize all losses in the laser [26].
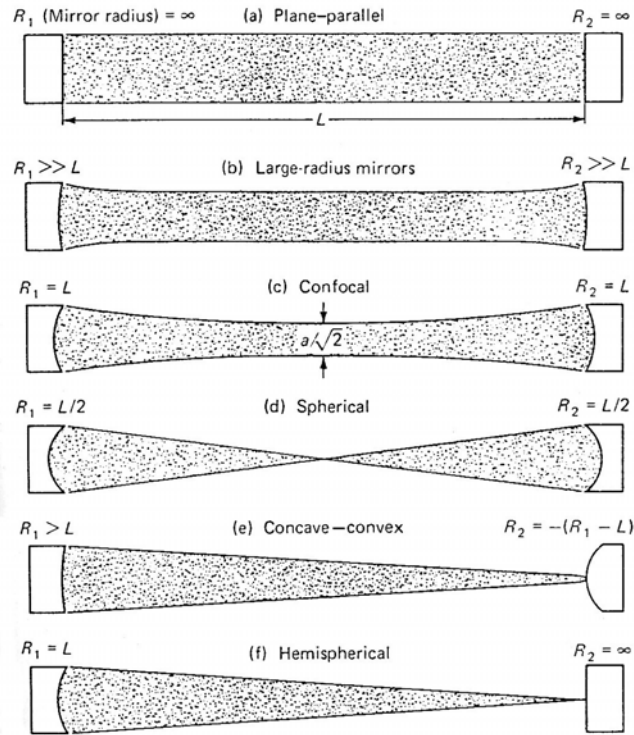
Fig. 2-7 Resonator configurations giving uniphase wavefronts (intracavity radiation pattern is shaded).

One source of loss is absorption by the mirrors. To reduce this, high reflectivity, multilayer dielectric coatings on the mirrors are used rather than metallic coatings. In these so-called multilayer stacks there is a sequence of quarter-wave (i.e. $\lambda/4$) layers of alternate high and low refractive index dielectric materials on a glass substrate. Because of the phase changes occurring at alternate interfaces all the reflected waves are in phase and add constructively. More than twenty such layers may be needed to give reflectivities in excess of 99.9% — lower reflectivities require fewer layers. Clearly the mirrors will only be effective over a narrow wavelength range [26]. A familiar example of this sort of process is the coating of camera lenses to reduce unwanted reflections. We can now derive a threshold condition in terms of the parameters of the whole system for laser oscillations to occur [26].

2.7 Threshold condition - laser losses

The steady state level of oscillation is reached when the rate of amplification is balanced by the rate of loss (this is the situation in continuous output (or CW) lasers; it is a little different in pulse lasers). Thus, while a population inversion is a necessary condition for laser action, it is not a sufficient condition because the minimum or threshold value of gain coefficient must be large enough to overcome the losses and sustain oscillations. The threshold gain, in turn, through the Equation (2-15) specifies population inversion required.

The total loss of the system is due to a number of different processes, the most important ones include:

(1) Transmission at mirrors - the transmission from one of the mirrors usually provides the useful output; the other mirror is made as reflective as possible to minimize losses.

(2) Absorption and scattering at the mirrors.

(3) Absorption in the laser medium due to transitions other than the desired transitions (most laser media have many energy levels not all of which will be involved in the laser action).

(4) Scattering due to optical inhomogeneities in the laser medium — this applies particularly to solid state lasers.

(5) Diffraction losses at the mirrors.

To simplify matters, all the losses are included except those due to transmission at the mirrors in a single effective loss coefficient γ which reduces the effective gain coefficient to $(k-\gamma)$. We can determine the threshold gain by considering the change in irradiance of a beam of light undergoing a round trip within the laser cavity. We assume that the laser medium fills the space between the mirrors M_1 and M_2 which have reflectances R_1 and R_2 and a separation L. Then in traveling from M_1 to M_2 the beam irradiance increases from I_o to I where:

$$I = I_o e^{(k-\gamma)L} \tag{2-16}$$

After reflection at M_2, the beam irradiance will be $R_2 I_o \exp(k - \gamma)L$ and after a complete round trip, the final irradiance will be such that the round trip gain G is:

$$G = \frac{FinalIrradiance}{InitialIrradiance} = R_1 R_2 e^{2(k-\gamma)L} \tag{2-17}$$

If G is greater than unity, a disturbance at the laser resonant frequency will undergo a net amplification and the oscillations will grow; if G is less than unity the oscillations will die out. Therefore, we can write the *threshold condition* as:

$$G = R_1 R_2 e^{2(k-\gamma)L} = 1 \tag{2-18}$$

where k_{th} is the threshold gain. It is important to realize that the threshold gain is equal to the steady state gain in continuous output lasers, i.e. $k_{th} = k_{ss}$. This equality is due to a phenomenon known as *gain saturation* which can be explained as follows. Initially, when laser action commences the gain may be well above the threshold value. The effect of stimulated emission, however, will be to reduce the population of the upper level of the laser transition so that the degree of population inversion and consequently the gain will decrease. Thus the net round trip gain may vary and be greater than or less than unity so that the cavity energy density will correspondingly increase or decrease. It is only when G has been equal to

unity for a period of time that the cavity energy (and laser output power) settles down to a steady state value, that is when the gain just balances the losses in the medium. In terms of the population inversion there will be a threshold value $N_{th} = |N_2 - (g_2/g_1)N_1|_{th}$ corresponding to k_{th}. In steady state situations $|N_2 - (g_2/g_1)N_1|$ remains equal to N_{th} regardless of the amount by which the threshold pumping rate is exceeded. The small signal gain required to support steady state operation depends on the laser medium through k and γ and on the laser construction through R_1, R_2 and L. From Equation (2-18) we can see that:

$$k_{th} = \gamma + \frac{1}{2L} \ln \left(\frac{1}{R_1 R_2} \right) \qquad (2\text{-}19)$$

where the first term represents the volume losses and the second the loss in the form of the useful output. Equation (2-15) shows that k can have a wide range of values, depending not only on $|N_2 - (g_2/g_1)N_1|$ but also on the intrinsic properties of the active medium. If k is high then it is relatively easy to achieve laser action, mirror alignment is not critical and dust can be tolerated on the mirrors. With low gain media, on the other hand, such losses are unacceptable and the mirrors must have high reflectivities, be scrupulously clean and carefully aligned [26].

It should be noted that a laser with a high gain medium will not necessarily have a high efficiency. The efficiency is the ratio of the light power to the input pumping power. It therefore depends on how effectively the pump power is converted into producing a population inversion, on the probabilities of different kinds of transitions from the upper level and on the losses in the system. With reference to Fig. 2-6 (b) and confining our attention to optical pumping we can easily see that the efficiency cannot exceed $(E_2 - E_1)/(E_3 - E_o) = \nu_{21}/\nu_{30}$ for the four level system and that it will be considerably less than this for the three level system where over half of the atoms have to be pumped out of the ground state before the population inversion is produced. The actual efficiencies, as defined above, are usually very much less than this because of the energy loss in converting electrical energy into optical energy at the pump frequency, and the fact that not all of the atoms pumped into level 3 will necessarily make transition to level 2. Certain lasers, for example CO_2, are characterized by having a high efficiency and a high small signal gain. Other lasers such as argon, although having a high gain, have a very low efficiency [26].

2.8 Lineshape function

In deriving the expression for the small signal gain we assumed that all the atoms in either the upper or lower levels would be able to interact with the (perfectly) monochromatic beam. In fact this is not so; spectral lines have a finite wavelength (or frequency) spread i.e. they have a spectral width. This can be seen in both emission and absorption and if, for example, we were to measure the transmission as a function of frequency for the transmission between the two energy states E_1 and E_2 we would obtain the bell-shape curve shown in Fig. 2-8 (a).

The emission curve would be the inverse of this, Fig. 2-8 (b). The shape of these curves is described by the *lineshape function g(ν),* which can also be used to describe a

frequency probability curve. Thus we may define $g(v)dv$ as the probability that a given transition between the two energy levels will result in the emission (or absorption) of a photon whose frequency lies between v and $v + dv$, $g(v)$ is normalized such that $\int\limits_{-\infty}^{\infty}g(v)dv = 1$.

Therefore we see that a photon energy may not necessarily stimulate another photon of energy hv. We then take $g(v)dv$ as the probability that the stimulated photon will have an energy between $h(v + dv)$.
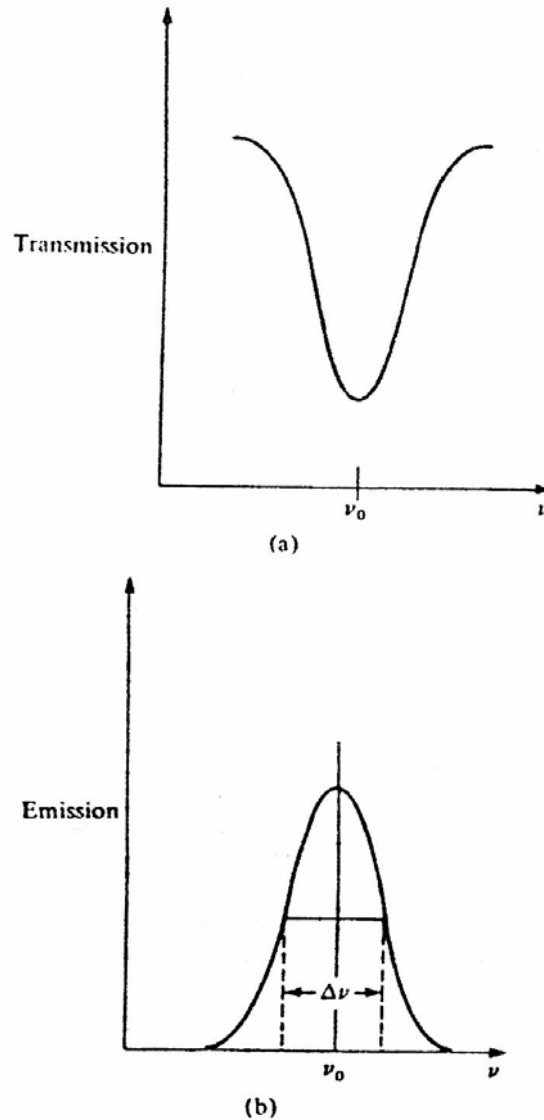
Fig. 2-8 (a) The transmission curve for transitions between energy levels E_1 and E_2 (b) the emission curve for transitions between E_2 and E_1 . The precise form of these cures (the lineshape) depends on the spectral broadening mechanisms.

When a monochromatic beam of frequency v_S interacts with a group of atoms with a lineshape function $g(v)$, the small signal gain coefficient may be written as:

$$k(v_s) = \left(N_2 - \frac{g_2}{g_1} N_1 \right) \frac{B_{21} h v_{21} n g(v_s)}{c} \qquad (2\text{-}20)$$

The form of the lineshape function $g(v)$ depends on the particular mechanism responsible for the spectral broadening in a given transition. The three most important mechanisms are: Doppler broadening, collision (or pressure) broadening and natural broadening [26].

2.9 Population inversion and pumping threshold conditions

We may now use Equation (2-20) to calculate the population inversion required to reach the lasing threshold. From Equation (2-20) we have:

$$\left(N_2 - \frac{g_2}{g_1} N_1 \right) = \frac{k(v_s)c}{B_{21} h v_s n g(v_s)} \qquad (2\text{-}21)$$

At the threshold the small signal gain coefficient is given by Equation (2-19), i.e.

$$k(v_s) = k_{th} = \gamma + \frac{1}{2L} \ln\left(\frac{1}{R_1 R_2} \right) \qquad (2\text{-}22)$$

and therefore:

$$\left(N_2 - \frac{g_2}{g_1} N_1 \right)_{th} = \frac{k_{th} c}{B_{21} h v_s n g(v_s)} \qquad (2\text{-}23)$$

From Equation (2-8) we have $B_{12} = c^3 A_{21} / 8\pi h v^3 n^3$. The quantity A_{21} may be determined experimentally by noting that it is the reciprocal of the spontaneous radiation lifetime τ_{21} from level 2 to level 1.

Thus combining the above equations we can write the threshold population inversion as:

$$N_{th} = \left(N_2 - \frac{g_2}{g_1} N_1 \right)_{th} = \frac{8\pi v_s^2 k_{th} \tau_{21} n^2}{c^2 g(v_s)} \qquad (2\text{-}19)$$

We note that the lasing threshold will be achieved most readily when $g(v)$ is a maximum, i.e. when v_s has the value v_o corresponding to the centre of the natural linewidth. We may therefore replace $g(v_s)$ by $1/\Delta v$ to give:

$$N_{th} = \frac{8\pi v_o^2 k_{th} \tau_{21} \Delta v n^2}{c^2}$$ (2-20)

We now proceed to calculate the pumping power required to reach threshold. To do this we must solve the rate equations for the particular system. The rate equations describe the rate of change of the populations of the laser medium energy levels in terms of the emission and absorption processes and the pump rate. We shall consider the ideal four level system shown in Fig. 2-9. We assume that $E_1 \gg kT$ so that the thermal population of level 1 is negligible; we also assume that the threshold population density N_{th} is very small compared to the ground state population so that during lasing the latter is hardly affected. If we let R_2 and R_1 be the rates at which atoms are pumped into levels 2 and 1 respectively we can write the rate equations for these levels as:

$$dN_2/dt = R_2 - N_2 A_{21} - \rho_v B_{21}(N_2 - N_1)$$ (2-21)

and

$$dN_1/dt = R_1 + \rho_v B_{21}(N_2 - N_1) + N_2 A_{21} - N_1 A_{10}$$ (2-22)
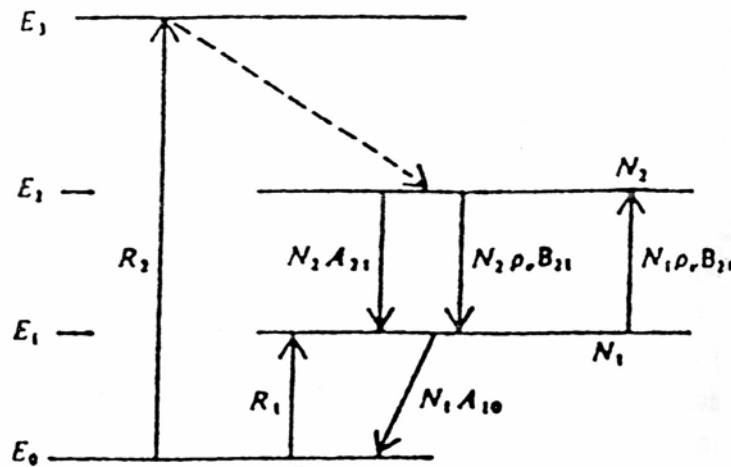
Fig. 2-9 Transitions within an ideal four level system.

Process R_1 which populates the lower laser level 1 is detrimental to laser action as clearly it reduces the population inversion. Although such pumping is unavoidable in many lasers, for example gas lasers pumped via an electrical discharge, we shall henceforth ignore R_1. If we assume that the system is being pumped at a steady rate then we have $dN_2/dt = dN_1/dt = 0$. Hence we may solve Equations (2-21) and (2-22) for N_1 and N_2. We can get:

$$N_1 = R_2/A_{10}$$

$$N_2 = R_2\left[1 + \frac{\rho_v B_{21}}{A_{10}}\right](A_{21} + \rho_v B_{21})^{-1}$$

and hence

$$N_2 - N_1 = R_2\left(\frac{1 - A_{21}/A_{10}}{A_{21} + \rho_v B_{21}}\right) \tag{2-23}$$

We can see that unless $A_{21} < A_{10}$, the numerator will be negative and no population inversion can take place. As the Einstein A coefficients are the reciprocals of the spontaneous lifetimes, the condition $A_{21} < A_{10}$ is equivalent to the condition $\tau_{10} < \tau_{21}$, i.e. that the upper lasing level has a longer spontaneous emission lifetime than the lower level. In most lasers $\tau_{21} \gg \tau_{10}$ and $(1 - A_{21}/A_{10}) \cong 1$.

Now below threshold we may neglect ρ_v since lasing has not yet commenced and most of the pump power appears as spontaneous emission; thus Equation (2-23) can be written as:

$$N_2 - N_1 = R_2\left(\frac{1 - A_{21}/A_{10}}{A_{21}}\right)$$

i.e., there is a linear increase in population inversion with pumping rate but insufficient inversion to maintain amplification [26].

At threshold, ρ_v is still small and assuming $g_1 = g_2$, we can express the threshold population inversion in terms of the threshold pump rate, i.e.

$$(N_2 - N_1)_{th} = N_{th} = R_2\left(\frac{1 - A_{21}/A_{10}}{A_{21}}\right) \tag{2-24}$$

or inserting the above approximation that $(1 - A_{21}/A_{10}) \cong 1$

$$R_{th} = N_{th}A_{21}$$

or

$$R_{th} = N_{th}/\tau_{21}$$

Each atom raised into level 2 requires an amount of energy E_3 so that the total pumping power per unit volume P_{th} at threshold may be written as:

$$P_{th} = \frac{E_3 N_{th}}{\tau_{21}}$$

We may substitute for N_{th} from Equation (2-20) to give:

$$P_{th} = \frac{E_3 8\pi v_o^2 k_{th} \tau_{21} \Delta vn^2}{\tau_{21} c^2}$$

or

$$P_{th} = \frac{E_3 8\pi v_o^2 k_{th} \Delta vn^2}{c^2} \qquad (2-25)$$

This is the point at which the gain due to the population inversion exactly equals the cavity losses. Further increase of the population inversion with pumping is impossible in a steady state situation, since this would result in a rate of induced energy emission which exceeds the losses. Thus the total energy stored in the cavity would increase with time in violation of the steady state assumption [26].

This argument suggests that $|N_2 - (g_2/g_1)N_1|$ must remain equal to N_{th} regardless of the amount by which the threshold pump rate is exceeded. Equation (2-23) shows that this is possible providing $\rho_v B_{12}$ is able to increase (once R_2 exceeds its threshold value given by Equation (2-24)) so that the equality:

$$N_{th} = R_{th} \left[\frac{1 - A_{21}/A_{10}}{A_{21} + \rho_v B_{21}} \right]$$

is satisfied. Now combining this equation with Equation (2-24) we have:

$$\frac{R_{th}}{A_{21}} = \frac{R_2}{A_{21} - \rho_v B_{21}}$$

and hence

$$\rho_v = \frac{A_{21}}{B_{21}} \left(\frac{R_2}{R_{th}} - 1 \right) \tag{2-26}$$

Since the power output W of the laser will be directly proportional to the optical power density within the laser cavity, and the pump rate into level 2 (i.e. R_2) will be proportional to the pump power P delivered to the laser, we may rewrite Equation (2-26) as:

$$W = W_o \left(\frac{P}{P_{th}} - 1 \right) \tag{2-27}$$

where W_o is a constant.

Thus if the pump rate is increased above the value P_{th} the beam irradiance is expected to increase linearly with pump rate. This is born out in practice and plots of population inversion and laser output as a function of pump rate are of the form shown in Fig. 2-10. The additional power above the threshold is channeled into a single (or few) cavity mode(s). Spontaneous emission still appears above threshold but it is extremely weak in relation to the laser output as it is emitted in all directions and has a much greater frequency spread.
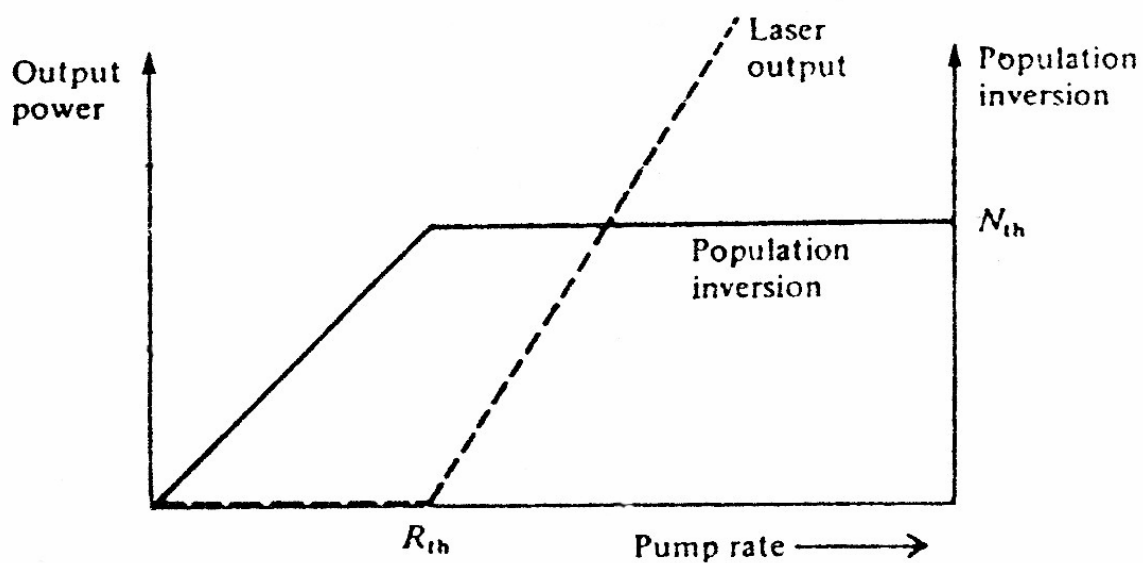
Fig. 2-10 Population inversion and laser power output as a function of pump rate.

2.10 Laser definitions

There are some definitions for laser which have to be mentioned here, they are:

Slope Efficiency:
The efficiency above threshold [10].

Quantum Efficiency:
The mean wavelength of the absorbed radiation divided by the lasing wavelength [10].

Saturation Flux:
The fluorescence energy of the crystal divided by the product of the absorption cross-section and the fluorescence lifetime [10].

Pumping Efficiency:
The fraction of absorbed photons at a given wavelength that produce upper-state atoms which participate in the lasing process [10].

Materials for laser operation must possess sharp fluorescent lines, strong absorption bands and a resonably high quantum efficiency for the fluorescent transition of interest. These characteristics are generally shown by solids (crystals or glass) which incorporate in small amounts elements in which optical transitions can occur between states of inner, incomplete electron shells. Thus the transition metals, the rare earth (lanthanide) series and the actinide series are of interest in this connection. The sharp fluorescence lines in the spectra of crystals doped with these elements result from the fact that the electrons involved in transitions in the optical regime are shielded by the outer shells from the surrounding crystal lattice. The corresponding transitions are similar to those of the free ions. In addition to a sharp fluorescence emission line, a laser material should possess pump bands within the

51

emission spectrum of readily available pump sources such as arc lamps and laser diode arrays [27].

The three principal elements leading to gain in a laser are:

1- *The host material* with its macroscopic mechanical, thermal and optical properties, and its unique microscopic lattice properties.

2- *The activator/sensitizer ions* with their distinctive charged states and free-ion electronic configurations.

3- *The optical pump source* with its particular geometry, spectral irradiance and duration.

These elements are interactive and must be selected self-consistently to achieve a given system performance.

The conditions for laser action at optical frequencies were first described by Schawlow and Townes in 1958. The first demonstration of laser action by Maiman was achieved in 1960 using ruby ($Cr^{3+}:Al_2O_3$), a crystalline solid system. The next step in the development of solid-state lasers was the operation of trivalent uranium in CaF_2 and divalent samarium in CaF_2 by Sorokin and Stevenson. In 1961 Snitzer demonstrated laser action in neodymium-doped glass. The first continuosly operating crystal laser was reported in 1961 by Johnson and Nassau using $Nd^{3+}:CaWO_4$. Since then laser action has been achieved from trivalent rare earths (Nd^{3+}, Er^{3+}, Ho^{3+}, Ce^{3+}, Tm^{3+}, Pr^{3+}, Gd^{3+}, Eu^{3+}, Yb^{3+}), divalent rare earths (Sm^{2+}, Dy^{2+}, Tm^{2+}), tranistion metals (Cr^{3+}, Ni^{2+}, Co^{2+}, Ti^{2+}, V^{2+}) and the actinide ion U^{3+} embedded in various host materials. Optically pumped laser action has been demonstrated in hundreds of ion-host crystal combinations covering a spectral range from the visible to the mid-infrared [26].

The exceptionally favourable characteristics of the trivalent neodymium ion for laser action were recognized at a relatively early stage of the search for solid-state laser materials. Thus, Nd^{3+} was known to exhibit a satisfactorily long fluorescence lifetime and narrow fluorescence lifewidths in crystals with ordered structures, and to possess a terminal state for the laser transition sufficiently high above the ground state so that cw operation at room temperature was readily feasible. Therefore, this ion was incorporated as a dopant in a variety of host materials, i.e., glass, $CaWO_4$, $CaMoO_4$, CaF_2, LaF_3, etc., in an effort to make use of its great potential. However, most of these early hosts displayed undesirable shortcomings, either from the standpoint of their intrinsic physical properties or because of the way in which they interacted with the Nd^{3+} ions. Finally, **Y**ttrium **A**luminum **G**arnet ("YAG") was explored by Geusic as host for Nd^{3+} and its superiority to other host materials was quickly demonstrated. Nd:YAG lasers displayed the lowest thresholds for cw operation at room temperature of any known host-dopant combination [27].

2.11 Nd:YAG lasers and related systems

2.11.1 Overview

Nd:YAG, because of its high gain and good thermal and mechanical properties, is by far the most important solid-state laser for scientific, medical, industrial and military

applications. Nd:glass is important for laser fusion drivers because it can be produced in large sizes. Very recently, Nd:Cr:GSGG has received considerable attention because of the good spectral match between the flashlamp emission and absorption of the Cr ions. The host of this laser is the **G**adolinium **S**candium **G**allium **G**arnet (GSGG). An efficient energy transfer between the Cr and Nd ions results in a highly efficient Nd:laser. Nd:YLF is a good candidate for certain specialized applications, because the output is polarized, and the crystal exhibits lower thermal bi-refringence. Nd:YLF has a higher energy storage capability (due to its lower gain coefficient) compared to Nd:YAG and its output wavelength matches that of phosphate Nd:glass. Therefore modelocked and Q-switched Nd:YLF lasers have become the standard oscillators for large glass lasers employed in fusion research. The host YLF is the uniaxial crystal **Y**ttrium **L**ithium **F**louride $YLiF_4$.

The Nd:YAG laser is by far the most commonly used type of solid-state laser. Neodymium-doped yttrium aluminum garnet (Nd:YAG) possesses a combination of properties uniguely favorable for laser operation. The YAG host is hard, of good optical quality, and has a high thermal conductivity. Furthermore, the cubic structure of YAG favours a narrow fluorescent linewidth, which results in high gain and low threshold for laser operation. In Nd:YAG, trivalent neodymium substitutes for trivalent yttrium in the lattice, so charge compensation is not required [27].

Five years after Geusic et al. reported the first successful lasing of Nd:YAG, rapid strides were made in improving both the quality of the material and pumping technique so that available cw power outputs rose from the fractional watt level initially obtained to several hundred watts from a single laser rod. On the other hand, in single-crystal Nd:YAG fibre lasers, thresholds were achieved with absorbed pump powers as small as 1 mW. Today, more than twenty years after its first operation, the Nd:YAG laser has emerged as the most versatile solid-state system in existence [27].

2.11.2 Physical properties

In addition to the very favourable spectral and lasing characteristics displayed by Nd:YAG, the host lattice is noteworthy for its unusually attractive blend of physical, chemical and mechanical properties. The YAG structure is stable from the lowest temperature up to the melting point, and no transformations have been reported in the solid phase. The strength and hardness of YAG are lower than ruby but still high enough so that normal fabrication procedures do not produce any serious breakage problems [27].

Pure $Y_3Al_5O_{12}$ is a colourless, optically isotropic crystal which possesses a cubic structure characteristic of garnets. In Nd:YAG about 1% of Y^{3+} is substituted by Nd^{3+}. The radii of the two rare earth ions differ by about 3%. Therefore, with the addition of the large amounts of neodymium, strained crystals are obtained – indicating that either the solubility limit of neodymium is exceeded or that the lattice of YAG is seriously distorted by inclusion of neodymium. Some of the important physical properties of YAG are listed in Table 2-1, together with optical and laser parameters [27].

Property		Value
Chemical formula		$Nd:Y_3Al_5O_{12}$
Weight % Nd		0.725
Atomic % Nd		1.0
Nd atoms/cm^3		1.38×10^{20}
Melting point		1970 °C
Knoop hardness		1215
Density		4.56 g/cm^3
Rupture stress		1.3-2.6 $\times$ 10^3 kg/cm^3
Modulus of elasticity		3 $\times$ 10^3 kg/cm^2
Thermal expansion coefficient	[100] orientation	8.2×10^{-6} C^{-1}, 0-250 C
	[110] orientation	7.7×10^{-6} C^{-1}, 10-250 C
	[111] orientation	7.8×10^{-6} C^{-1}, 0-250 C
Linewidth		4.5 Å
Stimulated emission cross-section	$R_2 - Y_3$	σ_{21}= 6.5×10^{-19} cm^2
	$^4F_{3/2} - {}^4I_{11/2}$	σ_{21}= 2.8×10^{-19} cm^2
Spontaneous fluorescence lifetime		230 μs
Photon energy at 1.06 μm		hv = 1.86
Index of refraction		1.82 at 1.0 μm
Scatter losses		$\alpha_{sc} \approx 0.002$ cm^{-1}

Table 2-1 Physical and Optical Propertieres of Nd:YAG.

2.11.3 Laser properties

The Nd:YAG laser is a four-level system as depicted simply in the energy level diagram in Fig. 2.5. The laser transition, having a wavelength of 1064.1 nm, originates from the R_2 component of the $^4F_{3/2}$ level and terminates at the Y_3 component of the $^4I_{3/2}$ level. At room temperature only 40 % of the $^4F_{3/2}$ population is at level R_2; the remaining 60 % are at the lower sub-level R_1 according to Boltzmann's law. Lasing takes place only by R_2 ions whereby the R_2 level population is replenished from R_1 by thermal transitions. The ground level of Nd:YAG is the $^4I_{9/2}$ level. There are a number of relatively broad energy levels, which together may be viewed as a comprising pump level 3. Of the main pump bands shown, the 0.81 and 0.75 μm bands are the strongest. The terminal laser level is 2111 cm^{-1} above the ground state and thus the population is a factor of exp($\Delta E/kT$) $\approx$ exp (-10) $\approx$ 10^{-5} of the ground-state density. Since the terminal level is not populated thermally, the threshold condition is easy to obtain [27].

The upper laser level, $^4I_{3/2}$ has a fluorescence efficiency greater than 99.5 % and a fluorescence lifetime of 230 μs. The branching ratio of the emission from $^4F_{3/2}$ is as follows: $^4F_{3/2} \rightarrow {}^4I_{9/2} = 0.25$, $^4F_{3/2} \rightarrow {}^4I_{11/2} = 0.60$, $^4F_{3/2} \rightarrow {}^4I_{13/2} = 0.14$ and $^4F_{3/2} \rightarrow {}^4I_{15/2} < 0.01$. This means that almost all the ions transferred from the ground level to the pump bands end up at the upper laser level, and 60 % of the ions at the upper laser level cause fluorescence output at the $^4I_{11/2}$ manifold [27].

At room temperature the main 1.06- μm line in Nd:YAG is homogeneously broadened by thermally activated lattice vibrations. The spectroscopic cross-section for the individual transition between Stark sub-levels has been recently measured to be $\sigma(R_2 - Y_3) = 6.5 \times 10^{-19}$

cm^2. At a temperature of 295 K, the Maxwell-Boltzmann fraction in the upper Stark sub-level is 0.427, implying an effective cross-section for Nd:YAG of $\sigma^*(^4F_{3/2} \rightarrow {}^4I_{11/2}) = 2.8 \times 10^{-19}$ cm^2. The effective stimulated-emission cross-section is the spectroscopic cross section times the occupation of the upper laser level, relative to the entire $^4F_{3/2}$ manifold population [26].

The active medium for Nd:YAG laser is yttrium aluminum garnet ($Y_2Al_5O_{12}$) with the rare ion neodymium Nd^{3+} present as an impurity. The Nd^{3+} ions, which are randomly distributed as substitutional impurities on lattice sites normally occupied by the yttrium ions, provide the energy levels for both the lasing transitions and pumping. Though the YAG host itself does not participate directly in the lasing action it does have two important roles [26].

When an Nd^{3+} ion is placed in a host crystal lattice it is subjected to the electrostatic field of the surrounding ions, the so-called *crystal field*. The crystal field of the host interacts with the electron energy levels in a variety of ways depending on such factors as its strength and symmetry, and on the electron configuration of the impurity [26].

A neodymium ion which is free to move in a gaseous discharge, for example, has many of its energy levels with the same energy; these are said to be degenerate. When the ion is placed in the host, the crystal field splits some of the energy levels thereby partly removing the degeneracy. A rather more important effect in the case of the Nd:YAG laser is that the crystal field modifies the transition probabilities between the various energy levels of the Nd^{3+} ion so that some transitions, which are forbidden in the free ion, become allowed [27].

The net result is that the ground and the first excited state energy levels of the Nd^{3+} ion split into the groups of levels shown in Fig. 2-11. The symbols used to describe the energy levels in this and succeeding diagrams depend on the exact nature of the ions and atoms involved. In the case under discussion the symbol for an energy level is written $^{2S+1}X_J$. Here S is the vector sum of the electron spins of the ion. X gives the vector sum L of the orbital angular momentum quantum numbers, where values of L = 0, 1, 2, 3, 4 ... are designed by S, *P, D, F, G*. Finally J is the vector sum of *S* and *L*. Thus in the $^4F_{3/2}$ level, $S = 3/2$ (there are three unpaired electrons in the *4f* sub-shell of the Nd^{3+} ion), $L = 3$ and $J = 3/2$. Whilst familiarity with this and similar notations for electron energy levels is not essential to appreciate the basics of a given laser, it is a prerequisite for a detailed understanding of the mechanisms involved [26].

The Nd:YAG laser is essentially a four level system. This is the terminal laser level $^4I_{11/2}$ and its room temperature population is very small. Whilst a number of laser transitions may occur between some of the pairs of levels shown to the right of the figure, the most intense line at 1.064 μm arises from the superposition of the two transitions shown. Fig. 2-11 shows the ratios of the radiation sharing in the parts of the lasing process, while Fig. 2-12 shows a detailed energy level diagram for the neodymium ion in YAG.

Pumping is normally achieved by using an intense flash of white light from a xenon flashtube. This excites the Nd^{3+} ions from the ground state to the various energy states above the $^4F_{3/2}$ state. There are, in fact, many more states at higher energy than those that are shown in Fig. 2-12. The presence of several possible pumping transitions contributes to the frequency of the laser when using a pumping source with a broad spectral output.
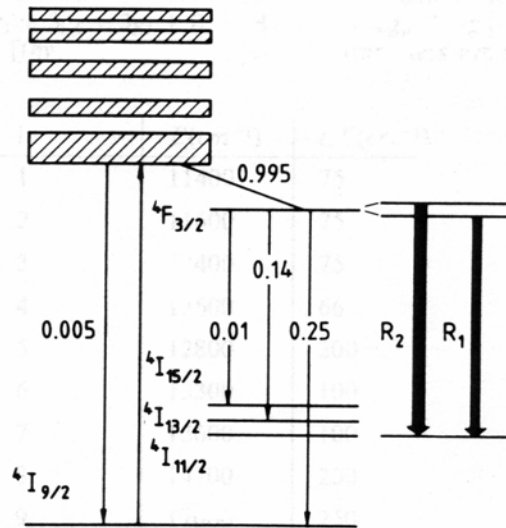
Fig. 2-11 The ratios of the radiation sharing in the parts of the lasing process.
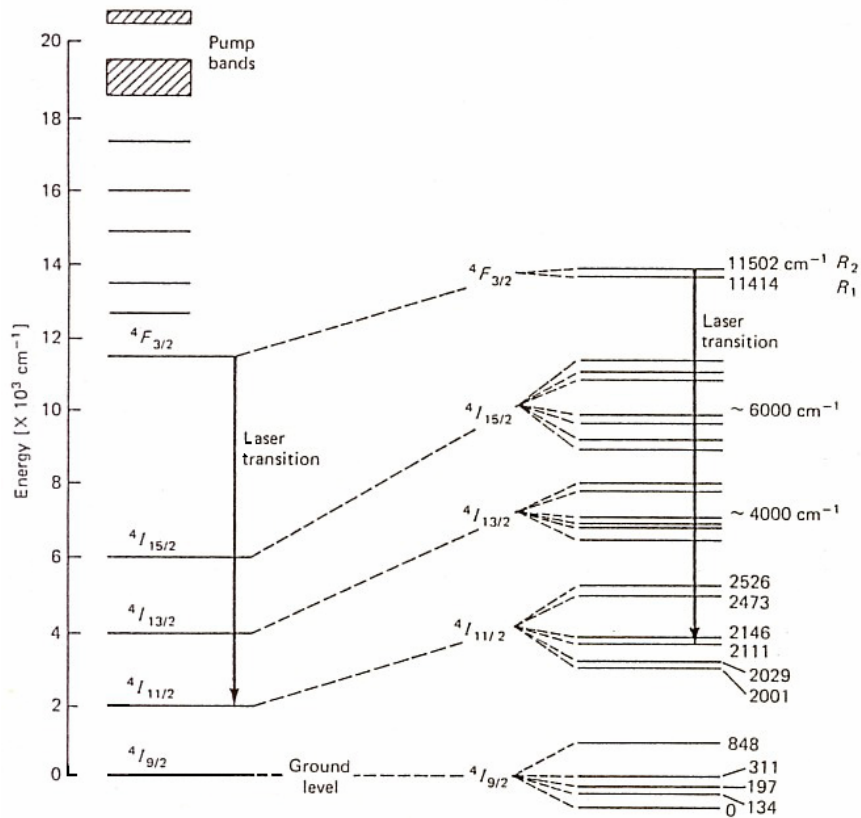
Fig. 2-12 Detailed energy level diagram for the neodymium ion in YAG showing the principal laser transitions. Laser emission also results from transitions between the $^4F_{3/2}$ levels and $^4I_{13/2}$ levels but at only one tenth of the intensity of the transition shown.

As the pumping flash lasts for only a short time (a few ms) the laser output is in the form of a pulse, which starts about 0.5 ms after the pumping flash starts. This represents the time for the population inversion to build up. Once started, stimulated emission builds up rapidly and thus depopulates the upper lasing level 2 — much faster in fact than the pumping can replace the excited atoms so that the laser action momentarily stops until population inversion is achieved again. This process then repeats itself so that the output consists of a large number of spikes of about 1 μs duration with about 1 μs separation. As the spikes are unrelated the coherence of the laser pulse, which lasts a total of about 0.5 ms, while being much greater than that of classical light sources, is not as great as might be expected [26].

Figure 2-13 shows the fluorescence spectrum of Nd^{3+} in YAG near the region of the laser output with the corresponding energy levels for the various transitions. The absorption of Nd:YAG in the range 0.3 to 0.9 μm is given in the Fig. 2-14. Thermal properties of Nd:YAG are summarized in Table 2-2 [27].
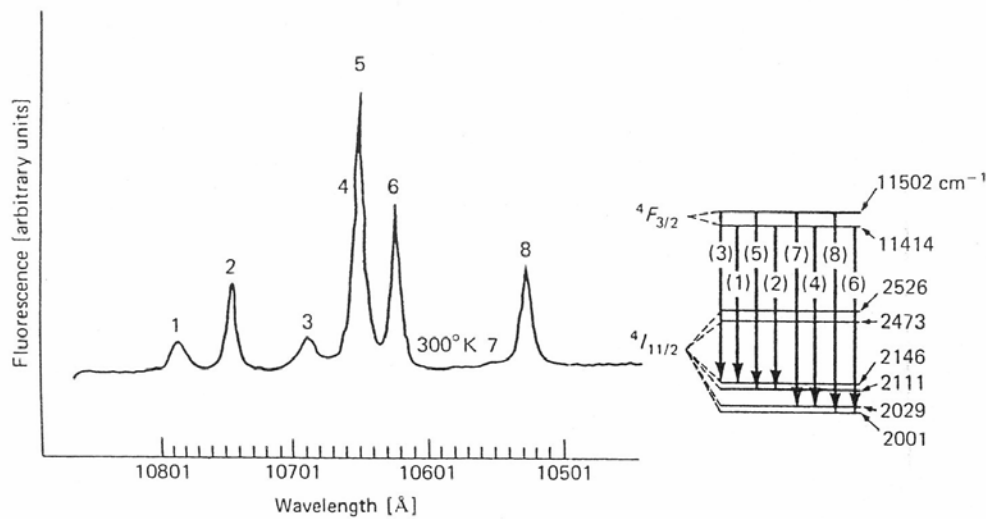
Fig. 2-13 Fluorescence spectrum of Nd^{3+} in YAG at 300 K in the region of 1.06 μm.
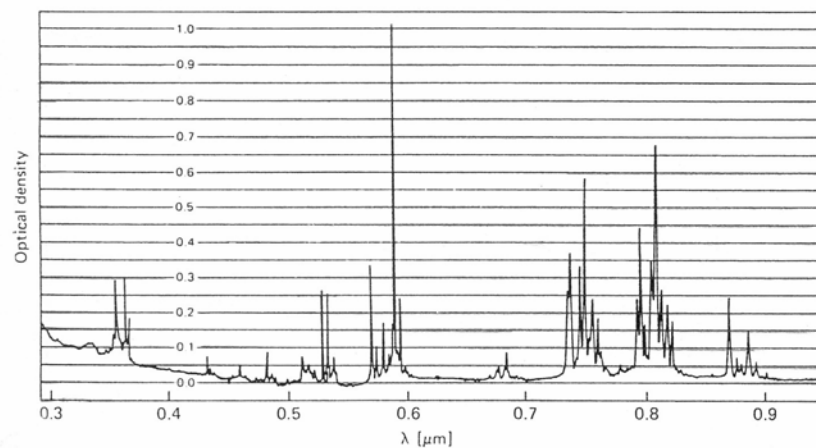
Fig. 2-14 Absorption spectrum of Nd:YAG at 300 K.

Property	Units	300 K	200 K	100 K
Thermal conductivity	W cm^{-1} K^{-1}	0.13	0.21	0.58
Specific heat	W s g^{-1} K^{-1}	0.59	0.43	0.13
Thermal diffusivity	cm^2 s^{-1}	0.046	0.10	0.92
Thermal expansion	K^{-1}	7.5	5.8	4.25
$\delta n/\delta T$	K^{-1}	7.3×10^{-6}	---	---

Table 2-2 Thermal properties of Nd:YAG

To ensure that as much radiation as possible from the flash tube is absorbed in the laser medium, close optical coupling is required. The usual arrangement is shown in Fig. 2-15; a linear flashtube and the lasing medium in the form of a rod are placed inside a highly reflecting elliptical cavity. If the flashtube is along the focal axis and the laser rod along the other, then the properties of the ellipse ensure that most of the radiation from the flashtube passes through the laser. The flashtube is fired by discharging a capacitor bank through the tube. During the opertaion, a low current "simmer" is maintained to facilitate the ignition of the flash lamp. This "simmer" current discharge is often initiated by high voltage (~ 20 kV) trigger pulse. The optical cavity may be formed by grinding the ends of the Nd:YAG rod flat and parallel and then coating them. More usually, however, external mirrors may be used as shown in Fig. 2-15. One mirror is made totally reflecting (HR) while the other transmits about 10 % [26].
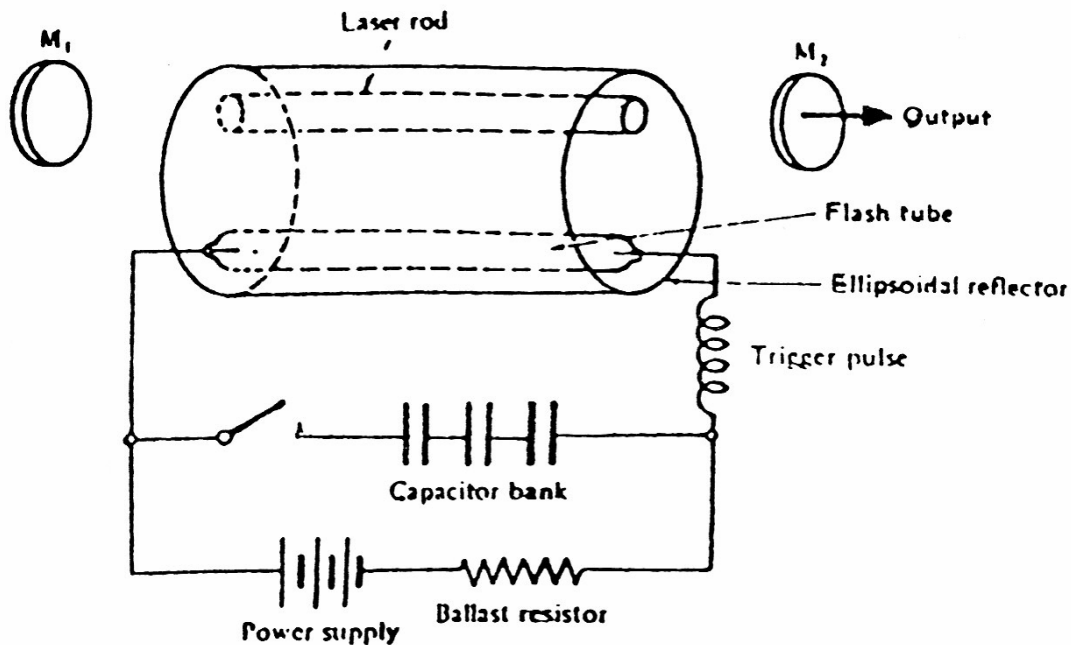
Fig. 2-15 Typical construction of a doped insulator laser showing the ellipsoidal reflector used to maximize optical coupling between the flashtube and laser rod.

A large amount of heat is dissipated by the flashtube and consequently the laser rod quickly becomes very hot. To avoid damage resulting from this, and to allow a reasonable

pulse repetition rate, cooling has to be provided by forcing air over the crystal using the reflector as a container. For higher power lasers it is necessary to use water cooling. Provided sufficient cooling is available it is possible to replace the xenon flashtube with a D.C. high pressure Kr discharge tube to operate the laser continuously [26].

A glance at the energy level diagram, Fig. 2-12, shows that the maximum possible power efficiency of the laser, ν_{21}/ν_{03}, is about 80%. In practice, because of the losses in the system, which include the loss in converting electrical to optical energy in the pumping source, the poor coupling of the pumping source output to the laser rod and the small fraction of the pumping radiation which is actually absorbed, the actual power efficiency is typically 0.1%. Thus a laser, which is pumped by a flash lamp operated by the discharge of a 1000 μF capacitor charged to 4-5 kV (that is an input energy of about 10 kJ), may produce an output pulse of about 10 J. As the pulse lasts for only about 0.5 ms, the average power, however, is then about 2 x 10^4 W. This may be greatly increased by a technique known as Q-switching [26].

2.11.4 Nd:YAG laser rods

Commercially available laser crystals are grown exclusively by the Czochralski method. Growth rates, annealing procedures and final size generally determine the manufacturing rate of each crystal. The boule axis or growth dimension is customarily in the [111] direction. The high manufacturing costs od the Nd:YAG are mainly caused by the very slow growth rate of Nd:YAG, which is of the order of 0.5 mm/h. Typical boules of 10 to 15 cm in length require a growth run of several weeks [27].

Boules grown from Nd:YAG typically contain very few optically observable scattering centres, and show negligible absorption in the lasing wavelength. However, all Nd:YAG crystals grown by Czochralski techniques show a bright core running along the length of the crystal when positioned between crossed polarizers. Strain flares are also visible, radiating from the core toward the surfaces of the crystal. Electron microprobe studies have revealed that in the core region the Nd connection can run as much as twice as high as in the surrounding areas. The cores originate from the presence of facets on the growth interface which have a different distribution coefficient for neodymium than the surrounding growth surface. These compositional differences cause corresponding differences in the thermal expansion coefficients which, in turn, give rise to the observed stress patterns during the cooling down of the crystals from the growth temperature. Annealing does not seem to eliminate the cores and thus far, no way has been found of avoiding the formation of facets on the growth interface. However, by choosing the growth direction carefully and by maintaining as steep an interface angle as is practical, the stresses can be confined to a very localized region and high-optical quality rods can be fabricated from the surrounding material. This means, of course, that in order to provide rods of a given diameter, the crystal must be grown with a diameter that is more than twice as large. The boules are processed by quartering into sections. At the present time, rods can be fabricated with maximum diameters of about 10 mm and in lengths of up to 150 mm. The optical quality of such rods is normally quite good and comparable to the best quality of Czochralski ruby or optical glass. For example, 6 mm by 100 mm rods cut from the outer sections of 20 mm by 150 mm boules may typically show only 1 to 2 fringes in a Twyman-Green interferometer [27].

Neodymium concentration by atom percent in YAG has been limited to 1.0 to 1.5 %. Higher doping levels tend to shorten the fluorescent lifetime, broaden the linewidth and cause strain in the crystal, resulting in the poor optical quality. The Nd doping level in YAG is sometimes expressed in different concentration units: A concentration of 1.0 % Nd atoms in the lattice is equivalent to 0.727 % Nd or 0.848 % Nd_2O_3 by weight, respectively. The concentration of Nd^{3+} sites in these cases is 1.386×10^{20} cm^{-3} [27].

In specifying Nd:YAG rods, the emphasis is on size, dimensional tolerence, doping level and passive optical tests of rod quality. Cylindrical rods with flat ends are typically finished to the following specifications: end flat to $\lambda/10$, ends parallel to $\pm$ 4 arc seconds, perpendicularity to rod axis to $\pm$ 5 minutes, rod axis parallel to within $\pm$ 5° to [111] direction. Dimensional tolerences typically are $\pm$ 0.5 mm on length and $\pm$ 0.025 mm on diameter. Most supliers furnish the laser crystals with a photograph showing the fringe pattern of the crystal as examined by Twyman-Green interferometer. A double pass Twyman-Green interferometer quickly reveals strained areas, small defects, or processing errors [27].

In a particular application the performance of a Nd:YAG laser can be improved by the choice of the optimum Nd concentration. As a general guideline, it can be said that a high doping concentration (approximately 1.2 %) is desirable for Q-switching operation because this will lead to high energy storage. For cw operation, a low doping concentration (0.6 to 0.8 %) is usually chosen to obtain good beam quality [27].

It is worth noting that in contrast to a liquid or a glass, a crystal host is not amenable to uniform dopant concentration. This problem arises as a result of the crystal-growth mechanism. In the substitution of the larger Nd^{3+} for a Y^{3+} in $Y_3Al_5O_{12}$, the neodymium is preferentially retained in the melt. The increase in concentration of Nd from the seed to the terminus of a 20-cm long boule is about 20 to 25 %. For a laser rod 3 to 8 cm long, this end-to-end variation may be 0.05 to 0.10 % of Nd_2O_3 by weight [27].

2.11.5 Different laser transition in Nd:YAG

Under normal operating conditions the Nd:YAG laser oscillates at room temperature on the strongest $^4F_{3/2} \rightarrow {}^4I_{11/2}$ transition at 1.0641 μm. It is possible, however to obtain oscillation at other wavelengths by inserting etalons or dispersive prisms in the resonator, by utilizing a specially designed resonant reflector as an output mirror, or by employing highly selective dielectrically coated mirrors. These elements suppress laser oscillation at the undesirable wavelength and provide optimum conditions at the wavelength desired. With this technique over 20 transitions have been made to laser in Nd:YAG. The relative output of those transitions at which room-temperature cw operation has been achieved is listed in the Table 2-3. The relative performance is compared to 1.064 μm emission for which 71.5 W output was obtained [27].

Wavelength ([μm], air)	Transition	Relative Performance
1.05205	$R_2 \rightarrow Y_1$	46
1.06152	$R_1 \rightarrow Y_1$	92
1.06414	$R_2 \rightarrow Y_3$	100
1.0646	$R_1 \rightarrow Y_2$	~ 50
1.0738	$R_1 \rightarrow Y_3$	65
1.0780	$R_1 \rightarrow Y_4$	34
1.1054	$R_2 \rightarrow Y_5$	9
1.1121	$R_2 \rightarrow Y_6$	49
1.1159	$R_1 \rightarrow Y_5$	46
1.12267	$R_1 \rightarrow Y_6$	40
1.3188	$R_2 \rightarrow Y_1$	34
1.3200	$R_2 \rightarrow Y_2$	9
1.3338	$R_1 \rightarrow Y_1$	13
1.3350	$R_1 \rightarrow Y_2$	15
1.3382	$R_2 \rightarrow Y_3$	24
1.3410	$R_2 \rightarrow Y_4$	9
1.3564	$R_1 \rightarrow Y_4$	14
1.4140	$R_2 \rightarrow Y_6$	1
1.4440	$R_1 \rightarrow Y_7$	0.2

Table 2-3 Main transitions at room temperature in Nd:YAG.

The 1.064- and 1.061-μm transitions, $^4F_{3/2} \rightarrow {}^4I_{11/2}$, provide the lowest threshold laser lines in Nd:YAG. At room temperature the 1.064-μm line $R_2 \rightarrow Y_3$ is dominant, while at low temperatures the 1.061-μm line $R_1 \rightarrow Y_1$ has the lower threshold. If the laser crystal is cooled, additional laser transitions are obtained, most notably the 1.839-μm line and the 0.946-μm line [27].

2.12 Nd:YVO$_4$ laser

2.12.1 Overview

Early spectroscopy and laser studies show that Nd:YVO$_4$ is an excellent laser crystal. For example, the laser emission cross-sections of Nd:YVO$_4$ crystal at 1.06 μm and 1.34 μm are 2.7 and 18 times larger than that in Nd:YAG respectively, and the crystal has good mechanical, physical and chemical properties. However, the difficulties to grow crystal with high optical quality hinder its application. In recent years much attention has been paid to the crystal again after some of the difficulties have been overcome in crystal growth. Nd:YVO$_4$ crystals were used as excellent laser material pumped by laser diodes (LD). They also allow doping with higher neodymium concentration and have larger absorption coefficient than Nd:YAG crystal. The length of Nd:YVO$_4$ crystal in lasers can be reduced greatly because of its advantages. Lasers using Nd:YVO$_4$ crystal produce cw laser radiation at 1.06 μm and 1.34 μm when pumped by LD at 808 nm. Because a Nd:YVO$_4$ crystal has a large thermal conductivity, it may be used in higher power laser systems. A Nd:YVO$_4$ crystal produces cw green laser radiation at 532 nm when nonlinear crystals such as KTP or LBO are used. The output power of 7 W at 532 nm has been obtained. Nd:YVO$_4$ crystals are being used commercially at present because of their excellent properties. It is important to study the

thermal-mechanical properties of Nd:YVO$_4$ crystal to determine if it can be used for high power. The thermal expansion is important for crystal growth and laser oscillation, and the specific heat is also one of important factors that influence the damage threshold of the crystal (XU). A large and good quality Nd:YVO$_4$ crystal was grown successfully by the Czochralski method. The thermal expansion and specific heat were measured. The large an-isotropy along a- and c-axis of the thermal expansion coefficients is explained by the structure of YVO$_4$ crystal. The laser at 1.06 mm is demonstrated pumped by a 3 W light diode, and the light-light conversion efficiency is 50 %, and the slope efficiency is 55.5%. Fig. 2-16 shows the thermal expansion of Nd:YVO$_4$ crystal as a function of its temperature in both a- and c-axes [28].
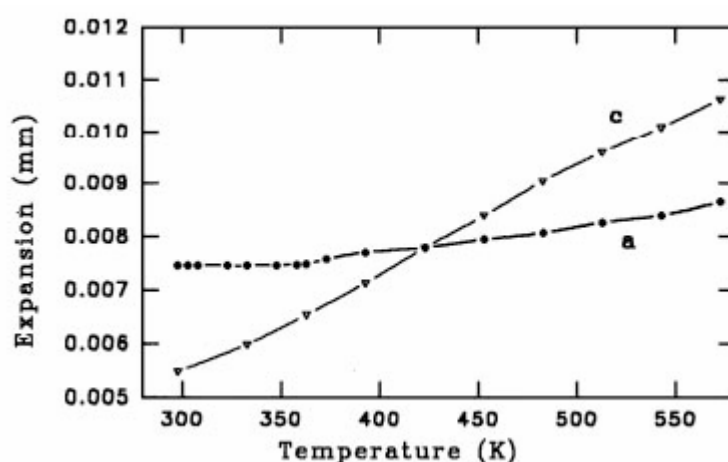
Fig. 2-16 The thermal expansions of Nd:YVO crystal as a function of Temperature in a- and c- axes. Scan rate: 5 °C/min [28].

2.12.2 Vanadate features

The vanadate has some features, which can be summerized as follows:

1- Low lasing threshold and high slope efficiency.

2- Large stimulated emission cross-section at lasing wavelength.

3- High absorption over a wide pumping wavelength bandwidth.

4- Optically uniaxial and large birefringence emiting polarized laser.

5- Low dependency on pumping wavelength and tends to produce single mode output.

2.12.3 Nd:YVO$_4$'s advantages over Nd:YAG

Here are some of the advantages of the Nd:YVO$_4$ over the Nd:YAG laser. It has:

1- An absorption coefficient five times larger over a wide pumping bandwidth around 808 nm. Therefore, the dependency on pumping wavelength is much lower and this is strong tendency to the single mode output.

2- A stimulated emission cross-section upto three times larger at the lasing wavelength of 1064 nm.

3- Lower lasing threshold and higher slope efficiency.

As a uni-axial crystal with a large birefringence, the emission is linearly polarized. Table 2-4 shows the basic properties of the $Nd:YVO_4$ laser crystal, while Table 2-5 shows its main optical properties. Moreover, the absorption curve of 0.5% $Nd:YVO_4$ of thickness 4 mm is shown in Fig. 2-17.

Property	Value
Crystal Structure Cell Parameter	Zircon Tetragonal, space group D_{4h}-I4/amd a = b = 7.1193 Å, c = 6.2892 Å
Density	4.22 g/cm^3
Atomic Density	1.26×10^{20} atoms/cm^3 (Nd 1.0 %)
Mohs Hardness	4-5 (Glass-like)
Thermal Expansion Coefficient (300 K)	$\alpha_a = 4.43 \times 10^{-6}$ /K $\alpha_c = 11.37 \times 10^{-6}$ /K
Thermal Conductivity Coefficient (300 K)	//C: 0.0523 W/cm/K $\perp$C: 0.0510 W/cm/K
Lasing wavelength	1064 nm, 1342 nm
Thermal optical coefficient (300 K)	$dn_o/dT = 8.5.10^{-6}$ /K $dn_e/dT = 2.9.10^{-6}$/K
Stimulated emission cross-section	25.10^{-19} cm^2 at1064 nm
Fluorescent lifetime	90μs
Absorption coefficient	31.4 cm^{-1} at 810 nm
Intrinsic loss	0.02 cm^{-1} at1064 nm
Gain bandwidth	0.96 nm at1064 nm
Polarized laser emission	π polarization; parallel to optical axis(c-axis)
Diode pumped optical to optical efficiency	>60%
Sellmeier equations	$n_o^2 = 3.77834+0.069736/(\lambda^2-0.04724)-0.010813\lambda^2$ $n_e^2 = 4.59905+0.110534/(\lambda^2-0.04813)-0.012676\lambda^2$

Table 2-4 Basic properties of $Nd:YVO_4$.

Property	Value
Lasing Wavelength:	1064 nm, 1342 nm
Thermal Optical Coefficient (at300K)	$dn_o/dT = 8.5 \times 10^{-6}$ /K $dn_e/dT = 2.9 \times 10^{-6}$ /K
Sellmeier Equation (for pure YVO4 crystals)	$n_o^2 = 3.77834 + 0.069736/(\lambda^2 - 0.04724) - 0.0108133\lambda^2$ $n_e^2 = 4.59905 + 0.110534/(\lambda^2 - 0.04813) - 0.0122676\lambda^2$
Stimulated Emission Cross-section	25×10^{-19} cm^2 at1064 nm
Fluorescent Lifetime	90 μs
Absorption Coefficient	31.4 cm^{-1} at 810 nm
Intrinsic Loss	0.02 cm^{-1} at1064 nm
Gain Bandwidth	0.96 nm at1064 nm
Polarized Laser Emission	π polarization; parallel to optic axis (c-axis)

Table 2-5 Optical properties of Nd:YVO$_4$.
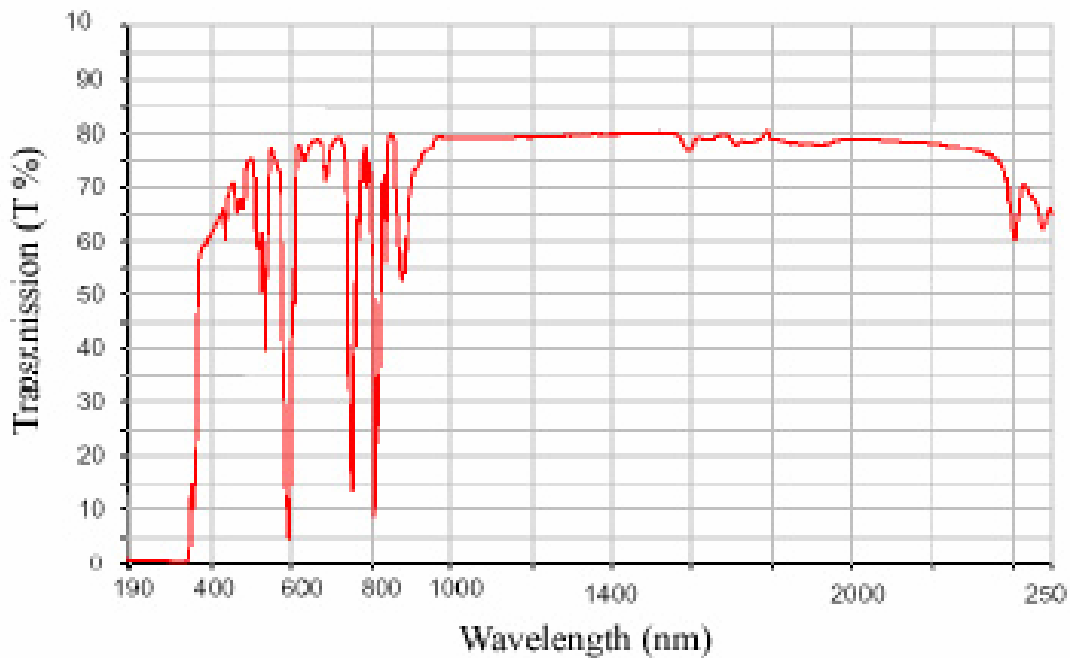
Fig. 2-17 Absorption Curve of 0.5% Nd:YVO$_4$ (thickness 4 mm).

2.12.4 Laser properties of Nd:YVO$_4$

During the work on the Nd:YVO$_4$, many studies have discovered some properties and advantages of using such a material as a lasing medium. We can summerize these properties in the following points [28]:

1. One most attractive character of Nd:YVO4 is - compared with Nd:YAG - its 5 times larger absorption coefficient in a broader absorption bandwidth around the 808 nm peak pump wavelength, which just matches the standard of high power laser diodes currently available. This means a smaller crystal could be used for the laser, leading to a more compact laser system. For a given output power, this also means a lower

64

power level at which the laser diode operates, thus extending the lifetime of the expensive laser diode. The broader absorption bandwidth of Nd:YVO4 which may be 2.4 to 6.3 times that of Nd:YAG. Besides more efficient pumping, it also means a broader range of selection of diode specifications. This will be helpful to laser system makers for wider tolerance and lower cost choice.

2. The Nd:YVO4 crystal has larger stimulated emission cross-sections, both at 1064 nm and 1342 nm. When the crystal is cut along the a-axis, the cross-section for stimulated emission at 1064 nm is about 4 times higher than that of Nd:YAG, while at 1340nm the stimulated cross-section is 18 times larger, which leads to a CW operation completely outperforming Nd:YAG at 1320 nm. This makes it lasers easier for a Nd:YVO4 to maintain a strong single line emission at the two wavelengths.

3. Another important character of Nd:YVO4 lasers is that it has an uni-axial rather than a higher cubic symmetry like Nd:YAG. It only emits a linearly polarized laser light, thus avoiding undesired birefringent effects on the frequency conversion. Although the lifetime of Nd:YVO4 is about 2.7 times shorter than that of Nd:YAG, its slope efficiency is still quite high for a properly designed laser cavity, because of its high pump quantum efficiency.

The major laser properties of Nd:YVO4 and Nd:YAG are listed in Table 2-6, including stimulated emission cross-sections (σ), Absorption Coefficient (α) Fluorescent lifetime (τ), Absorption Length (L_α), threshold Power (P_{th}) and Pump Quantum Efficiency (η). Moreover, Table 2-7 gives some measured values of input and output powers for both laser materials.

Laser crystal	Doping (ATM%)	σ ($\times 10^{-19}$ cm^2)	α (cm^{-1})	τ (ms)	L_α (mm)	P_{th} (mW)	η_s (%)
Nd:YVO4 (a-cut)	1.0 2.0	25 25	31.2 72.4	90 50	0.32 0.14	30 78	52 48.6
Nd:YVO4 (c-cut)	1.1	7	9.2	90		231	45.5
Nd:YAG	0.85	6	7.1	230	1.41	115	38.6

Table 2-6 Laser Properties of Nd:YVO$_4$ and Nd:YAG.

Crystals	Size (mm^3)	Pump Power	Output (at 1064 nm)
Nd:YVO$_4$	3×3×1	850 mW	350 mW
Nd:YVO$_4$	3×3×5	15 W	6 W
Nd:YAG	3×3×2	850 mW	34 mW

Table 2-7 Diode pumped Nd:YVO4 laser output compared with that of a Nd:YAG laser.

2.13 Solar lasers

Solar laser is one of the novel branches in recent technology. This branch has been developed from the combination of two sciences; solar energy and laser physics. Thinking about this branch gives a suggestion that the desirable laser for use in space communications, industries, medicine, photometry, etc. would be one that derives all its power from the Sun [1].

When thinking of laser power generation, some points immediately come to mind:

1- The population inversion must be produced by a simple and cheap method.

2- The lasing medium must be a simple and cheap material.

3- The produced laser power must be applicable in the conversion processes.

The optical and electrical pumping methods are well known. Some are expensive, difficult or problematic, so the trend of looking to the Sun as a natural power supply has common.

The building of continuously operating high power laser system using solar energy falls into two types:

(I) Indirect pumping

Indirect pumping can be made by a photovoltaic converter which converts solar radiation into the needed electricity as shown in Fig. 2-18.

When a solar powered electrical generator is used to run a conventional *Electric Discharge Laser (EDL)*, which have efficiencies of about 50 % or *Excimer Laser* which has an efficiency of about 15 %, then the system of this type consists of:

1- Photovoltaic collector.
2- Adaptive optics.
3- Electrical power converter.
4- Laser system.
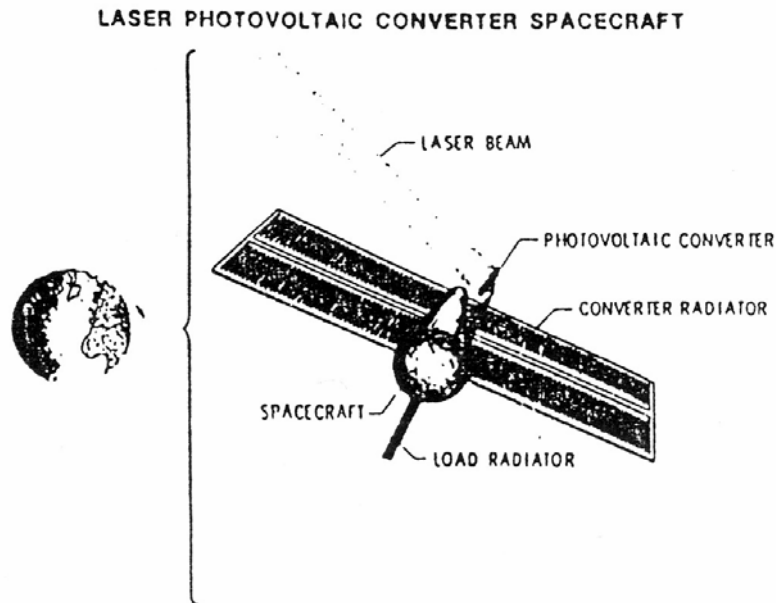
Fig. 2-18 Laser photovoltaic converter spacecraft typical of laser receiver systems.

(II) Direct pumping

Where large concentrators focus the image of the sun into a laser medium, a large lasing volume is directly pumped in this manner, depending on the threshold pumping power of the laser medium and the concentration ratios of the concentrators. A schematic example of this manner is shown in Fig. 2-19.
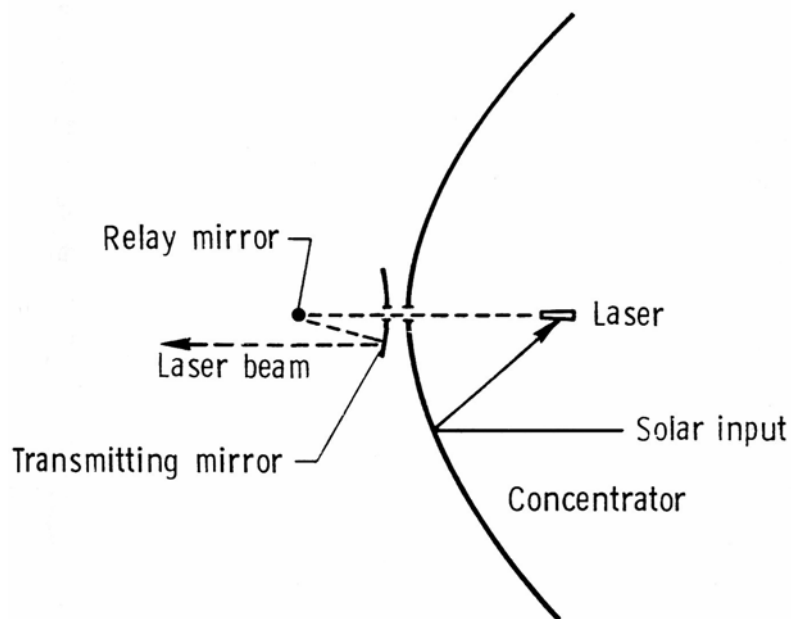
Fig. 2-19 Schematic of direct solar-pumped laser.

The disadvantage of indirect pumping is the large size of electric generators and the technology of the several steps needed. On the other hand, the disadvantage of direct pumping is the waste heat produced from the unutilised wavelengths by absorption in the lasing medium but this could be overcomed by cooling or chopping [1].

In speaking about solar laser, we have to define an important parameter. This parameter enters in the calculations and has an effect on the output laser power attained from the system of solar laser. This parameter is the overlap between the standard solar spectrum and the laser absorption one. This is because not all of the already concentrated solar spectrum is used in the laser pumping. Fig. 2-20 shows the absorption of Nd:YAG laser bands with respect to the standard solar spectrum. The overlapping ratio between them was calculated to be 0.14. This value can obviously differ according to the used laser system [10].
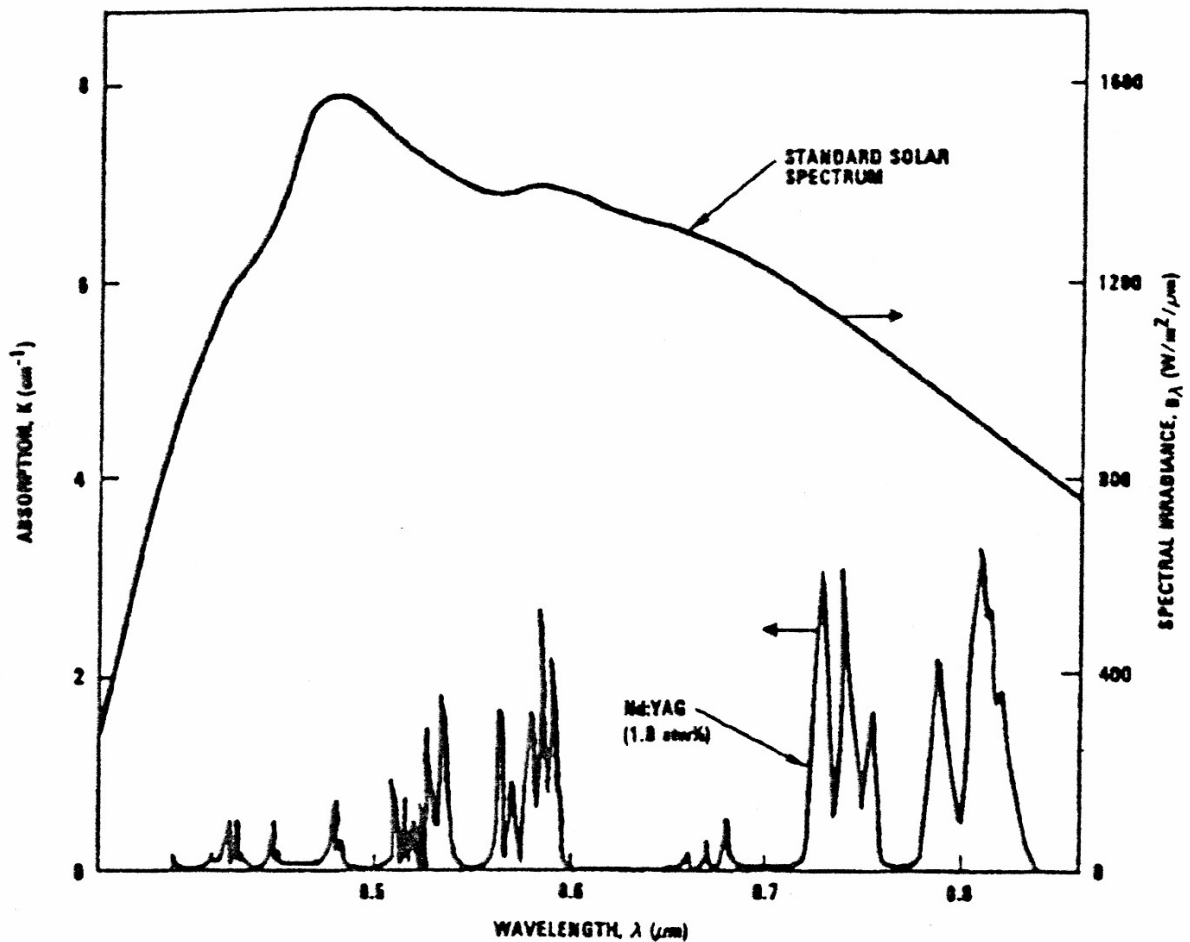
Fig. 2-20 Schematic of the Nd:YAG absorption bands and the standard solar spectrum.

Chapter 3: Concentrating Collectors

Overview

In this chapter, information about the types of optical concentrators is discussed in detail. Parameters which affect their concentration levels are also discussed. Their properties, designations and mathematical formulas are mentioned. Finally, their optimums are also determined for use in our work.

3.1 Introduction

For many applications it is desirable to deliver energy at intensities and temperatures higher than those possible under the normal conditions. Energy delivery intensities and temperatures can be increased by decreasing the area from which radiation and heat losses occur. This is done by interposing an optical device between the source of radiation and the energy absorbing surface.

Many designs have been set forth for concentrating collectors. Concentrators can be reflectors or refractors, cylindrical or surfaces of revolution, and continuous or segmented. Receivers can be convex, flat, or concave and can be coverd or uncovered. Many modes of tracking are possible. Concentration ratios (the ratios of collector aperture area to absorber area, which are approximately the factors by which radiation flux on the energy-absorbing surface is increased) can vary over several orders of magnitude. With this wide range of designs, it is difficult to develop general analyses applicable to all concentrators. Thus concentrators are treated in two groups: non-imaging collectors with low concentration ratio and linear imaging collectors with intermediate concentration ratio. We also note some basic considerations of three-dimensional concentrators that can operate at the high end of the concentration ratio scale.

Concentrators can have concentration ratios from low values of less than unity to high values of the order of 10^5. Increasing ratios mean increasing temperatures at which energy can be delivered and increasing requirements for precision in optical quality and positioning of the optical system. Thus the cost of delivered energy from a concentrating collector is a function of the temperature at which it is available. At the highest range of concentration and correspondingly highest precision of optics, concentrating collectors are termed solar furnaces; these are laboratory tools for studying properties of materials at high temperature process [2].

The target on which the radiation energy will be concentrated has many names such as: receiver, absorber or target. We can use all of them to nominate that target.

The instrument used in this action is called the concentrator or the collector or the solar furnace. Table 3-1 represents characteristics of the conventional "light" solar furnace [29].

Advantages	Disadvantages
• Very high temperatures (3500 º C).	• Large systems are required to produce large focal areas of uniform flux density.
• Solar radiation does not compinate process.	• Furnace can only operate during periods of high insolation.
• Rapid heating and cooling.	
• Low energy demand.	• System or part of system has to track the sun accurately.
• Material may be processed in many desired atmospheres.	• External optical surfaces have to be maintained to a high standard.
• Low Mass.	• Optical surfaces within furnace system have to be kept clean (i.e. windows).
• The sample need not have contact with other materials during the heating process.	• Potentially more hazards than conventional furnaces.
• The heating process may be observed at close range as radiant energy density, if low beyond the focal area.	
• The sample is accessible for various measurements.	

Table 3-1 Characteristics of the conventional "light" solar furnace.

3.2 Collector configurations

Many concentrator types are possible for increasing the flux of the radiation on the receivers. They can be reflectors or refractors. They can be cylindrical to focus on a "line" or circular to focus on a "point". Receivers can be concave, flat or convex. Examples of six configurations are shown in Fig. 3-1.

The first two are arrays of evacuated tubes with cylindrical absorbers spaced apart, with back reflectors to direct radiation on the area between the tubes to the absorbers. The first uses a flat diffuse back reflector and the second cusp-shaped specular reflectors. The configuration shown in Fig. 3-1 (c) has a plane receiver with plane reflectors at the edges to reflect additional radiation onto the receiver. The concentration ratios of this type are low,

with maximum value of less than 4. Some of the diffuse component of radiation incident on the reflectors would be absorbed at the receiver. These collectors can be viewed as flat-plate collectors with augmented radiation. Fig. 3-1 (d) shows a reflector of parabolic shape, which could have a cylindrical surface (with a tubular receiver) or a surface of revolution (with a spherical or hemispherical receiver). Cylindrical collectors of this type have been studied in some detail and are being applied [2].
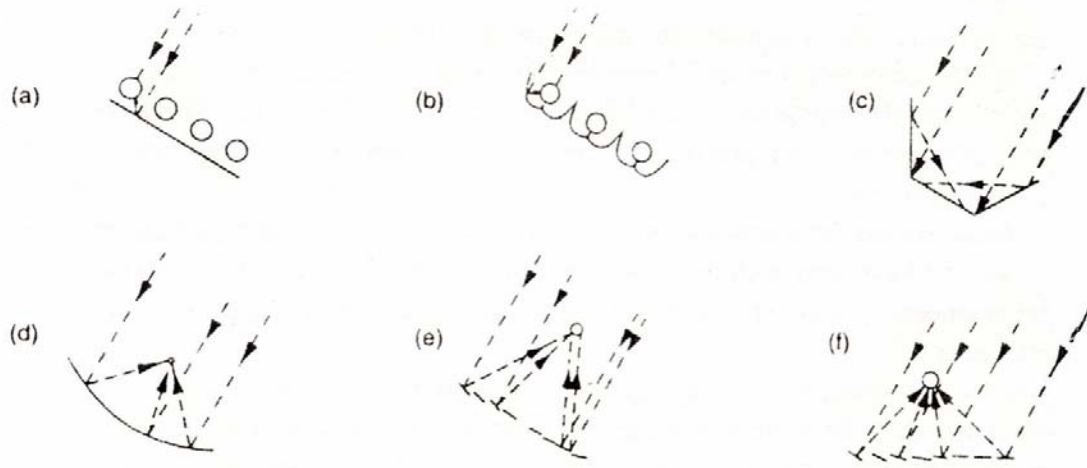
Fig. 3-1 Possible concentrating collector configurations: (a) tubular absorbers with diffuse back reflector; (b) tubular absorbers with specular cusp reflectors; (c) plane receiver with plane reflectors; (d) parabolic concentrator; (e) Fresnel reflector; (f) array of heliostats with central receiver.

The continuous parabolic reflector can be replaced by a Fresnel reflector; a set of flat reflectors on a moving array as shown in Fig. 3-1 (e), or by its refracting equivalent. The facets of the reflector can also be individually mounted and adjusted in position as shown in Fig. 3-1 (f). Large arrays of heliostats of this type, with receivers mounted on a tower, are the basis of designs of "central receiver" collectors.

For the concentrators shown on Fig. 3-1 (c)-(f), single-sided flat receivers may be used (if the receiver is not "inside" of the reflector). Cylindrical, hemispherical, or other convex shapes and cavity receivers may also be possible.

In general, concentrators with receivers much smaller than the aperture (the plane opening of the concentrator through which the solar radiation passes) are effective only on beam (direct) radiation. It is also evident that the angle of incidence of the beam radiation on the concentrator is important and that sun tracking will be required for these collectors. A variety of orienting mechanisms has been designed to move focusing collectors so that the incident beam radiation will always be reflected to the receiver. The motions required to accomplish tracking vary with the design of the optical system, and a particular resultant motion may be accomplished by more than one system of component motions.

Linear (cylindrical) optical systems focus beam radiation onto the receiver if the sun is in the central plane of the concentrator (the plane, including the focal axis and the vertex line of the reflector). These collectors can be rotated about a single axis of rotation, which may be north-south, east-west, or inclined and parallel to the earth's axis (in which case the rate of

rotation is 15°/h). There are significant differences in both quantity of incident beam radiation, its time dependence and the image quality obtained with these three modes of orientation [2].

Reflectors that are surfaces of revolution (circular concentrators) optically are oriented so that their axis is in line with the sun and thus must be able to move about two axes. These may be horizontal and vertical, or one axis of motion may be inclined so that it is parallel to the earth's axis of rotation (i.e. a polar axis) and the other perpendicular to it. The angle of incidence of beam radiation on a moving plane is indicated for the most probable modes of orientation of that plane in the Appendix II.

Orientation systems can provide continuous or nearly continuous adjustments, with movement of the collector to compensate for the changing position of the sun. For some low-concentration linear collectors it is possibile to adjust their position intermittently, with weekly, monthly, or seasonal changes possible for some designs. Continuous orientation systems may be based on manual or mechanized operation. Manual systems depend on the observations of operators and their skill at making the necessary corrections. This may be adequate for some purposes if concentration ratios are not too high and if labor costs are not prohibitive; they have been suggested for use in areas of very low labour cost.

Mechanised orienting systems can be sun-seeking systems or programmed systems. Sun-seeking systems use detectors to determine system misalignment and through controls make the necessary corrections to realign the assembly. Programmed systems, on the other hand, cause the collector to be moved in a predetermined manner (e.g. 15°/hr about the polar axis) and may need only occasional checking to assure alignment. It may also be advantageous to use a combination of these tracking methods, for example, by superimposing small corrections by a sun-seeking mechanism on a programmed "rough positioning" system. Any mechanized system must have the capability of adjusting the position of the collector from end-of-day position to that for operation early the next day, adjusting for intermittent clouds, and adjusting to a safe position where it can best withstand very high winds without damage [2].

3.3 Classification of optical concentrators

There is a variety of different concentrator designs. They are classified into two major optical categories:

(I) Imaging optics concentrators.
(II) Non-imaging optics concentrators.

In the imaging optics concentrators, we are concerned with the image formed by the optical concentrator on the receiver, so that the receiver must be small enough to attain some homogeneity in the distribution of the formed image (focus). Thus, the imaging optics concentrators have their advantage that they have a high value of concentration. On the other hand, in the non-imaging optics, we are not concerned with forming an image, and thus the receiver may be large with a homogeneity of the radiation on the receiver but its concentration is smaller than that of imaging optics concentrators.

3.4 Types of optical concentrators

Many types of optical concentrators are possible for increasing the flux of radiation on receivers. For the imaging type of concentrators, they can be "cylindrical" to focus on a "line" or circular to focus on a "point", while for the nonimaging one; they can be in troughlike shape for the long absorber or in conical shape for circular absorber. We will mention some of them here:

1- Flat Plate Collector (FPC).
2- V-Trough Concentrator.
3- Parabolic Trough Concentrator (PTC).
4- Compound Parabolic Concentrator (PTC).
5- Central Receiver Collector.
6- Fresnel Lens Concentrator.
7- Conical Concentrator.
8- Paraboloidal Concentrator.
9- Compound Elliptical Concentrator (CEC).
10- Hyperpoloidal Concentrator (Trumpet Concentrator).
11- Spherical Concentrator.
12- Pyramidical Concentrator.

Fig. 3-2 illustrates some types of the concentration collectors [30].
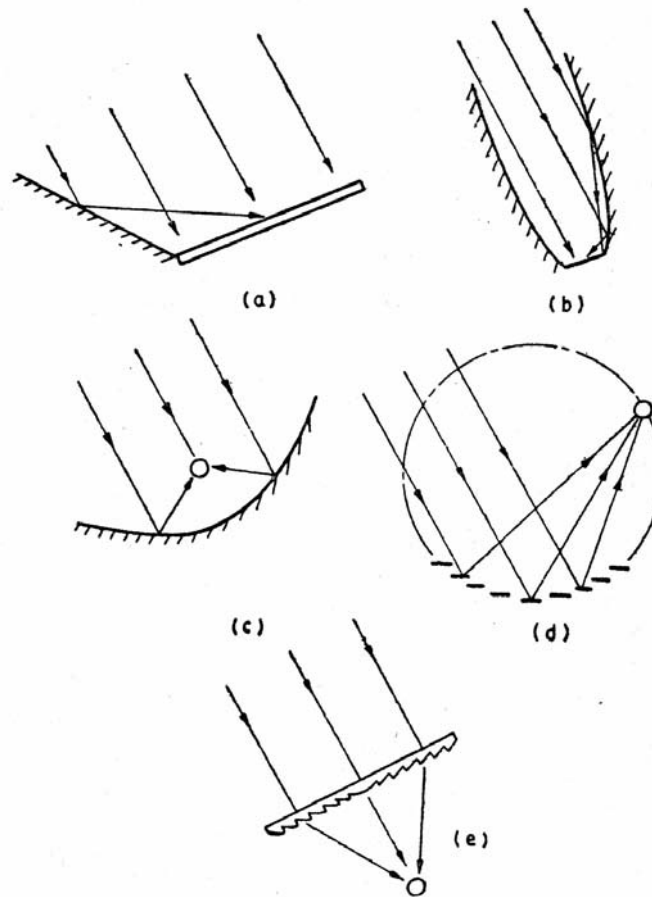
Fig. 3-2 Types of concentrating collectors:
    (c)   Flat plate collector with plane reflectors (FPC).
    (d)   Compound parabolic collector (CPC).
    (c) Cylindrical parabolic collector.
    (f)   Collector with fixed circular concentrator and moving receiver.
    (g)   Fresnel lens concentrating collector (FL).

Receivers can also take different forms; they can be concave, flat, convex or tubular.

3.5 Definitions

In order to be consistent in the use of terms, we will use the phrase *"concentrating collector"* to denote the whole system. The term *"concentrator"* will be used only for the optical subsystem which directs the solar radiation on to the absorber, while the term *"receiver"* will normally be used to denote the subsystem consisting of the absorber, its cover and other accessories.

We will now define five terms: aperture, concentration ratio, acceptance angle, intercept factor, and incidence angle modifier. The first three terms are common in both of the two main categories of concentrators mentioned above (imaging and noninaging optical concentrators), while the last two are only special for the imaging optical concentrators [30].

74

The Aperture (W):

It is the plane opening of the concentrator through which the solar radiation passes.

For a cylindrical or linear concentrator, it is characterized by the width, while for a surface of revolution it is characterized by the diameter of the opening.

The Concentration Ratio (C):

There are two natural definitions of concentration ratio that have been in use; to avoid confusion a subscript should be added whenever the context does not clearly specify which definition is meant. The first definition is strictly geometrical and named *"Geometric Concentration"* or *"Area Concentration"*, while the second one is in terms of the ratio of the measured intensity and named *"Intensity Concentration"* or *"Flux Concentration"*.

The Area Concentration (C_{area}):

It is the ratio of the effective area of the aperture to the surface area of the absorber.

$$C_{area} = A_a/A_r \qquad (3\text{-}1)$$

where A_a is the area of the aperture and A_r is the area of the receiver (the absorber) of the concentrator.

The Flux Concentration (C_{flux}):

It is the ratio of the intensity at the aperture to that at the absorber.

$$C_{flux} = I_a/I_r \qquad (2\text{-}2)$$

where I_a is the value of flux at the aperture and I_r is the value of the flux at the receiver (the absorber) of the concentrator.

Values of the concentration ratio vary from unity (which is the limiting case for a flat-plate collector) to a few thousand for a parabolic dish.

The Acceptance Angle ($2\theta_a$):

It is the angle over which beam radiation may deviate from the normal to the aperture plane and yet reach the absorber without moving all or part of the collector.

The geometrical optics and the second law of thermodynamics require that the maximum possible concentration for a given collector acceptance half angle θ_a is:

$$C_{ideal,2D} = 1/sin\,\theta_a \qquad (2\text{-}3)$$

for two-dimensional (troughlike) concentrators, and:

$$C_{ideal,3D} = 1/sin^2\theta_a \qquad (2\text{-}4)$$

for three-dimensional ones (cones, dishes, pyramids).

Collectors with large acceptance angles require only occasional adjustments, while collectors with small acceptance angles have to be adjusted continuously.

Since the angular radius of the sun is $\theta_s \approx 1/4°$, the optical and thermodynamic limit of a tracking solar concentrator is about 200 in two-dimensional (line focus) geometry, and about 40,000 in three-dimensional (point focus) geometry [31].

The Intercept Factor (γ):
It is the fraction of the reflected radiation which is incident on the absorbing surface of the receiver.

The Incident Angle Modifier (K):
It is the errors in concentrator contours, tracking (pointing) errors and errors in displacement of receivers from the focus which can lead to enlarged or shifted images and affected transmittance system and the absorptance of a receiver.

The concentration achievable in the practical systems is reduced by a number of factors [31]:

1- Most conventional concentrators, in particular focusing parabolas or lenses, are base on optical designs which fall short of the thermodynamic limits by a factor of 2 to 4.

2- Tracking errors and error in mirror contour and receiver alignment necessitate design acceptance angles considerably larger than the angular width of the sun.

3- No lens or mirror material is a perfectly specular reflector and, therefore, the acceptance angle must be enlarged further; the nonspecular effect is averaged by dirt and dust.

4- Due to atmospheric scattering, a significant portion of the solar radiation may come from directions other than the solar disc itself.

The concentration ratio in solar concentrator involves a compromise between optical and thermal performance. The absorber should be chosen as small as possible to reduce heat loss, yet large enough to intercept all, or almost all, incident radiation. One therefore has to consider the rays with the largest expected deviation θ_c from the design direction, i.e., the direction from collector aperture to the centre of the sun. This angular deviation θ_c is due to the finite size of the sun and to mirror and tracking errors. The example of the parabolic trough reflector with cylindrical absorber tube, in Fig. 3-3 illustrates the definition of θ_c. The absorber tube is placed concentrally around the focal line. If the ray with the largest deviation is to just reach the absorber, as shown by the dashed line in Fig. 3-3, then the concentration ratio must be:

$$C_{2D, parab, cyl, abs} = \frac{2x_A}{2\pi a} = \frac{\sin\phi}{\pi \sin\theta_c} = \frac{\sin\phi}{\pi} C_{ideal}$$

(2-5)

76

where ϕ is the rim angle $\angle$ AOB. The maximum occurs at $\phi = 90°$ and falls a factor π short of the ideal limit. This is typical of all single-stage focusing concentrators; i.e., they achieve only one-forth to one-half of the thermodynamic concentration limit. For practical installations, geometric concentration is not the only design criterion, and slightly different rim angles will be used. For example, rim angles beyond 90° and undersized absorbers can be used if the reflector cost is low [31].
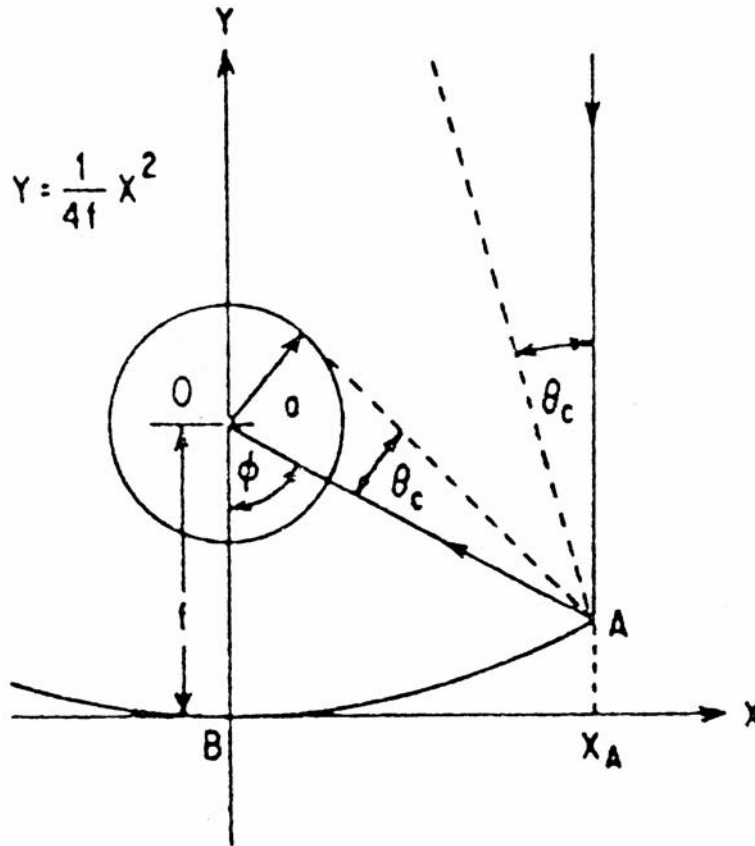
Fig. 3-3 Focusing parabola showing focal length f and acceptance half-angle θ_a.

There is, however, a class of non-imaging concentrators, which actually reaches the thermodynamic limit of concentration. Furthermore, a conventional focusing system with a matching CPC as second-stage concentrator can closely approach the thermodynamic limit. The choice of optimal concentration for a given application involves evaluation of many other factors optical, climatic, thermal and economic, etc. and it is unlikely that any single concentrator type will be the best for all applications. It is therefore appropriate to analyse many solar concentrator types [32].

The area concentration ratio has an upper limit that depends on whether the concentration is a three-dimensional (circular) concentrator such as a paraboloidal or a two-dimensional (linear) concentrator such as a cylindrical parabolic concentrator. The following development of the maximum concentration ratio, from Rabl [33], is based on the second low of thermodynamics applied to radiative heat exchange between the sun and the receiver.

Consider the circular concentrator with aperture area A_a and receiver area A_r viewing the sun of radius r at distance R, as shown in Fig. 3-4. The half angle subtended by the sun is θ_s. (The receiver is shown beyond the aperture for clarity; the argument is the same if it is on the same side of the aperture as the sun.)
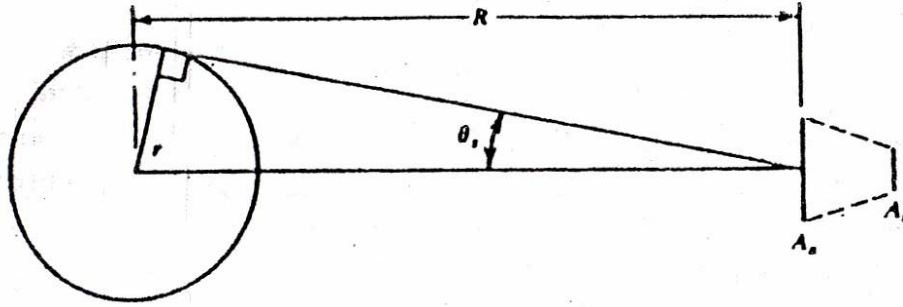
Fig. 3-4 Schematic of the sun at T_s at distance R from a concentrator
with aperture A_a and Receiver Area.

If the concentrator is perfect, the radiation from the sun on the aperture (and thus also on the receiver) is the fraction of the radiation emitted by the sun which is intercepted by the aperture. Although the sun is not a blackbody, for purposes of an approximate analysis it can be assumed to be a blackbody at T_s:

$$Q_{s \rightarrow r} = A_a \frac{r^2}{R^2} \sigma T_r^2$$

(3-6)

A perfect receiver (i.e., blackbody) radiates energy equal to $A_r T_r^4$, and a fraction of this, $E_{r\text{-}s}$, reaches the sun:

$$Q_{r \rightarrow s} = A_r \sigma T_r^4 E_{r\text{-}s}$$

(3-7)

When T_r and T_s are the same, the second law of thermodynamics requires the $Q_{s \rightarrow r}$ be equal to $Q_{r \rightarrow s}$. So from (2-6) and (2-7):

$$\frac{A_a}{A_r} = \frac{R^2}{r^2} E_{r-s}$$

(3-8)

and since the maximum value of $E_{r\text{-}s}$ is unity, the maximum concentration ratio for circular concentrators is:

$$\left(\frac{A_a}{A_r}\right)_{circular,\max} = \frac{R^2}{r^2} = \frac{1}{\sin^2\theta_s}$$

<div align="right">(3-9)</div>

A similar development for linear concentrators leads to:

$$\left(\frac{A_a}{A_r}\right)_{linear,\max} = \frac{1}{\sin\theta_s}$$

<div align="right">(3-10)</div>

Thus with $\theta_s = 0.27°$, the maximum possible concentration ratio for circular concentrators is 45,000, and for linear concentrators the maximum is 212 [2].

The higher the temperature at which energy is to be delivered, the higher must be the concentration ratio and the more precise must be the optics of both the concentrator and the orientation system. Fig. 3-5 shows practical ranges of concentration ratios and types of optical systems needed to deliver energy at various temperatures.
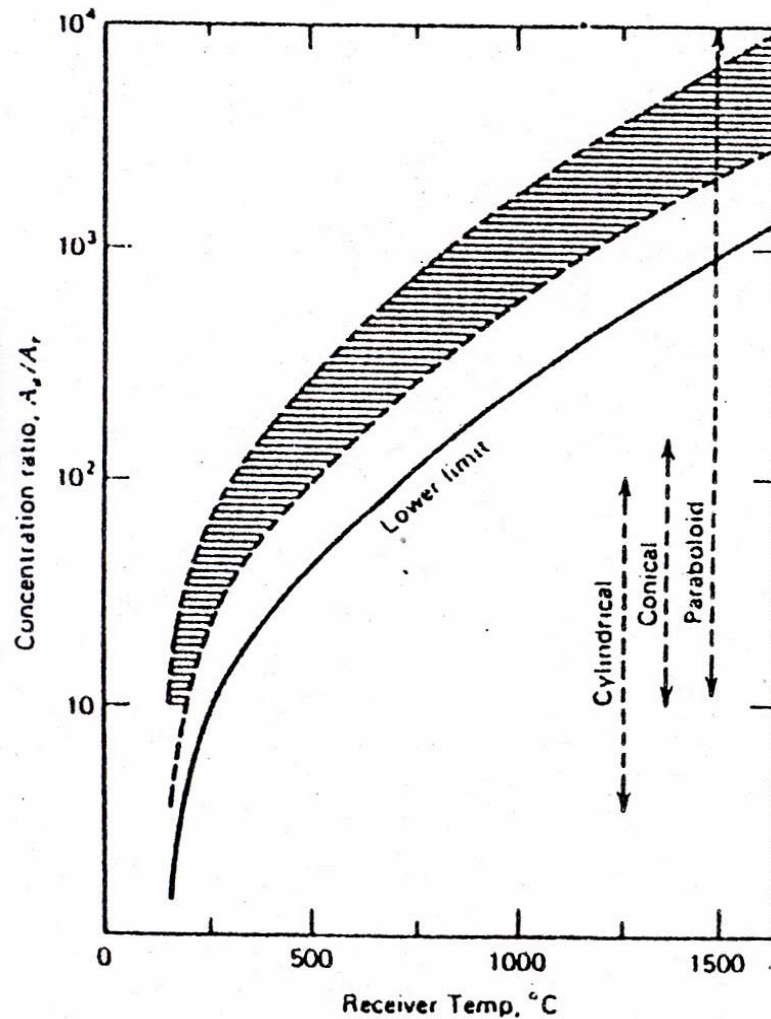
Fig. 3-5 Relationship between concentration ratio and temperature of receiver operation. The "lower limit" curve represents concentration ratios at which the thermal losses will equal the absorbed energy; higher ratios will then result in useful gain. The shaded range corresponds to collection efficiencies of 40 to 60% and represents a probable range of operation. Also shown are approximate ranges in which several types of reflectors might be used.

As we mentioned before, concentrators can be divided into two categories: non-imaging and imaging. Non-imaging concentrators, as the name implies, do not produce clearly defined images of the sun on the absorber but rather distribute radiation from all parts of the solar disc onto all parts of the absorber. The concentration ratios of linear non-imaging collectors are in the low range and are generally below 10. Imaging concentrators, in contrast, are analogous to camera lenses in that they form images (usually of very quality by ordinary optical standards) on the absorber [2].

3.6 Methods of classification

Concentrating collectors are of various types and can be classified in many ways. They may be of the reflecting type utilizing mirrors or of the refracting type utilizing Fresnel lenses. The reflecting surfaces used may be parabolic, spherical or flat. They may be

continuous or segmented. Classification is also possible from the point of view of the formation of the image, the concentrator being either imaging or nonimaging. Further, the imaging concentrator may focus on a line or at a point [30].

The concentration ratio is also used as a measure for classifying concentrating collectors. Since this ratio approximately determines the operating temperature, this method of classification is equivalent to classifying the collector by its operating temperature range.

A final possibility is to describe concentrating collectors by the type of tracking adopted. Depending on the acceptance angle, the tracking may be intermittent (one adjustment daily or every few days) or continuous. Further, the tracking may be required about one axis or two axes. Table 3-2 represents some applications of different concentrator types [31].

Tracking mode	Examples	Aprox. range of CR	Approx. maximum operating temperature
None (tilt fixed)	CPC	1.5 to 2.0	Up to 100 º C no vacuum
			Up to 150 º C vacuum
None (Two tilt adjustment per year)	V-trough	1.5 to 2.0	Up to 150 º C vacuum
	CPC	3.0	Up to 180 º C vacuum
None (Tilt adjusted seasonal to daily)	V-trough	2 to 3	Up to 180 º C vacuum
	CPC	3 to 10	100 to 150 º C no vacuum
			150 to 250 º C vacuum
One-axis tracking	Fresnel lens	6 to 30	100 to 200 º C
	Parabolic Trough	15 to 50	200 to 300 º C (with second-stage concentrator, vacuum, and selective absorber up to 400, perhaps 500 º C)
	Fresnel mirror		
	Fresnel mirror moving receiver		
Two-axis tracking	Fixed spherical reflector plus tracking receiver	50 to 150	300 to 500 º C
	Fresnel lens	100 to 1000	300 to 1000 º C
	Parabolic dish, Power tower	500 to 3000	500 to 2000 º C

Table 3-2 Summary of applications of different concentrator types.

3.7 Intercept factor

Definition:

The intercept factor γ is defined as the fraction of the reflected radiation that is incident on the absorbing surface of the receiver.

This concept is particularly useful in describing imaging concentrators [34]. An example of an image formed in the focal plane of a linear concentrator is shown in Fig. 3-6; if a receiver extends from A to B, the intercept factor will be:

$$\gamma = \frac{\int\limits_{A}^{B} I(y)\,dy}{\int\limits_{-\infty}^{\infty} I(y)\,dy}$$

<div align="right">(3-11)</div>

The objective in using concentrating systems is to reduce heat losses from the absorber by reducing its area. Most imaging collectors are built with receivers large enough to intercept a large fraction of the reflected radiation but not large enough to intercept the low-intensity fringes of the images. Values of γ greater than 0.9 are common [2].
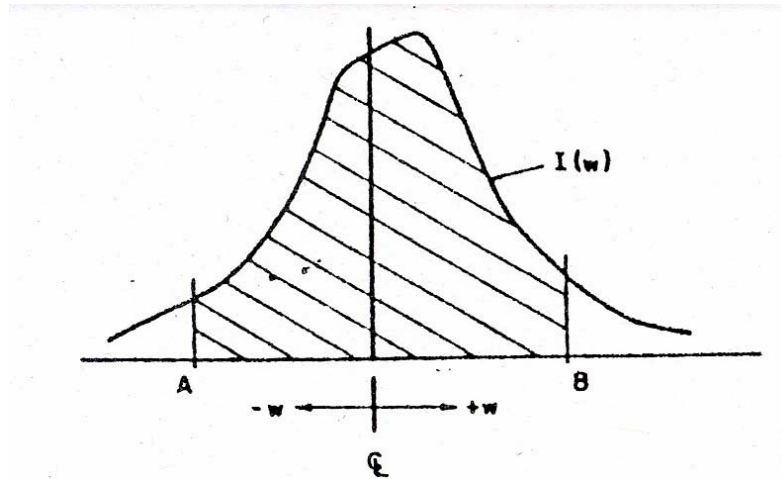
Fig. 3-6 An example of a flux distribution in the focal plane of a linear imaging concentrator. The receiver extends from A to B.

3.8 Incidence angle modifiers and energy balances

In practice, images do not often have well-defined boundaries, and it is usually best to use a receiver that will intercept less than all of the specularly reflected radiation. A trade-off between increasing thermal losses with increasing area and increasing optical losses with decreasing area is necessary to optimize long-term collector performance. This optimization problem was studied by Lof and Duffie [35, 36], with a result that for a wide range of conditions the optimum size receiver will intercept 90 to 95% of the possible radiation. Thus an optical loss, often in a range of 5 to 10 %, will be incurred in this type of collector. This has been expressed in terms of the intercept factor γ, the fraction of the specularly reflected radiation which is intercepted by the receiver. Fig. 2-11 (b) shows intercept factors as a function of receiver width in the focal plane for symmetrical collectors with perfect concentrators.

Errors in concentrator contours, tracking (pointing) errors and errors in displacement of receivers from the focus all lead to enlarged or shifted images and consequently affect γ.

82

These errors can also affect the transmittance of a cover system and the absorptance of a receiver. In addition, the spread of the image at the receiver of a linear concentrator depends on the angle of incidence of beam radiation θ. These effects can be represented by biaxial incidence modifiers, in the transverse (x-y) and longitudinal (x-z) planes [2].

In the transverse plane, γ will drop off sharply as the transverse component of the angle of incidence increases. This effect can be determined from information in curves like those of Fig. 2-12.

In the longitudinal plane, the major effects will be that of image spread as a function of θ, and variation with θ of the reflectance, transmittance and absorptance. It is not practical to generalise these effects, and experimental data are most useful to determine their magnitude. Fig. 3-7, from Gaul and Rabl [37], shows an example of measured incidence angle modifiers as a function of θ. In addition, if the trough is not extended far enough, there will be end effects as the image from the end of the trough is formed beyond the end of the receiver. Rabl [23] gave an example of an end effect correction for receivers that are of the same length L as the reflector and placed symmetrical over it:

$$K(\theta) = 1 - \frac{f}{l}\left(1 + \frac{a^2}{48f^2}\right)\tan\theta$$

(3-12)

As a first approximation the overall incidence angle modifier can be taken as the product of the transverse and longitudinal components. These factors are in general not simply expressed as analytic functions, and it is not now possible to write general equations for overall effects of the angles of incidence in the longitudinal and transverse planes.
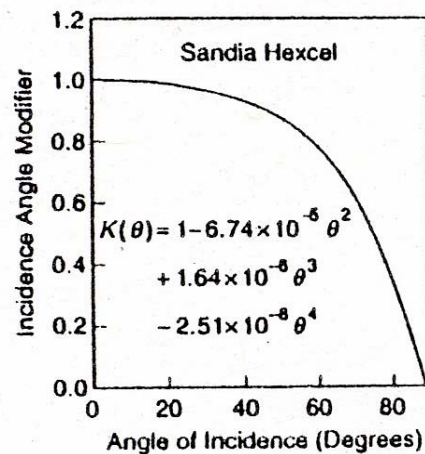
Fig. 3-7 Incidence angle modifier as a function of angle of incidence in the x-z plane for a Hexcel linear parabolic collector.

3.9 Parabolic Trough Concentrator (PTC)

PTC (Parabolic Trough Concentrator) is a cylindrical trough concentrator having a parabolic cross section and its receiver is cylindrical.

3.9.1 Geometry of PTC

To understand how this collector operates, it is necessary to describe its optical properties and the optical properties of the image produced (the distribution of the radiation flux across the focus).

For collectors of this type, the absorbed radiation per unit area of the aperture is given by:

$$S = I_b \rho (\gamma \tau \alpha) K \qquad (3\text{-}13)$$

Where I_b is the direct radiation value, ρ is the reflectivity of the concentrator, γ is the intercept factor, τ is the transmission of the concentrator cover, α is the absorption coefficient of the cover and K is the incidence angle modifier.

In order to evaluate S, it is necessary to know the characteristics of the image produced by reflectors. Theoretical images, i.e. those produced by perfect concentration which are perfectly aligned, depend on concentrator geometry. Cross-sections of a linear parabolic concentrator are shown in Fig. 3-8 and Fig. 3-9. The equation of the parabola, in terms of coordinate system shown is:

$$y^2 = 4fx \qquad (3\text{-}14)$$

The aperture is a, and the focal length (the distance of the focal point to the vertex) is f.

Fig. 3-8 Section of a linear parabolic concentrator showing major dimensions and the *x, y, z* coordinates.

Fig. 3-9 Image dimensions for a linear concentrator.

The radiation beam shown in Fig. 3-8 is incident on the reflector at point *B* at the rim where the mirror radius is a maximum at r_r. The angle ϕ_r is a maximum at r_r. The angle ϕ_r is the rim angle, described by *AFB*, and is given by:

$$\phi_r = \tan^{-1}\left[\frac{8(f/a)}{16(f/a)^2 - 1}\right] = \sin^{-1}\left(\frac{a}{2r}\right)$$

<div align="right">(2-15)</div>

For convenience, ϕ_r is plotted as a function of f/a in Fig. 3-10.
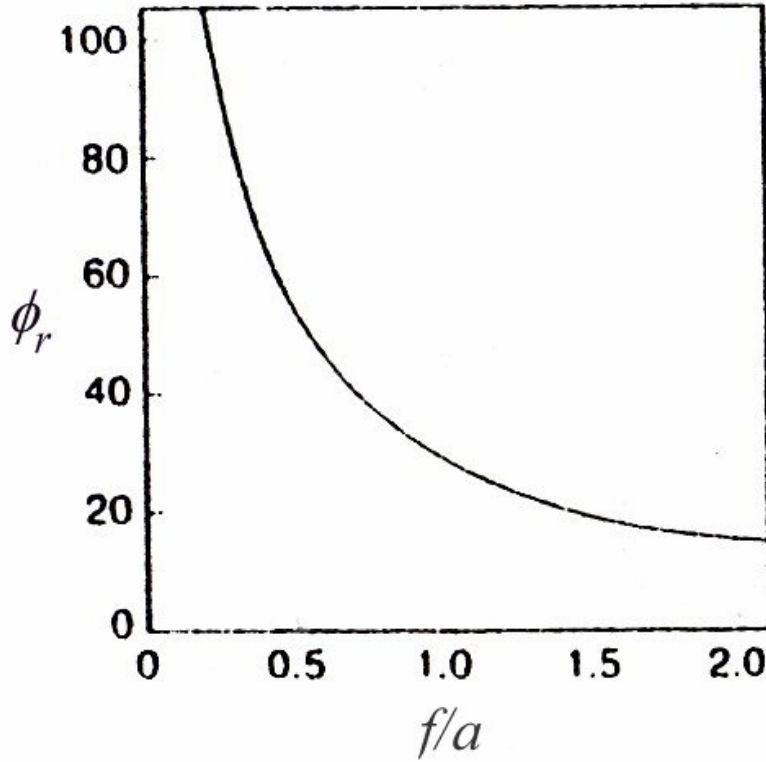
Fig. 3-10 Rim angle ϕ_r as a function of focal length-aperture ratio.

For any point of the parabolic reflector the local mirror radius is:

$$r = \frac{2f}{1 + \cos\phi}$$

<div align="right">(3-16)</div>

An incident beam of solar radiation is a cone with an angular width of 0.53° (i.e., a half-angle θ_s of 0.267°, or 16′). For present purposes, assume that the concentrator is symmetrical and that the beam radiation is normal to the aperture. Thus the beam radiation is incident on the concentrator in a direction parallel to the central plane of the parabola (the x-z plane described by the axis and focus of the parabola).

Fig. 3-11 shows schematically how the reflected radiation from the rim of the parabola determines the width of the focal zone. The width of the solar image in the focal plane increases with increasing the rim angle. The minimum sizes of the flat, circular and

semicircular receiver centred at the focal point to intercept all of the reflected radiation are shown. It is clear from this diagram that the angle of incidence of radiation on the surface of any of these receiver shapes is variable.

For specular parabolic reflectors of perfect shape and alignment, the size of the receiver to intercept the entire solar image can be calculated [2]. The diameter D of a cylindrical receiver is:

$$D = 2r_r \sin 0.267 = \frac{a \sin 0.267}{\sin \phi_r}$$

(3-17)

For a flat receiver in the focal plane of the parabola (the y-z plane through F, as shown in Fig. 3-8) the width W is:

$$W = \frac{2r \sin 0.267}{\cos\left(\phi_r + 0.267\right)} = \frac{a \sin 0.267}{\sin \phi_r \cos\left(\phi_r + 0.267\right)}$$

(3-18)

Note that W is also the diameter of a semicircular receiver.
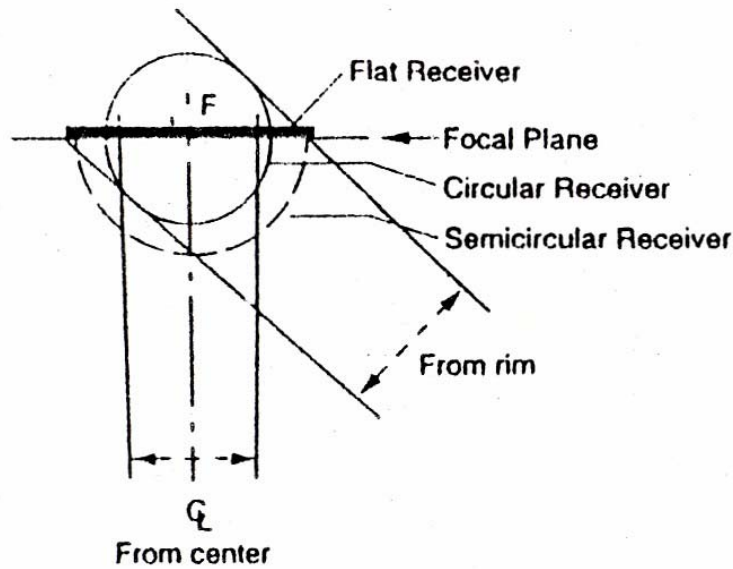
Fig. 3-11 Schematic of reflected radiation from centre and rim of a (half) parabolic reflector, with minimum plane, circular, and semicircular receivers to intercept all of the reflected radiation from a full parabola.

For a flat receiver, as ϕ varies from zero to ϕ_r, r increases from f to r_r and the theoretical image size in the focal plane increases from D (evaluated with r_r equal to f) to W. The focal length is a determining factor in size, and the aperture is a determining factor in

total energy; thus the image brightness or energy flux concentration at the receiver of a focusing system will be a function of the ratio *a/f*.

3.9.2 Images formed by perfect linear concentrator

We turn now to a more detailed consideration of the theoretical images produced by perfectly oriented cylindrical parabolic reflectors. Only images formed on planes perpendicular to the axis of the parabola will be considered; these examples provide the basis for an appreciation of the important factors in the operation of concentrators.

The radiation incident on a differential element of area of a reflector can be thought of as a cone having an apex angle of 32′, or a half-angle of 16′. The reflected radiation from the element will be a similar cone and will have the same apex angle if the reflector is perfect. The intersection of this cone with the receiver surface determines the image size and shape for that element, and the total image is the sum of the images for all of the elements of the reflector.

Consider a flat receiver perpendicular to the axis of a perfect parabola at its focal point, with beam radiation normal to the aperture. The intersection of the focal plane and a cone of reflected radiation from an element is an ellipse, with minor axis of *2rsin(16′)* and major axis of (x_1 - x_2), where x_1 is:

$$x_1 = rsin(16′)/cos(\phi - 16′) \qquad\qquad (3\text{-}19)$$

and x_2 is:

$$x_2 = rsin(16′)/cos(\phi + 16′) \qquad\qquad (2\text{-}20)$$

The total image is the sum of the ellipses for all of the elements of the reflector.

Evans [38] determined the distribution of energy flux in the integrated images on the focal plane for three models of the sun, including a non-uniform solar disc with an intensity distribution suggested by Lose [39] based on data of Abetti [40]. The non-uniform disc model takes into account the fact that the sun radiates more from its central portion than it does from the limb, or edge. Fig. 3-12 (a), 3-13, and 3-14, from Evans, show the distribution of energy across images for several perfect concentrators for the non-uniform solar disc.

The local concentration ratio $C_l = I(x)/I_{b,ap}$ is the ratio of intensity at any position x in the image to the intensity on the aperture of the concentrator. Local concentration ratios are shown in Fig. 3-12 (a). The abscissa is the distance from the image center, expressed in dimensionless form as *y/f*. A reflectance of 1 was assumed in these calculations. Distributions are shown for five rim angles of the reflector. As rim angle increases, the local concentration ratio increases, as does the size of the image. (If a uniform solar disc is assumed, the distributions show lower concentration ratios in the centre of the image and higher ratios in the outer portions of the images than for the non-uniform model.)
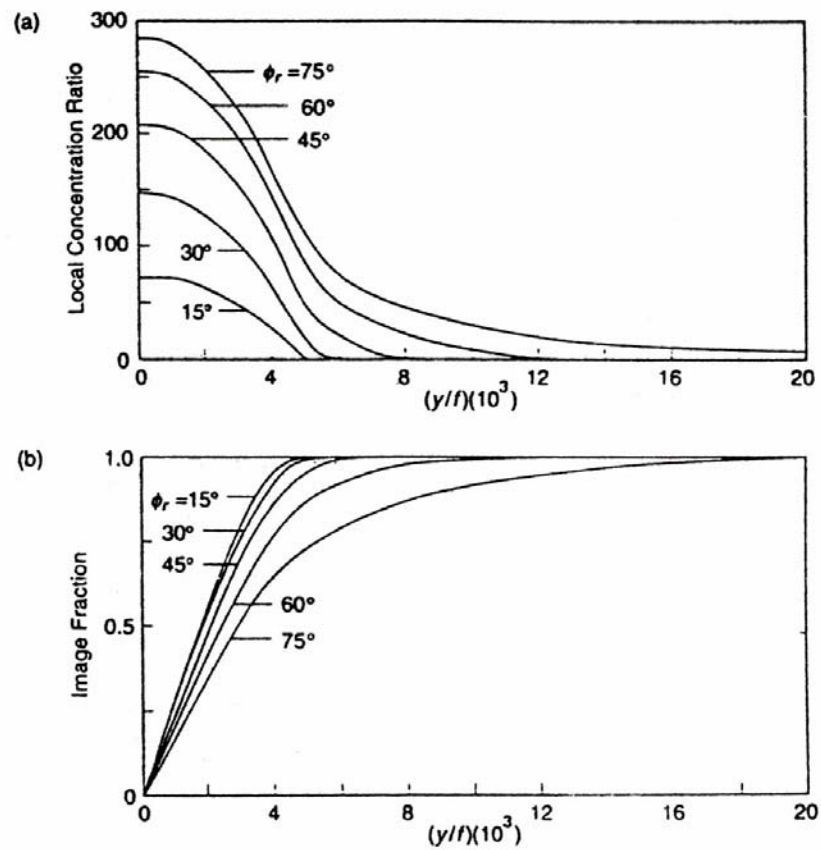
Fig. 3-12 (a) Image distributions for perfect concentrators for the uniform solar disc. (b) Intercept factors for images from perfect concentrators, obtained by integrating areas under curves of (a).
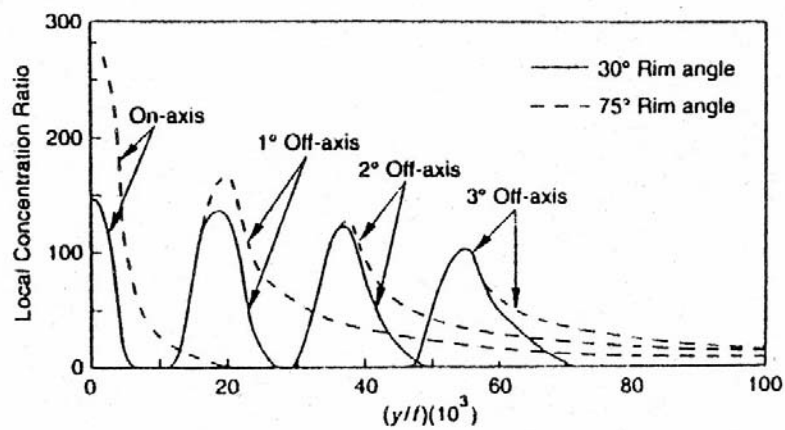
Fig. 3-13 Image distributions for the non-uniform solar disc for several pointing errors in the *x-y* plane.
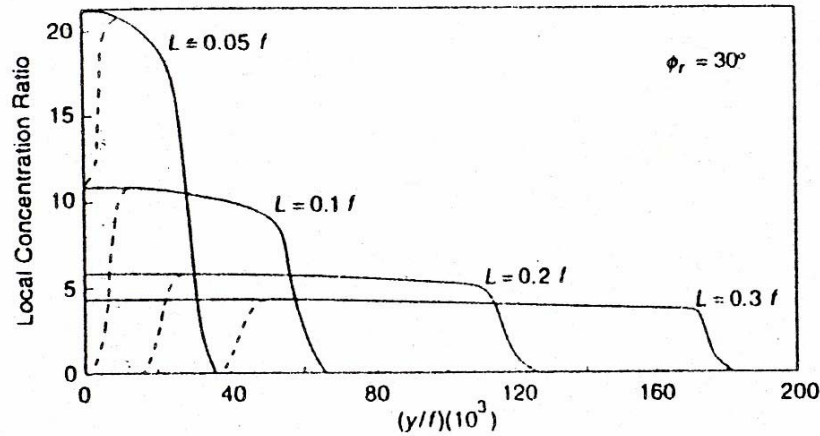
Fig. 3-14 Image distributions for 30° rim angle reflectors for several displacements of the plane of the image from the focal plane. The dashed curves show the effect of shading the reflector by the absorber.

The distributions of Fig. 3-12 (a) can be integrated from zero to y/f to show the intercept factor γ, the fraction of the total image that is intercepted by the flat receiver in the focal plane. Intercept factors are shown in Fig. 3-12 (b).

To this point, orientation of the collector has been considered to be perfect, i.e., with the beam radiation normal to the aperture. Two kinds of variation from this situation arise. The first is pointing errors in the x-y plane. The second is variation of the angle of incidence in the y-z plane that results from the mode of tracking.

Calculations similar to those resulting in Fig. 3-12 (a) were done by Evans [38] for perfect reflectors with alignment errors in the x-y plane. The results are shown in Fig. 3-13 for two rim angles and three alignment errors. Fig. 3-14 shows the effects of displacement L of the image plane from the focal plane for a perfect reflector with a rim angle of 30° and the radiation normal to the aperture. The dashed lines show the effect of shading of the reflector by the receiver widths of $0.05f$, $0.1f$, $0.2f$, and $0.3f$. It is clear that significant displacements of a receiver from the focal plane (or gross reflector distortions that lead to variation in focal length) lead to major changes in the nature of the image. The effect increases as rim angle increases [2].

Linear parabolic concentrators may be oriented in several ways to track the beam radiation. In general the beam radiation will be in the principal plane (the y-z plane) of the collector as described by the focus and vertex of the parabola but will not be normal to the aperture. Rabl [41] showed that under these circumstances a parabolic trough collector can be analyzed by projections in the x-y plane. Common modes of orientation are adjustment about horizontal axes, aligned either east-west or north-south; rotation about a polar axis is occasionally used. In these situations the angle of incidence θ of beam radiation on the aperture of the collector, if it is parallel to the central plane of the reflector, is described by the following equations for the following cases:

1- For a plane rotated about a horizontal east-west axis with continuous adjustment to minimize the angle of the incidence:

90

$$cos\,\theta = (1\text{-}cos^2 \delta \, sin^2 \omega)^{1/2}$$

(3-21a)

2- For a plane rotated about a horizontal north-south axis with continuous adjustment to minimize the angle of incidence:

$$cos\,\theta = (cos^2 \theta_z + cos^2 \delta \, sin^2 \omega)^{1/2}$$

(3-21b)

3- For a plane rotated about a north-south axis parallel to the earth's axis with continuous adjustment to minimize the angle of incidence:

$$cos\,\theta = cos\,\delta$$

(3-21c)

where θ is the angle of incidence of the radiation; δ is the declination of sun, the angular position of the sun at solar noon (i.e., when the sun is on the local meridian) with respect to the plane of the equator, north positive; $-23.45° \leq \delta \leq 23.45°$; ω is the hour angle, the angular displacement of the sun east or west of the local meridian due to rotation of the earth on its axis at 15° per hour, morning negative, after noon positive; θ_z is the zenith angle between the vertical and the line to the sun, i.e., the angle of incidence of beam radiation on a horizontal surface.

As the angle of incidence in the y-z plane increases, the apparent half-angle subtended by the sun (the projection on the x-y plane of the 0.267° half-angle) increases as $1/cos\theta$. The effect on image width W is obtained from Equation (3-19) by substituting $0.267/cos\theta$ for 0.267.

$$W = \frac{2r_r \, sin(0.267 / cos\,\theta)}{cos(\phi + 0.267 / cos\,\theta)}$$

(3-22)

The effect of θ on image width is best illustrated by W/W_o, the ratio of image width at incidence angle θ to the width at $\theta = 0$.

$$\frac{W}{W_o} = \frac{sin(0.267/cos\,\theta)}{sin\,0.267} \frac{cos(\phi_r + 0.267)}{cos(\phi_r + 0.267/cos\,\theta)} = \frac{1}{cos\,\theta}$$

(3-23)

This ratio does not change significantly with θ until the rim angle exceeds about 80°. Until θ becomes large, the second fraction varies little with θ and the dominant effect is that of the first fraction. Also the sine of a small angle is nearly equal to the angle, so W/W_o is very nearly equal to $1/cos\theta$.

The result of this image widening is that a linear parabolic concentrator oriented on a horizontal east-west axis would have an image on the receiver very much enlarged in the early and late hours of a day and of minimum size at noon. A collector oriented on a north-south horizontal axis would have an image size that would be less variable through the day. The effects of θ on image size are in the addition to the effect of the reduction of energy in the image (for a given I_{bn}) by the factor $cos\theta$.

3.9.3 Images from imperfect linear concentrators

The distributions shown in Fig. 3-12 to 3-14 are for perfect parabolic cylinders. If a reflector has small, two-dimensional surface slope errors that are normally distributed, the images in the focal plane created by these reflectors for perfect alignment are shown in Fig. 3-15. Distributions for reflectors with rim angles of 30° and 75° are shown for various values of the standard deviation of the normally distributed slope errors. Imperfect reflectors will, as is intuitively obvious, produce larger images than the theoretical.

A second method of accounting for imperfections in the shape of a parabola is to consider the reflected beam as having an angular width of (0.53 + δ) degrees, where δ is a dispersion angle, as shown in Fig. 3-16. Here δ is a measure of the limits of angular errors of the reflector surface. With δ, equations can be written for the size of images produced on cylinders or planes at the focus. The diameter of a cylindrical receiver that would intercept all of the image would be:

$$D = 2r_r \sin(0.267 + \delta / 2) = \frac{a \sin(0.267 + \delta / 2)}{\sin \phi_r}$$

(3-24)

The image width on the focal plane, if the incident radiation were normal to the aperture, would be:

$$W = \frac{2r_r \sin(0.267 + \delta / 2)}{\cos(\phi_r + 0.267 + \delta / 2)} = \frac{a \sin(0.267 + \delta / 2)}{\sin \phi_r \cos(\phi_r + 0.267 + \delta / 2)}$$

(2-25)

It may be possible to estimate δ from either flux distribution measurements, by ray trace methods if the distribution of angular errors is known, or by knowledge of the distribution of angular errors to be expected from the process used in manufacturing a reflector. An assumption of normally distributed angular errors may be closer to reality [2].
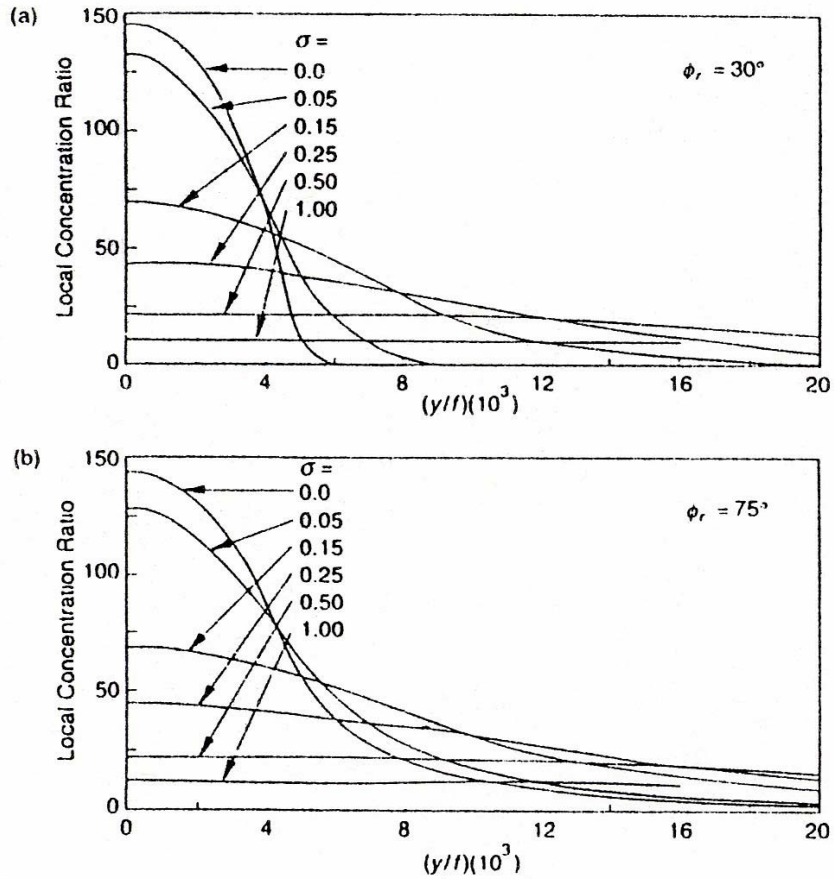
Fig. 3-15 (a) Image distributions for imperfect reflectors for 30° rim angle for various standard deviations of normally distribution reflector slope errors. (b) Image distributions for imperfect reflectors for 75° rim angle for various standard deviations of normally distributed reflector slope errors.
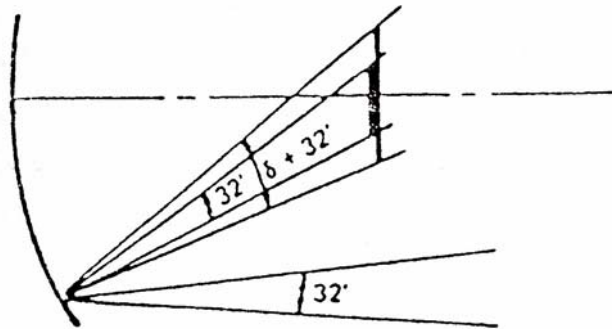
Fig. 3-16 Schematic of a portion of a concentrator with a dispersion angle δ added to the 0.53° solar intercept angle.

Equations (3-24) and (3-25) give the diameter and width of images of imperfect parabolic troughs that can be described by the dispersion angle δ. (Equations (3-16) and (3-

93

17) give the same information for perfect reflectors.) The ratio $(x/W)_\gamma = 1$ is defined as the ratio of the area of the aperture to the total area of the receiver when the receiver is just large enough to intercept all of the specularly reflected radiation (i.e., when $\gamma = 1$). From $(x/W)_\gamma = 1$ we can get C_{max}, the maximum area concentration ratio that leads to interception of total image. For a concentrator producing an image with well-defined boundaries and without pointing errors or mispositioning of the receiver of width W with a shadow W wide, the maximum area concentration ratio for $\gamma = 1$ is $(x/W)_\gamma = 1$. Then:

$$C_{max} = \frac{\sin\phi_r \cos\left(\phi_r + 0.267 + \delta/2\right)}{\sin\left(0.267 + \delta/2\right)}$$

(3-26)

3.9.4 Optical efficiency of the PTC

We now consider the optical efficiency of a cylindrical parabolic concentrating collector.

Assume that concentrator has an aperture W, length L and rim angle ϕ_r (Fig. 3-8). Also, assume that the absorber tube has a diameter D.

The beam radiation normally incident on the collector aperture is $I_b R_b$ where R_b is the tilt factor given by the relation:

$$R_b = \frac{\cos\theta}{\cos\theta_z} = \frac{\sin\delta\sin(\phi - \beta) + \cos\delta\cos(\phi - \beta)\cos H}{\sin\phi\sin\delta + \cos\phi\cos\delta\cos H}$$

(3-27)

where θ is the angle of incidence of radiation, θ_z is zenith angle, δ is the declination of the sun, ϕ is the latitude at which the concentrator is fixed, and β is the tilt angle of the concentrator.

In some tracking modes, the sun's rays are incident at an angle and therefore, come to focus a little beyond the length of the concentrator. We assume that the absorber tube is long enough to intercept this image. In practice this would mean that the absorber tube might be a little longer (say about 10 percent) than the concentrator and the flux falling on the tube would not be uniform along the length. For the purposes of analysis, however, we will not take into account this extra tube length, and will assume that the radiation flux is the same all along the length. We will also make the assumption that the temperature drops across the absorber tube and the glass cover are negligible.

The concentration ratio of the collector is given by:

$$C = \frac{1}{\sin\theta_s}$$

(3-28)

94

where θ_s is the half of the angle subtended by the sun in the eye on the earth which is equal to 16′ or 0.267°.

The absorbed flux S [24]:

$$S = I_b R_b r\gamma(\tau\alpha) + I_b R_b (\tau\alpha)\left(\frac{D}{W-D}\right)$$

(3-29)

where I_b is the incident solar radiation, r is the reflectivity of the concentrator material, γ is the intercept factor which represents the fraction of reflected radiation which intercept the absorber, τ is the transmissivity of the concentrator cover (if found), α is the absorption coefficient of the absorber, D is the diameter of the absorber and W is the width of the concentrator aperture [42].

The optical efficiency η_o can be defined by the fraction of the solar radiation incident on the aperture of the collector which is at the surface of the absorber tube [30]. Thus:

$$\eta_o = \frac{S}{I_b R_b}\frac{(W-D)}{W}$$

(3-30)

3.10 Compound Parabolic Concentrator (CPC)

The basic concept of the Compound Parabolic Concentrator is shown in Fig. 3-2. This concentrator belongs to the non-imaging category of concentrators, in which there is no dealing with image forming. It has a large acceptance angle and requires only intermittent tracking. The usefulness of the geometry of the CPC for solar energy collection was noted by R. Winston [43] and it has been the subject of considerable development in the last few years.

3.10.1 Geometry of CPC

The geometry of the two-dimensional CPC is shown in Fig. 3-17. The concentrator consists of two segments *AB* and *DC* which are parts of two parabolas 1 and 2. *AD* is the aperture of width *W* and *BC*, the absorber surface of width b. The axes of the two parabolas are oriented to each other at an angle that the point *C* is the focus of parabola 1 and point B is the focus of parabola 2. Tangents drawn to the parabolas at points *A* and *D* are parallel to the axis of the CPC.
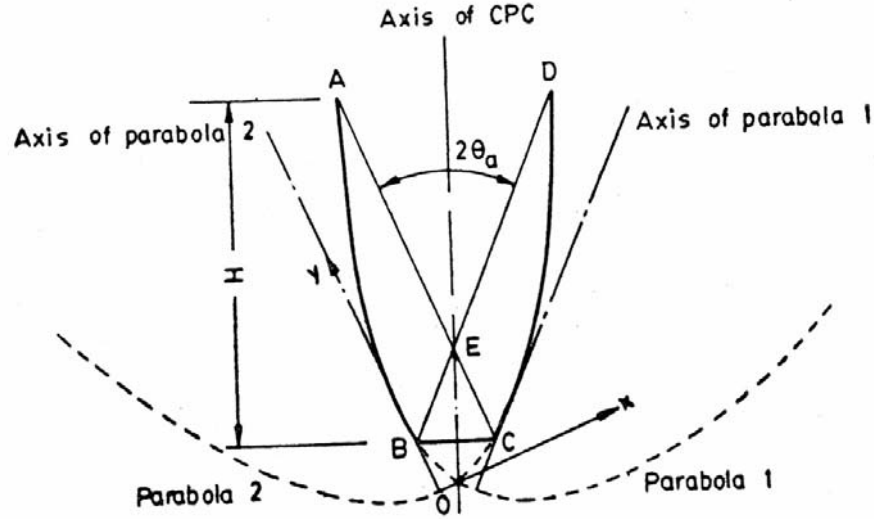
Fig. 3-17 Geometry of a compound parabolic concentrating collector.

The acceptance angle of the CPC is the angle AED ($2\theta_a$) made by the lines obtained by joining each focus to the opposite aperture edge. The concentration ratio is given by:

$$C = (W/b) = (1/\sin\theta_a) \tag{3-31}$$

and this concentration ratio is the maximum possible for the acceptance angle $2\theta_a$.

Using the x-y coordinate system shown in Fig. 3-17, with origin O at the vertex of parabola 2, it is easy to show that the equation for parabola 2 is:

$$y = \frac{x^2}{2b\left(1 + \sin\theta_a\right)} \tag{3-32}$$

where the focal length is given by:

$$OB = \frac{b}{2}\left(1 + \sin\theta_a\right) \tag{2-33}$$

The coordinates of the end points of the segment CD are as follows:

Point C: $$x = b\cos\theta_a \tag{3-34}$$

96

$$y = \frac{b}{2}\left(1 - \sin\theta_a\right)$$

(3-35)

Point D:
$$x = \left(b + W\right)\cos\theta_a$$

(3-36)

$$y = \frac{b}{2}\left(1 - \sin\theta_a\right)\left(1 + \frac{1}{\sin\theta_a}\right)$$

(3-37)

The height to aperture ratio of the concentrator is given by:

$$\frac{H}{W} = \frac{1}{2}\left(1 + \frac{1}{\sin\theta_a}\right)\cos\theta_a = \frac{1}{2}(1 + C)\left(1 - \frac{1}{C^2}\right)^{1/2}$$

(3-38)

The surface area of the concentration is obtained by integrating along the parabolic arc. Rabl has shown that the ratio of the surface area of the concentrator to the area of the aperture is given by the expression:

$$\frac{A_{con}}{WL} = \sin\theta_a\left(1 + \sin\theta_a\right)$$

$$\left[\frac{\cos\theta_a}{\sin^2\theta_a} + \ln\left\{\frac{\left(1 + \sin\theta_a\right)\left(1 + \cos\theta_a\right)}{\sin\theta_a\left[\cos\theta_a + \left(2 + 2\sin\theta_a\right)^{1/2}\right]}\right\} - \frac{\sqrt{2}\cos\theta_a}{\left(1 + \sin\theta_a\right)^{3/2}}\right]$$

(3-39)

For values of concentration ratio greater than 3, it can be shown that the following simple expression (which predicts values to an accuracy better than 5%) may be used in place of Equation (3-39):

$$\frac{A_{con}}{WL} = 1 + C$$

(3-40)

Rabl has also shown that the average number of reflections m undergone by all radiation falling within the acceptance angle before reaching the absorber surface is given by the expression:

$$m = \frac{1}{2 \sin \theta_a} \left(\frac{A_{con}}{WL} \right) - \frac{\left(1 - \sin \theta_a\right)\left(1 + 2 \sin \theta_a\right)}{2 \sin^2 \theta_a}$$

(3-41)

where the value of (A_{con}/WL) is to be calculated from Equation (3-39). Thus, the effective reflectivity of the concentrator surface is given by:

$$\rho = r^m$$

(3-42)

where ρ is the effective reflectivity and r is the reflectivity value for a single reflection [24].

We will find that compared to a cylindrical parabolic collector, a CPC is very deep and requires a large concentrator area for a given aperture. Fortunately, however, it has been shown that a large portion of the top of a CPC can be removed with negligible loss in performance. Thus, in practice, a CPC is generally truncated (reduced in height) by about 50% in order to reduce its cost. A truncated CPC is shown in Fig. 3-19. The dashed plot in Fig. 3-18 shows the spread of the image for the truncated concentrator. Limited truncation affects the acceptance angle very little, but it does change the height-to-aperture ratio, the concentration ratio and the average number of reflections undergone by radiation before it reaches the absorber surface. The effects of truncation are shown for otherwise ideal CPCs in Fig. 3-20 to Fig. 3-22. Fig. 3-20 shows the height-to-aperture ratio and Fig. 3-21 shows the ratio of reflector area to aperture area. Fig. 3-22 shows the average number of reflections undergone by radiation entering the aperture before it reaches the absorber. If the truncation is such that the average number of reflections is below the $(N)_{min}$ curve, thataverage number is at least ($1-1/C$). Rabl [44] gave equations for all of these quantities.
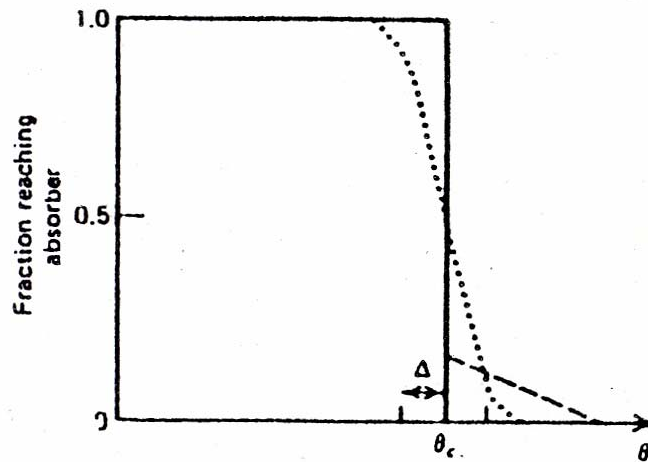
Fig. 3-18 Fraction of radiation incident on the aperture of a CPC at angle θ which reaches the absorber surface if $\rho = 1$. θ_a is the acceptance half-angle and Δ is an angular surface error. Full CPC with no surface errors, (continuos line); truncated CPC with no surface errors, (dashed line); full CPC with surface errors, (dotted line).
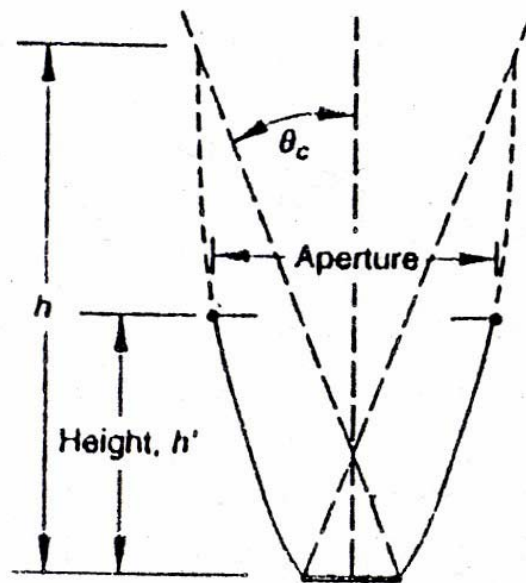
Fig. 3-19 A CPC truncated so its height-aperture ratio is about one-half of the
full CPC.
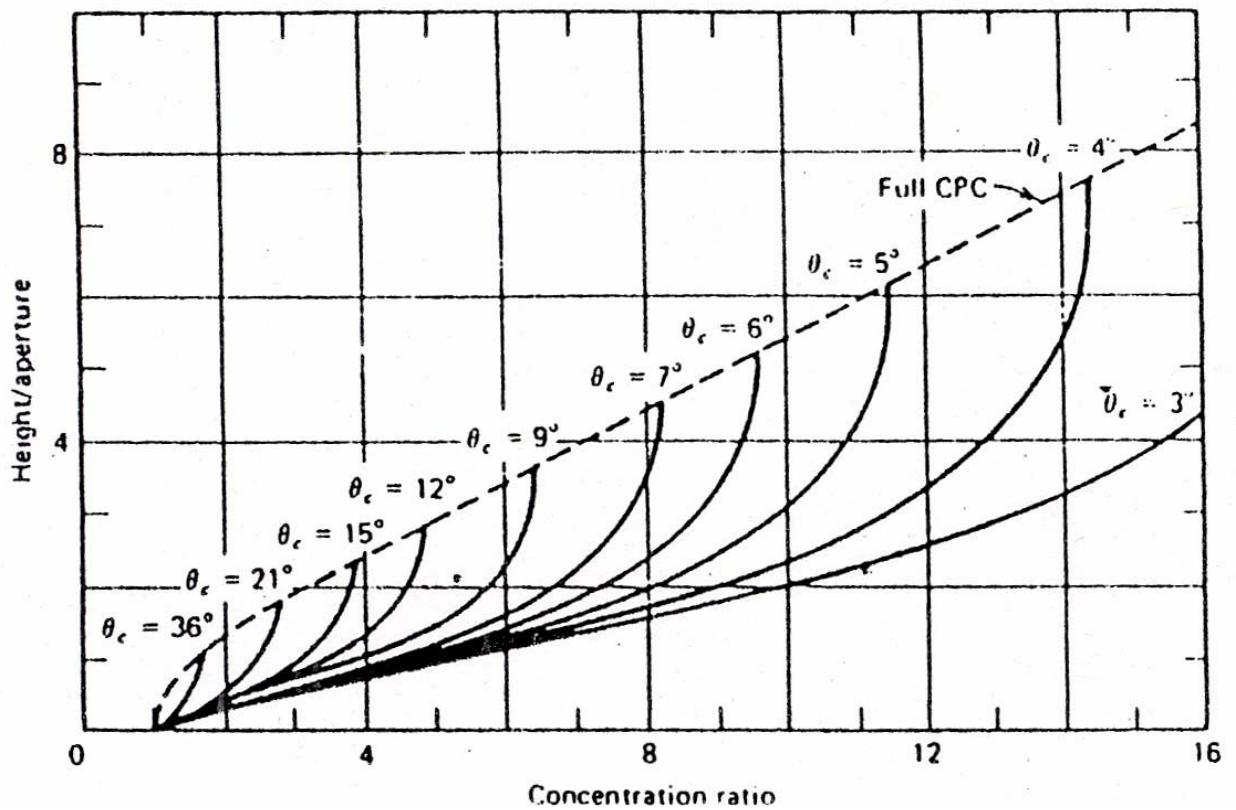
Fig. 3-20 Ratio of height to aperture for full and truncated CPCs as a function of C and θ.
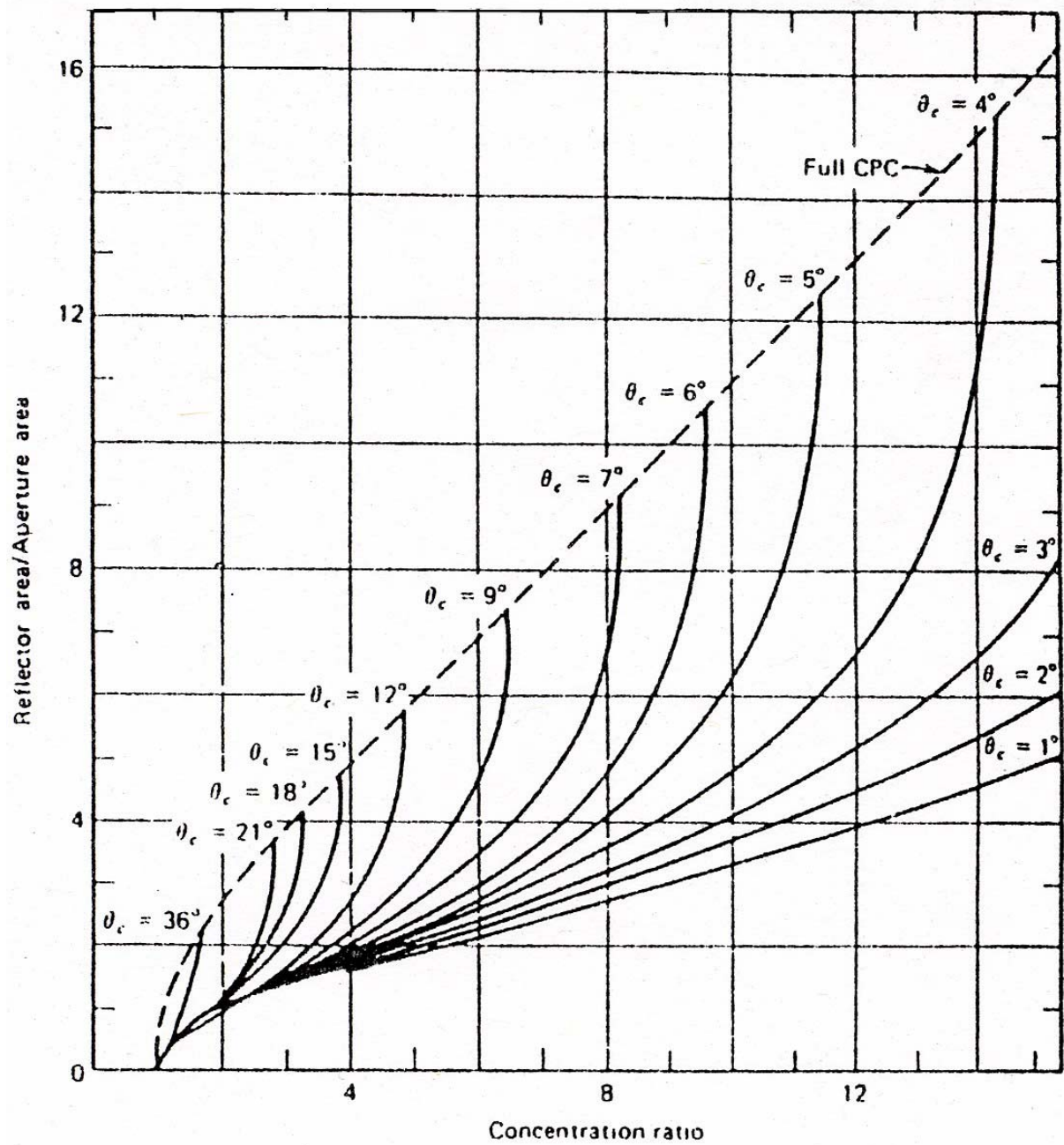
Fig. 3-21 Ratio of reflector area to aperture area for full and truncated CPCs.
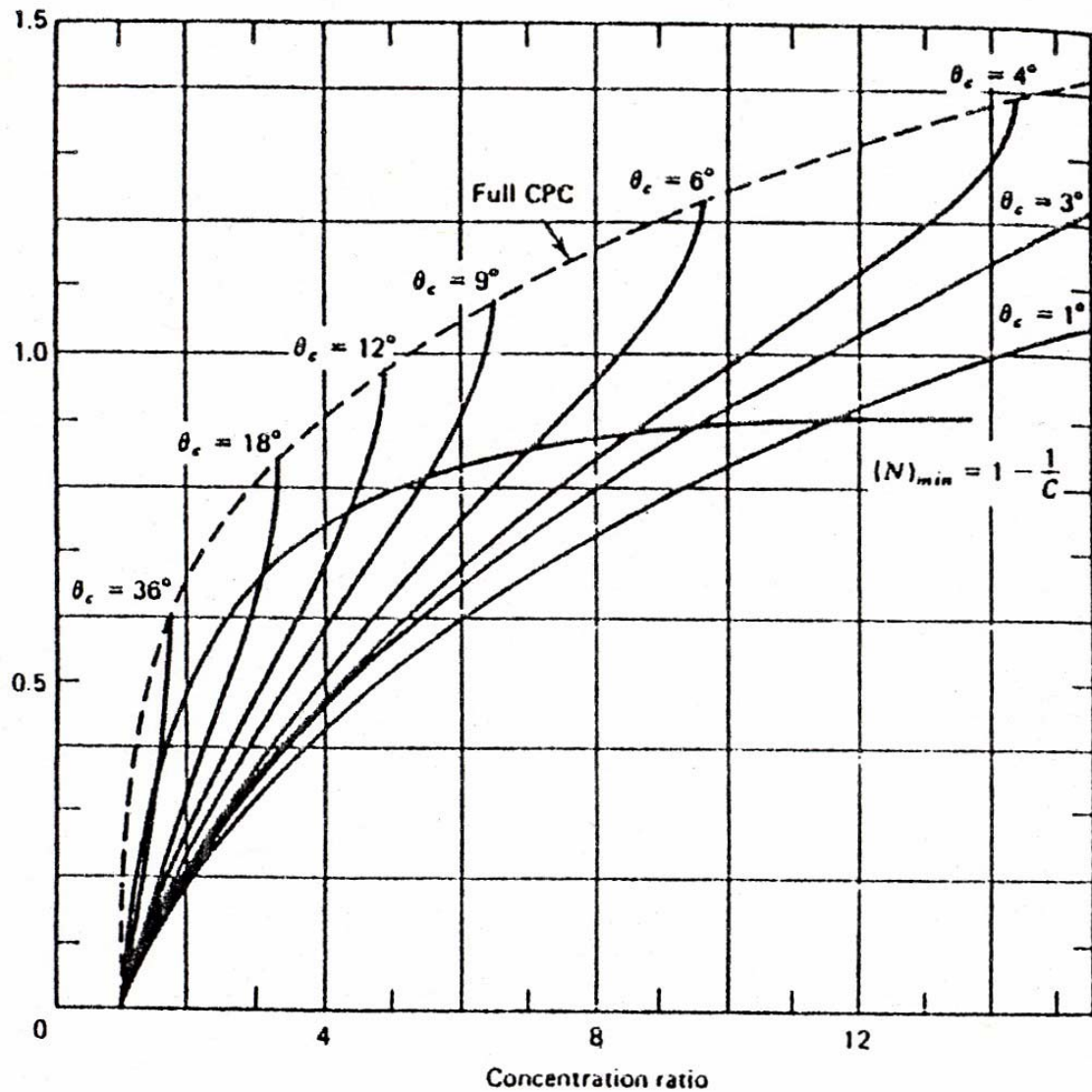
Fig. 3-22 The average number of reflections undergone by radiation within the acceptance angle reaching the absorber surface of full and truncated CPCs.

The use of these plots can be illustrated as follows. An ideal full CPC has an acceptance half angle θ_a of 12°. From Fig. 3-20 the height-to-aperture ratio is 2.8 and the concentration ratio is 4.8. From Fig. 3-21 the area of reflector required is 5.6 times the aperture. The average number of reflections undergone by radiation before reaching the absorber surface is 0.97 from Fig. 3-22. If this CPC is truncated so that its height-to-aperture ratio is 1.4, from Fig. 3-20 the concentration ratio will drop to 4.2. Then from Fig. 3-21 the reflector area-aperture area ratio is 3.0 and from Fig. 3-22 the average number of reflections will be at least 1-1/4.2 = 0.76.

CPCs with flat receivers should have a gap between the receiver and the reflector to prevent the reflector from acting as a fin, conducting heat from the receiver. The gap results in a loss of reflector area and a corresponding loss in performance and should be kept small [2].

The preceding discussion has been based on flat receivers occupying the plane between the two foci Fig. 3-19. Other receiver shapes can be used; CPC can be developed with aperture W which will concentrate incident radiation with incidence angles between $\pm\theta_a$ onto any convex absorber with circumstance $W\sin\theta_a$. The method of generation of the shape of the CPC is illustrated by Fig. 3-23, which shows a special case of interest, a cylindrical absorber. Parts *AB* and *AC* of the reflector are convolutes of parts *AF* and *AG* of the absorber. The requirement for the rest of the reflector is that at any point *P*, the normal to the reflector *NP* must bisect the angle between the tangent to the absorber *PT* and the line *QP*, which is at an angle θ_a to the axis of the CPC. This CPC is used with evacuated tubular receivers. They can be truncated in the same way as other CPCs.

This method can be used to generate a reflector for any convex receiver shape. Thus a set of CPC-type concentrators (not necessarily parabolas) can be evolved that permit a range of choices of receiver shape. CPCs can be used in series; the receiver for a primary concentrator can be the aperture of a secondary concentrator. The concentrator need not be symmetrical.

Tubular absorbers are often used with CPC reflectors [45, 46]. The reflector shape leading to maximum absorption of radiation by cylindrical absorbers is an involute, shown in Fig. 3-24. McIntire [47] derived a mathematical analysis for using an absorber of a tubular shape in the CPC.
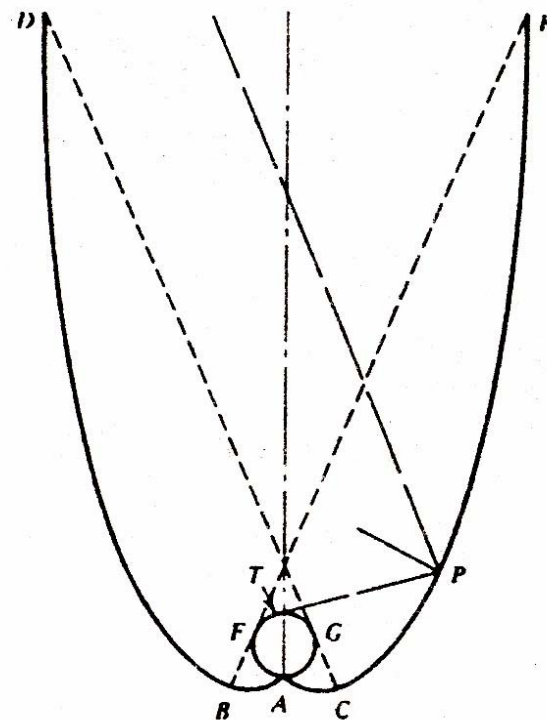
Fig. 3-23 A CPC for a tubular receiver.
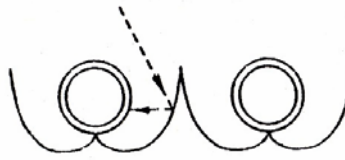
Fig. 3-24 Involute reflector for use with cylindrical absorber.

3.10.2 Orientation and absorbed energy for CPC collectors

The advantages of CPCs are that they can function without continuous tracking and still achieve some concentration. However, they must be properly oriented to maximize the absorbed radiation when output from the collector is needed. It is necessary to calculate the absorbed radiation in order to determine the operation at any time. This is a step to finding the best orientation. A particularly critical question is whether or not the beam radiation will be absorbed.

A logical orientation for such a collector is along a horizontal east-west axis, sloped toward the equator and adjustable about that axis. The CPC is arranged so that the pseudo incidence angle of beam radiation (the projection of the angle of incidence on the north-south vertical plane) lies within the limits $\pm\theta_a$ during the times when output is needed from the collector. In practice, compromises are necessary for movement of the collector and the concentration ratio, with higher ratios associated with small acceptance angles and relatively frequent positioning [2].

To estimate the radiation absorbed by the receiver of a CPC, it is necessary to determine if the angle of incidence of the beam radiation is within the acceptance angle $2\theta_a$, and then estimate the contributions of the beam and diffuse radiation, plus the ground-reflected radiation if it is within the acceptance angle. The absorbed radiation can be estimated as:

$$S = A_a(G_{b,CPC}\tau_{c,b}\tau_{CPC,b}\alpha_b + G_{d,CPC}\tau_{c,d}\tau_{CPC,d}\alpha_d + G_{g,CPC}\tau_{c,g}\tau_{CPC,g}\alpha_g) \qquad (3\text{-}43a)$$

$$G_{b,CPC} = Fg_{bn}cos\theta \qquad (3\text{-}43b)$$

$$G_{d,CPC} = \frac{G_d}{C} \qquad \qquad if\ (\beta + \theta_a) < 90°$$

$$(3\text{-}43c)$$

$$G_{d,CPC} = \frac{G_d}{2}\left(\frac{1}{C} + \cos\beta\right) \qquad if\ (\beta + \theta_a) > 90°$$

$$G_{g,CPC} = 0 \qquad \qquad if\ (\beta + \theta_a) < 90°$$

103

$$G_{g,CPC} = \frac{G_d}{2}\left(\frac{1}{C} - \cos\beta\right) \qquad \qquad if \ (\beta + \theta_a) > 90°$$

The first term in Equation (3-43a) is the beam contribution to S, the second is the contribution of the diffuse and the third is the contribution of the ground-reflected radiation. In the first term, $G_{b,CPC}$ is the beam radiation on the aperture that is within the acceptance angle, τ_{cb} is the transmittance for beam radiation of any cover which may be placed over the concentrator array and α_b is the absorptance of the receiver for the beam radiation. The factor $\tau_{CPC,b}$ is the "transmittance" of the CPC which accounts for reflection losses and is a function of the average number of reflections. The factors in the terms of diffuse and ground-reflected radiation are analogous to those which for the beam radiation.

The ground-reflected radiation is only effective if $(\beta + \theta_a) > 90°$, i.e., if the receiver "sees" the ground. The angles are shown in Fig. 3-25. Equations (3-43c) and (3-43d) account for the contribution or lack thereof of the ground-reflected radiation is assumed to be isotropic.
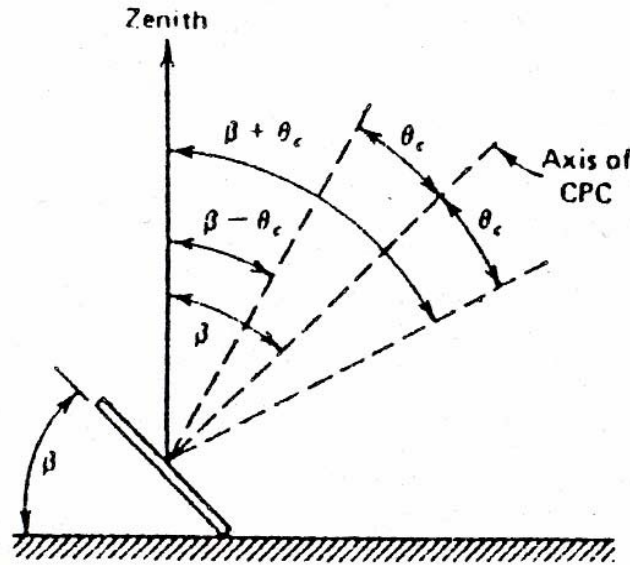
Fig. 3-25 Projection on a north-south plane of CPC acceptance angles and slope for a CPC on an east-west axis.

Fig. 3-25 shows the acceptance angle of a CPC on a vertical north-south plane for a CPC oriented east-west. Two angles, $(\beta - \theta_a)$ and $(\beta + \theta_a)$, are the angles from the vertical in this plane to the two limits describing the acceptance angle. It has been shown that the following condition must be met in order for the beam radiation to be effective:

$$(\beta - \theta_a) \leq tan^{-1}(tan\theta_z cos\gamma_s) \leq (\beta + \theta_a) \qquad (3-44)$$

It is convenient to introduce the control function F in Equation (3-43b) which is 1 if the criterion of Equation (3-44) is met and 0 otherwise. If the beam radiation is incident on the aperture within the acceptance angle, $F = 1$ and the beam radiation term will be included in the calculation of S.

A CPC collector will probably have a transparent cover over the array of the reflectors. This serves both to protect the reflecting and absorbing surfaces and to reduce thermal losses from the absorber. The beam and diffuse radiation effectively entering the CPC are reduced by the transmittance of the cover τ_c.

Only part of the incident diffuse radiation effectively enters the CPC, and that part is a function of the acceptance angle. A relationship between the mean angle of incidence of effective diffuse radiation and the acceptance half-angle θ_a is shown in Fig. 3-26. This is based on the assumption that the diffuse radiation is isotropic. The relationship depends on the nature of the cover system, and the figure shows a band of solutions including one and two covers, with refractive indices of 1.34 and 1.526. An equation for the equivalent angle incidence θ_e (the dashed line) is:

$$\theta_e = 44.86 - 0.0716\theta_a + 0.00512\theta_a^2 - 0.00002798\theta_a^3 \qquad (3\text{-}45)$$
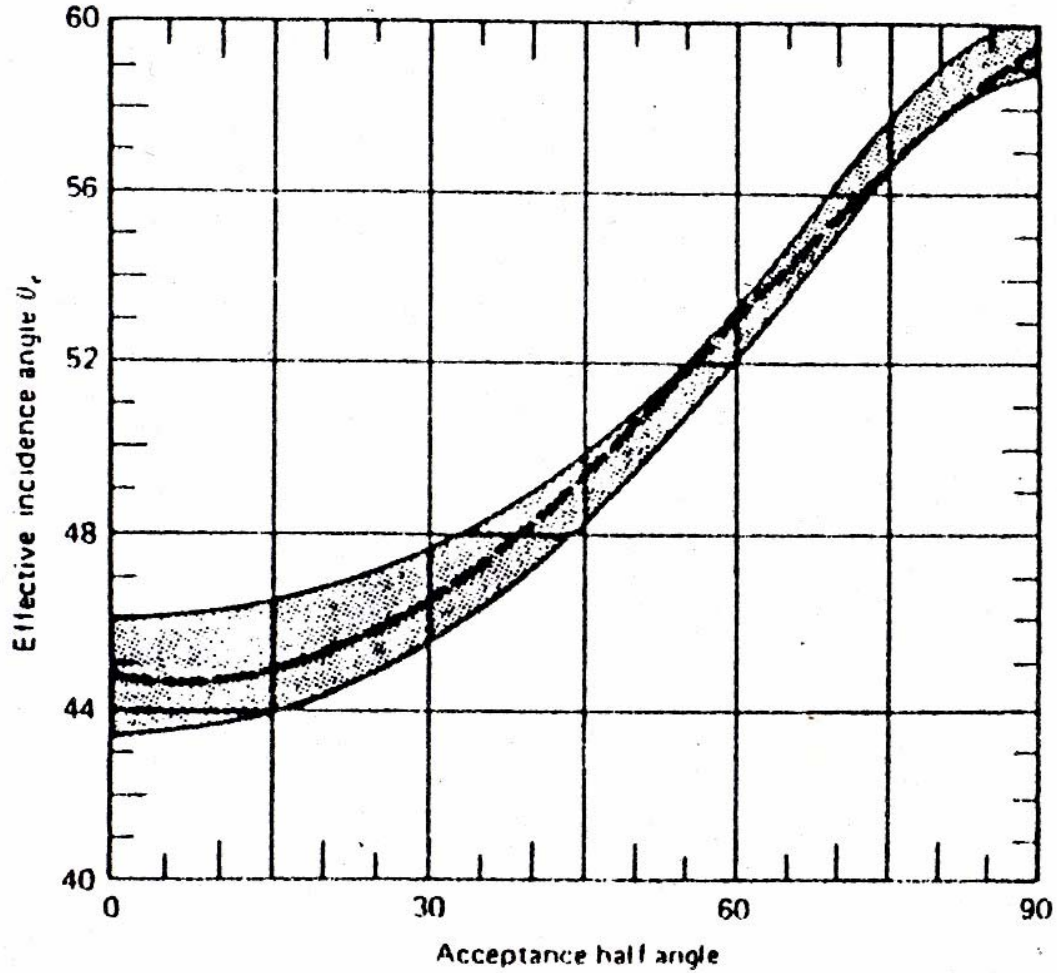
Fig. 3-26 Equivalent incidence angle for reflections undergone for isotropic diffuse radiation for a CPC as a function of acceptance half angle.

Thus for a CPC with $\theta_a = 20°$, the mean angle of incidence of effective diffuse radiation is $45°$ and the transmittance of the cover for this radiation is that of beam radiation at $45°$. The terms $\tau_{CPC,b}$, $\tau_{CPC,d}$, and $\tau_{CPC,g}$ in Equation (3-43a) are transmittances of the CPC that account for the specular reflectance of the concentrator and the average number of reflections. The terms are usually treated as the same, and an appropriate value to be applied to all three of them is estimated from the number of reflections m from Fig. 3-21 and the reflectance r by the equation:

$$\rho_{CPC} = r^m \qquad (3\text{-}46)$$

Here it is assumed that end effects are negligible or that the ends are highly reflective.

The absorptances α_b, α_d, and α_g of the receiver surface depend on the angles of incidence of the radiation on the surface. The angles of incidence vary depending on the angle of incidence of the radiation on the aperture of the CPC, the number of reflections undergone by the radiation and the shape of the reflecting and receiving surfaces. If the

106

average number of reflections is small, as it will be for large acceptance angles, then as a first approximation the absorptance can be taken as that corresponding to the angle of incidence of the effective radiation on the aperture of the CPC; however, this will generally result in over-estimation of α. Due to lack of design information, there may be no alternative.

3.10.3 Optical efficiency of the CPC

The definition of the optical efficiency is the efficiency by which the concentrator can reflect and concentrate the radiation.

M. A. Mosalam Shaltout, M. Medhat, and Y. A. Hadi [48, 49] have studied the efficiency of the Compound Parabolic Concentrator (CPC) and its application in the photovoltaic applications.

Optical efficiency can be given by the relation:

$$\eta_o = \gamma r^m$$

or $\qquad \eta_o = \gamma \rho$ $\qquad\qquad$ (3-47)

where γ is the fraction of total insulation accepted by the CPC; r is the reflectivity of the concentrator plate for a single reflection; m is the number of reflections undergone by the concentrator; ρ is the reflectivity of the concentrator for m reflections.

The factor γ depends on the turbidity of the atmosphere and on the acceptance angle. On clear days, values of $\gamma \cong 92\%$, for threefold and $\gamma \cong 88\%$ for tenfold concentration have been measured [44].

For all of the concentrator system with a cover of transmission τ and an absorber with an absorption coefficient α, the optical efficiency can be calculated from [50]:

$$\eta_o = \gamma \tau \rho \alpha$$ $\qquad\qquad$ (3-48)

3.11 Paraboloidal Concentrator (Parabolic Dish)

Paraboloidal concentrator (Parabolic dish) is one of the high concentration concentrators; it concentrates the radiation falling onto it, into a point focus with high value of concentration.

Paraboloidal concentrator, in its shape has a parabolic cross-section with a circular aperture; we can also say that it can be described as a three-dimensional parabolic reflector. A similar analysis which had been done for the Parabolic Trough Concentrator (PTC) can also

be done for the paraboloidal concentrator. In a section through the axis of the paraboloid, this collector is represented by Fig. 3-8 and 3-9, and the rim angle ϕ_r and the mirror radius r are analogous to those for the linear concentrator. Dispersion also occurs in the paraboloidal concentrator, and equations analogous to Equation (3-23) can be written for collectors without tracking errors. Fig. 3-27 shows a three-dimensional view of the parabolic dish, while Fig. 3-28 shows a segmented mirror approximation to the paraboloidal dish. For spherical receivers (allowing for minimum shading for the receiver):

$$
C_{max} = \frac{\sin^2 \phi_r}{4\sin^2(0.267 + \delta/2)} - 1
\tag{3-49}
$$

For flat receivers:

$$
C_{max} = \frac{\sin^2 \phi_r \cos^2(\phi_r + 0.267 + \delta/2)}{4\sin^2(0.267 + \delta/2)} - 1
\tag{3-50}
$$

where ϕ_r is the rim angle of the absorber, and δ is the dispersion.
C_{max}. is defined as the maximum that can be obtained, based on the interception of all of the specularly reflected radiation which is within the cone of angular width ($0.53 + \delta$).
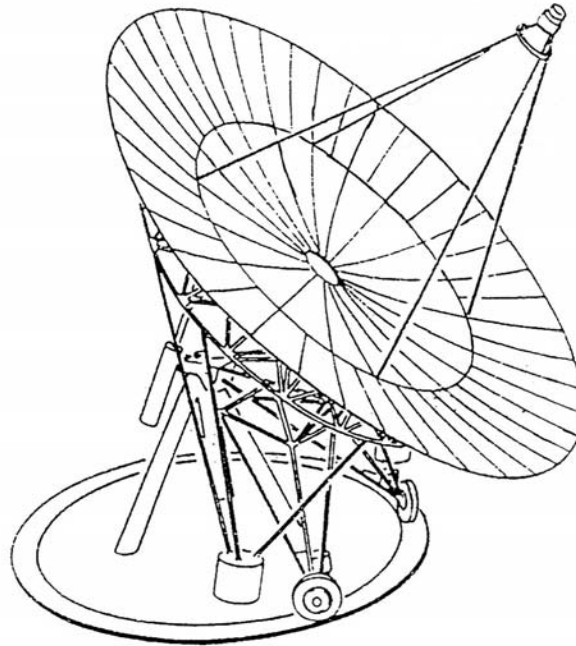
Fig. 3-27 Typical point focusing solar collector of the type of parabolic dish.
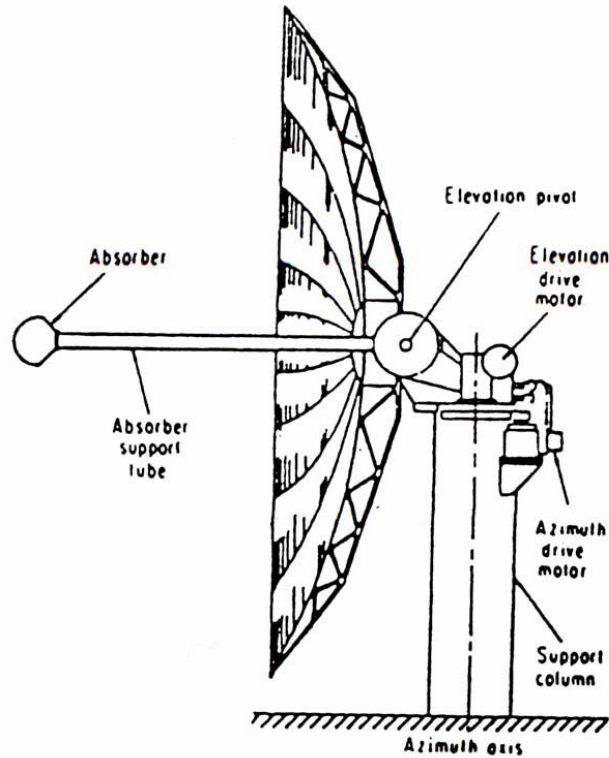
Fig. 3-28 Segmented mirror approximation to parabolic dish.

Cavity receivers may be used with paraboloidal concentrators to increase absorptance and to reduce convective losses from the absorbing surface. The equations for the optical properties of systems with flat receivers will also apply to cavity receivers if appropriate absorptances of the cavities are used.

Absorbed energy for a paraboloidal collector depends on properties in the same way as linear parabolic collectors. However, at the higher concentration ratios achieved by these collectors, any absorption of solar radiation in the cover material would lead to heating of the cover, and as a result covers are usually not used. In the absence of a cover, the absorbed energy for the unshaded aperture area of the collector is then:

$$S = I_{b,a}\rho(\gamma\alpha)_n K_{\gamma\alpha} \tag{3-51}$$

where $I_{b,a}$ is the beam radiation, ρ is the reflectivity of the material of the concentrator, γ is the intercept factor, α is the absorption coefficient of the absorber, and $K_{\gamma\alpha}$ is the incidence angle modifier.

The incidence angle modifier may be circularly symmetrical; if the optical system is not symmetrical or biaxial, other modifiers may have to be used. The modifier accounts for focussing errors in the alignment of the collector.

Calculation of thermal losses is very much a function of receiver geometry and may be complicated by the existence of temperature gradients on the surface of a receiver. For example of these estimations, see reports of Martin Marietta, Boeing and McDonnell-Douglas on the receiver subsystems of central receiver solar thermal power systems [2].

3.12 Conical Concentrator

Conical concentrator is a cone-like concentrator in the shape as shown in Fig 3-29. It is a three-dimensional nonimaging optical concentrator.

(a)   (b)
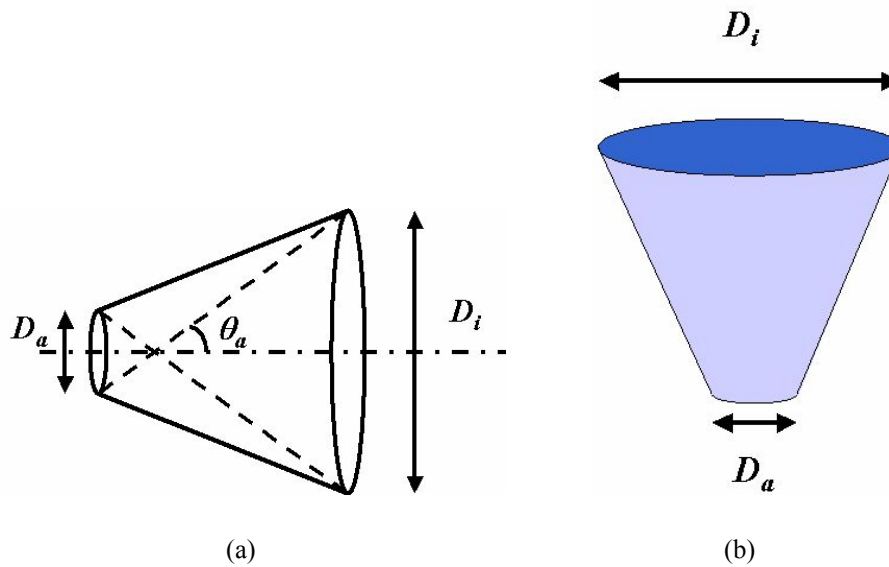
Fig. 3-29 Schematic design of the conical concentrator.

Fig. 3-30 shows schematically how the conical concentrator works. We can see that this type of concentrator has a relatively larger acceptance angle, which means that the conical concentrator has lower concentration ratios comparing with that of other non-imaging concentrators like the compound parabolic concentrators (CPC) [51].
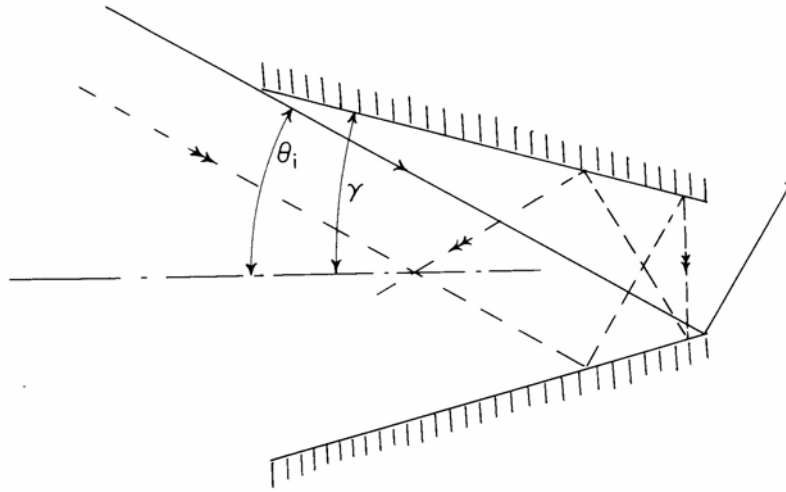
Fig. 3-30 Reflected rays inside the conical concentrator.

The analysis of this type of concentrators is the same as that of the Compound Parabolic Concentrator (CPC). The concentration ratio of this type of concentrators can be given by the formula:

$$C = \frac{1}{\sin^2 \theta_a}$$

(3-52)

where θ_a is the acceptance half angle mentioned before. A Conical Concentrator is simple to construct [52]. It needs tracking in two axes for adjustment. As we see from the equation (3-50), its concentration ratio value is the square of that of the Compound Parabolic Concentrator's one. Its efficiency analysis is the same of that of the CPC.

3.13 Central Receiver Collectors

The central receiver or "power tower" concept for generation of electrical energy from the solar energy is based on the use of very large concentration collectors. The optical system consists of a field of large number of heliostats, each reflecting beam radiation onto a central receiver. The result is a Fresnel-type concentrator, i.e. a parabolic reflector broken up into small segments, as shown in Fig. 3-1(f). Several additional optical phenomena must be taken into account. Shading and blocking can occur (shading of incident beam radiation from a heliostat by another heliostat and blocking of a reflected radiation from a heliostat by another which prevents that radiation from reaching the receiver). As a result of these considerations, the heliostats are spaced apart, and only a fraction of the ground area ψ is covered by mirrors. A ψ of about 0.3 to 0.5 has been suggested as a practical value [2].

The maximum concentration ratio for a three-dimensional concentrator system with radiation incident at an angle θ_i on the plane of the heliostat array ($\theta_i = \theta_z$ for a horizontal array), for a rim angle of φ_r, and a dispersion angle of δ, if all reflected beam radiation is to be intercepted by a spherical receiver, is:

$$C_{max} = \frac{\psi \sin^2 \phi_r}{4\sin^2(0.267 + \delta/2)} - 1 \qquad (3\text{-}53)$$

For a flat receiver, the concentration ration is:

$$C_{max} = \psi \left[\frac{\sin\phi_r \cos(\phi_r + 0.267 + \delta/2)}{\sin(0.267 + \delta/2)} \right]^2 - 1 \qquad (3\text{-}54)$$

As with linear concentrators, the optimum performance may be obtained with an intercept factor of less than unity. The designer of these collectors has additional considerations to take into account. The heliostat field need to be symmetrical. The ground cover ψ does not have to be uniform, and the heliostat array is not necessarily all in one plane. These collectors operate with high concentration ratios and at relatively high receiver temperatures [2].

3.14 Fresnel Lenses

3. 14.1 What is the Fresnel lens?

The Fresnel lens is a lens resembling a plano-convex or plano-concave lens that is cut into narrow rings and flattened out. If the steps are narrow, the surface of each step is gradually made conical and not spherical. Fresnel lenses can be large glass structures as in lighthouses, floodlights, or traffic signals, or thin molded plastic plates with fine steps, often used for field lenses. Fig 3-31 shows a schematical view of a Fresnel lens.

| (a) | (b) | (c) |
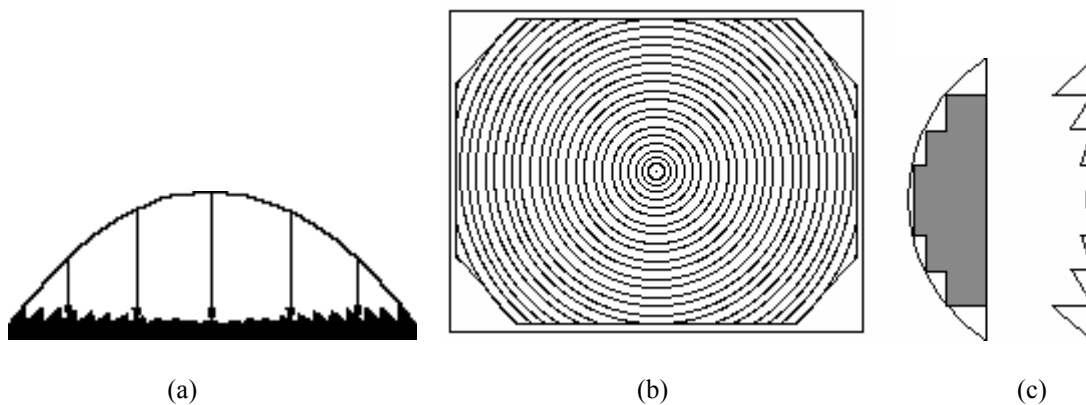
Fig. 3-31 Schematical view of a Fresnel lens.

Also, Fig. 3-32 shows a representation of a Fresnel lens according to corresponding normal lens.
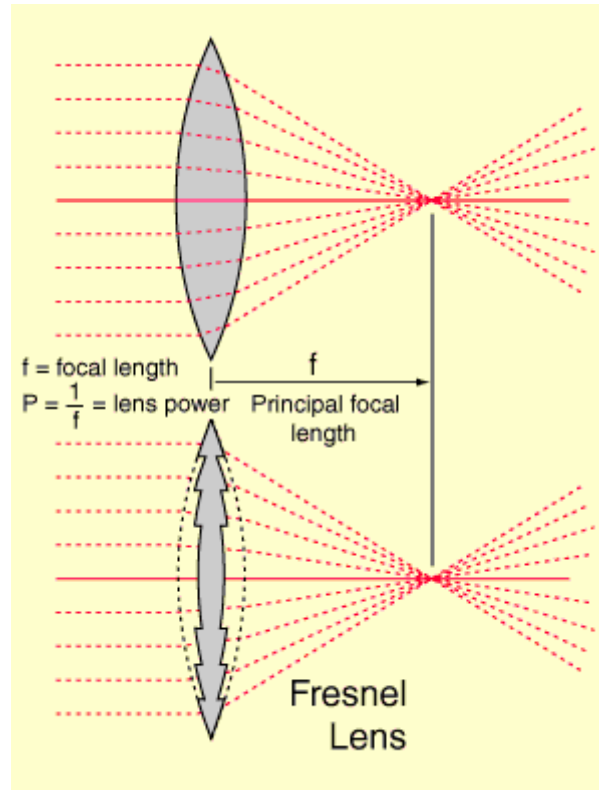
Fig. 3-32 Representation of a Fresnel lens according to the corresponding normal one.

Obviuosly, one can consider the Fresnel lens as an ensemble of many prisms as shown in Fig.3-33.

(a)   (b)
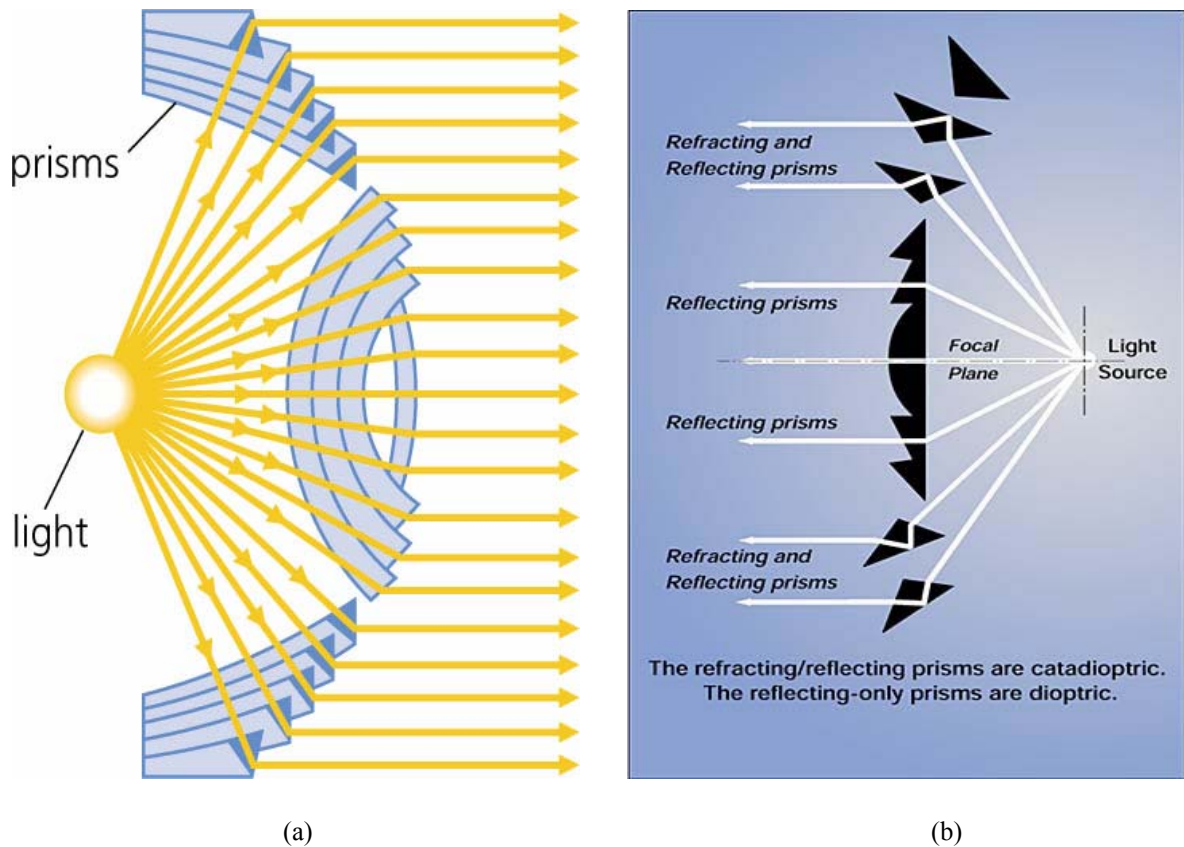
Fig. 3-33 Fresnel lens as an ensemble of many single prisms.

Figure 3-34 shows graphically how the Fresnel lens works. To bend and focus the rays to form a single, concentrated beam of high intensity light, the catadioptric prisms refract and reflect; the dioptric prisms and center bull's eye lens refract. With just a 1000 watt bulb, a first-order Fresnel lens can generate a 680,000 candlepower beam visible up to 21 miles out to sea if set high enough.
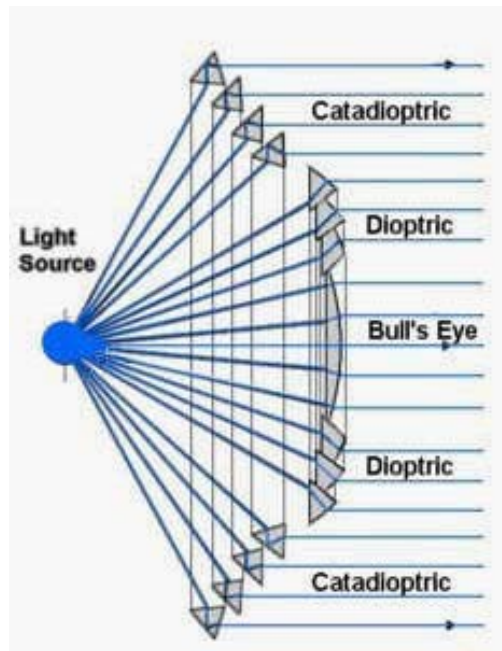
Fig. 3-34 A schematic diagram showing how the Fresnel lens works.

Fresnel lenses, in many different forms, find many applications in today's modern world. They are used in the lens of traffic signals and to shape the light beam in overhead projectors as well as in molded plastic versions which are sometimes placed on the rear windows of motorhomes to broaden the drivers' rearward field of view.

3.14.2 Historical view

Centuries ago, it was recognized that the contour of the refracting surface of a conventional lens defines its focusing properties. The bulk of material between the refracting surfaces has no effect on the optical properties of the lens, (other than increasing absorption losses). In a Fresnel lens (focus point), the bulk of material has been reduced by the extraction of a set of coaxial annular cylinders of material, as shown in Fig. 3-35. (Positive focal-length-Fresnel lenses are almost universally plano-convex.) The contour of the curved surface is thus approximated by right circular cylindrical portions, (do not contribute to the lens optical properties), intersected by conical portions called "grooves" which are nearly parallel to the plane face. Toward the outer edge, the inclined surfaces become extremely steep, especially for lenses of low f-number. The inclined surface of each groove is the corresponding portion of the original aspheric surface translated toward the plano surface of the lens; the angle of each groove is modified slightly from that of the original aspheric profile to compensate for this translation.
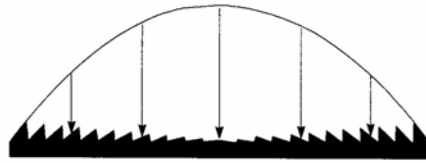
Fig. 3-35 Construction of a Fresnel lens from its corresponding asphere. Each groove of the Fresnel lens is a small piece of the aspheric surface, translated toward the plano side of the lens. The tilt of each surface must be modified slightly from that of the original portion of aspheric surface, in order to compensate for the translation.

The earliest stepped-surface lens was suggested in 1748 by Count Buffon, who proposed to grind out material from the plano side of the lens until he was left with thin sections of material following the original spherical surface of the lens, as shown schematically in Fig. 3-36 (a). Buffon's work was followed by that of Condorcet and Sir D. Brewster, both of whom designed built up lenses made of stepped annuli.

The aspheric Fresnel lens is the 1822 invention of French physicist and mathematician Augustine Fresnel (1788 – 1827), who invented a lens that would make his name commonplace along the seacoasts of Europe and North America. Fresnel's original lens was used in a lighthouse on the river Gironde; the main innovation embodied in Fresnel's design was that the centre of curvature of each ring receded along the axis according to its distance from the centre, so practically eliminating spherical aberration. Fresnel's original design, icluding the spherical-surfaced central section, is shown schematically in Fig.3-36 (b).

a)   b)
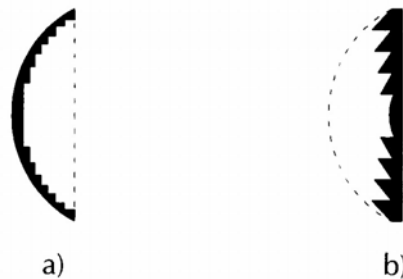
Fig. 3-36 Early stepped-surface lenses. In both illustrations the black area is material, and the dashed curves represent the original contours of the lenses. (a) shows the lens suggested by Count Buffon (1748), where material was removed from the plano side of the lens in order to reduce the thickness. (b) shows the original lens of Fresnel (1822), the central ring of which had a spherical surface. In Fresnel's lens, the center of curvature of each ring was displaced according to the distance of that ring from the center, so as to eliminate spherical aberration.

116

The early Fresnel lenses were cut and polished in glass – an expensive process, and one limited to a few large grooves. Fig. 3-37 shows a Fresnel lens, constructed in this way, which is used in the lighthouse at St Augustine, Florida, USA. The large aperture and low absorption of Fresnel lenses were especially important for use with weak lamps found in lighthouses before the invention of the high brightness light sources in the 1900s. The illustrated system is catadioptric: the glass rings above and below the Fresnel lens band in the center of the light are totally-internally-reflecting prisms, which serve to collect an additional fraction of the light from the source. The use of catadioptric systems in lighthouses was also due to Fresnel. Fig. 3-38 shows a photo of the lighthouse St Augustine, Florida, USA.
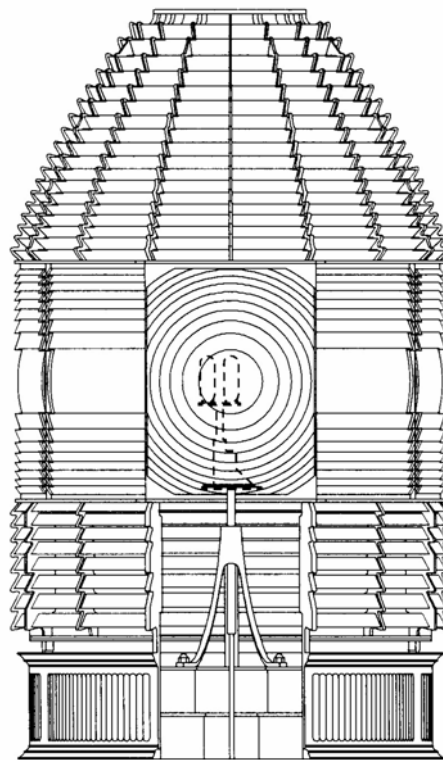
Fig. 3-37 The light from the St Augustine, Florida (USA) lighthouse, showing the glass Fresnel optical system used in the lighthouse. The optical system is about 12 feet (3.5 m) tall and 7 feet (2 m) in diameter.

Most lenses were handmade and shipped unassembled from France. Others were made in England. Early lens designs resembled a giant glass beehive, with a light at the centre. The lens could be as tall as twelve feet high with concentric rings of glass prisms above and below a centre drum section to bend the light into a narrow beam. Later designs incorporated a bull's eye design in the centre of the lens shaped like a magnifying glass, so the concentrated beam was even more powerful. Tests showed that while an open flame lost nearly 97% of its light, and a flame with reflectors behind it still lost 83% of its light, the Fresnel lens was able to capture all but 17% of its light. Because of its amazing efficiency, a Fresnel lens could easily throw its light 20 or more miles to the horizon.

117

Fig. 3-38 Photo of the lighthouse St Augustine, Florida, USA.

Early Fresnel lenses were of standard shapes and designs with little deviation such as the one pictured above. They had an oil lantern that burned constantly from dusk until dawn with no flashing or blinking as you may think of them today. Once they started being used along the coasts in greater numbers the mariner could not tell where they were at night because nothing distinguished one light from another. For a lighthouse to be effective as an aid to navigation, it not only had to be seen, it also had to be identified as a unique location. This was necessary if ships were to use it to determine their own location and avoid hazards. From here on, different lenses were made with different characteristics and as required by different lens designs. This meant that a lot of lenses were now unique because they would require flash panels or bull's eyes to distinguish one light from the next. The need to clearly identify each lighthouse was often solved by a specific pattern of flashes per minute. Although sometimes lighthouses identified themselves by using colored light, most made use of a flash of light, followed by a period of darkness. This pattern was called the lighthouse's "characteristic". Once electricity was introduced a light could use a flashing mechanism to give it a unique characteristic flash pattern. Now a sea captain could tell where he was by looking at a map and the flash pattern of the light.

There are many sizes of Fresnel lenses, called 'orders', the largest being a first order, which is made up of hundreds of glass prisms. The lenses decrease in size through second order, third order, etc. Some have red panels, in order to shine a red light seaward. The glass prisms are shaped and positioned in such a way that the light from the single source inside the lens is reflected outward horizontally through each prism. In this way, the light streaming outward in all different directions is maximized into large beams shining out to sea. The number of beams depends on the configuration of the prisms, which can vary greatly. Different lighthouses must display beams for differing periods of time in order to be distinguished from one another.

Fresnel lenses are divided into 6 classes (called "orders"). The order is determined by the distance of the light source to the lens. The "First Order Fresnel lens" is the largest lens widely used, and was installed in many of the largest "sea coast lights". Two larger sizes were built in limited quantity and they are for a couple of special installations. Smaller Fresnel lenses, such as the sixth-order lens, were installed in smaller lighthouses, such as breakwater lighthouses.

118

3.14.3 The advantages of the Fresnel lenses

The use of Fresnel lens as an optical concentrator is due to the following advantages:

1- Fresnel lense can be designed and manufactured in very large sizes with light weight due to less than 4 mm thickness, so the cost will be lower than traditional magnifiers. In contrast, a conventional glass lens would be 200 mm thick at the edge, weigh over 50 kgs and cost thousand of dollars.

2- Its lightweight allows for the use of a larger diameter lens which collects more light from the light source.

3- Fresnel lenses also allow for very low focal length, keeping the focal length and assembly short and small and enabling smaller diameter spot size at the image plane.

4- The design of the lens also corrects for spherical aberrations to allow for more uniformed illumination at the image plane and finally in the final configuration a smooth, cleanable outer surface is desired which is enabled by having the grooves facing inward and avoiding the use of another component to cover the grooves.

3.14.4 Chart of Fresnel Lenses

Table 3-3 shows schematically the chart of Fresnel lenses orders categorised according to their sizes [53]. Some photos of different types of lenses are shown in the following figures from Fig 3-39 to Fig. 3-45.

Order	Height	Inside Diameter
First	7' 10"	6' 1"
Second	6' 1"	4' 7"
Third	4' 8"	3' 3"
Third and half	3' 0"	2' 5 1/2"
Fourth	2' 4"	1' 8"
Fifth	1' 8"	1' 3"
Sixth	1' 5"	1' 0"

Table 3-3 The chart of Fresnel lenses orders categorised according to their sizes.

Fig. 3-39 A First Order lens found at the Ponce De Leon Inlet Lighthouse near Daytona Beach Florida. No First Order lenses were used in the Great Lakes. These lenses are huge.

Fig. 3-40 A Second Order lens from Standard's Rock lighthouse in Lake Superior. One of only a small hand-full of this size lens is used in the Great Lakes. This one has bull eyes in the centre and is meant to create a flash pattern as it is rotated.
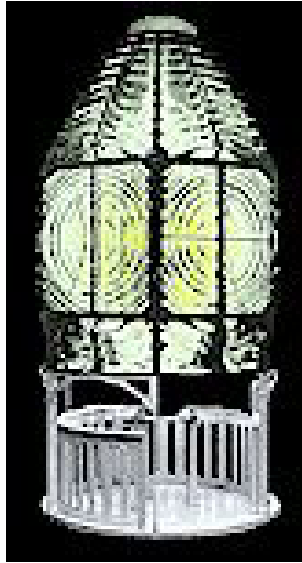
Fig. 3-41 A Third Order lens with bulls eye flash panels installed. This lens was meant to be rotated to provide a flashing characteristic. Some of these lenses are on display around Michigan Museums.
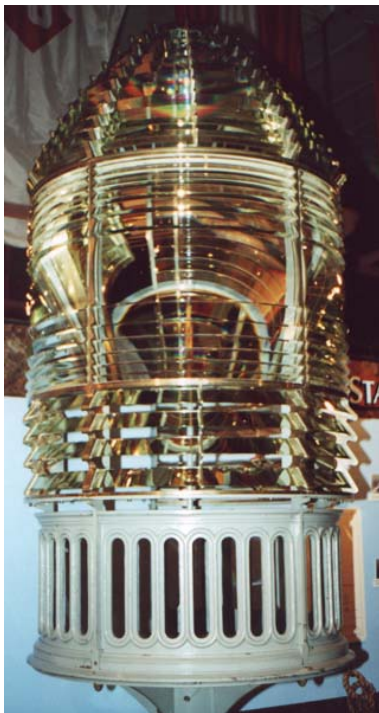
Fig. 3-42 A Third and a Half Order lens. It was one typically built for service on the Great Lakes as it was a medium size between a Fourth and Third Order lens, a Fourth was too small and a Third was just too large for the intended use. This lens is from Big Bay Point on Lake Superior. The pedestal that it sits on is pictured to the right. This is a drum lens and not a rotating lens.

Fig. 3-43 A Fourth Order lens was very typical on the Great Lakes and especially Michigan. A lot of pier head lights and lighthouses displayed one of these lenses. It was a lens size most commonly used throughout the lakes and some ocean coastal harbour stations.

Fig. 3-44 A Fifth Order lens from the Ontonagon lighthouse. This lens exhibited a red light and as such had a red chimney placed around the lamp inside to change the lens colour. This is what is called a beehive type design. Although some Fourth Order lenses had flash panels installed on them this one does not. This lens can be seen in downtown Ontonagon at the local museum.

Fig. 3-45 A Sixth Order lens. It is the smallest of the lenses made for lighthouses. It was designed for small light stations or pier head type lights. This one is on display inside the Saulte Saint Marie Coast Guard Station. These lights were common in the Great Lakes on small harbours or piers. A Sixth Order lens can still be seen installed at the Grand Marie Range lights rear tower from the parking lot.

Chapter 4: Sun Tracking Laser Systems

Overview

In this chapter, we investigate the possibility of pumping a solar laser system. We also devised for the first time some new systems of pumping the laser using Fresnel lenses. We developed a new concentration system consisting of a Fresnel lens and a glass compound spherical concentrator. We applied this new concentration system to a slab laser of Nd:YAG and a laser rod of Nd:YVO$_4$.

4.1 Introduction

The typical concentration systems consist of a primary concentrator of the type of parabolic dish (sometimes called paraboloidal concentrator), a secondary concentrator of the type of non-imaging 2- or 3-dimensional compound parabolic concentrator, a conical or pyramidic concentrator and the laser cavity. The use of the primary concentrator is to reach the high concentration level needed to overcome the pumping threshold of the laser, while the secondary concentrator plays two roles. It increases the concentration level and distributes the high concentrated solar radiation evenly onto the laser medium to avoid damaging the laser material.

We began to study the possibility to construct such a system by calculating the threshold pumping power of the laser itself. Thus, we could determine the power needed to reach the threshold of the lasing process. From this value, one can calculate the optimal dimensions needed to design such a concentrator system.

There are many optical devices which can be used as concentrators. Previously, mainly parabolic dishes were used as primary concentrators. But there are some problems in using such concentrators like the difficulty of their fabrication and their higher costs. Therefore, we thought of using the Fresnel lens for example as a primary concentrator. We considered it as an alternative concentrator for the parabolic dish.

In our work, we used both pumping techniques; end- and side-pumping. End pumping technique was used with a slab laser of the type Nd:YAG laser with convex lens as a secondary concentrator. Side pumping technique was used for a Nd:YVO$_4$ laser rod and a glass compound spherical concentrator (CSC) as a secondary concentrator. In both techniques, two large rectangular Fresnel lens were used as primary concentrators. The whole system was placed on an astronomical mount to track the apparent motion of the sun during the day.

4.2 Simulation of a solid-state solar pumped laser systems using standard concentrators

As a beginning, one could use a concentration system consisting of a paraboloidal concentrator, as a primary concentrator, and a non-imaging concentrator like the compound parabolic concentrator (CPC) or the conical concentrator, as a secondary one. The calculations were made to optimize the dimensions for both concentrators.

4.2.1 Laser material parameters

The suggested laser material for the simulation models was a rod of Nd:YAG laser. It showed theoretically and experimentally a good performance evidences. The requirements for such a laser rod of the type Nd:YAG are given in Table 4-1.

Parameter	Symbol	Value
Rod Length	L_a	40 mm
Rod Diameter	D_a	5 mm
Absorption Coefficient	α	0.59
Quantum efficiency	η_q	0.63
Pumping efficiency	ε	0.67
Overlap Ratio	η_{ovp}	0.14
Loss across the rod	γ_l	0.016
Fluorescence of the crystal (Saturation flux)	I_s	12.5 W/mm^2
Slope Efficiency	η_s	0.009
Transmissivity of the output coupler	T	0.02

Table 4-1 Theoretically suggested laser parameters as a test to generate the solar laser.

The threshold pumping power of the laser rod can be calculated from the formula [10]:

$$P_{th} = \frac{A_a I_s}{\eta_q \eta_{ovp} \alpha}\left(\frac{2\gamma_l - \ln R}{2\varepsilon}\right) \qquad (4\text{-}1)$$

where A_a is cross-sectional area of the rod which is equal to $\pi D^2/4$. The other parameters are defined in Table 4-1.

We can also calculate the value of the slope efficiency (the efficiency above the threshold) [23] using the Equation (4-2).

$$\eta_s = \eta_q \eta_{ovp} \alpha \varepsilon \left(\frac{T}{(2\gamma_l - \ln R)}\right) \qquad (4\text{-}2)$$

where the value η_q is the quantum efficiency (the mean wavelength of absorbed radiation divided by the lasing wavelength) [10] and can be calculated from the Equation (4-3).

$$\eta_q = \frac{\lambda_s}{\lambda_L} \qquad (4\text{-}3)$$

and η_{ovp} is the overlap of laser absorption with the solar spectrum [10] and can be calculated from the Equation (4-4).

$$\eta_{ovp} = \frac{\int_a^b g_\lambda d\lambda}{\int_0^\infty g_\lambda d\lambda} \qquad (4\text{-}4)$$

where g_λ is the standard solar spectral irradiance. Note that:

$$\int_0^\infty g_\lambda d\lambda = I_o \qquad (4\text{-}5)$$

λ_s in Equation (4-3) is defined as the mean absorbed and intensity weighted solar radiation wavelength, i.e.,

$$\lambda_s = \frac{\int_a^b g_\lambda \lambda d\lambda}{\int_a^b g_\lambda d\lambda} \qquad (4\text{-}6)$$

The laser output power P_{out} can be written as:

$$P_{out} = (A_a I_s) \frac{T}{(2\gamma_l - \ln R)} [g_o - (\gamma_l - \ln \sqrt{R})] \qquad (4\text{-}7)$$

where I_s is the saturation flux, T and R are the output mirror transmission and reflectivity, respectively, g_o is the small signal gain; and γ_l is the loss per pass in the laser [10].

126

Put into a form that is often used when presenting solid-state laser performance data, the output power can also be written as:

$$P_{out} = \eta_s(P_{in} - P_{th}) \qquad\qquad (4\text{-}8)$$

The measured laser threshold power, as a function of the output coupler mirror reflectivity R, can be used to determine both the loss per pass L and the mean pumping efficiency ε [10].

Accordingly, the threshold pumping power for our laser rod was calculated theoretically to have the value of approximately 280 W.

Depending on the pumping geometry (side pumping or end pumping), we have to choose an appropriate secondary concentrator.

4.2.2 Side pumping of a cylindrical rod

A non-imaging secondary concentrator of the following types is chosen: a two-dimensional compound parabolic concentrator (2D-CPC) or a V-trough. The non-imaging secondary concentrator helps to distribute the pumping radiation evenly over the surface of the cylindrical laser rod. Concentrators of the type CPC are preferable in such a case because they give suitable and large acceptance angles for relatively small dimensions. These types of concentrators avoid building massive, large and expensive constructions. A schematic diagram of such a manner of pumping is shown in Fig. 4-1.
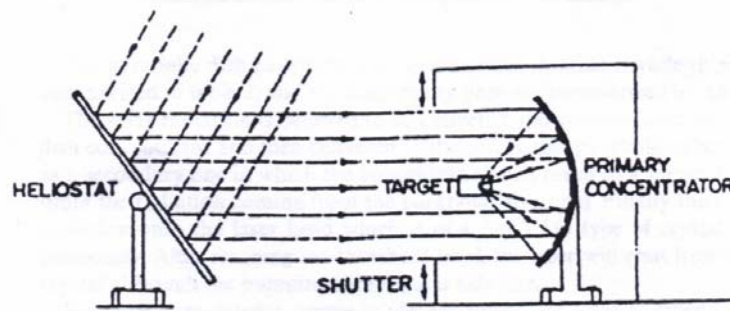
Fig. 4-1 Typical side pumping technique for the solar laser.

Optimal dimensions for a needed two-dimensional compound parabolic concentrator (2D-CPC) are shown in Table 4-2.

Parameter	Symbol	Value
Acceptance Angle	θ_a	30º
Concentration Ratio	C	2
Reflectivity	r	0.7
Concentration Ratio in the case of a cylindrical absorber	C_t	1.732
Height	H	6.5 mm
Efficiency	η	0.629

Table 4-2 Theoretically suggested secondary concentrator (CPC) parameters.

Accordingly, one can choose the dimensions of the primary concentrator (paraboloidal concentrator) to be as shown in Table 4-3.

Parameter	Symbol	Value
Rim Angle	ϕ_r	44.867
Diameter	D	6.817 m
Focal length	f	4.128 m
Concentration ratio	C	1.14×10^4
Reflectivity	r	0.7
Interception factor	γ	0.85
Efficiency	η	0.535

Table 4-3 Theoretically suggested primary concentrator (Parabolic Dish) parameters.

The calculations of this model gave a laser output power of approximately 20 W corresponding to an intensity of 10^6 W/m^2 where the mean insolation level is 600 W/m^2.

4.2.3 End pumping of a cylindrical rod

A non-imaging secondary concentrator of the following types is chosen: a conical concentrator or a three-dimensional compound parabolic concentrator (3D-CPC). The laser rod will be placed from its end on the exit opening of the secondary concentrator. Also, it is important to mention that the 3D-CPC is preferable to use in such a manner because it fulfills two purposes; a relatively small acceptance angle with a relatively higher concentration ratio, and a relatively small dimension of the primary concentrator. A schematic diagram of such a manner of pumping is shown in Fig. 4-2.
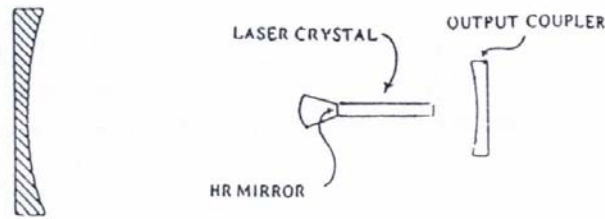
Fig. 4-2 Typical end pumping technique for the solar laser.

The optimal dimensions of the needed conical concentrator where calculated and are shown in Table 4-4.

Parameter	Symbol	Value
Acceptance Angle	θ_a	20°
Concentration Ratio	C	8.549
Reflectivity	r	0.7
Height	H	13 mm
Efficiency	η	0.56

Table 4-4 Suggested theoretical secondary concentrator (Conical Concentrator) parameters.

Again, one can choose the dimensions of the primary concentrator (parapoloidal concentrator) to be as shown in Table 4-5.

Parameter	Symbol	Value
Rim Angle	ϕ_r	44.867°
Diameter	D	1.561 m
Focal length	f	0.945 m
Concentration ratio	C	1.14×10^4
Reflectivity	r	0.7
Interception factor	γ	0.85
Efficiency	η	0.535

Table 4-5 Suggested theoretical primary concentrator (Parabolic Dish) parameters.

The calculations of this model gave a laser output power of 0.54 W representing an intensity of 2.75×10^4 W/m^2 where the mean insolation level is 600 W/m^2. If the acceptance angle of the conical concentrator was increased to greater than 22°, we were unable to overcome the pumping threshold and hence no laser output was observed. Therefore, a conical concentrator as an easily manufactured concentrator is less useful as such an application

In case of a CPC, the concentration ratio as a function of the transmission angle is nearly constant up to a transmission angle around the acceptance angle. In the case of a conical concentrator, the concentration ratio is strongly decreasing with transmission angle. In both cases, the transmission is blocked for transmission angles larger than the acceptance angle.

Therefore, the concentrators of the type three-dimensional compound parabolic concentrator (3D-CPC) are preferable in such a case because they can give suitable large acceptance angles with relatively small dimensions. The use of these types of concentrators therefore avoids the building of massive, large and expensive constructions. One can estimate the dimensions of the necessary three-dimensional compound parabolic concentrator (3D-CPC) to be as shown in Table 4-6.

Parameter	Symbol	Value
Acceptance Angle	θ_a	20°
Concentration Ratio	C	8.549
Reflectivity	r	0.7
Height	H	9.22 mm
Efficiency	η	0.6

Table 4-6 Suggested theoretical secondary concentrator (3D-CPC) parameters.

Again, one can choose the dimensions of the primary concentrator (paraboloidal concentrator) to be the same as shown before in Table 4-5.

The calculations of this model gave a laser output power of 0.75 W representing an intensity of 3.84×10^4 W/m^2 where the mean insolation level is 600 W/m^2.

From the previous calculations, it can be seen that it would be a large, massive and expensive system because of its large and expensive elements. Imagine such mirrors with these diameter values. It would be really expensive and difficult to control. Moreover, it is considered as an old technique which has been already realised in various experiments since 1966 using different optical components.

Therefore, if we want to improve this large scale project of a solar pumped laser, we have to find new techniques which could realize two important goals needed. These two important goals are:

1- The simplicity of such a system, i.e. to construct such a system from portable components, which are easy to be controlled and repaired.

2- Lower costs for constructing and manufacturing such a system.

The Fresnel lens should be considered because on the one hand it has a relatively high level of optical concentration, and on the other hand it is relatively inexpensive. A practical solution would be to mount the Fresnel lens on an astronomical mount in order to track the sun. The high concentration level of the Fresnel lens is already known. The main disadvantage of such a system would be the relatively low obtainable concentration ratio which would be insufficient to overcome the lasing threshold one.

Another reasonable idea is the use of a mirror array concentrator (sometimes called Fresnel reflector). Such an array can work as a massive imaging parabolic concentrator if each single mirror has a certain angle in order to collect all of the reflected radiations into a certain place which we will call here the focus. If all of the mirrors have the same dimensions, this focus will theoretically have the dimensions of a single mirror. The main disadvantage for such a system could be the difficulty to keep the resulted focus in the same place because of the apparent motion of the sun during the day.

In this chapter, we will concentrate on the Fresnel lens technique and study its advantages and disadvantages in reaching the concentration level needed to obtain solar powered lasing. In the next chapter we will discuss the use of mirror array concentrators.

4.3 The use of Fresnel lenses as primary concentrators

We have investigated two large Fresnel lenses (named FLI and FLII). Each one was used as a primary concentrator for pumping the laser. Both of them have a rectangular form and are made from PMMA. They are held in a wooden frame fixed by aluminium arms onto an optical bench that is placed on an astronomical mount, tracking the sun by means of an electrical DC-motor. This mount EX6 is powered by 4 batteries of 1.5 Volts. A schematic design of this set-up is shown in the Fig. 4-3 [5, 6, 54, 55].
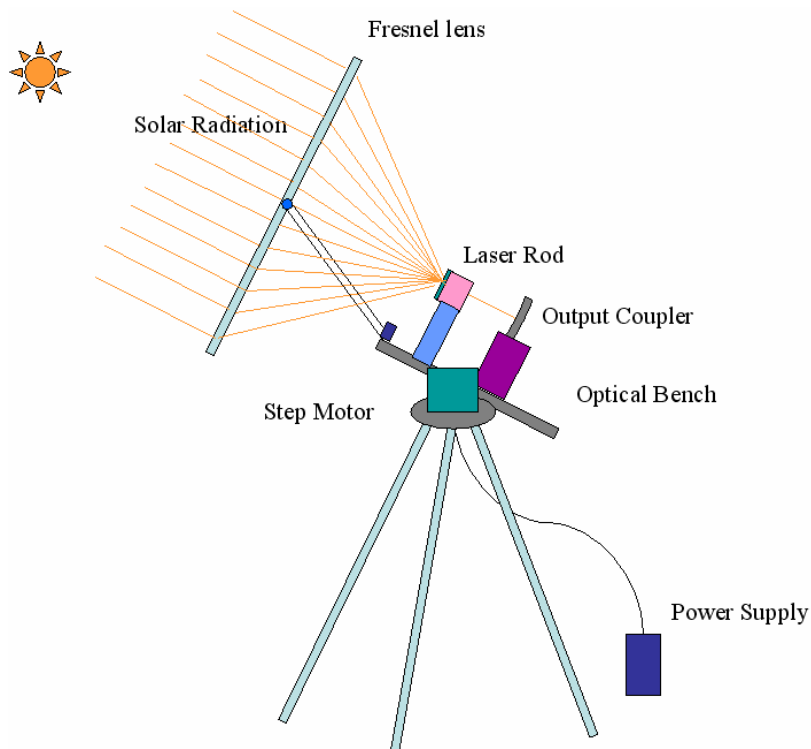
Fig. 4-3 Solar-pumped solid state laser with a Fresnel lens fixed on an astronomical mount.

Framing the lens FLI reduced its dimensions to 59.5 cm × 58.5 cm, while framing of the lens FLII reduced its dimensions to 103.5 cm × 79.5 cm. The astronomical mount is

designed to track the sun during its apparent motion during the day from east to west, if its axis of rotation is parallel to the earth axis.

We tested the properties and calculated the maximum concentration ratio of both Fresnel lenses FLI and FLII. The calculations showed that the image of the solar disc for the lens FLI has a radius of about 3.6 mm which represents an area of about 40 mm^2, while that for the lens FLII has a radius of about 4.7 mm which represents an area of about 69 mm^2.

Table 4-7 shows the parameters for both of the Fresenel lenses FLI and FLII and Fig. 4-4 shows a photo of both of them. It has to be noted here that the values of the radius of the solar disc made by both Fresnel lenses and their concentration ratios are theoretically calculated.

Parameter	FLI	FLII
Dimensions	60 cm × 59 cm	104 cm × 80 cm
Lens dimensions after framing	59.5 cm × 58.5 cm	103.5 cm × 79.5 cm
Aperture area (after framing)	≈ 0.35 m^2	≈ 0.82 m^2
Focal length	76.1 cm	100 cm
Radius of the solar disc	3.546 mm	4.66 mm
Rim angle	30°	32°
Theoretical Concentration ratio	8.787×10^3	1.206×10^3

Table 4-7 The geometrical properties for both of the Fresnel lenses.

Fig. 4-4 Typical Fresnel lenses used in the solar laser.

The complete mounting system is shown in Fig. 4-5. One can see the Fresnel lens in its wooden frame placed onto an optical bench using two metallic arms which in turn are fixed onto an astronomical mount. We also can see the image formed by the Fresnel lens, detected on an aluminum screen positioned in the focal plane, in Fig. 4-6.

Fig. 4-5 Fresnel lens on the Mount.

Fig. 4-6 The image formed by the Fresnel lens detected on an aluminum screen positioned in the focal plane.

Using that system, we recorded the solar radiation for a typical sunny day as shown in Fig. 4-7 [6].
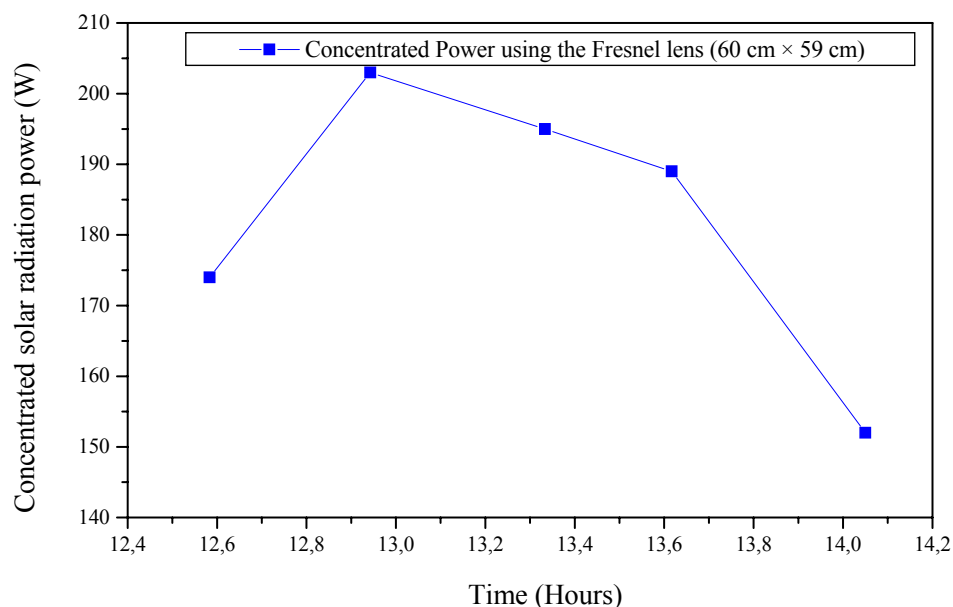
Fig. 4-7 Concentrated solar radiation with the Fresnel lens (FLI).

The area of the focus was measured to be 38 mm^2 (diameter of 7 mm). For this Fresnel lens system, we have measured the incident solar radiation on a normal sunny day in Berlin which is sufficient to obtain laser action. According to the measured solar radiation, we reached an intensity of 510 W/m^2, which represents a power of 177.5 W. This was focused through the Fresnel lens onto the laser crystal of dimensions (28 mm ×25 mm × 7 mm).

4.4 Measurement of the global solar radiation with and without both Fresnel lenses

We have investigated the properties of the two Fresnel lenses and their concentration ratios under out door conditions. Using a sensor of type Gentec PS-150 in connection with a power meter (type Gentec TPM-300), we recorded the power and the intensity of the concentrated solar radiation. These measurements are summarized in Table 4-8.

Experiment	Power (W)	Intensity (W/m^2)
Without focussing	2.99	1.06×10^3
With Fresnel lens (595 mm × 585 mm)	230	2.6×10^6
With Fresnel lens (1030 mm × 790 mm)	440	2.25×10^6

Table 4-8 Recorded values of solar radiation with and without both Fresnel lens.

134

Therefore, we can summarize the parameters of both Fresnel lenses in Table 4-9 according to the experimentally measured data [6].

	FLI	FLII
Focal length	0.76 m	1.0 m
Area	0.36 m^2	0.82 m^2
Theoretical focus diameter	7 mm	9.32 mm
Real focus diameter	12	18
Rim angle	30°	32°
Maximum pumping power	230 W	440 W
Maximum pumping intensity	2.6×10^6 W/m^2	2.25×10^6 W/m^2

Table 4-9 Fresnel lenses' parameters according to the experimental measurements.

From Table 4-8 and Table 4-9, one can calculate the temperature at the focus. It will be approximately 2500 °K (2173 °C) using the small Fresnel lens (FLI) and 2675 °K (2401 °C) using the bigger one (FLII) if the radiation is totally absorbed in the focus. Therefore, one has to use material with a high melting point to avoid damaging of those components.

4.5 Measurement of the focus distribution of both Fresnel lenses

Continuing the study of the Fresnel lenses' behaviour and properties, we studied the shape of the solar image in the focal plane to test the distribution of the concentrated radiation. According to this information, we can get an idea about the absorber and if one needs to employ an additional secondary concentrator. We photographed the images of the solar disc formed by both Fresnel lenses on an optical screen. The diameter of the solar disc is 12 mm using FLI and 15 mm using FLII. We found that more than 70 % of the concentrated solar radiation locate in a spot of a diameter of 10 mm. The images of the solar disc in the focal plane are displayed in Fig. 4-8 and Fig. 4-9 respectively. The photographs had been taken using a red filter to overcome the chromatic aberration of the Fresnel lens [6].
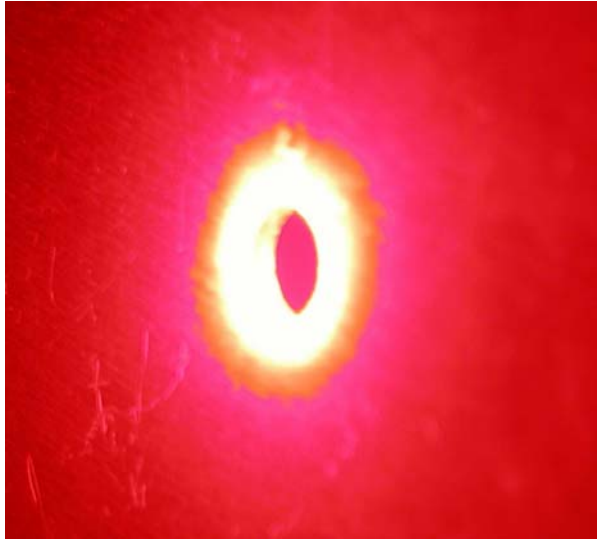
Fig. 4-8 The focus of the small Fresnel lens (595 mm × 585 mm) taken with a red filter.
The hole in the center of the screen has a diameter of 6 mm.

Fig. 4-9 The focus of the big Fresnel lens (1030 mm × 790 mm) taken with a red filter.

We used three optical screens to study the image profile of the focus position of the Fresnel lens FLI. Each optical screen was just an aluminium plate with a hole in its central point. The hole diameters of the optical screens were 6 mm, 9 mm and 12 mm respectively. We measured the solar radiation power behind these optical screens. Fig. 4-10 shows the power behind these optical screens as an arbitrary unit in order to give an idea about the concentrated radiation profile at the focus [6].
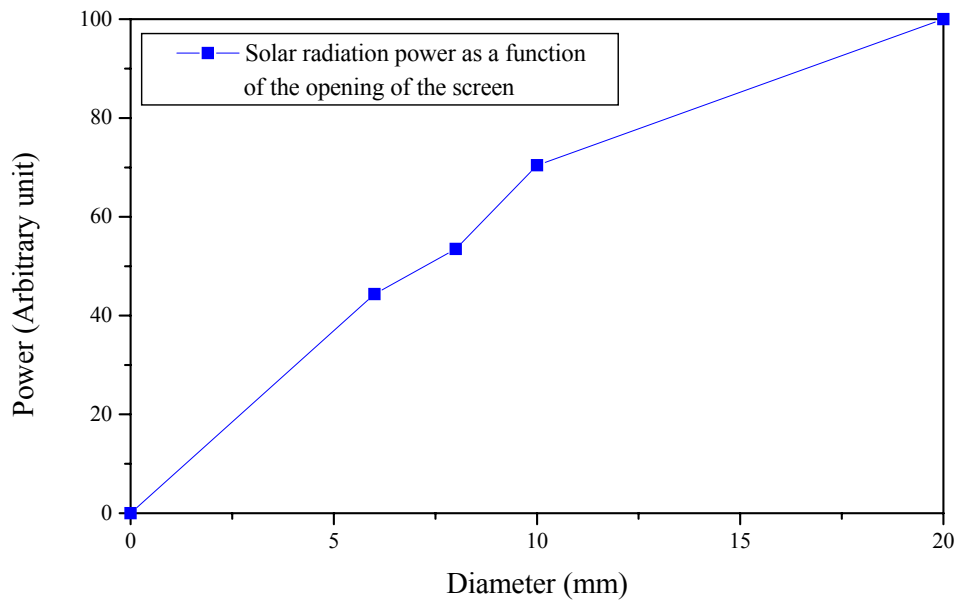
Fig. 4-10 Solar radiation power distribution in the focus of the Fresnel lens FLI.

4.6 Testing the quality of the Fresnel lenses

The adjustment of Fresnel lens as a solar concentrator is difficult because of the large intensity, which might damage the experimenter and/or the equipment. In order to investigate the lens and the adjustment errors all at the same time, we have to decrease the concentrated solar radiation intensity during the adjustment phase.

Therefore, we have designed two masks with a partially transmitting surface consisting of an array of 3 × 3 holes each of 3 cm diameter. Placed in front of the Fresnel lens, it is easier to find the focal plane for a particular wavelength. This mask is shown in the Fig. 4-11.

The use of the Fresnel lens is difficult because of three reasons:

1- The intensity of the concentrated solar radiation is very high.
2- The image should be observed in the red part of the spectrum, as this is the predominant pumping wavelength.
3- Tilting against the optical axis deteriorates the image quality considerably.

As we know, the chromatic error is one of the well-known lens' errors. Because the lens itself can be considered as a collection of many prisms, the focusing of the visible light through a lens shows different focus places depending on the wavelength. Such a difference can affect the concentration of our Fresnel lens. In the laser pumping process, only red light is needed use. Therefore, we used a red filter to test the lens focus in the red region of the spectrum.

137
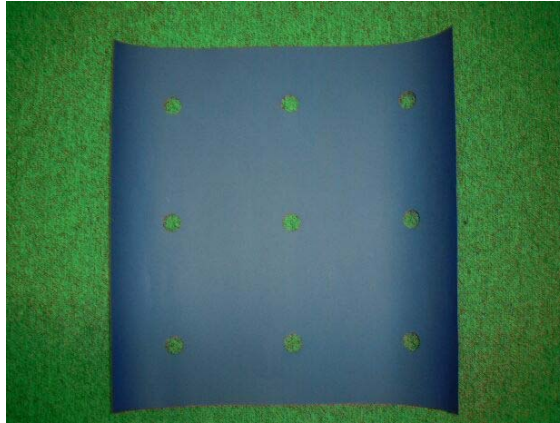
Fig. 4-11 Mask for characterizing Fresnel lens FLI. A similar mask was used to test
Fresnel lens FLII.

4.7 Testing the quality of the Fresnel lens FLI

After some trials, two experiments were done; the first one was an experiment without using any filter and the second one was an experiment with a red filter. The records were taken at different distances from the Fresnel lens around its known focal plane.

A digital camera of Medion (resolution 4.1 Megapixel) was used to record the images of the adjusted Fresnel lens. After studying the previous photos, we could calculate the internal and the external diameter of the focus. Fig. 4-12 shows the setup of the experiments.

Fig. 4-12 The setup of testing the Fresnel lens FLI.

4.7.1 The first experiment

In this experiment, we made some photos of the sun disc image projected by the Fresnel lens for different positions from the lens itself. One of those positions was the position of the focus. The shapes of the images are shown in Fig. 4-13.

(a) At 700 mm from the lens.　　(b) At 720 mm from the lens.　　(c) At 740 mm from the lens.

(d) At 760 mm from the lens.　　(e) At 761 mm from the lens
　　　　　　　　　　　　　　　　　　　　(optimum focus).

Fig. 4-13 The behaviour of the images made by the Fresnel lens FLI (595 mm × 585 mm) for different positions regularly measured from the lens itself.

4.7.2 The second experiment

In this experiment, we made similar photos of the solar image using a red filter. The results are displayed in Fig. 4-14.

| (a) At 700 mm | (b) At 720 mm | (c) At 740 mm | (d) At 760 mm |

| (e) At 761 mm | (f) At 770 mm | (g) 780 mm | (h) 800 mm |
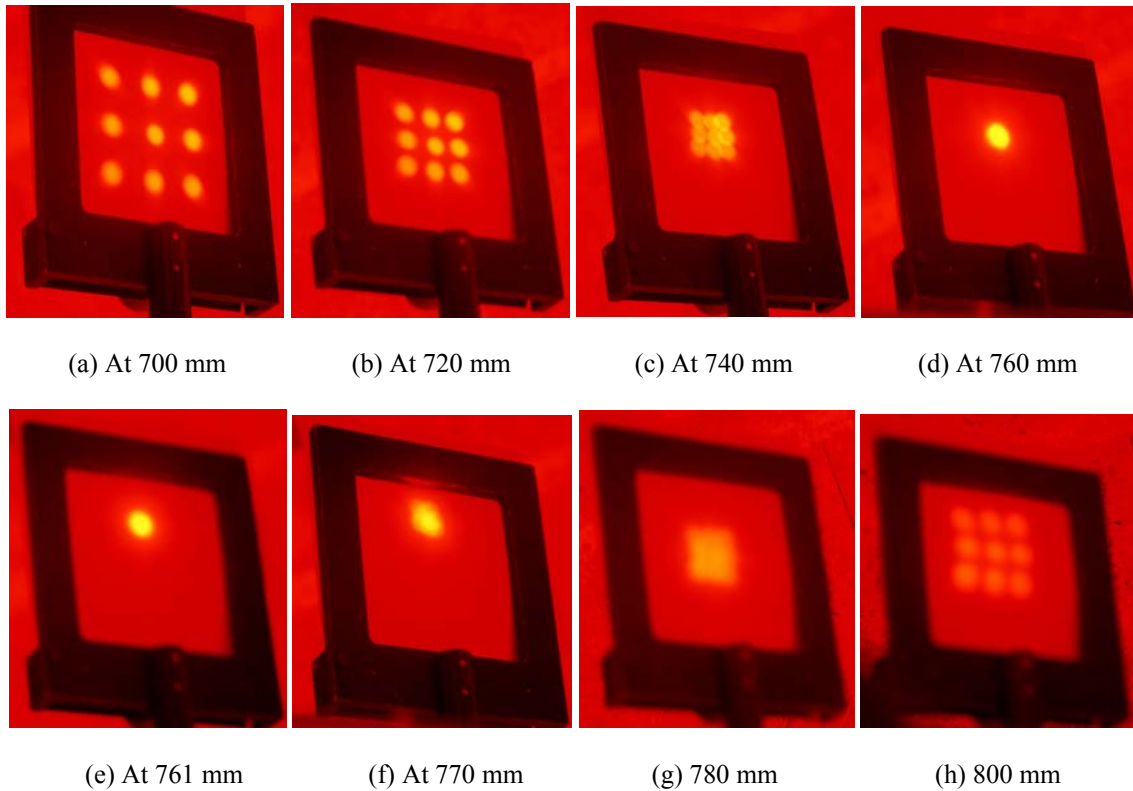
Fig. 4-14 The behaviour of the images made by the Fresnel lens FLI (595 × 585 mm) for different positions regularly measured from the lens itself using a red filter.

In this experiment, the images using a red filter are better because there is no chromatic error.

4.8 Testing the quality of the Fresnel lens (FLII)

Similarly, after some trials, two experiments were done; the first one was an experiment without using any filter and the second one was an experiment with a red filter. The images were taken at different distances from the Fresnel lens around its known focal plane.

We calculated the internal and the external diameter of the focus and compared the experimental value of the image diameter with the calculated one. Fig. 4-15 shows the setup of the experiments.

Fig. 4-15 The setup of testing the Fresnel lens FLII (1035 mm × 795 mm).

4.8.1 The first experiment

In this experiment, we took some photos of the solar disc image made by the Fresnel lens for different distances from the lens without using any filter. One of those positions was the position of the focus. We can see the behaviour of the images for those positions in Fig. 4-16.
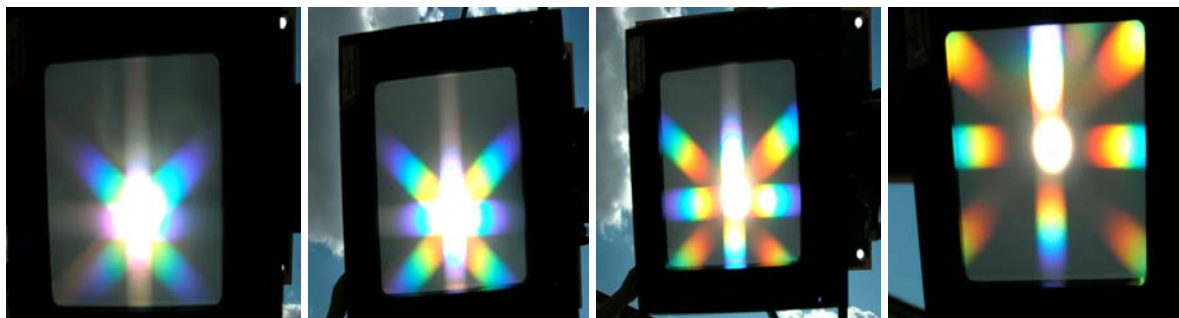
| (a) At 940 mm. | (b) At 960 mm. | (c) At 980 mm. | (d) At 1000 mm. |

| (e) At 1006 mm. | (f) At 1020 mm. | (g) At 1040 mm. | (h) At 1060 mm. |

Fig. 4-16 The behaviour of the images made by the Fresnel lens FLII (1035 × 795 mm)
for different positions regularly measured from the lens itself.

4.8.2 The second experiment

We repeated the previous experiment using a red filter. We can see the behaviour of the images for those positions in Fig. 4-17

(a) At 940 mm.	(b) At 960 mm.	(c) At 980 mm.	(d) At 1000 mm.
(e) At 1006 mm.	(f) At 1020 mm.	(g) At 1040 mm.	(h) At 1060 mm.
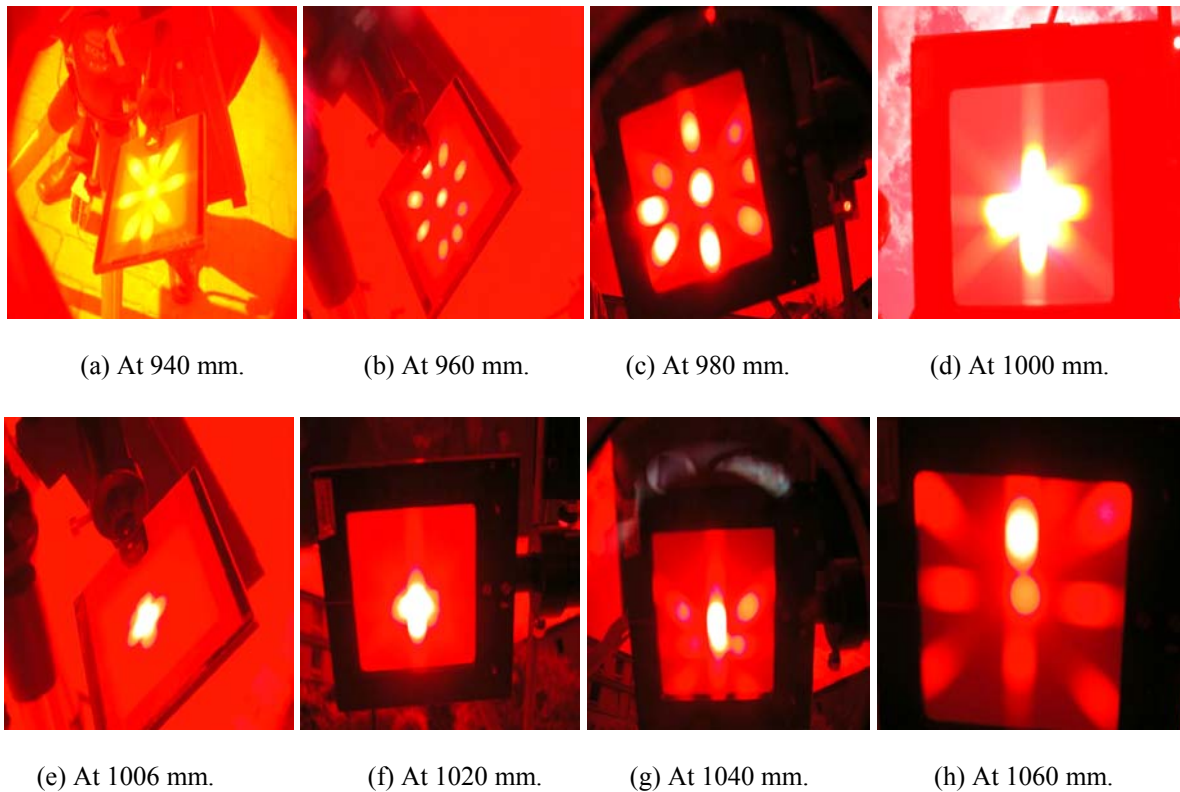
Fig. 4-17 The behaviour of the images made by the Fresnel lens FLII (1035 × 795 mm) for different positions regularly measured from the lens itself using a red filter.

4.9 Testing the image quality of the Fresnel lenses (FLI and FLII) using an optical collimator

In this test, we studied the image profiles of both Fresnel lenses FLI and FLII using a parallel light from a collimator. The collimator consists of an illuminated slit of dimensions 1000 μm × 39.6 μm which was positioned in the focus of an off-axis parabolic mirror. The instrument produced a parallel beam of light with a diameter of 30 cm. The images of this test were recorded using a CCD camera connected to a computer through the (LabView) software. No imaging optical instruments were used for the CCD camera.

The CCD camera we used is of the type CCD 1300 D VDS Vosskühler and has the properties shown in Table 4-10.

Property	Value
Pixel area	6.25 μm × 6.25 μm per pixel
Resolution	1024 × 1024 Pixel
Dynamic	12 Bit

Table 4-10 The properties of the used CCD camera in testing the Fresnel lenses.

The image produced by the Fresnel lens is detected by the CCD camera controlled by a Lab View programme that translates the recorded photo into an intensity map unit and then into a graphical representation showing the shape of the focused light.

The experiments were performed in the large Lens Test Laboratory of the Institute of Optics of the Technical University of Berlin. The setup of this experiment is shown in Fig. 4-18, while its photos are shown in Fig. 4-19.
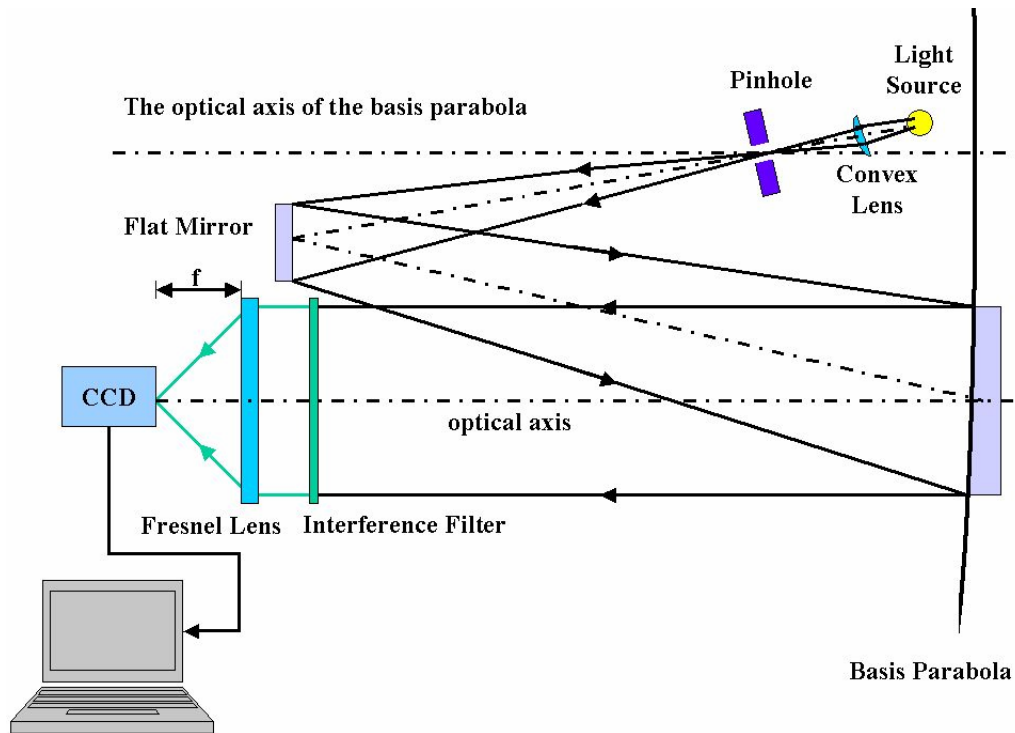
Fig. 4-18 Setup of testing the quality of the Fresnel lens in the Lens Test Laboratory.

(a) Fresnel lens tested with a CCD camera.

(b) The experimenters with the setup.

(c) The setup connected with a computer.

(d) The CCD camera with its connection.

Fig. 4-19 Photos of the setup of testing the Fresnel lenses using a CCD camera.

4.10 Testing the image of the Fresnel lens FLI (595 mm × 585 mm)

Two experiments were done with this system. They will be shown in the following paragraphs. The width of the image at the best focus was calculated to be 12.05 μm.

4.10.1 Testing the images formed by Fresnel lenses at different distances

In this experiment, we studied the image shape around the focus position. Therefore, we made photos in front of and behind this position. The word (in front of) here means that the distance of the Fresnel lens is smaller than the focal length, while the word (behind) here means that this distance is greater than the focal length. The recorded photos of this experiment are shown in Fig. 4-20, while the intensity distributions (image profiles) are shown in Fig. 4-21.

(a) At 10 mm in front of the focus.

(b) At 5 mm in front of the focus.

(c) At the focus.

(d) At 5 mm behind the focus.

(e) At 10 mm behind the focus.
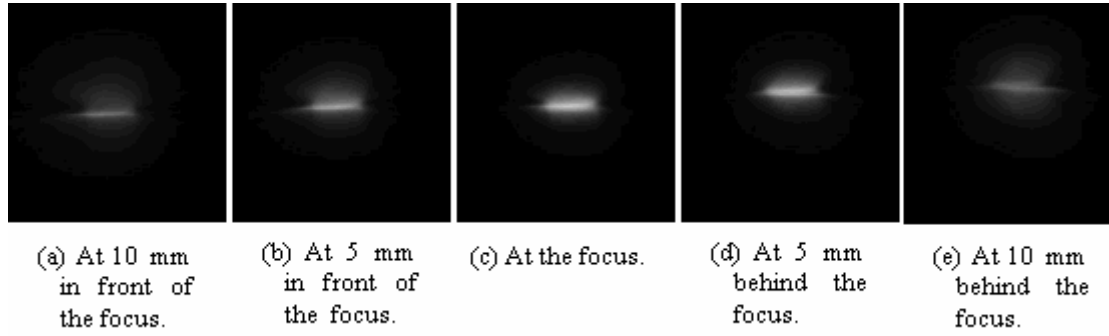
Fig. 4-20 Profiles showing the image of the Fresnel lens FLI in different positions refering to its focus one.
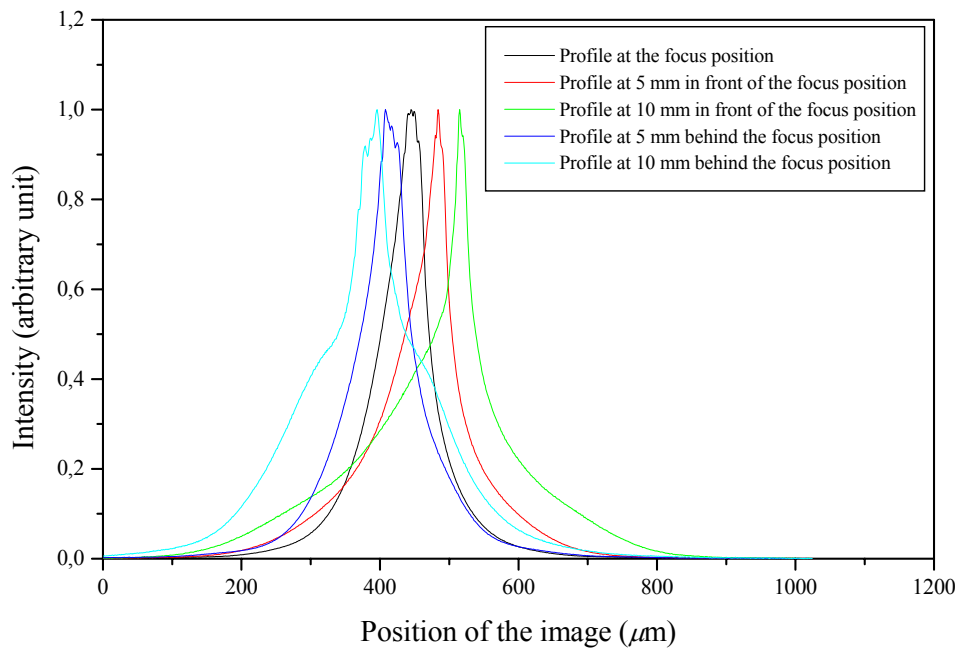
Fig. 4-21 Image profile of the Fresnel lens FLI around the focus position.

4.10.2 Testing the image form of Fresnel lens with different tilting angles

In this experiment, we studied the effect of tilting the Fresnel lens against the optical axis by tilting the Fresnel lens clockwise and counter clockwise. The recorded photos of this experiment are shown in Fig. 4-22, while the intensity distributions (image profiles) are shown in Fig. 4-23.

(a) 10° tilting.   (b) 5° tilting.   (c) No tilting.   (d) -5° tilting.   (e) -10° tilting.
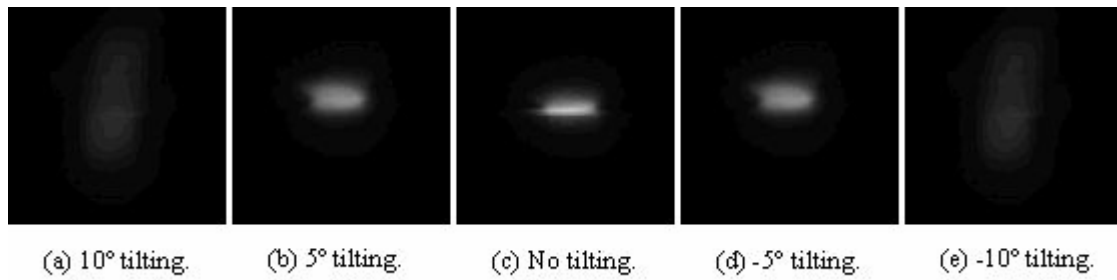
Fig. 4-22 Profiles showing the image of the Fresnel lens in different tilting angles in the focus position.
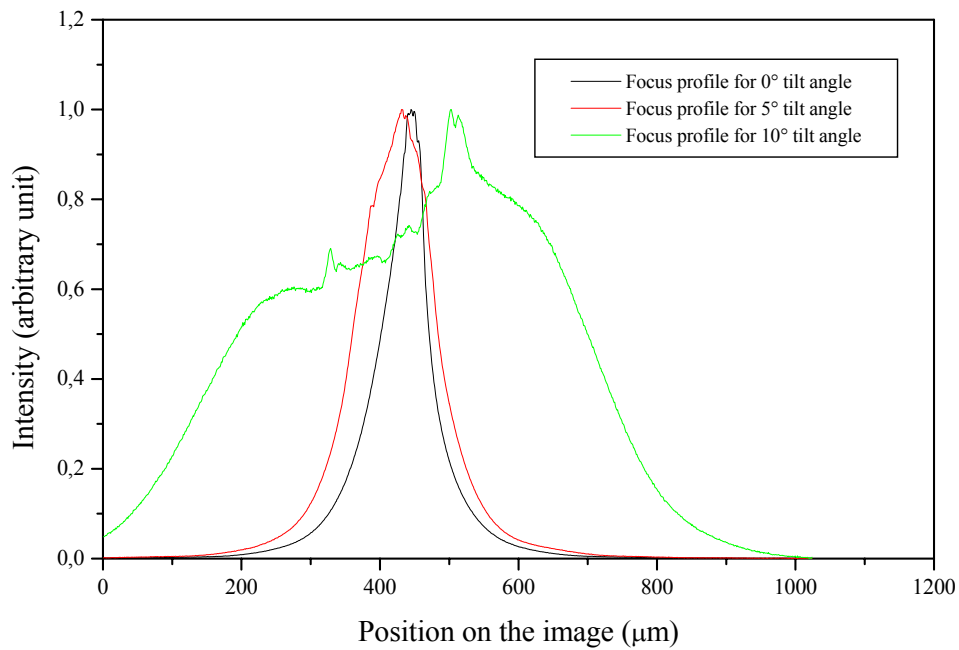
Fig. 4-23 Image profile of the Fresnel lens FLI for different tilting angles in the focus position.

4.11 Testing the image quality from the Fresnel lens FLII (1035 mm × 795 mm)

Similar experiments were performed for Fresnel lens FLII. The image width at the best focus was calculated to be 15.89 μm. The recorded photos of this experiment are shown in Fig. 4-24, while the intensity distributions (image profiles) are shown in Fig. 4-25.

146
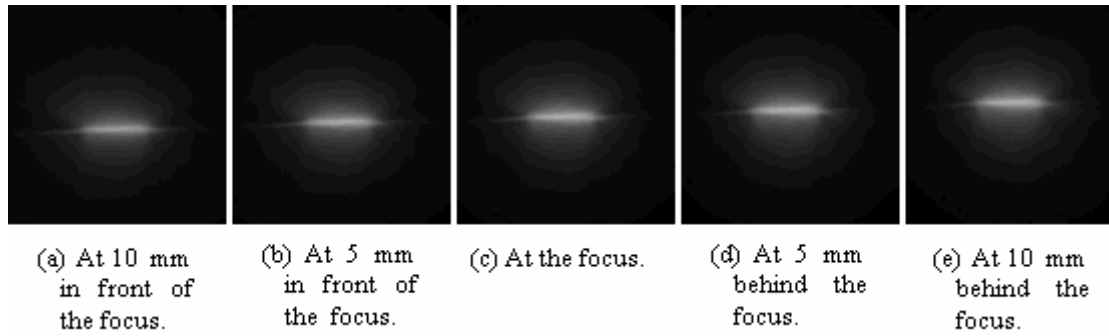
Fig. 4-24 Profiles showing the image of the Fresnel lens in different positions refering to its focus one.
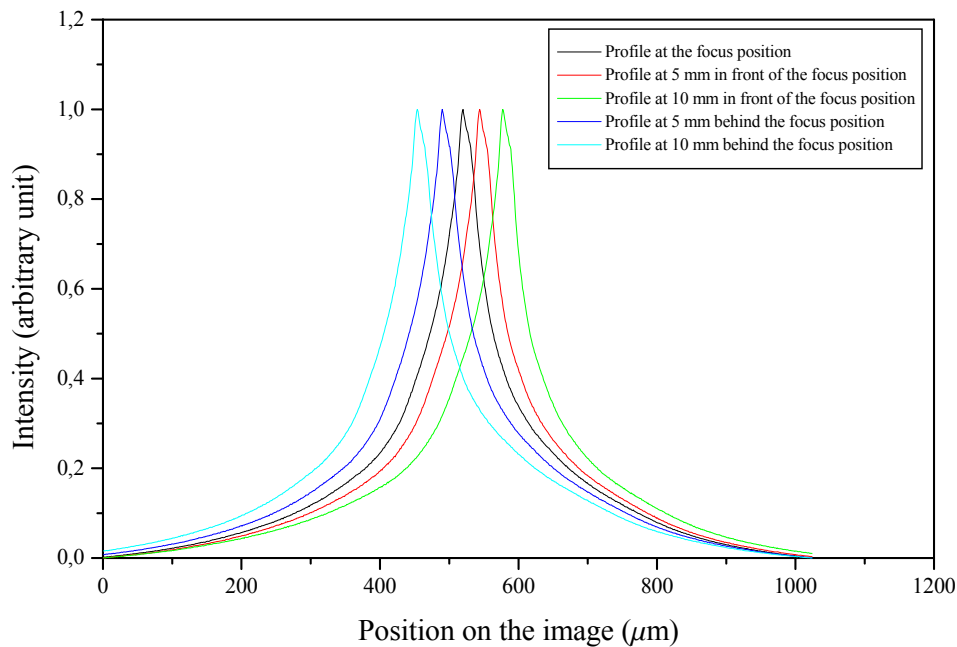
Fig. 4-25 Image profile of the Fresnel lens around the focus position.

From the comparison of Fig. 4-21 with Fig. 4-25, we conclude that the Fresnel lens FLI has better optical quality than FLII because its profile around the focus is sharper than that of the latter. We found an image width of 75 μm for Fresnel lens FLI and of 100 μm for FLII.

4.12 The solar Slab-Laser system

The system consists of a focusing device (Fresnel lens) and a resonator consisting of a coated slab (one side HR and one side AR) and a plane mirror as an output coupler. The laser used in this system is of type Nd:YAG Slab crystal. The crystal properties are shown in Table 4-11. The Nd:YAG slab crystal was chosen because it compensates for the thermal lensing

effect. Its shape and dimensions are shown in Fig. 4-26. It has been constructed in order to stand in the focus position on the optical bench.
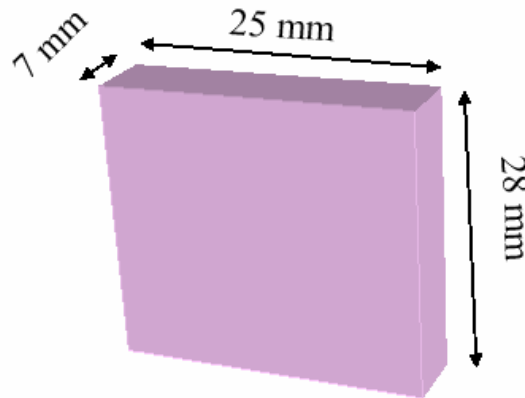
Fig. 4-26 Slab laser crystal used with its dimensions.

Property	Symbol	Value
Fluorescence of the crystal (Saturation flux)	I_s	12.5 W/mm^2
Quantum efficiency.	η_q	0.63
Overlap ratio between sun- and laser radiation	η_{ovp}	0.14
Pumping efficiency	ε	0.67
Absorption coefficient	α	0.59
Loss across the laser crystal	γ_l	2.333 $\times 10^{-3}$
Reflectivity of the output coupler	R	0.98
Threshold pumping power	P_{th}	176.138 W
Slope efficiency of the the system	η_s	0.028

Table 4-11 Optical properties of the Nd:YAG slab laser crystal.

The laser crystal was inserted into a copper holder through which the coolant (distilled water) passes. The contact between the crystal and the cooling bars provides the heat exchange needed to cool the crystal during the pumping process. Fig. 4-27 shows the crystal in the cavity placed on a holder that can be moved on an optical bench. This enables us to change the position of the whole cavity during the work if any correction is needed in the focus postion.

148
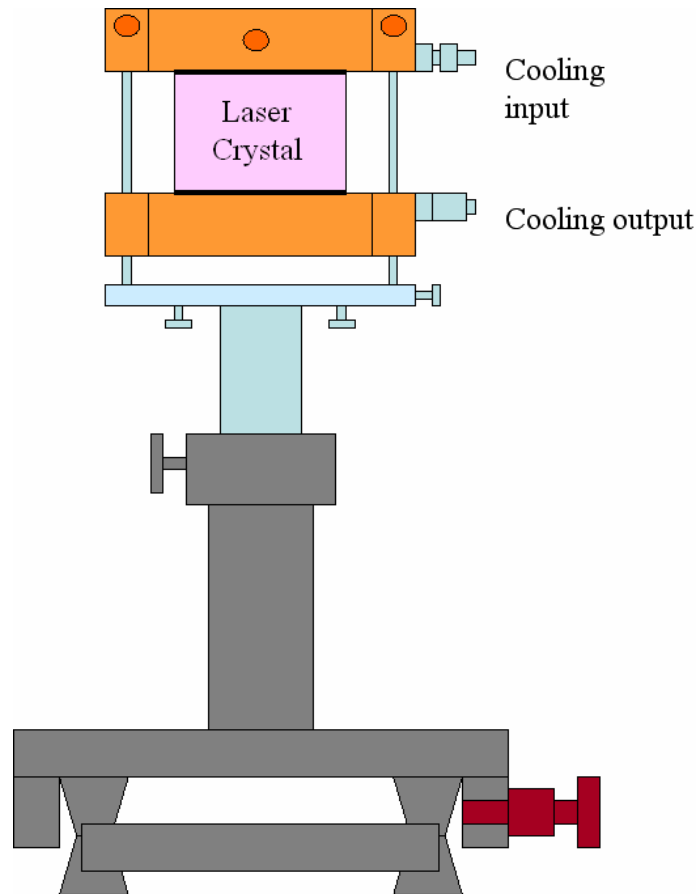
Fig. 4-27 The slab laser crystal fixed in a cooling cavity on a movable holder on the
optical bench.

An output coupler in the form of a plane mirror, coated to have a reflectivity 98 % at λ = 1064 nm, was used. With this output coupler of high reflectivity, we wanted to increase the feedback process within the laser cavity and to lower the threshold. The optical and geometrical properties of that output coupler are shown in Table 4-12.

Parameter	Symbol	Value
Reflectivity	R	0.98 / 1064 nm / 0º
Transmission	T	0.02 / 1064 nm / 0º
Diameter	D_o	25 mm
Thickness	T_o	6.5 mm

Table 4-12 Optical and geometrical properties of the output coupler.

4.13 Generating the laser in the laboratory using the diode laser crystal

The schematic of the experiment is shown in the Fig. 4-28. The pump beam is generated by a diode laser and is collimated through a cylindrical lens onto the laser crystal.

149

The resonator consists of the slab crystal, whose outer surface is coated by a HR dielectric mirror and the inner surface of the output coupler, which has a reflectivity of 98 %.
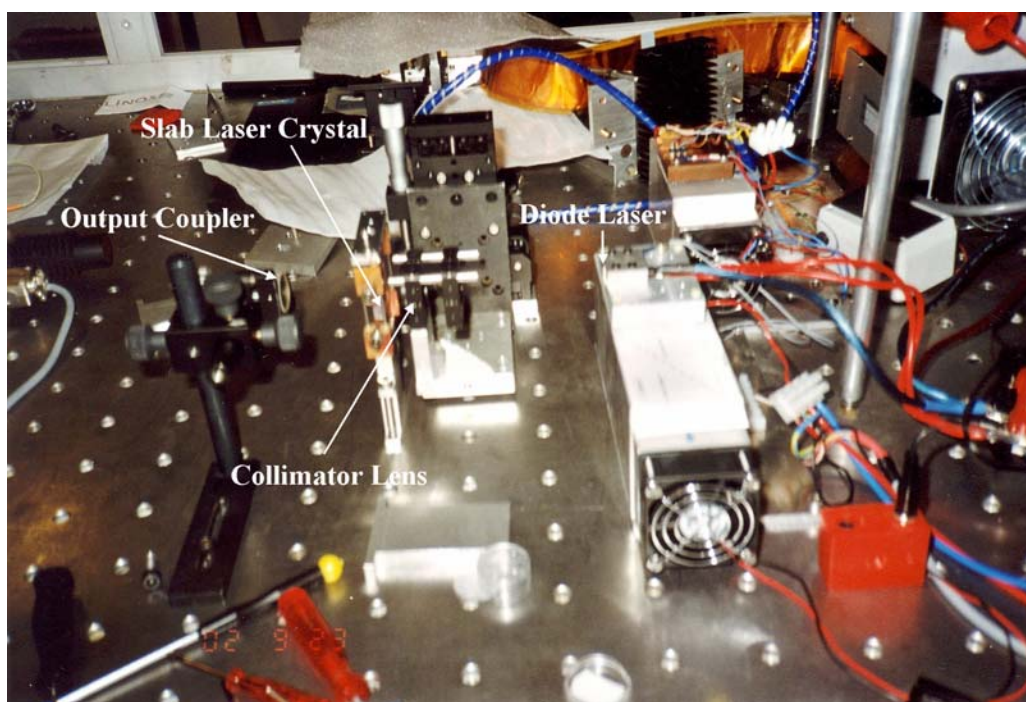
Fig 4-28 Laboratory set-up for testing the slab laser with a diode laser.

As a result of this experiment, we detected the laser on the screen and recorded it using a CCD camera. The generated laser is shown in the Fig. 4-29.
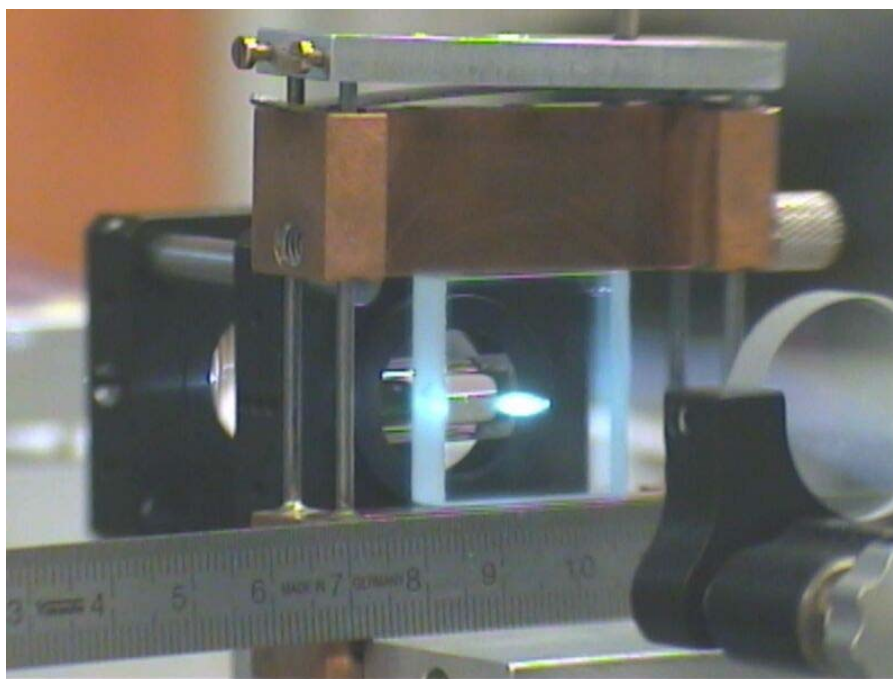
Fig. 4-29 Testing the slab laser with a diode laser.

4.14 Theoretical model for the solar laser applying the Fresnel lens on the slab laser

Using Fresnel lens FLI with the laser crystal described and with a recorded real measured solar radiation of 2.17 W (767.5 W/m^2), we had an input power of 267.14 W falling on an area of the focal length from the crystal that share in the lasing process. This means that the concentrated solar radiation intensity will be 6.8×10^6 W/m^2. After the lasing process, we found the output laser power we got from the system to be 2.552 W which can be translated into an intensity of 6.458×10^4 W/m^2 with a slope efficiency of 0.028 as described in Equation (4-2).

Applying this model to a really measured concentrated radiation during a sunny day in Berlin (Germany), we calculated the values represented in the curve shown in Fig. 4-30.
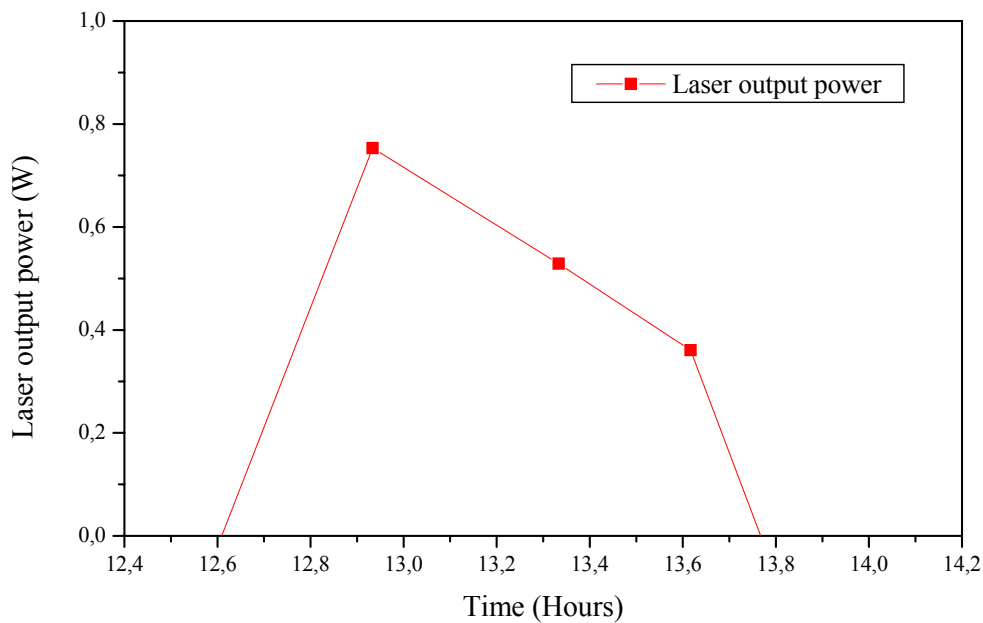
Fig. 4-30 Calculated laser output power for the solar input power during the day according to the concentrated solar radiation values measured by the Fresnel lens FLI (595 mm × 585 mm).

4.15 Adjusting the slab laser in the resonator

The slab laser and the output coupler were adjusted like a normal rod laser cavity using an optical bench. A schematic diagram of the adjusting process is shown in Fig. 4-31, while Fig. 4-32 shows a photo of this process in the laboratory from the side and from above respectively. A He-Ne pilot laser was used to adjust the slab laser system with the output coupler.
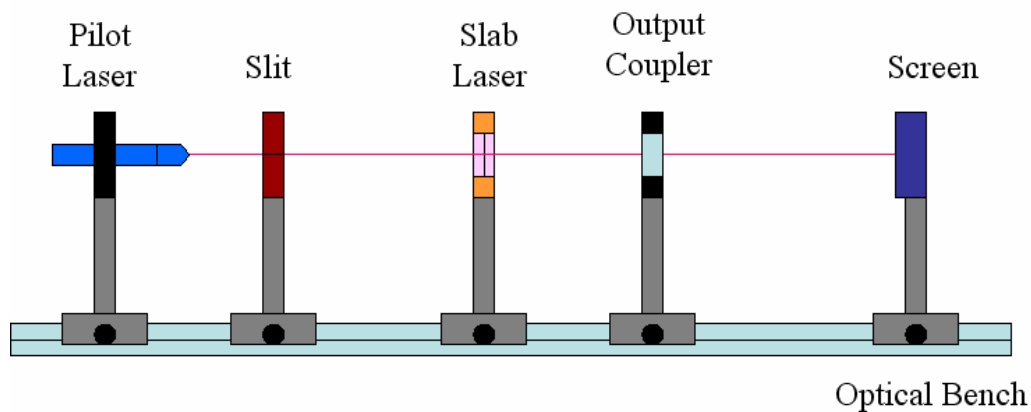
Fig. 4-31 Schematic diagram of the setup of slab laser adjustment.
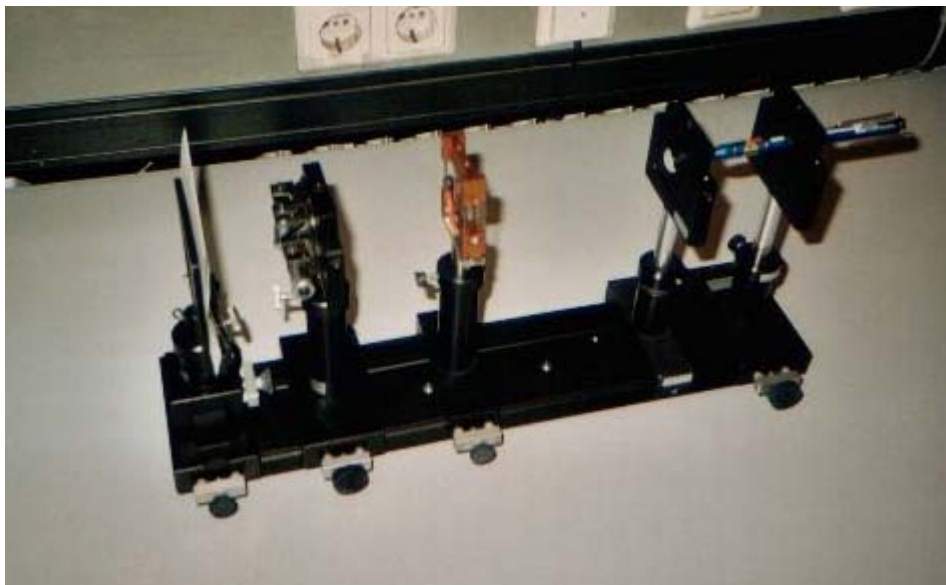
Fig. 4-32 Laser adjustment setup in the laboratory.

The laser beam of the pilot laser was transmitted through the slit, the laser crystal and the output coupler to hit the screen at one point. The reflected beams from both crystal surfaces must hit the pilot laser back at the same point. If this condition is fulfilled, the laser resonator (the copper cavity with the slab laser and the output coupler) is adjusted.

4.16 The first experiments to generate the solar laser

All system components (the resonator and Fresnel lens) were positioned on an optical bench placed on the astronomical mount. The first trials of this system have shown that the incident solar radiation power was not enough to overcome the power threshold of the laser crystal. But they also showed that the measured diameter is 12 mm instead of the calculated one of 7 mm. This means that the focus diameter will be reduced by a factor of 1.7 and the area will be reduced by a factor of 2.86.

Another reason for the power not being sufficient is the inhomogeneous distribution of the warmth on the crystal and the components. Therefore, the system was modified by adding a collimator lens in order to reach a higher level of intensity till factor 4.

Accordingly, we suggested using an additional collimating concentrator of the form of a lens. The use of this collimator lens is to reduce the focusing area of the Fresnel lens, which will therefore increase the concentration level of the whole system.

4.17 Using an additional lens as a beam collimator

According to the results of the previuos experiment, the following modifications were recommended to obtain laser action:

1- Using a collimator between the laser crystal and the Fresnel lens at the side of the HR to collimate the solar radiation on the laser crystal. This collimator could be a convex lens.
2- Using a concave mirror as an output coupler to reach a more stable resonator.
3- Decreasing the resonator length.
4- At the beginning, we used a plane HR mirror as an output coupler. It gave a very small output but a lower threshold.

The additional collimator lens was chosen to be a convex lens of diameter of 7.85 cm and with a focal length of 5 cm. A special holder was designed and constructed in the workshop to adapt it for the system. Fig. 4-33 shows the lens in its holder, while Fig. 4-34 and Fig. 4-35 show the construction of the collimator lens with the laser resonator [6, 54].
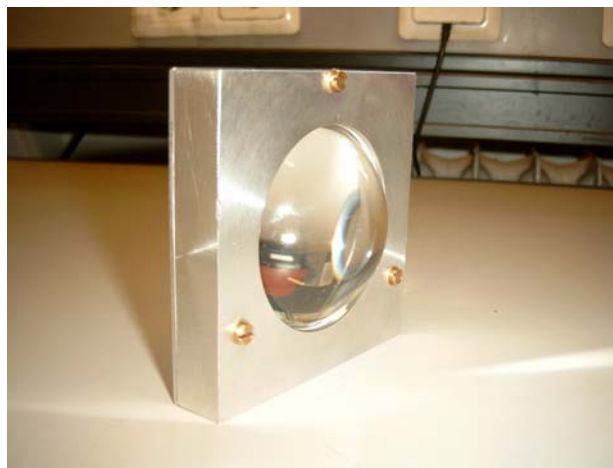
Fig. 4-33 The additional collimator lens in its holder.
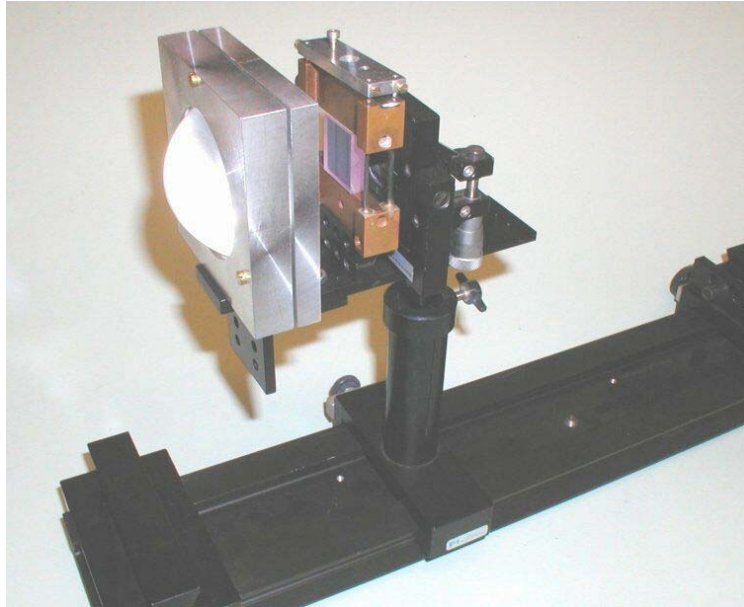
Fig. 4-34 First laser resonator with collimator lens.
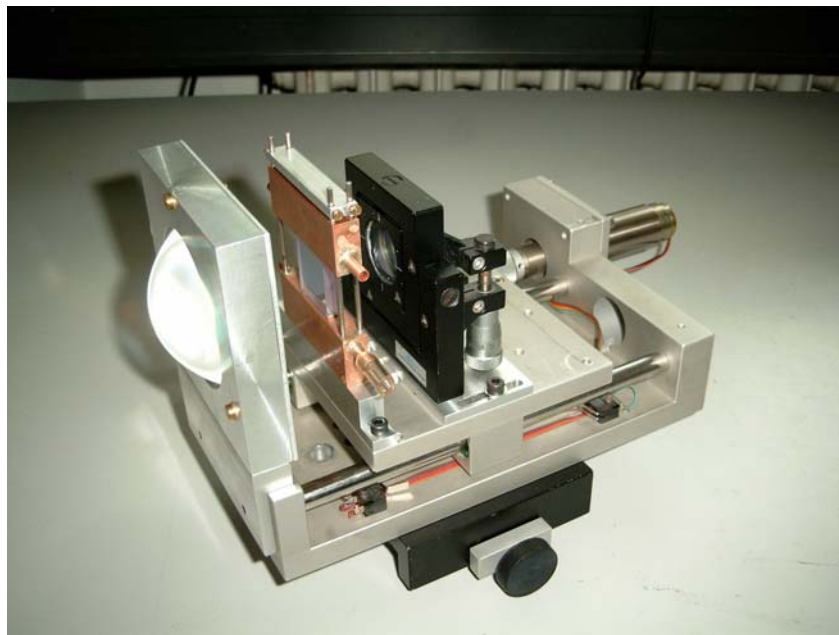
Fig. 4-35 Modified laser resonator with collimator lens.

The solar laser system after inserting the new collimator is shown in Fig. 4-36.
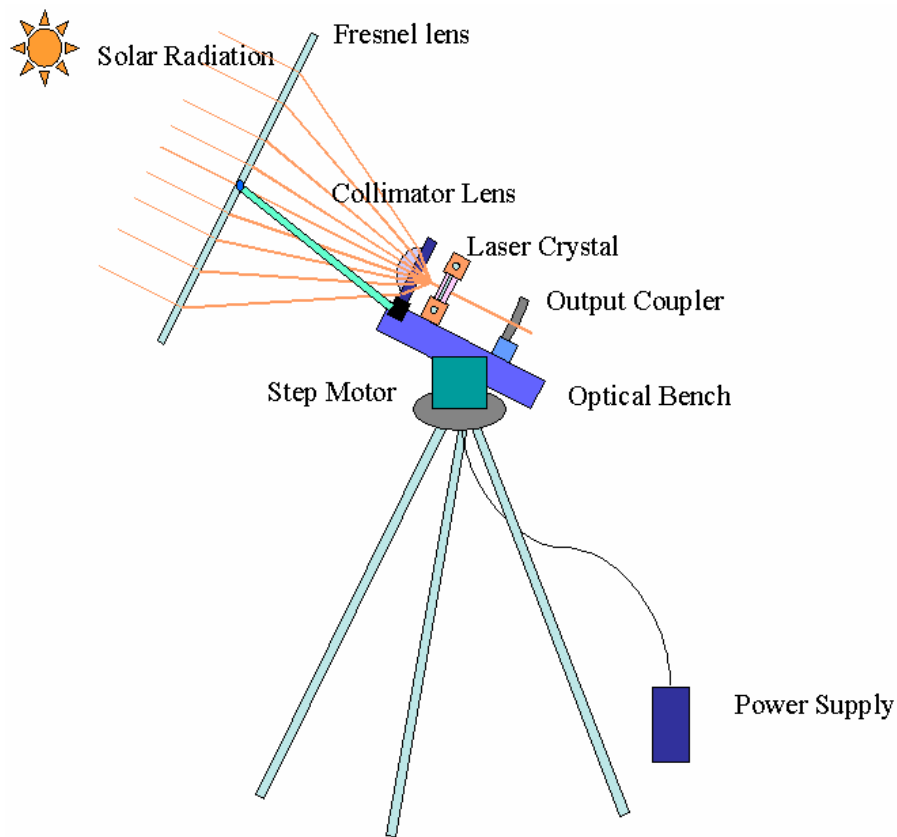
Fig. 4-36 Typical solar-pumped solid state laser with a Fresnel lens and an additional convex lens as a beam collimator fixed on an astronomical mount.

Again, we tested the two Fresnel lenses (FLI and FLII) with the new collimator using the same procedure as described in 4.7 and 4.8 to see if the additional collimator will increase the concentration value to obtain the laser action.

4.18 Testing the Fresnel lens FLI (595 mm × 585 mm) with a collimator lens

We tested the laser setup using the additional lens concentrator. The focus diameter did not decrease sufficiently to obtain the laser action. The setup of this experiment is shown in Fig. 4-37, while the photo of the resulted focus of the whole system is shown in Fig. 4-38.
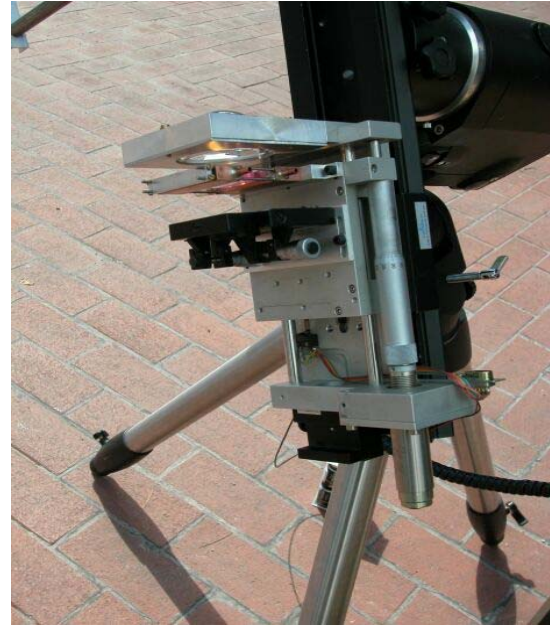
Fig. 4-37 The setup of testing the Fresnel lens FLI (595 mm × 585 mm).
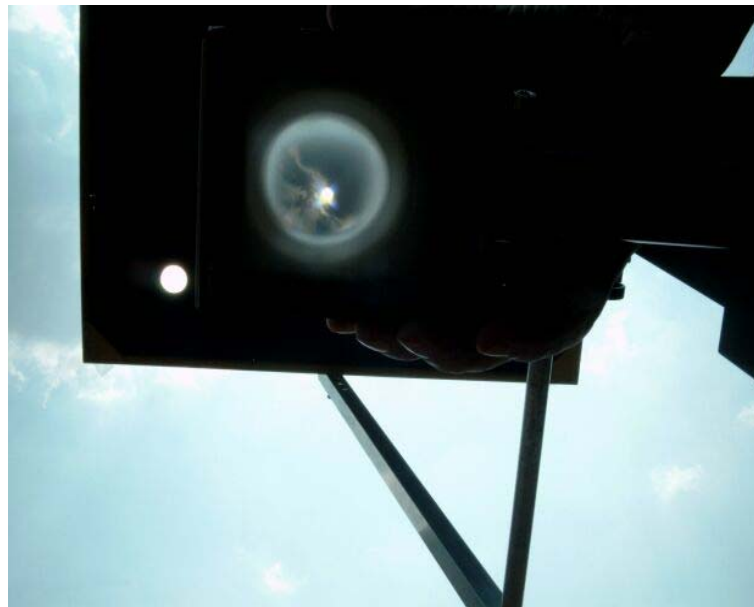
Fig. 4-38 Focus of the combination of the Fresnel lens FLI (595 mm × 585 mm) and the additional collimator lens.

4.19 Testing the Fresnel lens FLII (1035 mm × 795) mm with a collimator lens

Regarding the mounting of the system of the mountainer with the Fresnel lens FLII, a collimator lens (D = 60 mm, f = 5 cm) was added to improve the quality of the resultant focus. The setup of this experiment is shown in Fig 4-39, while the photos of the resultant focus made by the lens combination are shown in Fig. 4-40.
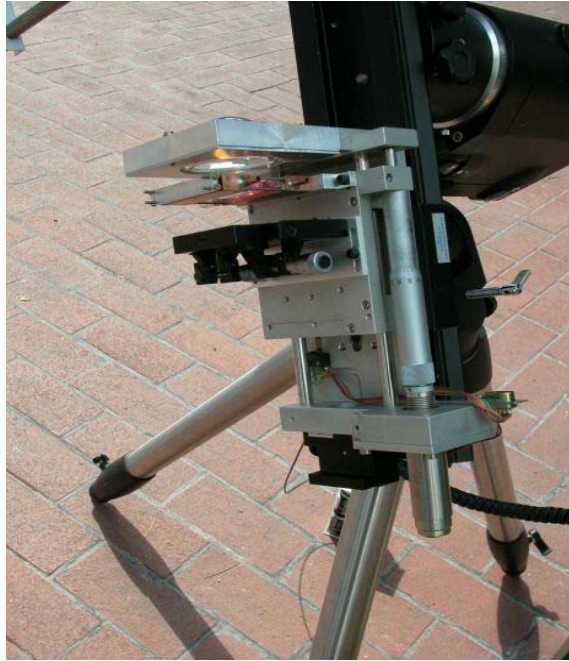
Fig. 4-39 The setup for testing the Fresnel lens (1035 mm × 795 mm).

Fig. 4-40 Focus of the combination of the Fresnel lens (1035 mm × 795 mm) and the additional collimator lens.

4.20 The improved laser set-up

In order to improve the concentration ratio, we considerably changed the design of the system:

1- End pumping was replaced by side pumping.

2- The secondary imaging concentrator was replaced by a non-imaging concentrator.

3- The dimension of the active laser volume was decreased.

4- The Nd:YAG laser material was replaced by Nd:YVO$_4$, because of its lower pumping threshold.

4.20.1 Design of a side pumped cavity for direct solar pumping

From the known non-imaging concentrators suitable for side-pumping the Trough Concentrator (TC) and the Compound Parabolic Concentrator (CPC) have been taken into consideration. Additionally, a new type of concentrator has been devised using special surfaces as boundaries. All concentrators have the property of distributing the light more evenly over the active medium, therefore decreasing the danger of local overheating.

Manufactory, the concentrator from solid bulk material (e.g. glass) rather than using highly reflecting curved surfaces has further advantages:

1- Rays are reflected due to the total reflectivity of the boundary surfaces.

2- The acceptance angle of the concentrator is increased proportionally to the index of refraction of the bulk material.

The compound parabolic concentrator is optimally adapted to the task using the existing primary concentrators FLI and FLII. However, it is very difficult to manufacture this type of non-imaging concentrator due to its unusual surfaces.

Although easier to manufacture, the trough concentrator has a much lower acceptance angle compared to a CPC and – as is shown below – as a CSC.

The Compound Spherical Concentrator (CSC) combines the advantages of a CPC with ease of production. It consists of spherical boundaries and can be manufactured from thick glass lenses from which segments are cut as shown in Fig. 4-41. Several CSC's can be cut from a single lens where only the plane cuts have to be polished. Such a concentrator is much easier to obtain than a CPC and has only slightly worse properties.

(a)   (b)   (c)
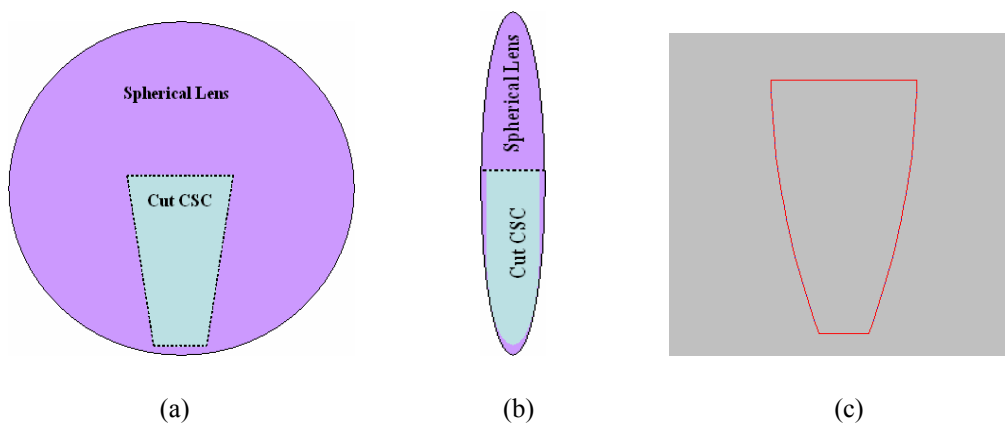
Fig. 4-41 Compound Spherical Concentrator (CSC) cut from a thick glass lens.

The schematic design of a side pumped laser system consists of a primary Fresnel lens as a primary concentrator, a secondary Compound Spherical Concentrator (CSC) and a water-cooled ceramic cavity in which a Nd:YVO$_4$ laser rod of 12 mm long and 1.5 mm diameter as the active medium to be inserted.

The CSC concentrator has been cut out of a BK7 glass lens which has an index of refraction of 1.52. We designed this CSC concentrator with dimensions which match the dimensions of the laser rod (length: 12 mm, diameter: 1.5 mm, radius of curvature: 100 mm) with the image produced by the Fresnel lens using a ray trace programme (WinLens). It was then cut from an appropriate lens with the help of the optical workshop of the Institute of Optics of the Technical University of Berlin. The concentrator has a height of 2.7 cm, upper aperture dimensions of 1.5 cm × 1.35 cm and lower aperture dimensions of 0.5 cm × 1.5 cm. Such a concentrator has a geometrical concentration ratio (according to area ratio) of 3.24.

As mentioned above, the CSC concentrator has some curvature in going from the upper aperture to the lower one in order to get the depth of the lower area smaller than that of the upper one. This means that the area of the lower aperture will be modified to be 0.5 cm × 1.1 cm. Accordingly, the geometrical concentration ratio will be changed to be 3.68. This value of concentration ratio is more promising for increase the concentration level of the whole system in order to overcome the threshold pumping power of the laser.

The Nd:YVO$_4$ laser rod used in our work is shown in Fig. 4-42, the accordingly designed glass Compound Spherical Concentrator with its dimensions is shown in Fig. 4-43 and a photo of that concentrator is shown in Fig 4-44.

Fig. 4-42 Laser rod of Nd:YVO$_4$ type.
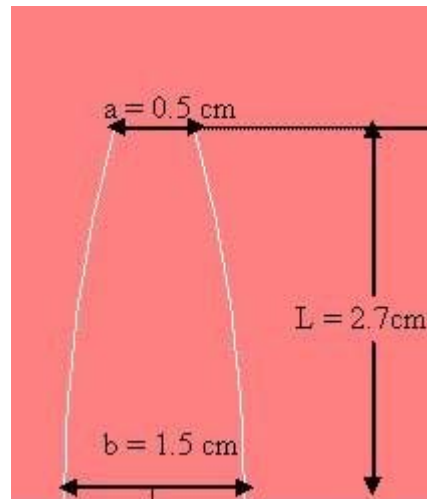
Fig. 4-43 The CSC concentrator with it dimensions.
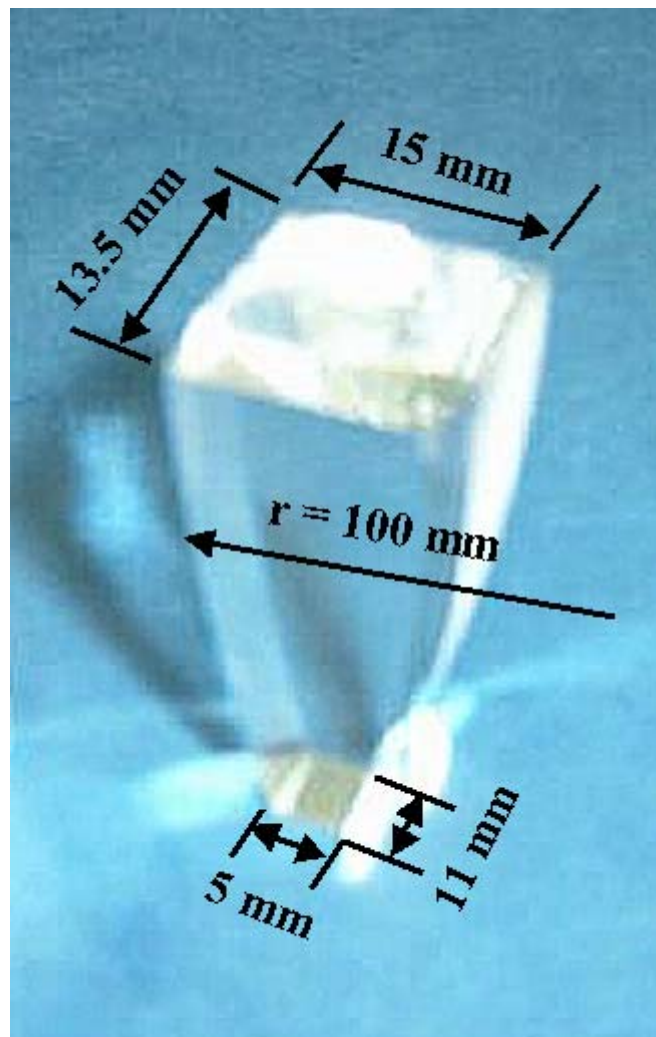
Fig. 4-44 Glass Compound Spherical Concentrator (CSC).

4.21 Testing the Compound Spherical Concentrator (CSC)

We tested the quality of the Compound Spherical Concentrator (CSC) for concentrating the light. We measured the maximum concentration ratio experimentally and the limits at which that concentrator fails to concentrate.

Using a normal light of an office lamp (Elux) 230 V, 60 W as a light source, a Silicon photo-detector and a current meter (Voltcraft M-4630) as a measuring unit, we tested the behaviour of the concentration ratio of the Glass Compound Spherical Concentrator (CSC) as a function of the incidence angle of the light. The distance between the light source (the lamp) and the detector was 38 cm.

We measured the current of the photocell without and with the concentrator in steps between 0º and ±40º (± means the direction of the angle of incidence). A photo of this experiment is shown in Fig 4-45, while the recorded data are represented in the diagram shown in Fig. 4-46.

The results showed a relatively high concentration ratio of 4 at normal incidence, while they showed a drop in value for the larger angles of ±30º. It could be interpreted in the following terms:

1- The reflection of the planar entry and exit surfaces of the CSC is strongly increasing with the transmission angle.

2- At large transmission angles, many incident light trajectories will be reflected in such a way that they exit the concentrator at the entrance plane.

3- The incidence angle inside the CSC is decreasing with increasing the transmission angle. Therefore, some parts of the side surfaces will no longer exhibit total reflection.
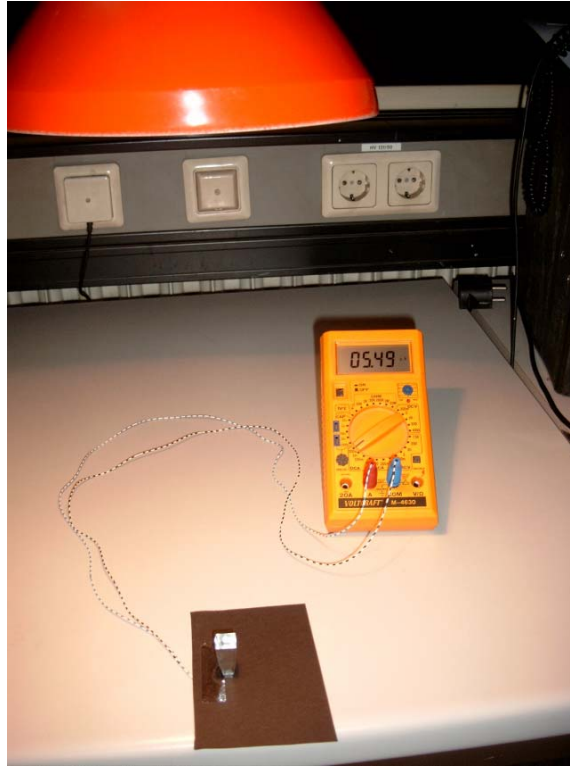
Fig. 4-45 Testing the CSC concentrator using a Si-photodetector.
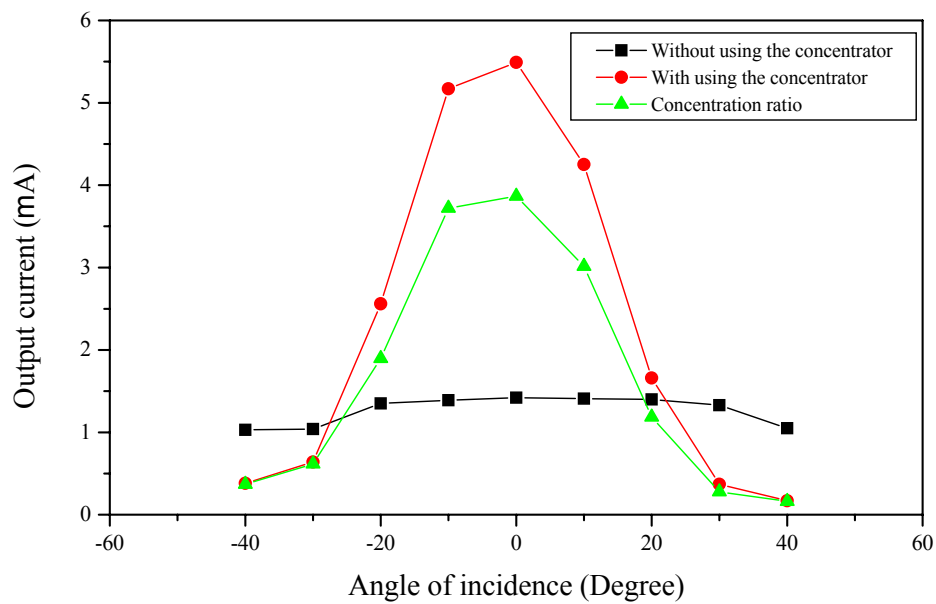
Fig. 4-46 The behaviour of the concentration ratio of the Glass Compound Spherical Concentrator (CSC).

The previous reasons get the given concentrator out of use outside the interval of angle of incident –30º and +30º. It may be preferred to use the concentrator even within the interval of angle of incidence –20º and +20º the best cases of the concentration. Outside this range,

the concentrator will not work any more. Moreover, it will attenuate the radiation needed to be concentrated.

4.22 Design of the laser cavity

To adapt the laser rod (length: 12 mm, diameter: 1.5 mm) to the concentrator, we put the laser into a cavity that has the following properties:

1- A high melting point to avoid damaging from the highly concentrated solar radiation during the operation.

2- The dimensions of the secondary concentrator (CSC) are adapted to the shape of the laser rod and the rim angle of the Fresnel lens.

We chose a special type of ceramic as material for the design of the cavity. It is able withstand very high temperatures (up to 2000 °C), has a very high reflectivity and can be easily machined.

We designed the cavity and it was machined in the mecahnical workshop of the Technical University of Berlin. Fig. 4-47 shows a top and front view of the ceramic cavity, while Fig. 4-48 shows its photo. Two holes (3 mm diameter) beside the hole of the laser rod were designed in order to allow the coolant (destilled water) to pass to and out from the laser room. The concentrated solar radiations reach the sides of the laser rod through a window covered by a thin glass plate, fixed using a two-component-glue (epoxy). On the other end of the cavity, a front alumimium plate was used to press a rubber plate which fixes the laser rod in its hole and protects the coolant (destilled water) from going out of the cavity.

(a)   (b)
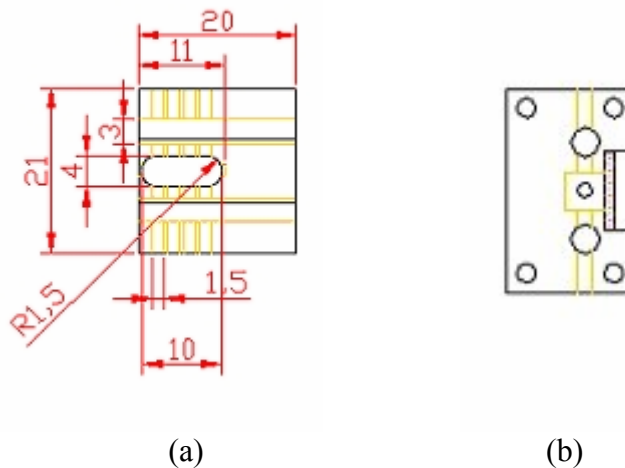
Fig. 4-47 Top and front view of the ceramic cavity.

Fig. 4-48 Ceramic laser cavity.

To fix the concentrator upon the cavity, two additional lateral support plates have been added as shown in the Fig. 4-49. Pictures of the ceramic cavity with its two supporting glass plates are shown in Fig. 4-50.
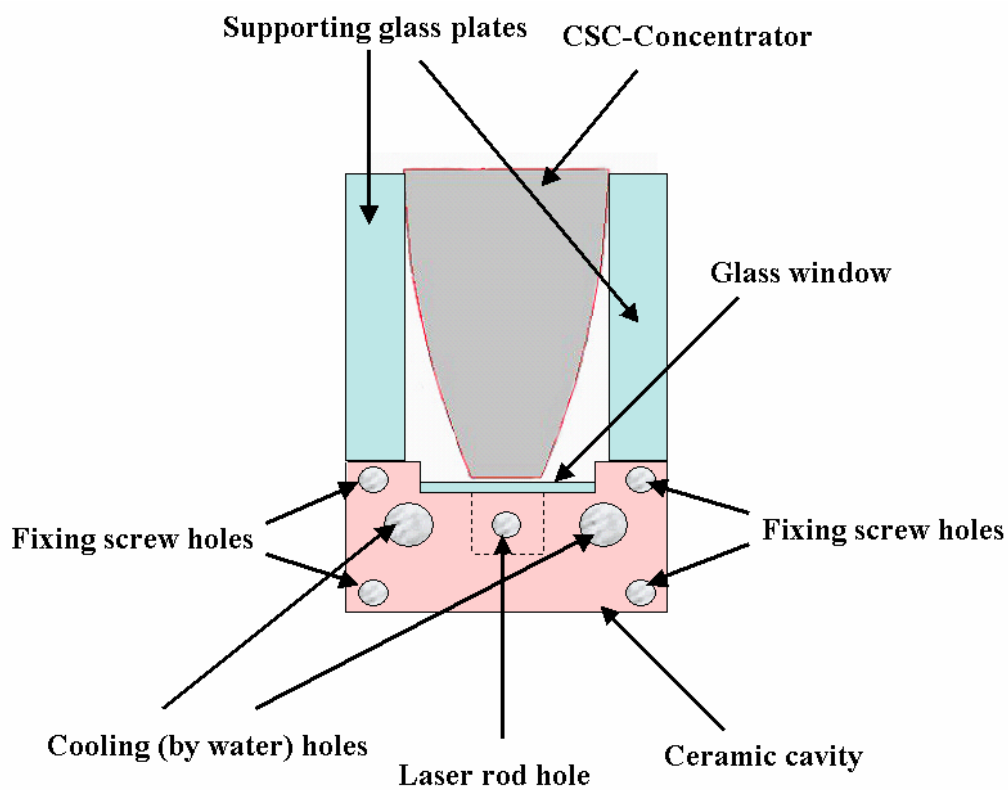
Fig. 4-49 Schematic diagram for the CSC-concentrator with the ceramic cavity.

164

<div align="center">(a)</div> <div align="center">(b)</div>
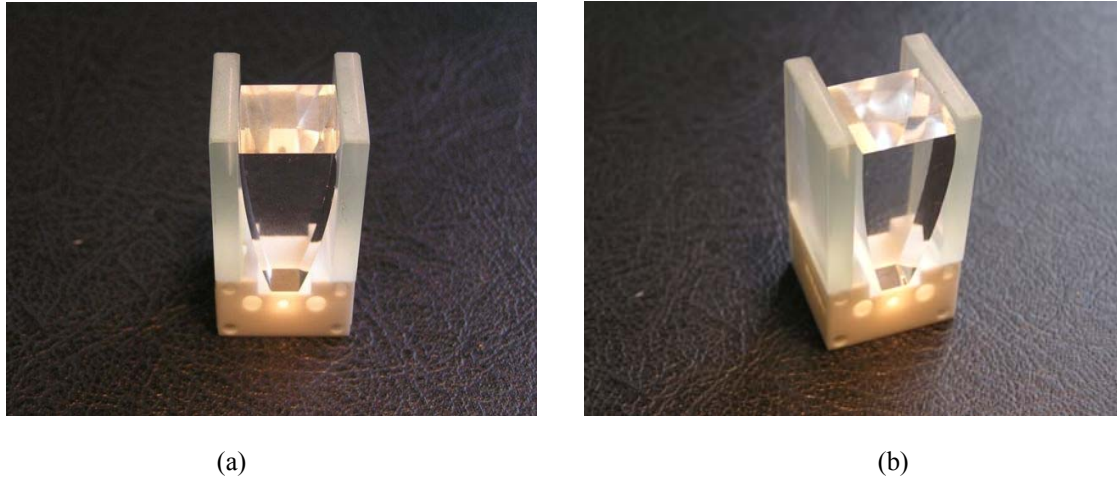
<div align="center">Fig. 4-50 CSC-concentrator fixed on the ceramic laser cavity.</div>

The compound spherical concentrator (CSC) was fixed on the glass plate that was constructed on the laser window. The concentrator is strongly fixed during the rotation of the optical bench, because of tracking the sun during the day, by the two supporting glass plates on either sides of the ceramic cavity. We tried to use a Teflon U-Profile with plastic screw that presses it to prevent it from slipping out.

Finally, the CSC was clamped to the above described ceramic cavity by a special device made from PMMA. Fig. 4-51 shows a schematic design of the ceramic cavity with the CSC clamped together, while Fig 4-52 shows its photos from different sides.
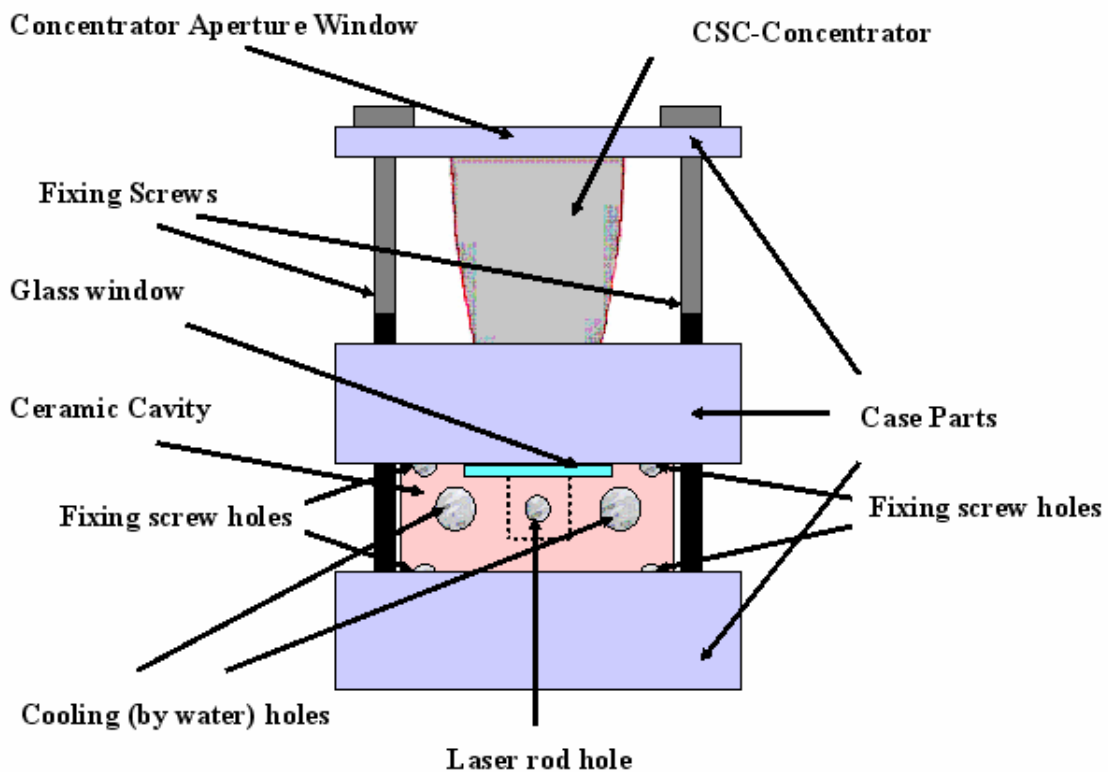
<div align="center">Fig. 4-51 Schematic diagram of the system of laser cavity and CSC-concentrator
fixed with a case.</div>
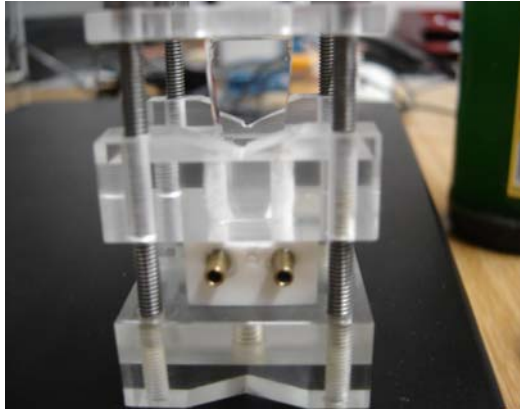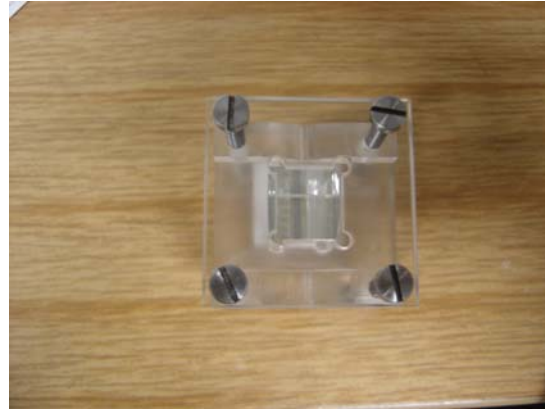
<center>(a)</center>   <center>(b)</center>
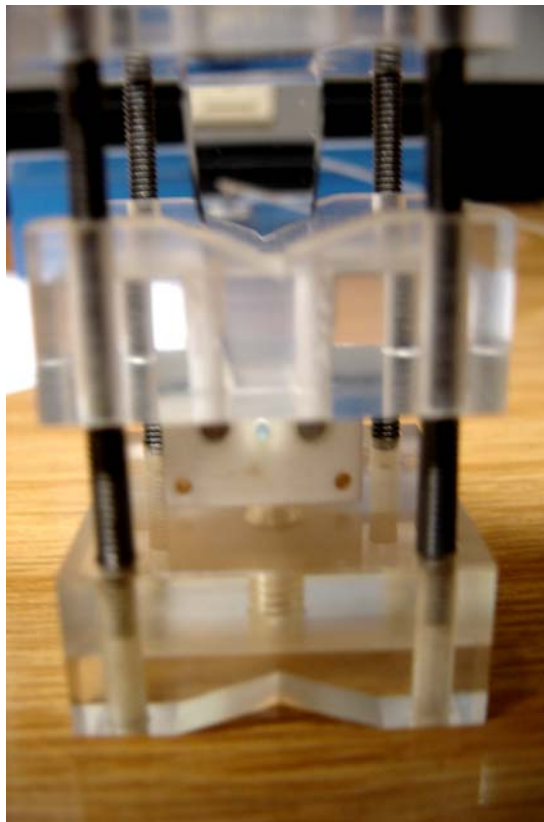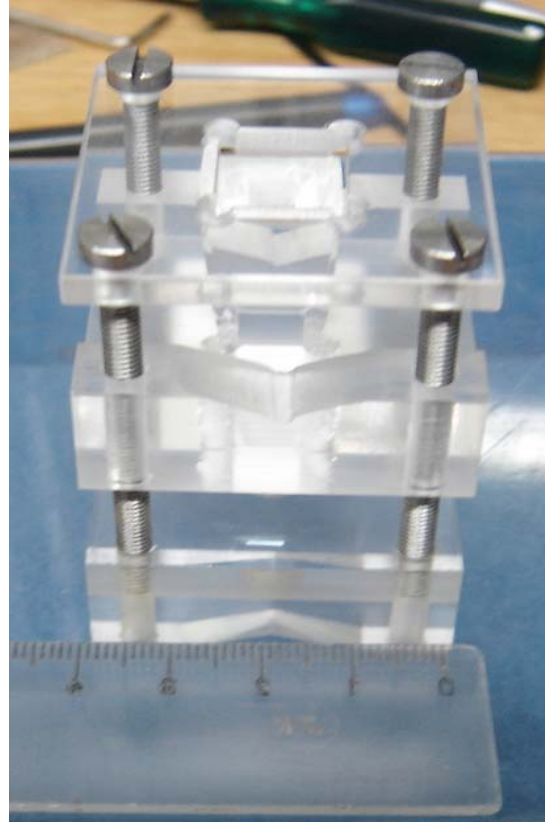
<center>(c)</center>   <center>(d)</center>

<center>Fig. 4-52 Laser cavity and CSC-concentrator fixed with a case.</center>

As an extension of this work, we have designed another CSC-Concentrator with a tubular hole as the role of the cavity. The idea of this hole comes from studying the path of the reflected rays inside the lens from which the CSC-concentrator is cut as shown in Fig. 4-53. The position of this hole will be chosen in the position of collection of the radiation. One can insert the laser rod through the hole without the need of any laser cavity. Fig. 4-54 shows the construction of this concentrator in comparing with the previously mentioned one, while Fig. 4-55 shows its photo.
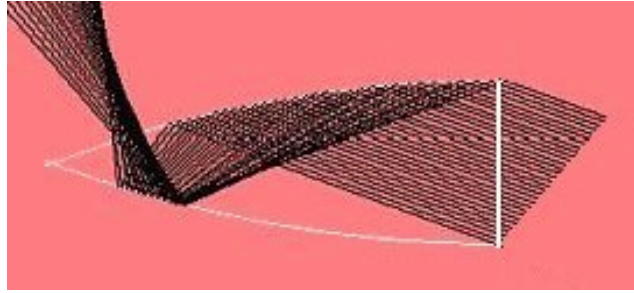
Fig. 5-53 The path of the internal reflected rays (from right to left) inside the lens
from which the CSC-concentrator is cut.
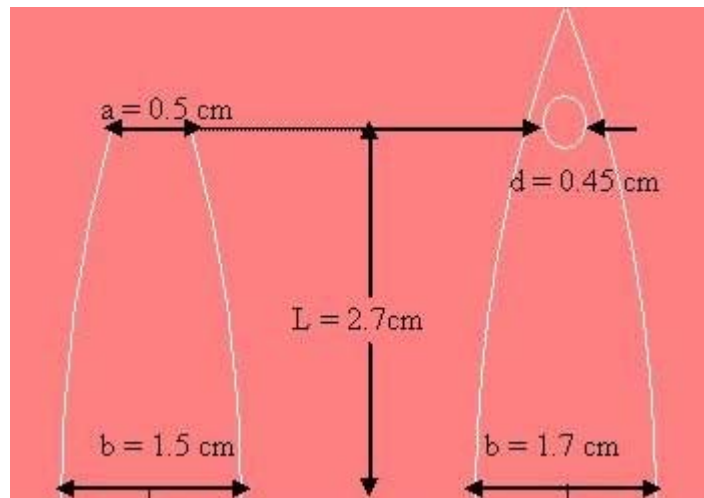
Fig. 4-54 Design of two types of CSC-concentrators; the first one is with a flat output
aperture and the second one is with a tubular hole.

Fig. 4-55 CSC-concentrators with a tubular hole.

4.23 The cooling system

We used a cooling system consisting of a reservoir and a stainless steel gear pump, which circulated the cooling liquid (destilled water) through the laser cavity. Fig. 4-56 shows the used cooling system.
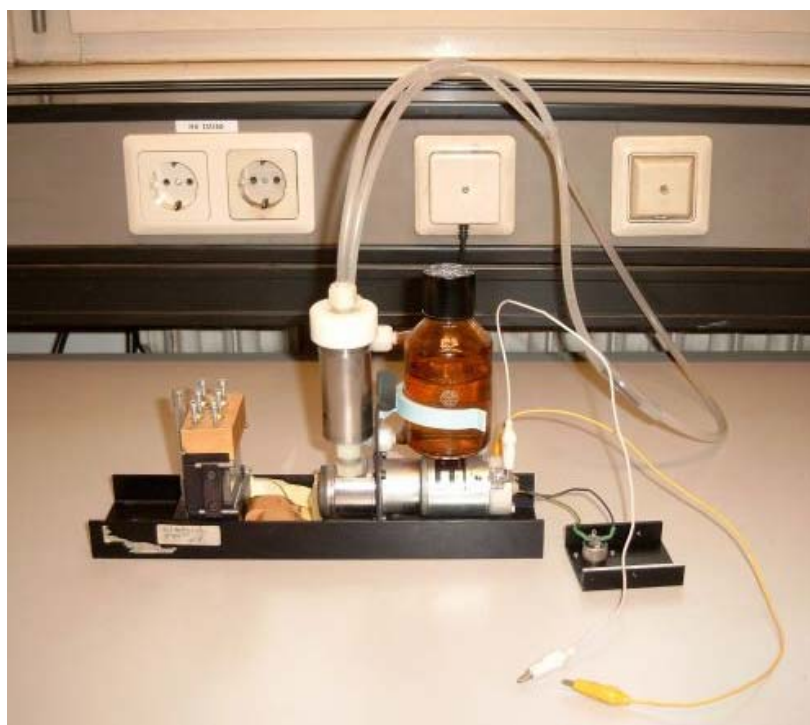
Fig. 4-56 Cooling system used to cool the laser cavity.

4.24 Testing the laser rod in the laboratory

As mentioned before, the laser rod is of the type Nd:YVO$_4$. Early spectroscopy and laser studies show that Nd:YVO$_4$ is an excellent laser crystal with high cross-section for stimulated emission. For example, the laser emission cross-sections of Nd:YVO$_4$ crystal at 1.06 μm and 1.34 μm are 2.7 and 18 times larger than that in Nd:YAG respectively. The crystal has good mechanical, physical and chemical properties. However, the difficulties to grow a crystal with high optical quality hinder its application. In recent years much attention has been paid to the crystal again, after some of the difficulties have been overcome in crystal growth. Nd:YVO$_4$ crystal has been used as an excellent laser material pumped by laser diodes for Nd:YVO$_4$ crystal allows doping with higher neodymium concentration and has larger absorption coefficient than Nd:YAG crystal. The length of Nd:YVO$_4$ crystal in lasers can be reduced greatly because of its advantages. Nd:YVO$_4$ crystal can produce cw laser radiation at 1.06 μm and 1.34 μm and can be pumped at 808 nm. Because the Nd:YVO$_4$ crystal has large thermal conductivity, it may be used in higher power laser systems. Nd:YVO$_4$ crystal can also produce cw green laser at 532 nm when nonlinear crystals such as KTP or LBO are used, the output power at 532 nm has reached 7 W just recently.

168

The laser rod used was coated in the laboratory with 21 layers in order to get one side high reflective (HR) and the other one is antireflective (AR). Fig. 4-57 shows the measured transmission through the laser rod against the wavelengths. One can see that the rod with its coating layers has no transmission at the wavelength between 1000 nm and 1100 nm.
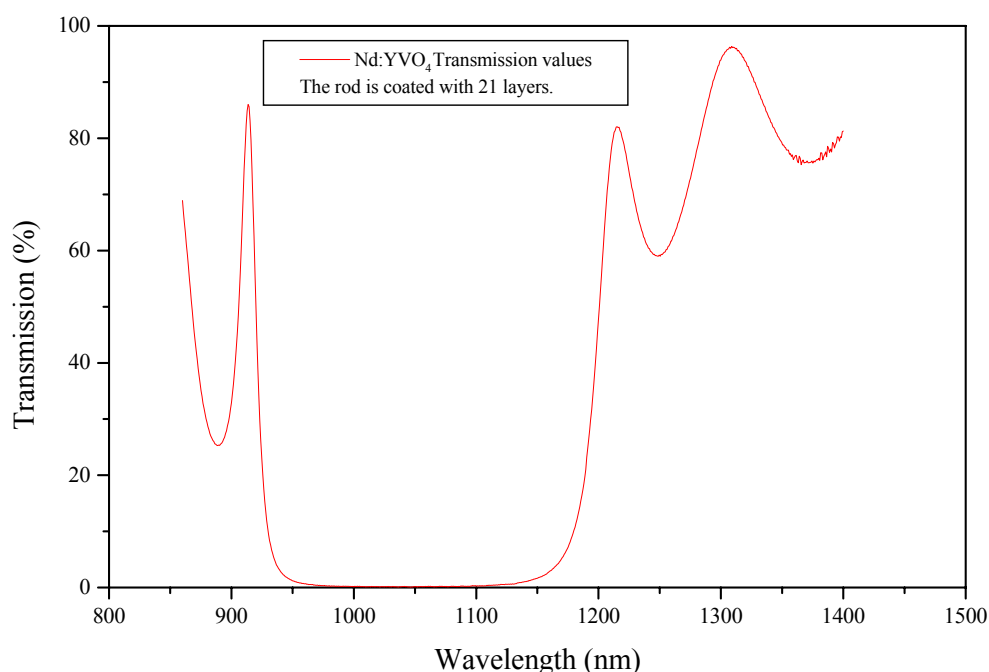
Fig. 4-57 Transmission through the $Nd:YVO_4$ laser rod against the wavelength.

The laser rod was tested and adjusted its cavity in the laboratory using a diode laser to see the effect of the CSC-Concentrator on the laser output. Therefore, two types of data were recorded; the output power without the concentrator and with it. Fig. 4-58 shows the laser cavity with the CSC-Concentrator built in the complete testing setup from its side and from above, while Fig. 4-59 shows a graphical representation of the test data for both cases. Laser output of 10 mW has been obtained using an input power of 650 mW from a laser diode (808nm).
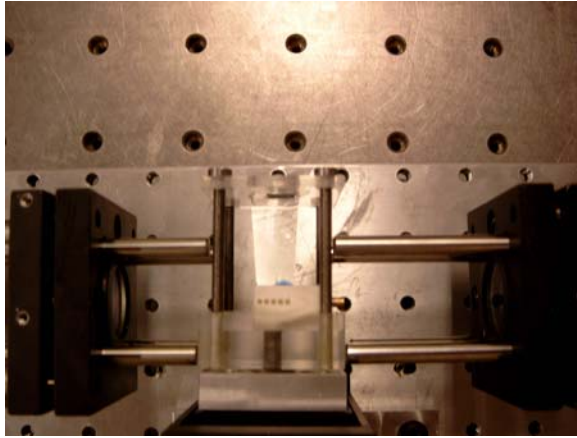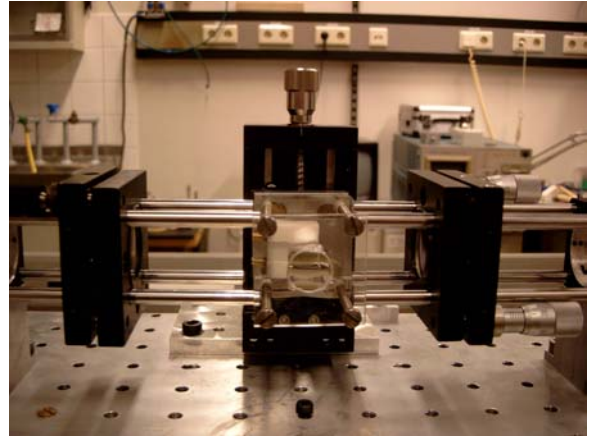
(a)   (b)

Fig. 4-58 The laser cavity with the CSC-concentrator built in the complete testing setup
(a) from its side and (b) from above.
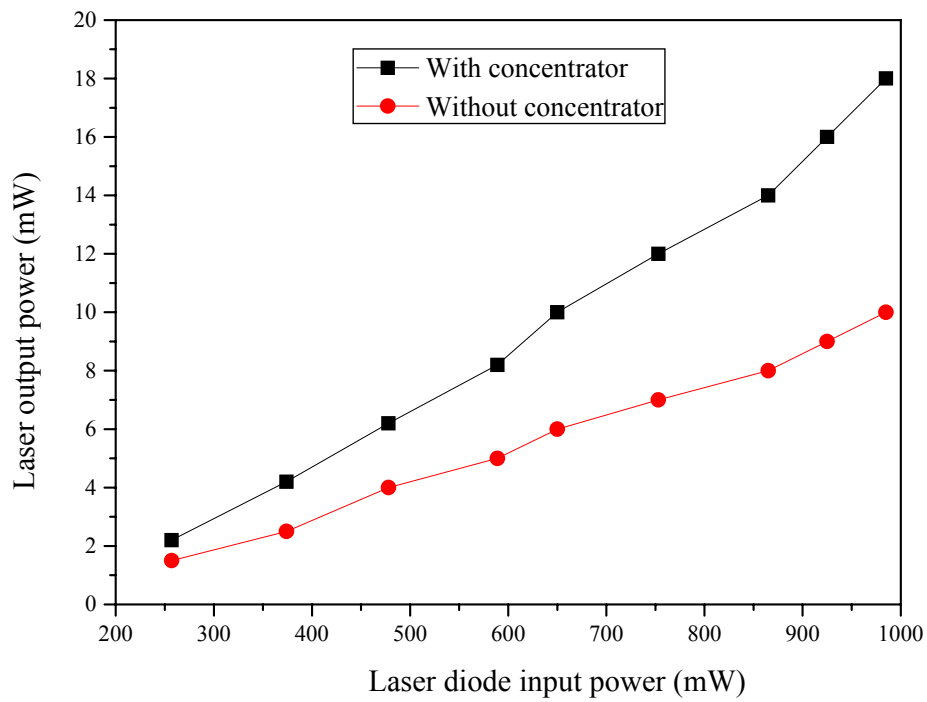
Fig. 4-59 Output power of Nd:YVO$_4$ laser rod (length = 12 mm and diameter = 1.5 mm)
pumped by a diode laser (λ=808 nm) with pulse duration of 19 ms and a frequency of
50 Hz.

Chapter 5: Fixed mounted solar laser system using adaptive mirrors

Overview

In this chapter, a new concentrator using adaptive mirrors is described. The system consists of a mirror array which tracks the sun during the day in order to keep the focus fixed in the same position. The tracking process is achieved by changing the angles of the mirrors using mechanical transmission and electrical motors, which are controlled by a computer programme. Additionally, we used a Fresnel lens to further increase the concentration level of the whole system.

5.1 Introduction

The typical solar-pumped-laser systems of intermediate output power are so far in most cases based on the idea of using large concentration devices like large parabolic mirrors or spherical lenses. These systems are massive, stationary and extremely expensive. Therefore, we wanted in this work to introduce a new idea for new solar-pumped-laser systems, which are easy to be constructed, transported and inexpensive.

Solar lasers developed so far have been using large (and heavy) mirror systems for concentration of the solar radiation. These systems are stationary and cannot be moved to different locations; most applications of solar pumped lasers should however be movable. We have therefore devised a system of small mirrors which focuses the solar radiation onto a target held in a fixed position with respect to the ground. The best performance would be obtained if the normal vector of each mirror would be pointed to an angle bisecting the fixed direction of the laser system and the time dependent direction of the sun. This would involve a complicated drive for each mirror (similar to those used in mirror fields of solar towers). As the angular speed of the sun is constant, the angular speed of all mirrors around the "vertical" axis is constant at half the sun's angular speed, when the target (the laser system) is positioned in the plane given by the rotation of the sun, i.e. the "vertical" rotational axis of the mirror system is parallel to the rotational axis of the earth. If this is not the case the angular speed of the mirror rotation is maximal at noon and decreases with time difference to noon. If the target is positioned outside that plane the angular speed around the "vertical" axis is not constant. It has maximum speed around noon and decreases towards morning and afternoon.

The idea is to use a mirror array system to provide the pump light for a solar laser which comes from what is called the central receiver concentrator, in which many mirrors would be placed at different angles to reflect the solar radiation onto a single point. Therefore, we will use the term focus or resultant focus to describe the complete overlap of all single mirror images. Theoretically, the area of that resultant focus equals approximately the area of the single mirror corrected for the finite size of the solar disc. Practically, we have a slightly larger image (resultant focus) depending on the distance chosen for the focus. Fig. 5-1 shows a schematic design of a solar pumped laser using a solar tower that depends on the idea of the central receiver concentrator theory [2, 5, 6, 30, 54, 55, 57].
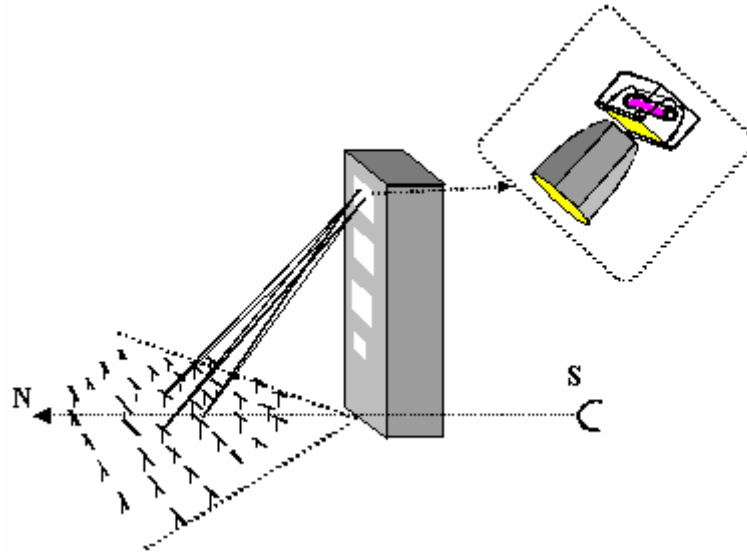
Fig. 5-1 Schematic design of a typical solar tower used to pump the laser.

5.2 Stationary mirror array system for the solar-pumped-laser system

Theoretically, it may be easier to construct a stationary mirror array system than a system with a large concentrator (mirror or lens) because of the manufacturing difficulties, large costs, controlling and adjustment difficulties. It is obvious that all of the reflected radiation by the array would not remain coincident at the same position during the day and accordingly during the year's seasons as well. We tried to find out how far this uncoincidence is. If the reflected images deviate without separating totally, then one can put the laser cavity in the place where the images of each single mirror always have overlap. But if the deviation is so large that the images separate totally, then we have to think of a way to keep them in the same place. Y. Chen et al. designed a non-imaging focusing mirror array (heliostat) for effective use of thermal solar energy [57]. Fig. 5-2 shows the mirror array reflecting and focusing the solar radiation into a single image that be considered as the resultant focus of the system.
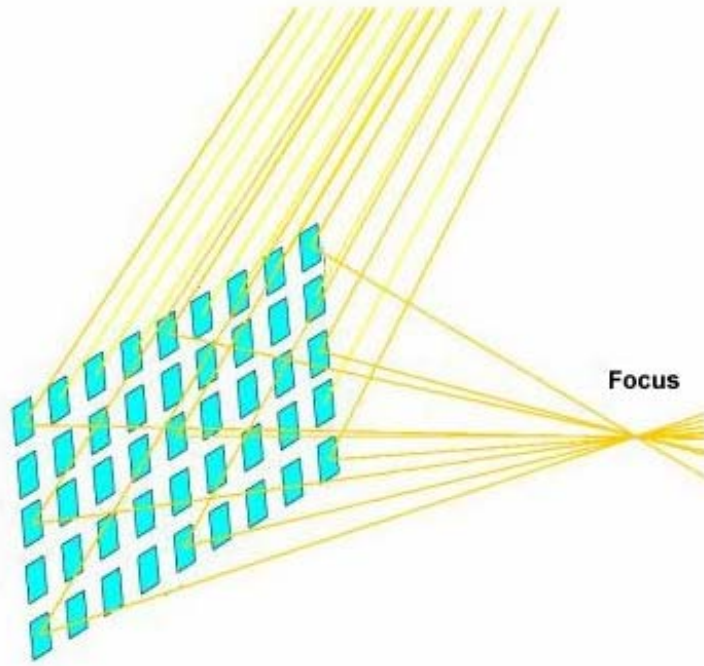
Fig. 5-2 A schematic representation of a mirror array reflecting the solar radiation into a focus.

We developed a programme with (MathCad 2000) to estimate the positions of the images as a function of time. In this programme, we used the following parameters:

1- The position of the system at the Technical University of Berlin in Germany.
2- Mirror dimensions.
3- The distance between each two mirrors.
4- The desired resultant focal length of the array.

Table 5-1 shows the values of these parameters for this case.

Parameter	Symbol	Value
Position	φ, λ	Berlin (Latitude $\varphi = 52.53$, Longitude $\lambda = 13.58$)
Mirror dimensions	d_d	15 cm × 15 cm
The horizontal distance between each two mirrors	d_m	23 cm
The resultant "focal" length	f	3 m

Table 5-1 The values of the parameters used in the simulation of a static mirror array system.

Firstly, we considered that a system of 3 rows and 7 columns of fixed mirrors with the dimensions given in the Table 5-1. The directions of the mirrors were chosen in such a way that maximum overlap would occur at the noon. According to a simulation programme based on calculation of the solar positions during the day astronomically, the curves of Fig. 5-3 for the vertical component of the motion of the sun's image (in the direction of the altitude), and

173

that of Fig. 5-4 for the horizontal component of the motion of the sun (in the direction of the azimuth) were calculated.
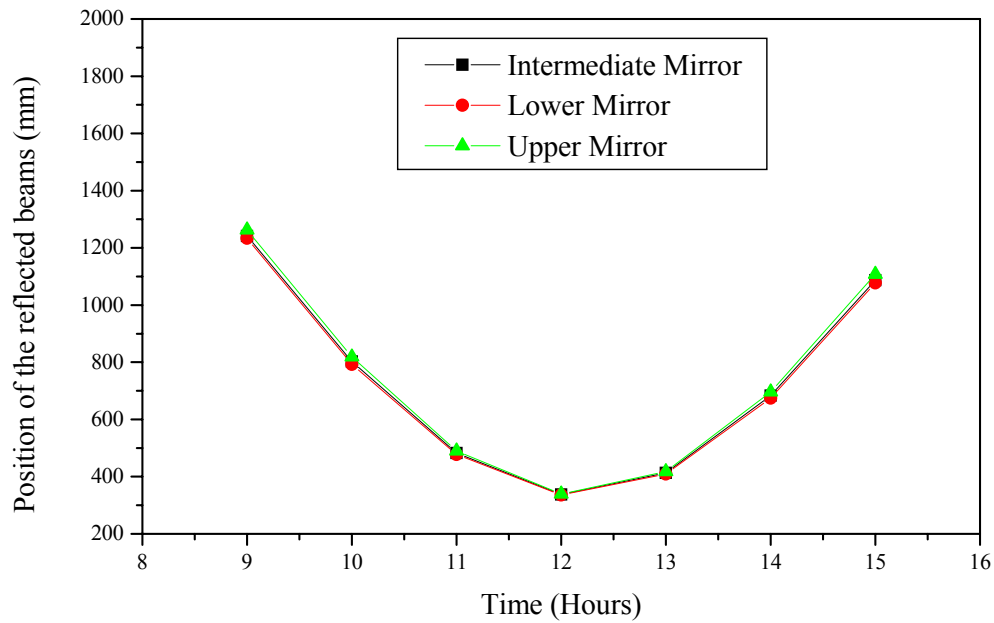
Fig. 5-3 The vertical positions of the images obtained by the mirrors of the central receiver concentrator. The mirrors are positioned such that they are optimized for the true noon point.
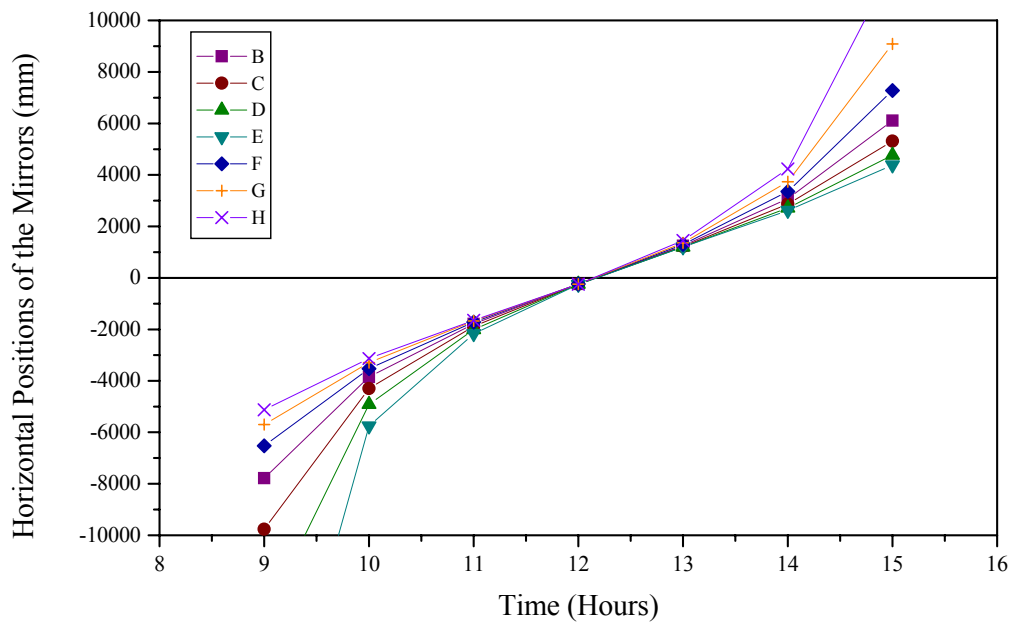
Fig. 5-4 The horizontal positions of the images obtained by the mirrors of the central receiver concentrator. The mirrors are positioned such that they are optimized for the true noon point.

174

After there, we designed a model for calculating the vertical and the horizontal deviation of an array consisting of 9 mirrors and controlled by two motors for the vertical and the horizontal motions. In this model, we tried to find out correction factors for the deviation in both directions in order to find optimum adjusting angle in which the system should be directed. Fig. 5-5 shows the vertical deviation, while Fig. 5-6 shows the horizontal deviation of the reflected beams from each other, according to the apparent motion of the sun.
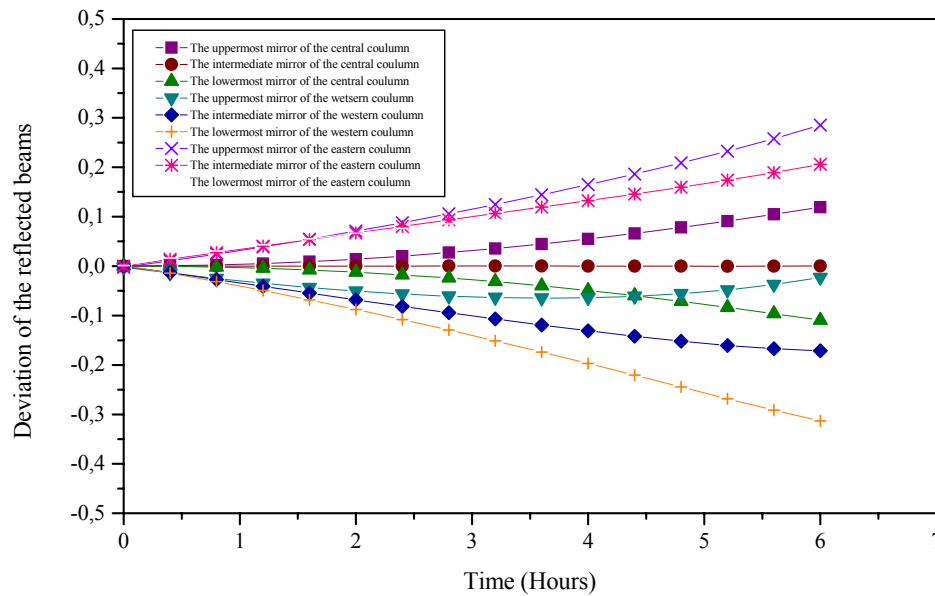
Fig. 5-5 The vertical deviation formed by the mirror array during the day.
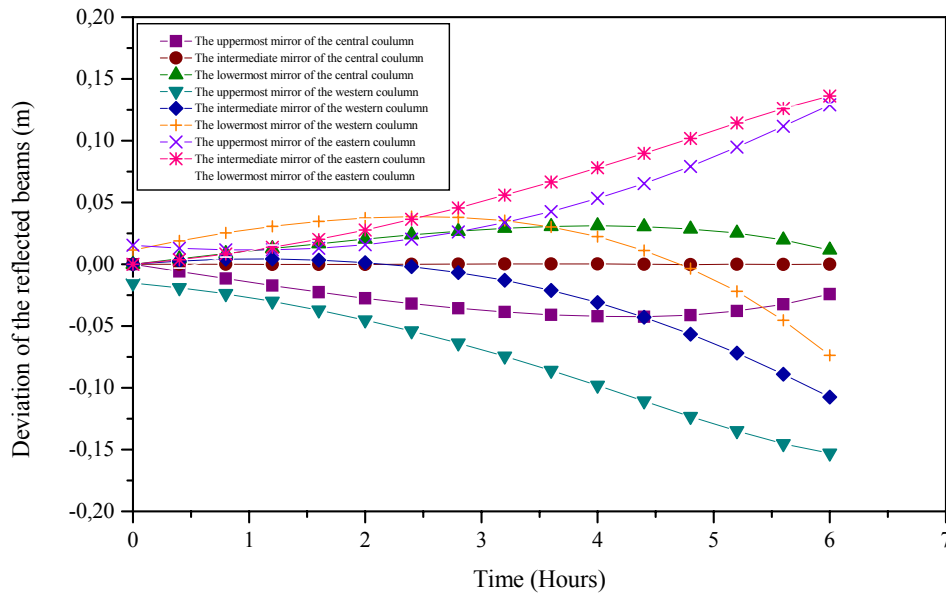
Fig. 5-6 The horizontal deviation formed by the mirror array during the day.

After studying the previous curves, we saw the deviation of the image positions was large especially in the vertical direction. This means we have not a stable concentrated solar radiation needed for generating the laser for more than a half-an-hour. Afterwards, we found that each mirror image had a different position. Therefore, we needed to develop a method by which we can get better overlap of the mirror images before and after noon time.

5.3 Adaptive mirror array system for the solar-pumped-laser system

In principle, a system of mirrors could be designed so that each mirror can be positioned in two directions, i.e. all images will overlap at a given pre-defined distance. In analogy to the properties of concave mirrors, we called this distance the focal length of the mirror array, and the position where we have the maximum overlap of the images the "focus" point of the mirror array. The position of the normal of each mirror has to bisect the angle defined by the two vectors pointing to the sun V_S and pointing to the focus position V_F into equal parts as shown in Fig. 5-7.

176
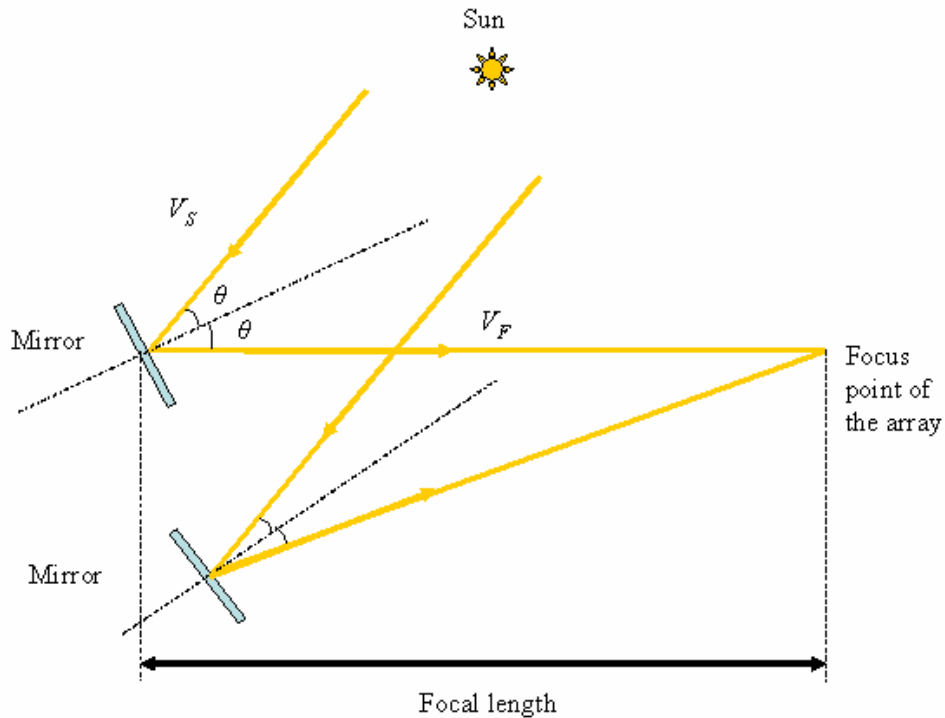
Fig. 5-7 Schematic diagram of a mirror array system using the vector representation.

The focus point and the focal length can be arbitrarily chosen by the positioning of the mirrors and their setting angles. As the position of the sun changes during the day, the direction of the mirrors has to be continuously or semi-continuously adjusted to fulfil the condition that the reflected solar radiations of them all has to be ovelaped in a single position. If one wants to obtain the maximum overlap, this has to be done for all mirrors of the array. In the case like the one presented here which implies time dependent conditions, adjustment of all of the 105 mirrors would need 210 computer-controlled electrical motors. To simplify this requirement, we have simplified the design and reduced the number of motors to 6.

We have subdivided the array into 3 sub-arrays of 35 mirrors, with separate inclination angles. These angles are changed by 3 separate computer-controlled low-speed VDC-motors. The angles increase before noon and decrease after noon. Each sub-array is further subdivided into 7 columns (panels) of 5 plate mirrors. These 5 mirrors of each column are finally such that at a particular time of the day they generate images of maximum total overlap. The columns can be rotated around the "vertical" axis which is perpendicular to the normal vector of the sub-array. All 7 columns are mechanically connected in such a way that they point to the same horizontal angle [54].

A good way of thinking to get the reflected solar radiation by an array of mirrors fixed for a longer time is to use some motors to control each single mirror or each group of mirrors. These motors have to be different in their speeds in order that the positions of all images are at the same location the whole time. For such a system of solar pumped laser, one can imagine that it would need a very large number of mirrors to achieve a reasonable optical concentration level needed for generating the laser, especially in the geographical regions which do not have high level of solar radiation. This means, we need accordingly a huge number of motors to control each single mirror. This would be a massive, expensive and complicated system.

A better way to solve this problem would be to reduce the number of motors needed to control the whole system in terms of controlling each group of mirrors with a single motor, focussing each group of mirrors for itself and enlarging the mirror dimensions if it is needed.

We decided to use this last choice but without enlarging the mirror dimensions for a good reason. It is easier to work on lasers of relatively small dimensions. Therefore, we need the focus to be consistent with the dimensions of the laser cavity. Moreover, if we enlarged the mirror dimensions, the error in the focussing could be enlarged. That means, we again may not reach the level of the concentration needed to generate the laser beam.

To realize the previously mentioned idea, we have been using a motor that rotates a tooth wheel or a gear wheel that in turn is connected with the mirror's rotational axis through a tooth belt. The motor in this case has to be either a step motor that tracks the sun during the day or a gear motor that changes its rotation rate through a group of tooth wheels. Fig. 5-8 shows a schematic realization of this idea.
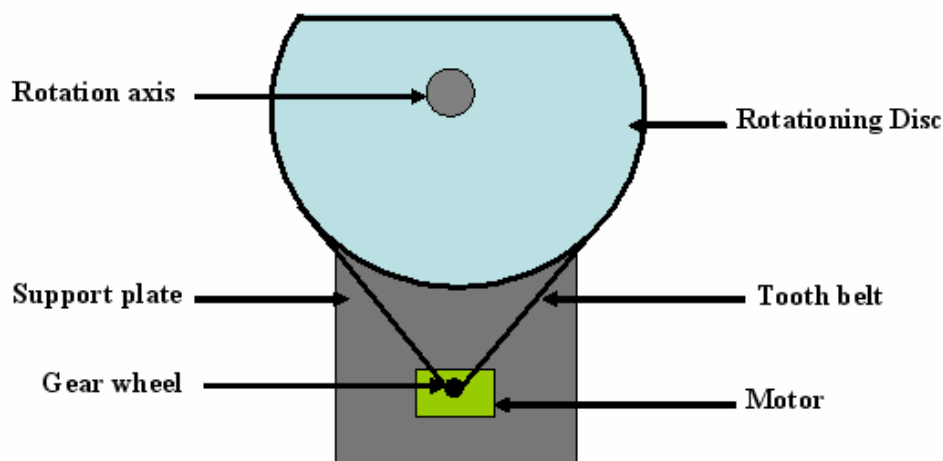
Fig. 5-8 Schematic design of a gear motor with a tooth belt.

The mirrors are divided into groups, and each group are mounted on a rotable plate (mirror panel). We decided that each panel carry five mirrors setting with different angles depending on its position on the panel and the position of the panel itself within the whole array. In this manner, the panels as mirror holders rotate around the axis of rotation when the motor starts to rotate. With this rotation, the system can track the sun during its daily motion if some of those panels are connected together with a motion connecting axis. Moreover, the system can be expanded to accept the other component of motion. We want to track the sun through following its motion horizontally and vertically by using two motors for each group of panels, set in turn with different angles depending again on their position in the array. The variation of the angle of each single mirror can be made with a couple of screws going through the aluminium plate and touching the mirror at its outer side, while the inner side must be sturdily screwed to the plate using a couple of clips. Through turning the screws below the outer side of the mirror, it will be gradually tipped over. This means, its angle will be changed. Accordingly, the reflected beam will change its direction in an angle equal to double the difference between the value of the first and the last ones. The panels, the

178

rotational disc and the support plate shown in the Fig. 5-8 were manufactured from aluminium. This is because it is a light, cheap and relatively weather resistant material. Fig. 5-9 shows a schematic design of a five-mirrors-unit used in this system.
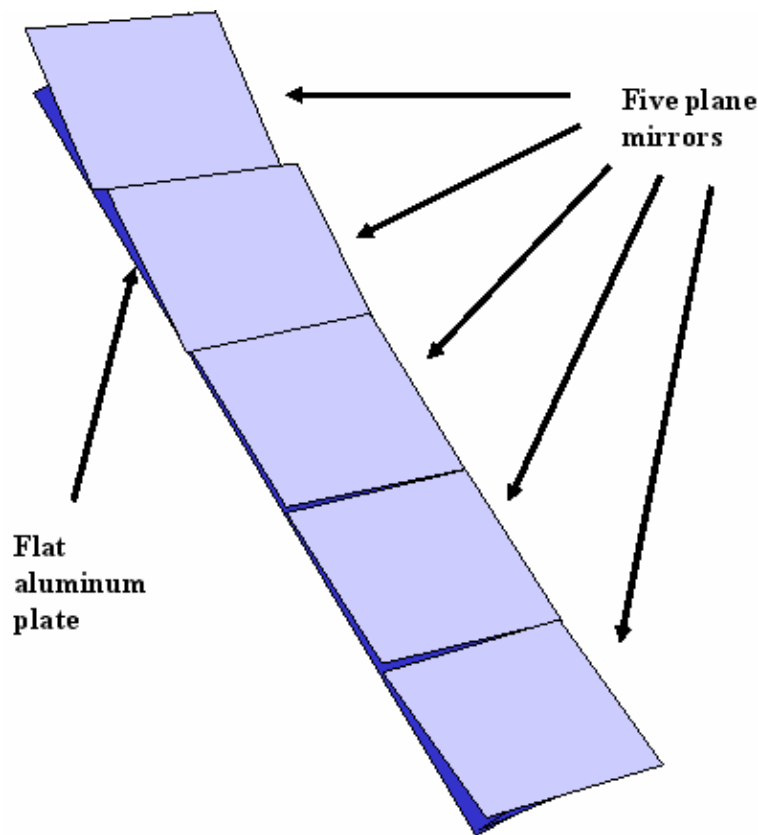
Fig. 5-9 Schematic design of a five-mirror-unit.

The rotations of the motors in both directions are controlled using a special programme coupled with this system using an 8-bit-processor.

After manufacturing a single prototype as described above, we found that it was not stable enough to carry five mirrors. Moreover, such a panel can stand approximately vertically because the whole system will be adjusted according to the optimum angle of the work location. Because we are working in Berlin which has a latitude of 53° 32′ and a longitude of 13° 35′, the optimum angle of the whole system was calculated to be 60°, i.e. the angle of the normal should be 30°. This means, the mirrors could slip out and fall down. Therefore, we have to find a manner by which the mirrors can be fixed on the panels safely.

To make the aluminium plate safer for the mirrors L-profiles were used for stopping the mirrors from falling down if the fixing clips and screws failed. But all the same, we found the panel afterthere too heavy and massive. To make it easier a square aluminium panel with the dimensions (15 cm × 15 cm) was taken as the base. On this base, a couple of L-profiles of 80 cm long were sturdily screwed, longitudinal and opposing each other. Finally, additional two L-profiles of 15.6 cm were transversely fixed opposing each other at the two ends of the previous ones. In other words, to save weight and to increase the stability, we used aluminium frames from L-profiles fixed on a smaller aluminium panel of dimensions (15 cm

× 15 cm). This gave us a sturdy frame that was not too heavy. Schematical designs for describing such a 5-mirrors-holder are shown in Fig. 5-10, 5-11, 5-12 and 5-13.
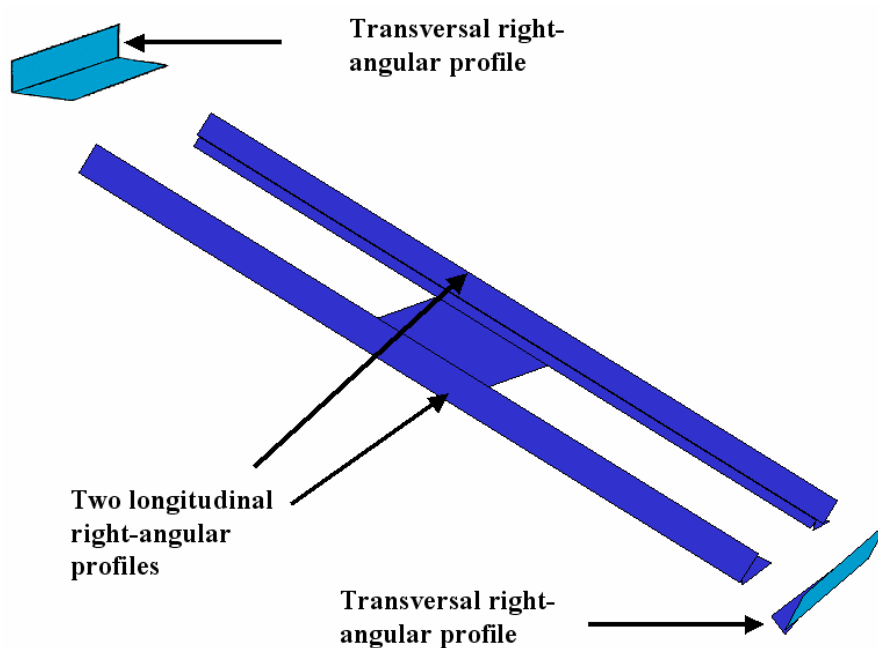
Fig. 5-10 Rectangular aluminium frame for five mirrors (15 cm × 15 cm) made from four L-profiles.
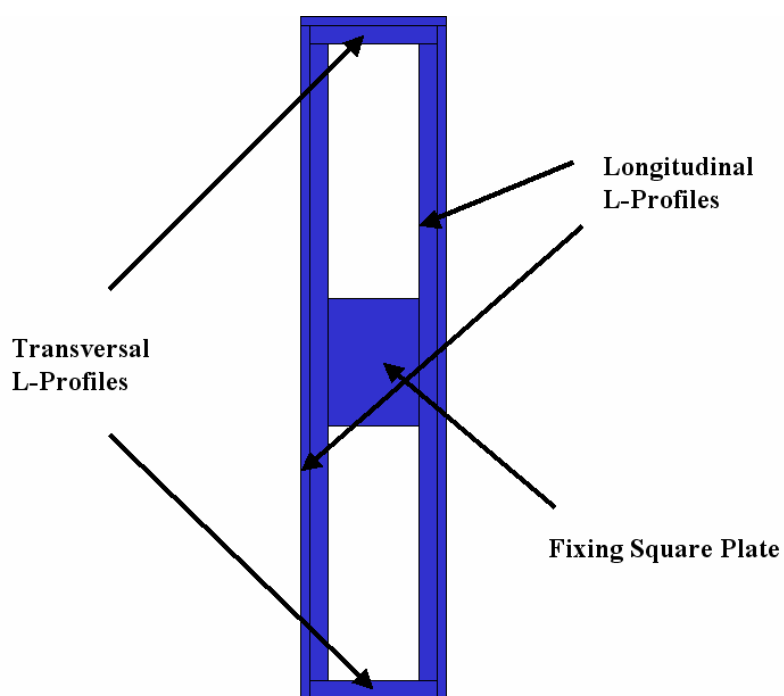
Fig. 5-11 Rectangular aluminium frame for five mirrors (15 cm × 15 cm) made from four L-profiles (Top view).
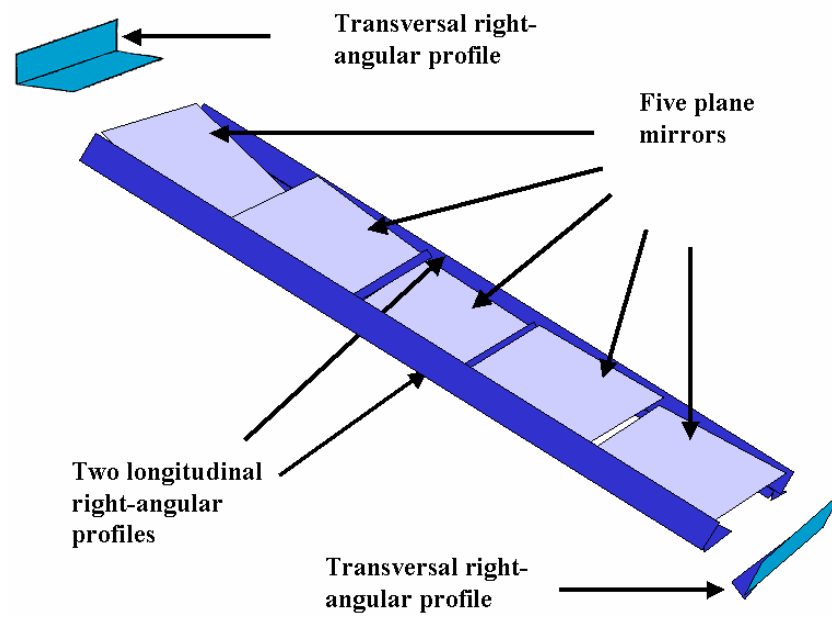
Fig. 5-12 A schematic design of a five-mirrors-unit with a frame consisting of four right-angular profiles.
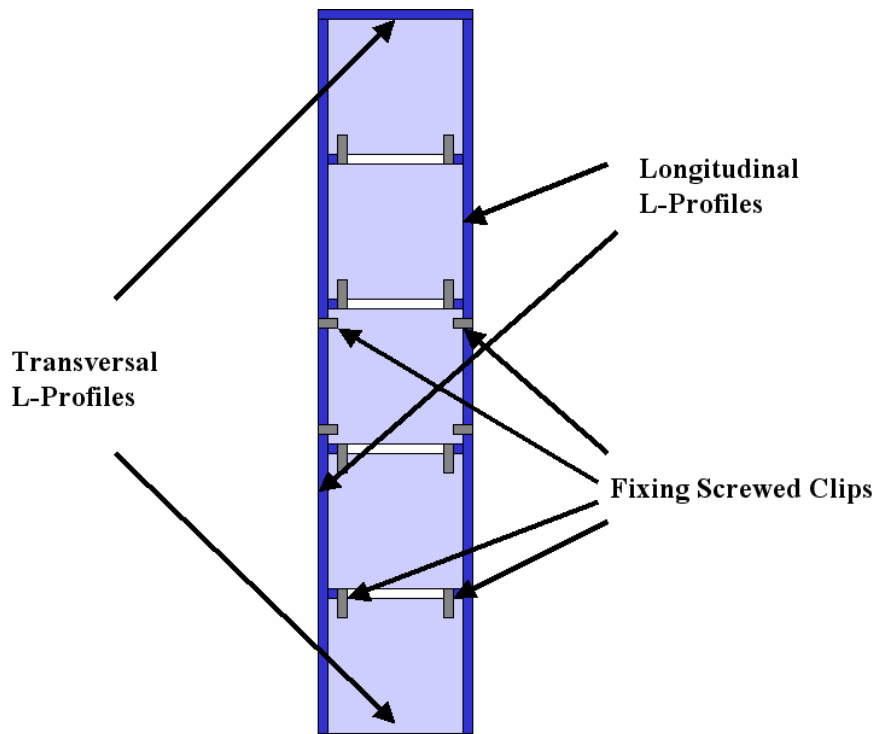
Fig. 5-13 A schematic design of a five-mirrors-unit with a frame consisting of four right-angular profiles (Top view).

According to the large number of those panels in our whole setup, we can imagine that the idea of the motion through gear wheels and tooth belts may be not the suitable one to control such a system. The mechanical force from a normal motor may be too small to rotate the aluminium disc that connects with the panels. The use of a tooth belt is also disadvantageous because it may be damaged by the motion if it couldn't transfer it from the motor to the disc. Therefore, we had to exclude the idea of the gear wheel and the tooth belt.

A better idea is to use a stronger motor with a head that is able to rotate a screw bar fixed on. During the rotation of the motor with this screw bar, it goes through a screw-nut fixed on a bar connected with the mirror unit. In this manner, the angle of the mirror unit will be changed because of it rotation around an axis in the middle of the unit itself. Accordingly, the motor itself needs an additional degree of freedom to change its angle due to the motion. Therefore, the idea of using a ball bearing to give the motor this degree of freedom was the most reasonable idea for our system.

The idea in that construction can be easily summarized in giving a certain number of the pulses to the motor. These pulses are coupled into certain screw steps needed to move the perpendicular holder connected with the mirror panel a certain distance needed to tip the panel itself with a certain angle. The motion of the perpendicular holder takes place by the rotation of the screw bar through a hole in the holder itself. In our screw bar, we could calculate that one screw step (1.5 mm) needs motor 512 pulses.

The system now consists of 3 rows, each one carries 7 panels. On each panel there are 5 plane mirrors with the dimensions (15 cm × 15 cm). Therefore, the total number of the mirrors used in such a concentration system is 105 ones. The mirror of each panel can be adjusted so that they could be set in different angles in order to get an image of a single mirror dimensions theoretically. After considering the effect of the half subtended angle of the sun along the focal length of the system (3 meters), we get an image of dimensions of approximately 18 cm × 18 cm theoretically. A mistake in the system will make the dimensions larger.

As we know, the apparent solar motion during the day has two components: one in the direction of the altitude and another in the direction of the azimuth. The equation that describes the altitude of the sun as function of the date and the time can be given in Equation (5-1) [2, 30].

$$a = \sin^{-1}\left[\cos\phi\cos\delta\cos H + \sin\phi\sin\delta\right] \tag{5-1}$$

where φ is the latitude of the observer, δ is the declination of the sun and H is the hour angle. While the equation that describes the azimuth of the sun as a function of the same parameters can be given Equation (5-2) [2, 30].

$$A_z = \tan^{-1}\left[\frac{\sin H}{\cos H \sin\phi - \tan\delta\cos\phi}\right] \tag{5-2}$$

To keep the focus of the system fixed during the day, we have to adjust the mirrors for initial conditions in which their normal axes have the half angles of the sun in their two previous components. Afterwards, the motors are adjusted and supplies with pulses, so that the position during the day is held constant. Two programmes are used to do this. The first of them was written to calculate the positions of the sun during the day, according to the Equation (5-1) and Equation (5-2), and accordingly the positioning of the mirrors translated to numbers of pulse differences which must be supplied to the motor to keep the focus fixed. The other programme takes the numbers of the pulse differences and supplies them to the motors to let them direct the mirrors according the needed angles.

To study the vertical component of the motion, we have derived the Equations (5-3), (5-4) and (5-5), which represent the value of the mirror unites angles during the day of 7th June as functions of the altitude of the sun. Fig. 5-14 shows the parameters used in the analysis of this derivation. If a is the altitude of the sun, d_v is the distance between each two units, f is the focal length of the array, and α_o the tilting angle of the whole system (which is chosen to be 60° as the optimum tilting angle for Berlin (Germany)), the angles of the intermediate unite α, the lower unite β and the upper unite γ are given respectively as the following:

$$\alpha = \frac{a}{2} \qquad (5\text{-}3)$$

$$\beta = \frac{a + \tan^{-1}\left(\frac{d \sin \alpha_o}{f - d \cos \alpha_o}\right)}{2} \qquad (5\text{-}4)$$

$$\gamma = \frac{a - \tan^{-1}\left(\frac{(d \sin \alpha_o)}{f + d \cos \alpha_o}\right)}{2} \qquad (5\text{-}5)$$

Fig. 5-14 The parameters of the analysis of the vertical angles.

The resulted curves of these angles are shown in Fig. 5-15, which shows the behaviour of the vertical angle of each single panel in one row during the same day.

Fig. 5-15 Vertical mirror angles during the day.

Similarly, to study the horizontal component of the motion, we have derived the Equations (5-6), (5-7), (5-8), (5-9), 5-10), (5-11) and (5-12), which represent the value of the mirror unites angles during the day of 7th June as functions of the altitude of the sun. Fig. 5-16 shows the parameters used in the analysis of this derivation. If A_z is the azimuth of the sun, d_h is the horizontal distance between each two units and f is the focal length of the array, the angles of the intermediate unite η_o, the eastern unites (η_{E1}, η_{E2}, η_{E3}) and the western unites (η_{W1}, η_{W2}, η_{W3}) are given respectively as the following:

$$\eta_o = \frac{A_z}{2} \tag{5-6}$$

For the eastern units:

$$\eta_{E1} = \frac{A_z - \tan^{-1}(\frac{d_h}{f})}{2} \tag{5-7}$$

$$\eta_{E2} = \frac{A_z - \tan^{-1}(\frac{2d_h}{f})}{2} \tag{5-8}$$

$$\eta_{E3} = \frac{A_z - \tan^{-1}(\frac{3d_h}{f})}{2} \tag{5-9}$$

For the western units:

$$\eta_{W1} = \frac{A_z + \tan^{-1}(\frac{d_h}{f})}{2} \tag{5-10}$$

$$\eta_{W2} = \frac{A_z + \tan^{-1}(\frac{2d_h}{f})}{2} \tag{5-11}$$

$$\eta_{W3} = \frac{A_z + \tan^{-1}\left(\frac{3d_h}{f}\right)}{2}$$ (5-12)
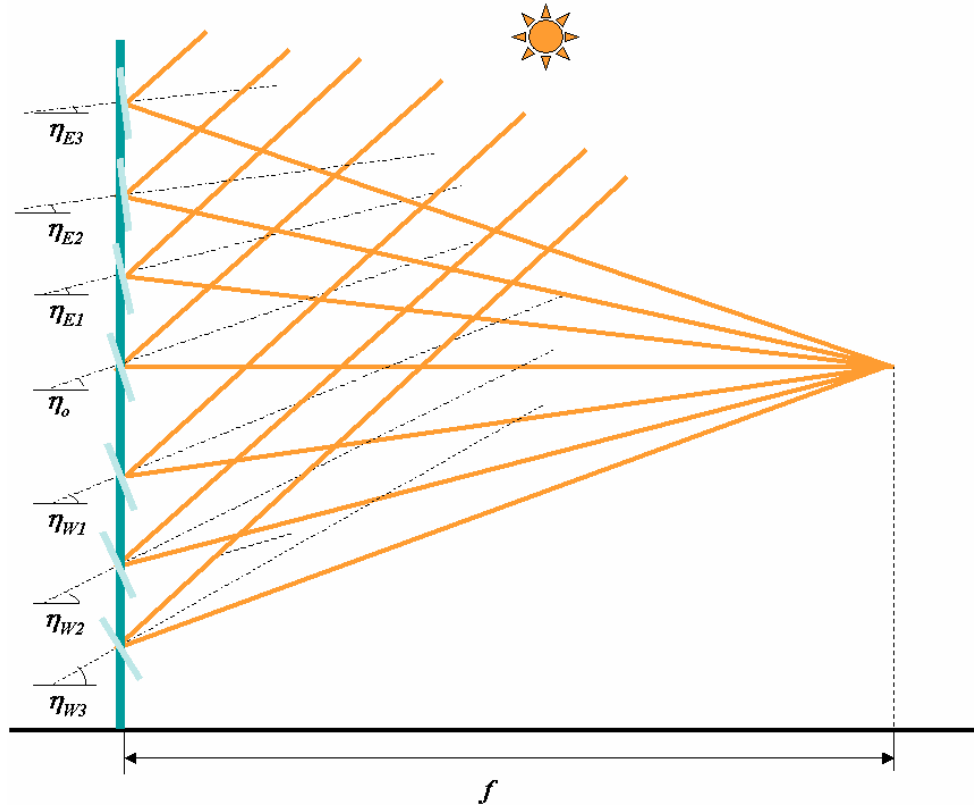
Fig. 5-16 The parameters of the analysis of the horizontal angles.

The resulted curves of these angles are shown in Fig. 5-17, which shows the behaviour of the horizontal angle of each single panel in one row during the same day.
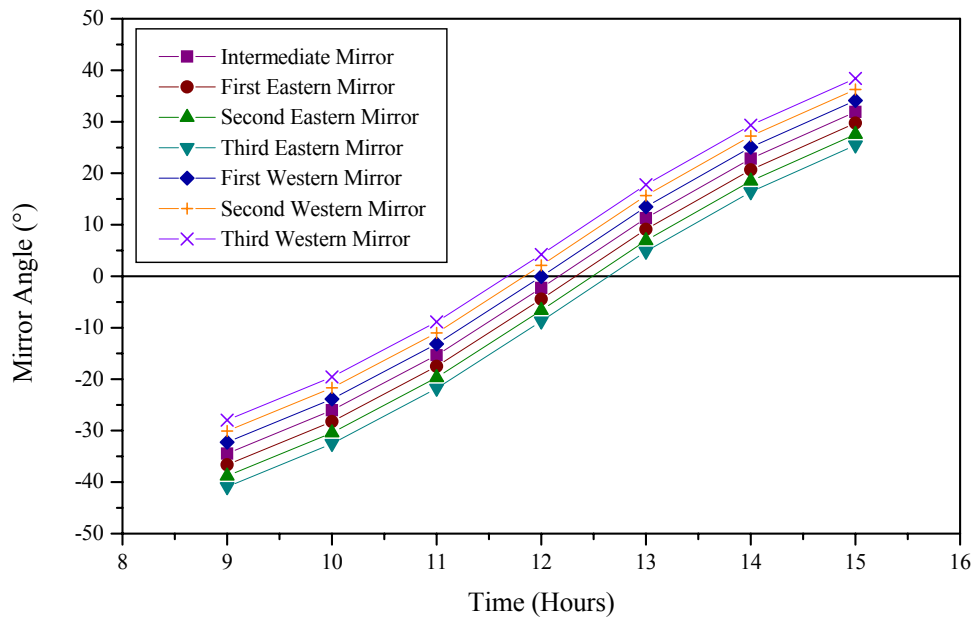
Fig. 5-17 Horizontal mirror angles during the day.

This system is considered as a geometrically easy but a relatively mechanically difficult system. This is because it is difficult to get the screw-nut fixed and easily moving through the day because the panel rotates around an axis in its centre line. To make it mechanically easier, we can add a single modification, which is relatively easy. The panel must be higher than the main plane of rotation and the normal coupler of the holder itself rotates around an axis in the main plane. In this manner, we could get a mechanically easier system although it could be geometrically difficult. A side view of the mirror unit with the new modification is shown in Fig. 5-18, while a top view of it is shown in Fig. 5-19.
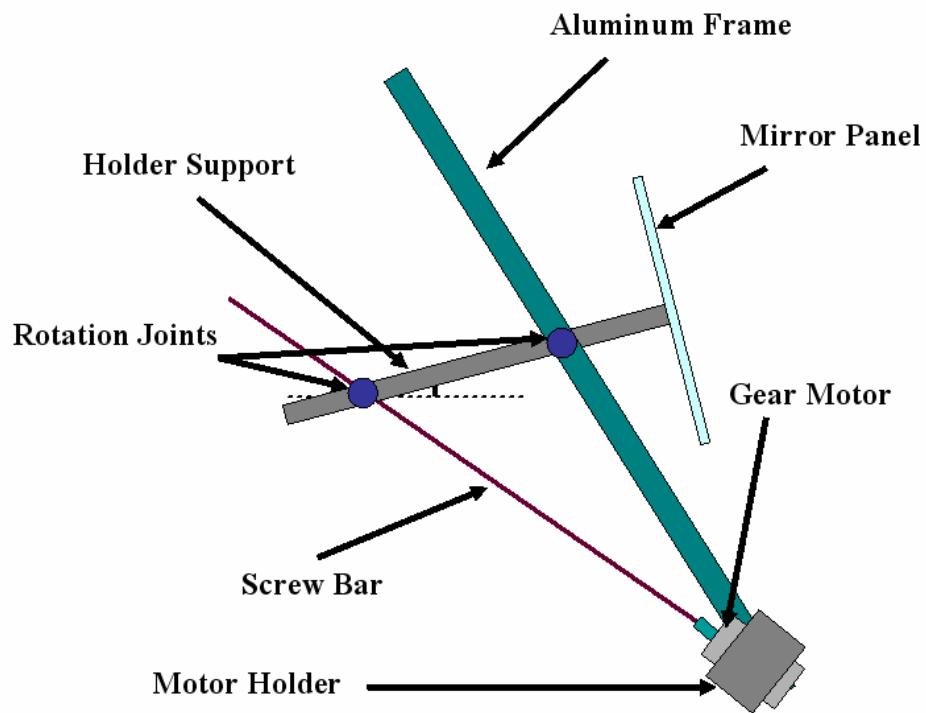
Fig. 5-18 Mirror unit controlled with a gear motor (Side view).
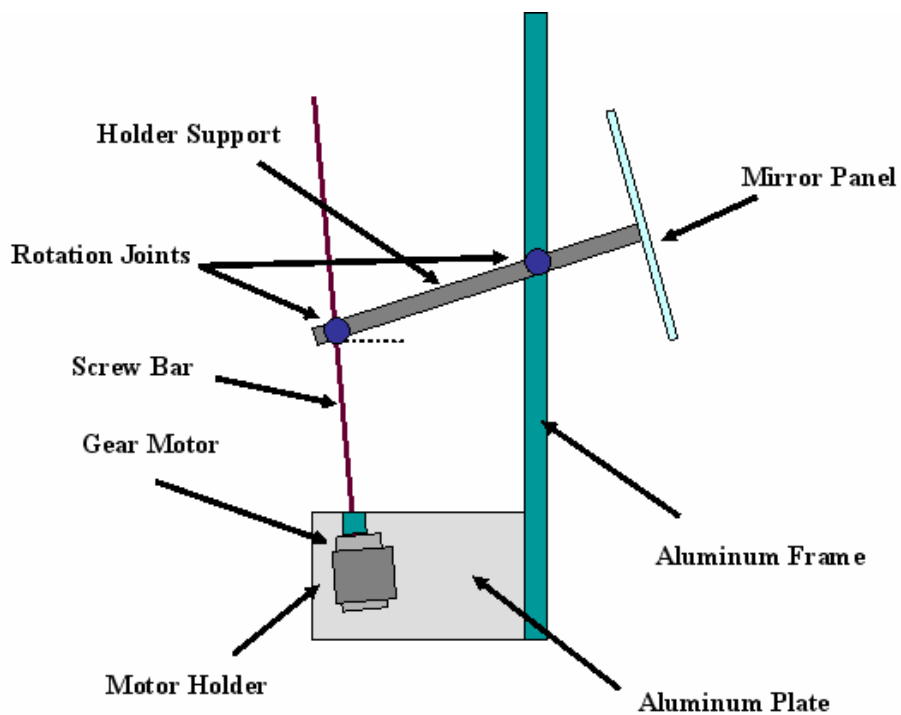
Fig. 5-19 Mirror unit controlled with a gear motor (Top view).

5.4 The new desktop-controlled adaptive mirror array system

In order to simplify the movement of the mirrors we chose a system with mechanically coupled mirrors, i.e. not all mirrors were controlled individually. We designed an array of 105 plane mirrors (15 cm × 15 cm amounting to approximately 2.5 m^2 of mirror area) which was divided into 3 separate rows as shown in Fig. 5-20. Each of these rows consists of 7 columns (panels) of mirror assemblies which are mechanically coupled in such a way that each column has the same angular speed as shown in Fig. 5-21. They are driven by a low voltage cw-motor. Each column consists of 5 manually adjustable mirrors positioned sequentially in the vertical direction. The vertical inclination of the panel is adjusted by another cw-motor. Altogether, the 3 rows are adjusted by 6 cw-motors, 3 for tracking the angular movement of the sun and 3 for adjusting the inclination angle of the mirrors. The inclination has a maximum around noon and is zero at sunrise and sunset. The motors controlling this movement have therefore to be reversed at noon. Figs. 5-22, 5-23, 5-24 and 5-25 show the electronic control circuits of the mirror-array-system and their relevant components [54, 55].

An array consisting of 105 flat mirrors focuses the sunlight onto the laser system approximately 3 m away. The target is fixed in space; the mirrors track the sun's movement. A secondary concentration device (Fresnel lens) is located between the mirror array and the target. A third concentration device concentrates the radiation onto the laser rod. The primary spot size is maximum 20 cm × 20 cm. A small computer controls the mirror movement.
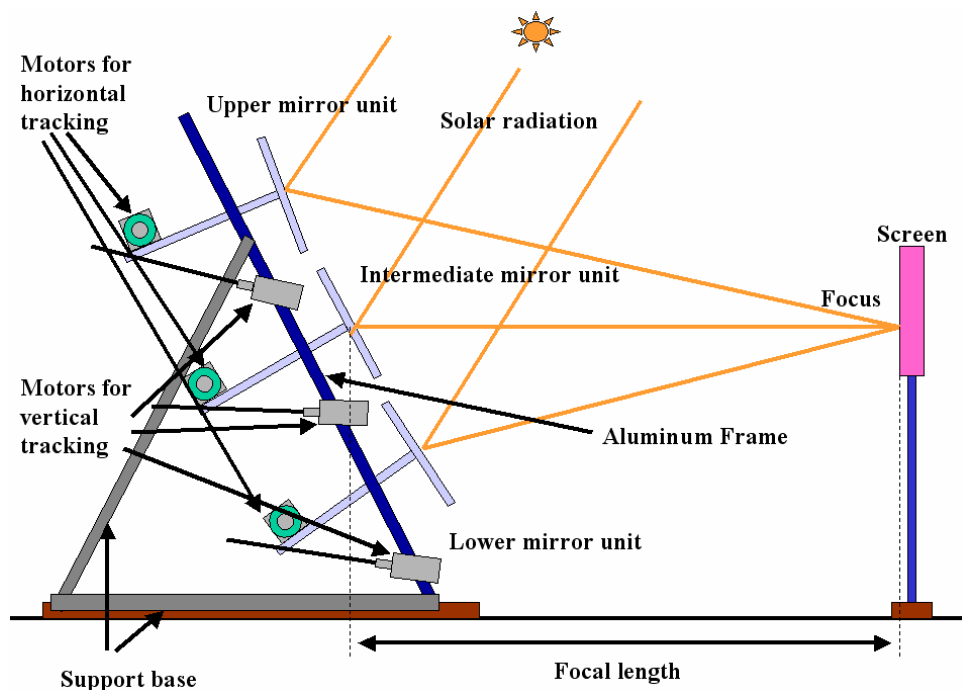
Fig. 5-20 Side view of the mirror array system.
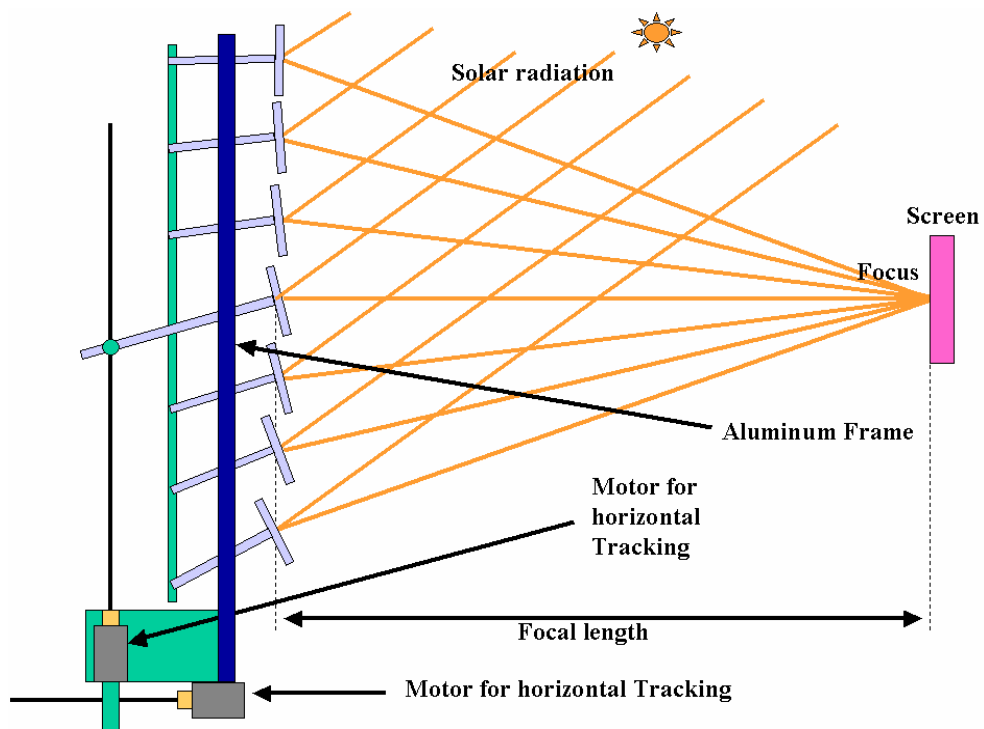
Fig. 5-21 Top view of the mirror array system.
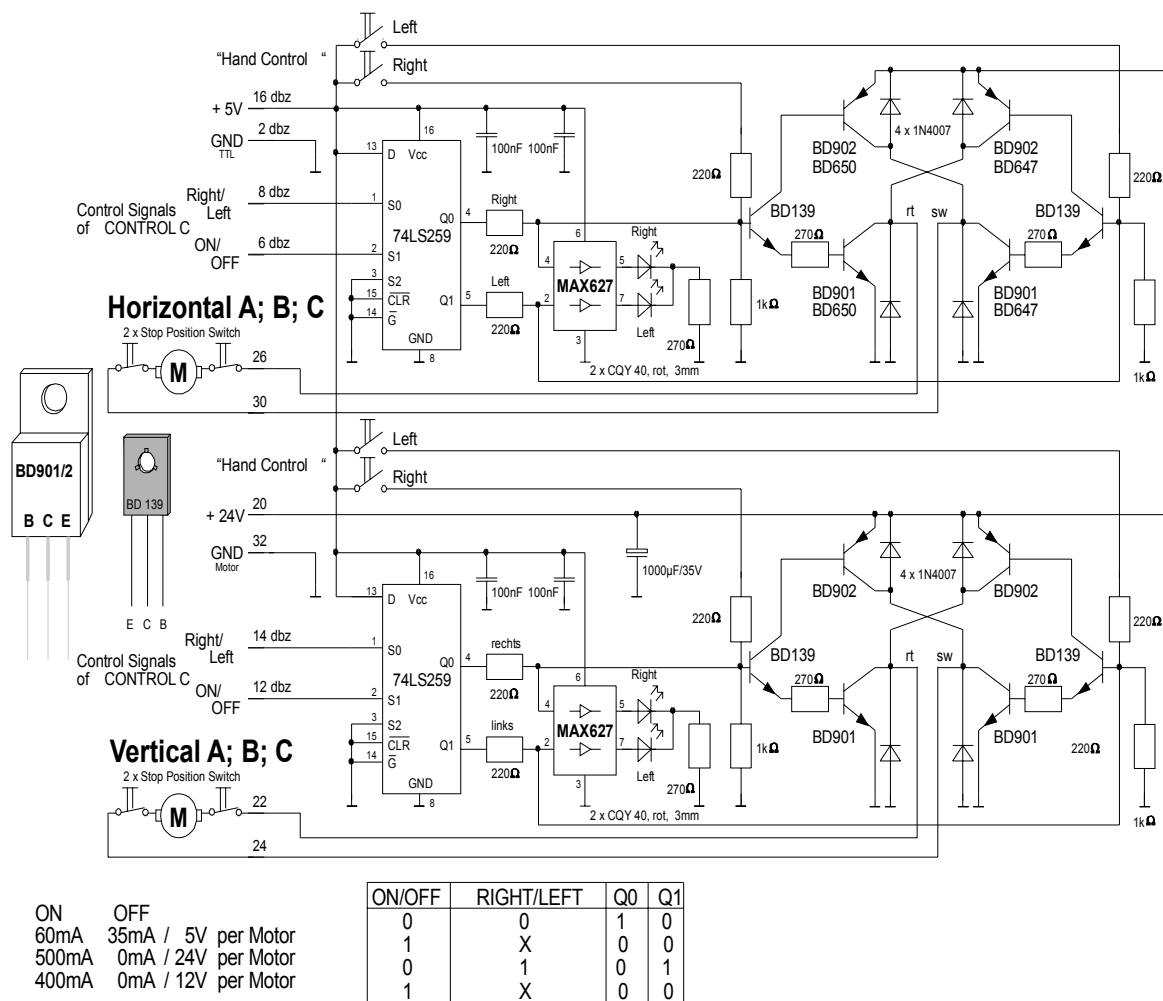
Fig. 5-22 Circuit diagram of the motor control unit.

Circuit Diagram

IR-Photoelectric Barrier MRL601
or
IR-LED (LD 261) and Photo Transistor (SFH 305-2/3)

Frequency in
Dependence
of Motor Voltage
24V = 50Hz
18V = 35Hz
12V = 20Hz
6V = 8Hz
4V = 3Hz

Caution:
It must be a leteral
seeing protection
between LED and Photo-
transitor.

Board Connector Fixation with
2 Distance Pieces, 5 mm High
and 2 Screws M4 x 12

Component Side
of
Platine

Conductor Side
of
Platine

Power Supply - Module for Accu-Operation

Fig. 5-23 Circuit diagram of the rotation sensor.

Wiring Plan for Motor Control

Horizontal A
Motor Control A
Vertical A
Horizontal B
Motor Control B
Vertical B
Horizontal C
Motor Control C
Vertical C
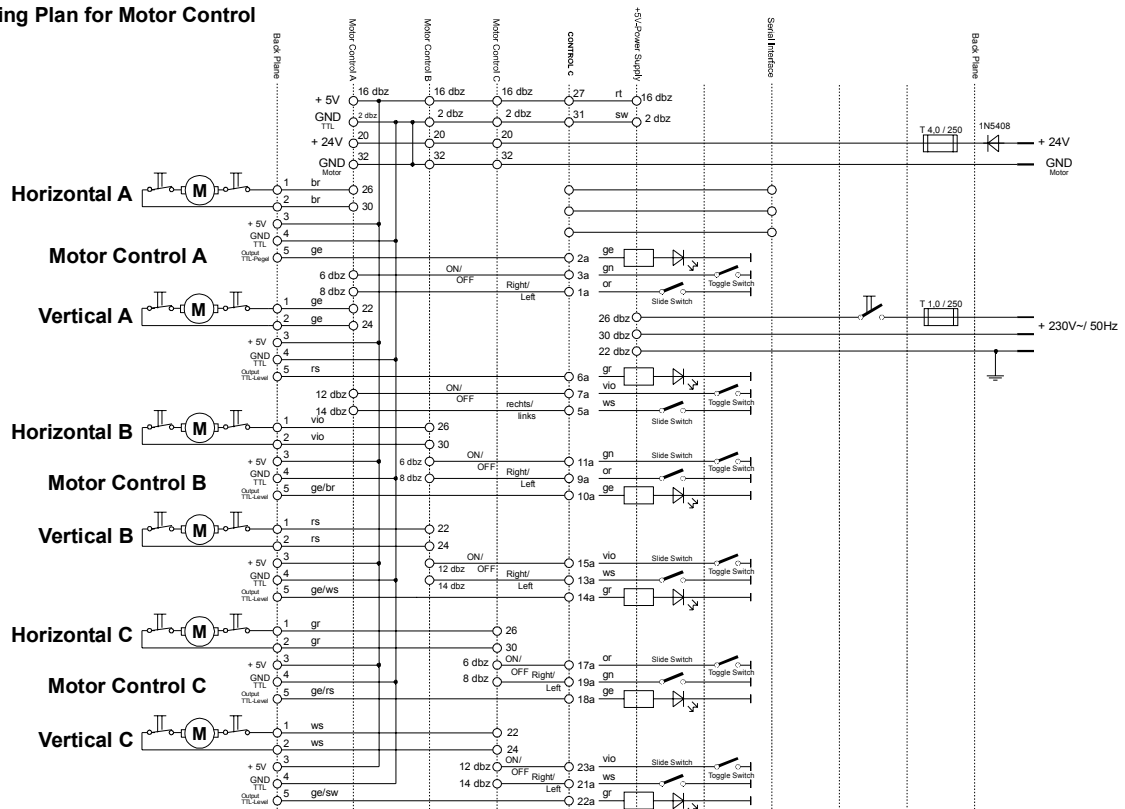
Fig. 5-24 Circuit diagram of the motor manual control unit.

192
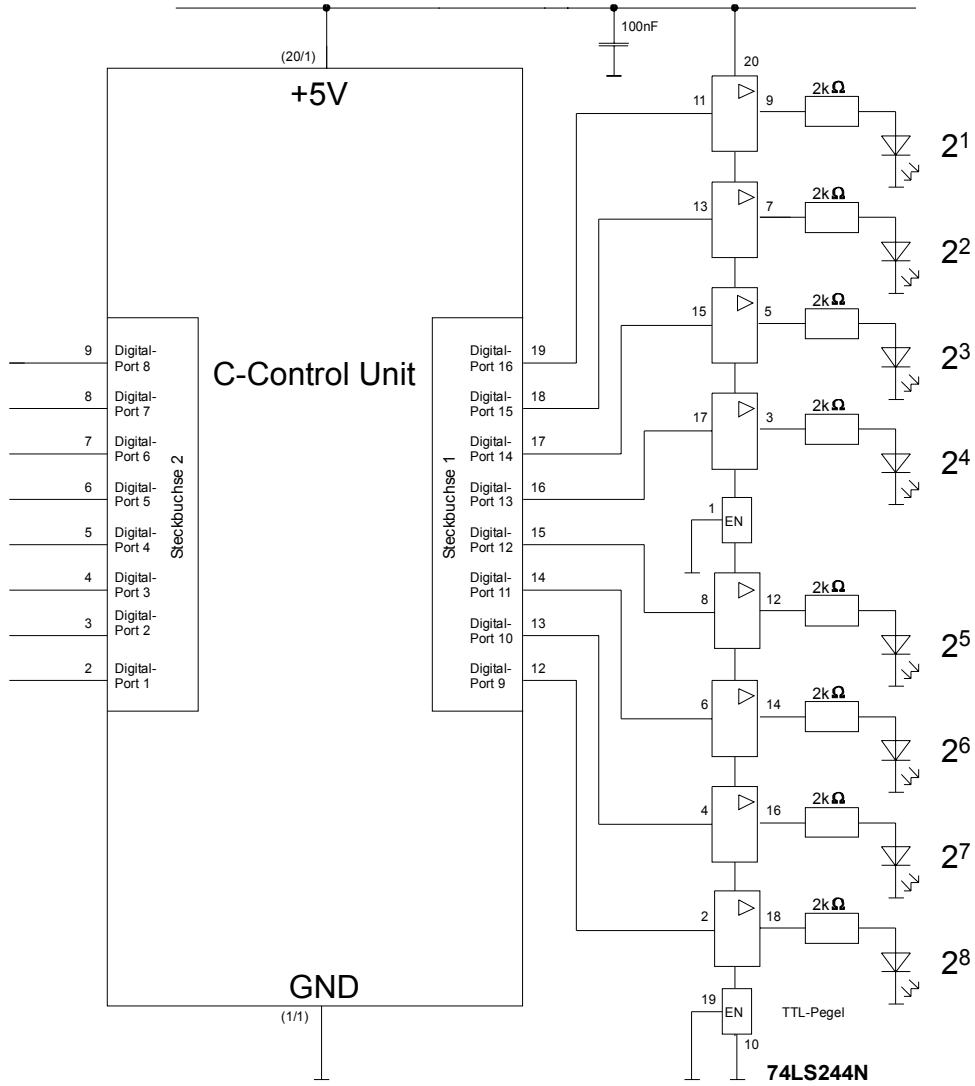
Fig. 5-25 Electronical control unit of the mirror-array-system.

5.5 Calculation of the system rotational angles

To study the vertical component of the motion, we have derived the Equations (5-13), (5-14) and (5-15), which represent the value of the mirror unites angles during the day of 7th June as functions of the altitude of the sun. Fig. 5-26 shows the parameters used in the analysis of this derivation. If a is the altitude of the sun, d_v is the distance between each two units, d_m is the distance resulted by the existence of the holder length h projected along the frame of the array, f is the focal length of the array, α_o the tilting angle of the whole system (which is chosen to be 60° as the optimum tilting angle for Berlin (Germany)) and α_i is an optimum angle of the intermediate unit (which was chosen to be the half of the maximum altitude of the sun), the angles of the intermediate unite α is given as the half of the altitude angle as shown in the following equation:

$$\alpha = \frac{a}{2}$$

(5-13)

while the angles of the lower unite β and the upper unite γ have to obey the following equations respectively:

$$\tan(2\beta - a) = \frac{(d_v + d_m)\sin\alpha_o - h\sin\beta}{f + h\cos\alpha_i + \dfrac{h\sin\alpha_i}{\tan\alpha_o} - (d_v + d_m)\cos\alpha_o - h\cos\beta} \qquad (5\text{-}14)$$

$$\tan(a - 2\gamma) = \frac{(d_v - d_m)\sin\alpha_o + h\sin\gamma}{f + h\cos\alpha_i + \dfrac{h\sin\alpha_i}{\tan\alpha_o} + (d_v - d_m)\cos\alpha_o - h\cos\gamma} \qquad (5\text{-}15)$$

Equations (5-14) and (5-15) can be numerically solved for β and γ respectively using Newton method. There is no symbolic solutions expresses them explicitly.
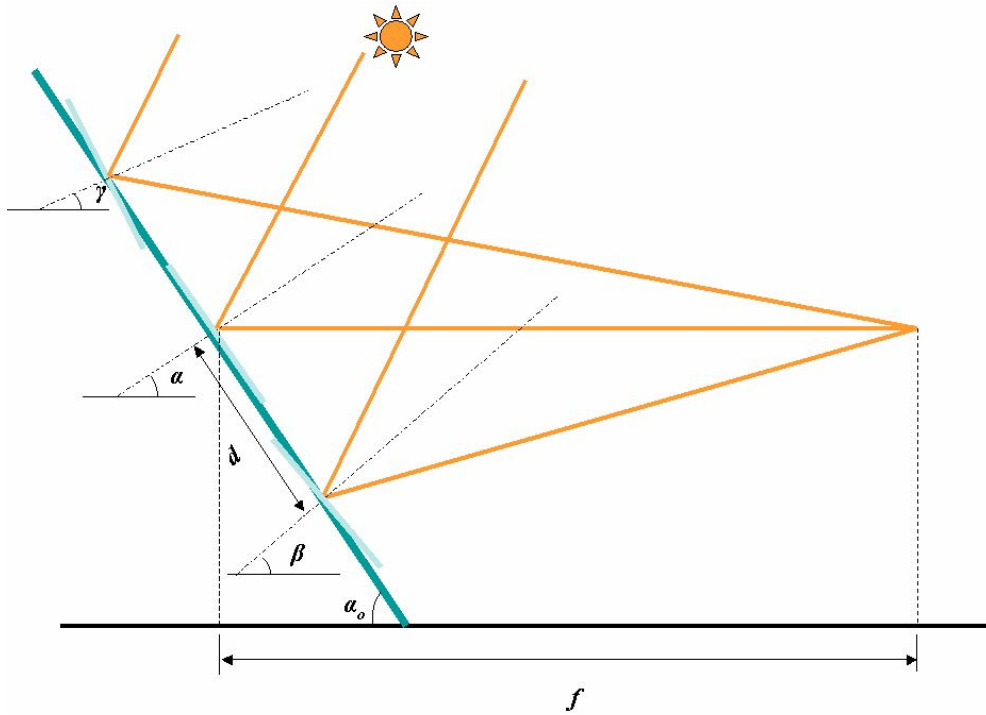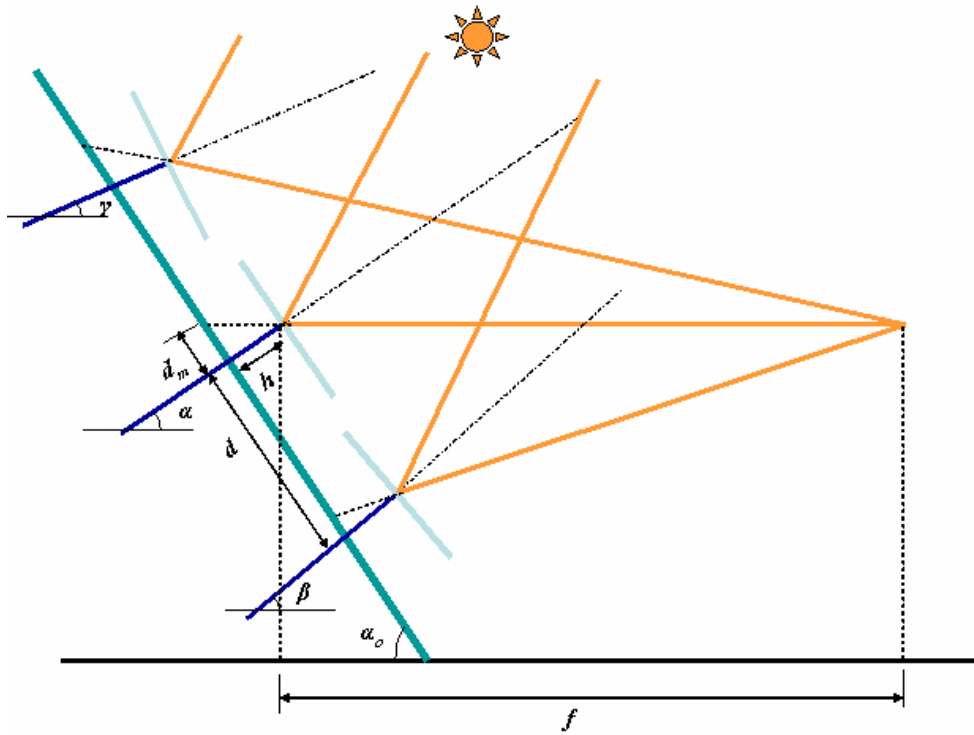

Fig. 5-26 The parameters of the analysis of the vertical angles.

The resulted curves of these angles are shown in Fig. 5-27, which shows the behaviour of the vertical angle of each single panel in one row during the same day.
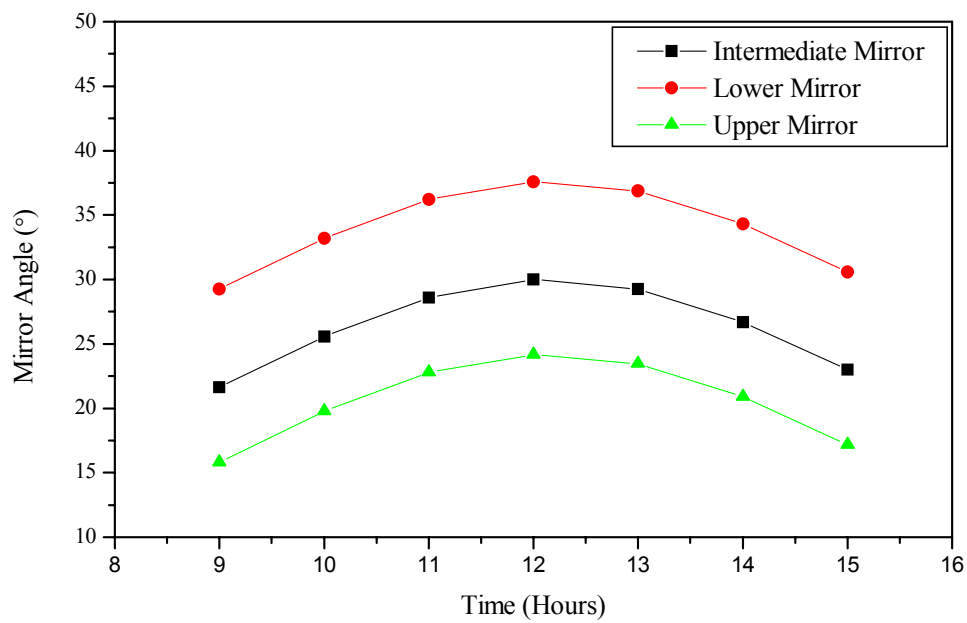
194
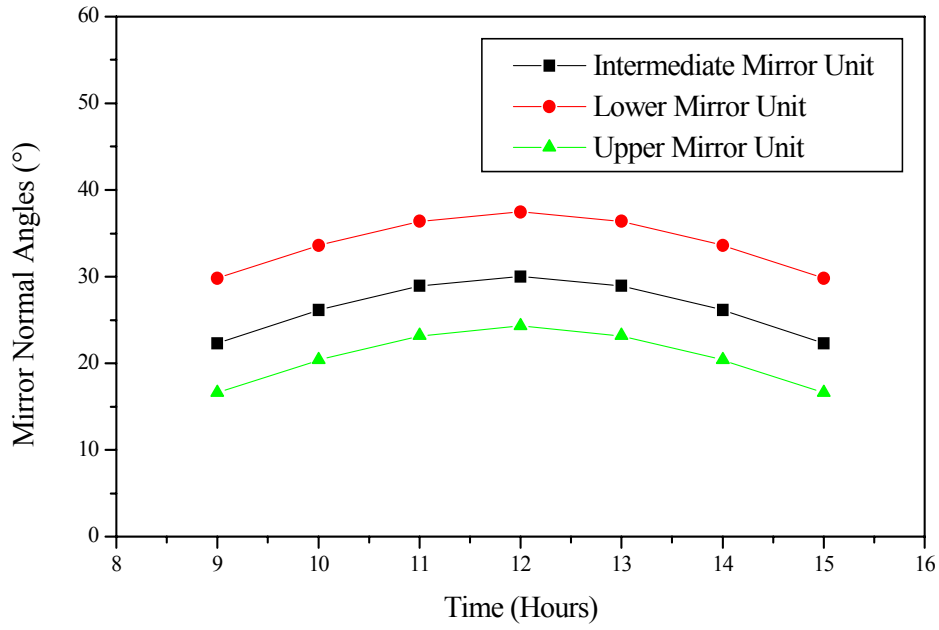
Fig. 5-27 Variation of the angles of the rows of mirror array during the day in the vertical direction.

Similarly, to study the horizontal component of the motion, we have derived the Equations (5-16), (5-17), (5-18), (5-19), 5-20), (5-21) and (5-22), which represent the value of the mirror unites angles during the day of 7th June as functions of the altitude of the sun. Fig. 5-28 shows the parameters used in the analysis of this derivation. If A_z is the azimuth of the sun, d_h is the horizontal distance between each two units, d_{zm} is the distance resulted by the existence of the holder length h projected horizontally along the frame of the array, f is the focal length of the array and η_i is an optimum angle of the intermediate unit (which was chosen to be zero (the half of azimuth angle at noon)), the angles of the intermediate unite η_o, the eastern unites (η_{E1}, η_{E2}, η_{E3}) and the western unites (η_{W1}, η_{W2}, η_{W3}) are given respectively as the following:

$$\eta_o = \frac{A_z}{2} \qquad (5\text{-}16)$$

For the eastern units:

$$\tan(a - 2\eta_{E1}) = \frac{(d_h - d_{zm}) + h\sin\eta_{E1}}{f + h\cos\eta_i - h\cos\eta_{E1}} \qquad (5\text{-}17)$$

195

$$\tan(a - 2\eta_{E2}) = \frac{(2d_h - d_{zm}) + h\sin\eta_{E2}}{f + h\cos\eta_i - h\cos\eta_{E2}} \qquad (5\text{-}18)$$

$$\tan(a - 2\eta_{E3}) = \frac{(3d_h - d_{zm}) + h\sin\eta_{E3}}{f + h\cos\eta_i - h\cos\eta_{E3}} \qquad (5\text{-}19)$$

For the western units:

$$\tan(2\eta_{W1} - a) = \frac{(d_h + d_{zm}) - h\sin\eta_{W1}}{f + h\cos\eta_i - h\cos\eta_{W1}} \qquad (5\text{-}20)$$

$$\tan(2\eta_{W2} - a) = \frac{(2d_h + d_{zm}) - h\sin\eta_{W2}}{f + h\cos\eta_i - h\cos\eta_{W2}} \qquad (5\text{-}21)$$

$$\tan(2\eta_{W3} - a) = \frac{(3d_h + d_{zm}) - h\sin\eta_{W3}}{f + h\cos\eta_i - h\cos\eta_{W3}} \qquad (5\text{-}22)$$

Similarly, Equations (5-17), (5-18), (5-19), (5-20), (5-21) and (5-22) can be numerically solved for η_{E1}, η_{E2}, η_{E3}, η_{W1}, η_{W2} and η_{W3} respectively using Newton method. There is no symbolic solutions expresses them explicitly.

But as shown in Fig. 5-21, the horizontal tracking process is based on the central mirror unit, with which the other units are mechanically connected. Accordingly, only the central unit will be adjusted during the tracking process. The adjustment of the other units can be done using the adjustment screws. Therefore, we can use the the equations from Equation (5-17) to Equation (5-22) only to determine the angles of the mirror units after adjusting with these screws. To get the real angles of the siderial mirrors and the pulses needed to be given by the motors, we have to use the equations from Equation (5-6) to Equation (5-12).
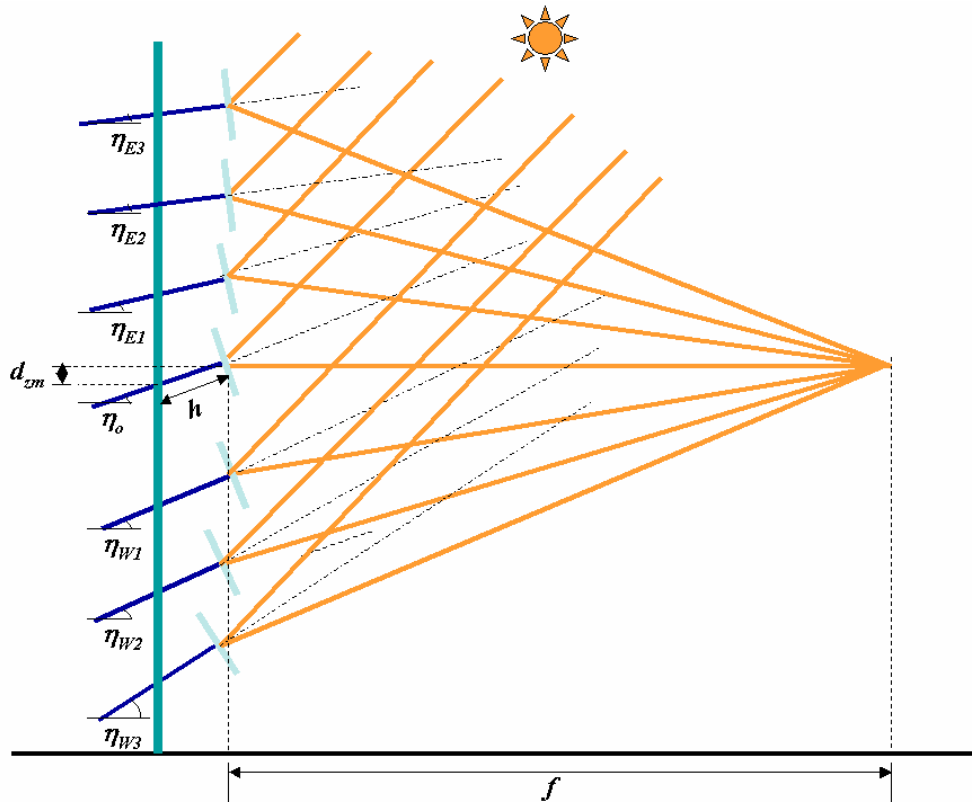
Fig. 5-28 The parameters of the analysis of the horizontal angles.

The resulted curves of these angles are shown in Fig. 5-29, which shows the behaviour of the horizontal angle of each single panel in one row during the same day.
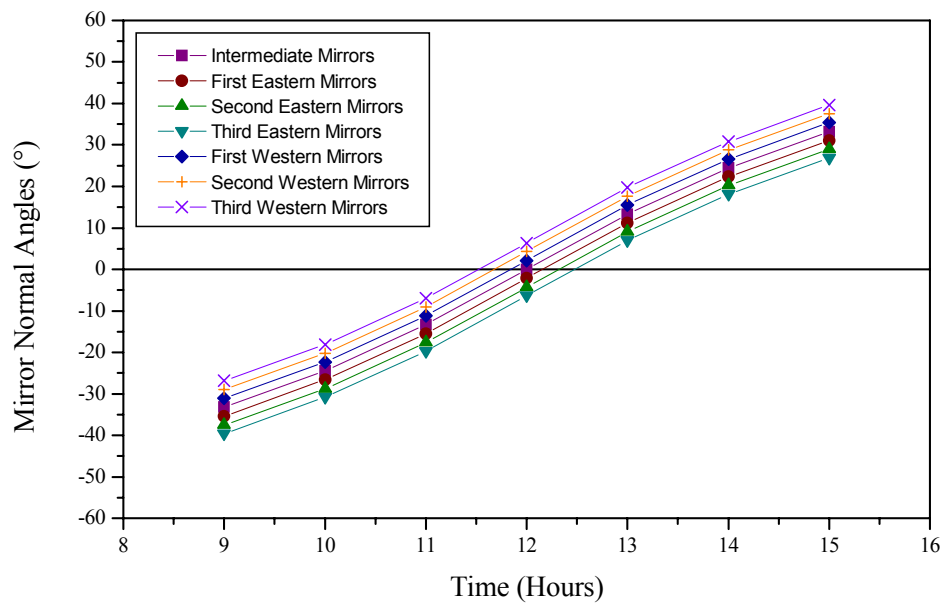

Fig. 5-29 Variation of the angles of the rows of mirror array during the day in the horizontal direction.

5.6 Estimation of the theoretical maximal concentration ratio of the Mirror-Array-System

If we apply the maximum concentration ratio of the central receiver collectors that consists of a field of a large number of heliostats, we can estimate the theoretical maximal concentration ratio of our system. Equations 5-23 and 5-24 show the maximum concentration ratio for a three-dimensional concentrator system with incident radiation making an angle θ_i to the plane of the heliostat array, for a rim angle of ϕ_r, an area fraction covered by the heliostats ψ, and the dispersion angle of δ, if all the reflected beam radiation is to be intercepted by a spherical and a flat receiver respectively [2].

$$C_{max} = \frac{\psi \sin^2 \phi_r}{4 \sin^2 (0.267 + \delta/2)} - 1 \tag{5-23}$$

$$C_{max} = \psi \left[\frac{\sin\phi_r \cos(\phi_r + 0.267 + \delta/2)}{\sin(0.267 + \delta/2)} \right]^2 - 1 \tag{5-24}$$

As our receiver is a flat one, we have to use the second equation. Considering the dispersion angle which represents the error tends to zero because of the rotation and the controlling, we can get a concentration behaviour of our mirror array system shown in the curve of Fig. 5-30 during the day. From this figure, we see that the concentration ratio of the mirror array system varies during the day between 2071.24 and 2085.22. Moreover, the maximum values of this concentration ratio are reached at the beginning and the end of the day, while the minimum value is reached at the noon.

If one uses a parabolic dish concentrator (paraboloidal concentrator) with the same focal length (3 m) and a diameter of 1.5 m, a concentration ratio value up to about 3000 times can be reached. This means that with our adaptive mirror array system, we could approach the values of the concentration ratios of the parabolic dish concentrators of the same dimensions.
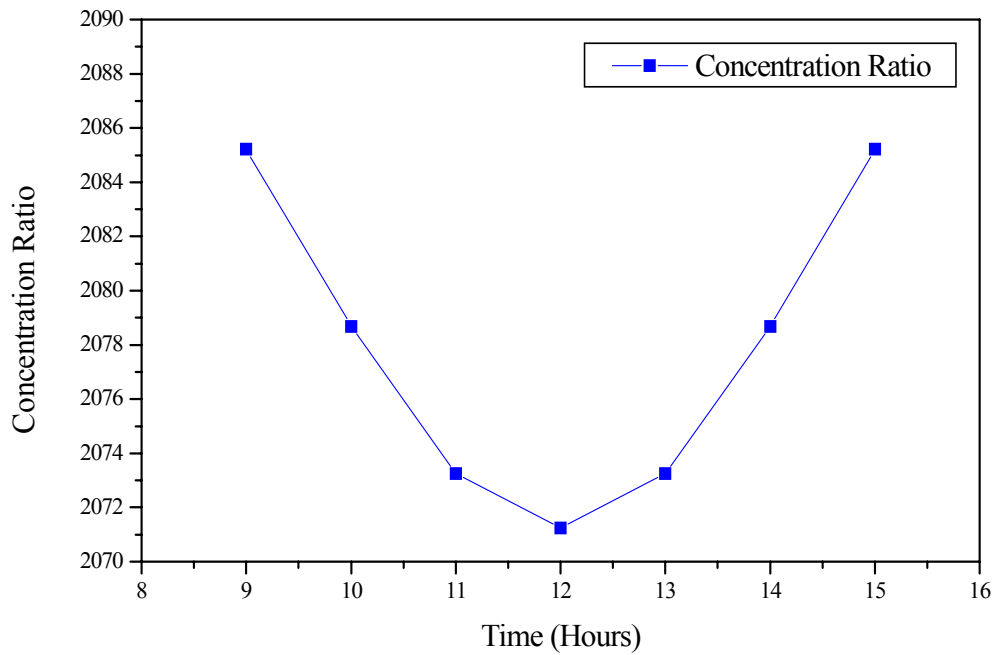
Fig. 5-30 Theoretical estimation for the maximum concentration behaviour during the day.

5.7 Systems using a combination of a Mirror Array and Fresnel lens

A secondary concentration device (Fresnel lens) is located between the mirror array and the target. This Fresnel lens has a focal length of 279.4 mm, 406.4 mm free aperture and 0.508 mm groove distance. The main goal of using such a Fresnel lens is to increase the concentration ratio and accordingly the input power given to the target (the laser head) through decreasing of the focus single area. From such a lens, one can expect to decrease the focussing area by a factor of more than one half. This would double the concentration ratio delivered to the target [54, 55]. Fig. 5-31 shows a schematic representation of a mirror array with an additional Fresnel lens, from the side, while Fig. 5-32 shows a photo of the whole mirror array construction in the laboratory before mounting it on the rooftop of the main building of the Technical University of Berlin campus.
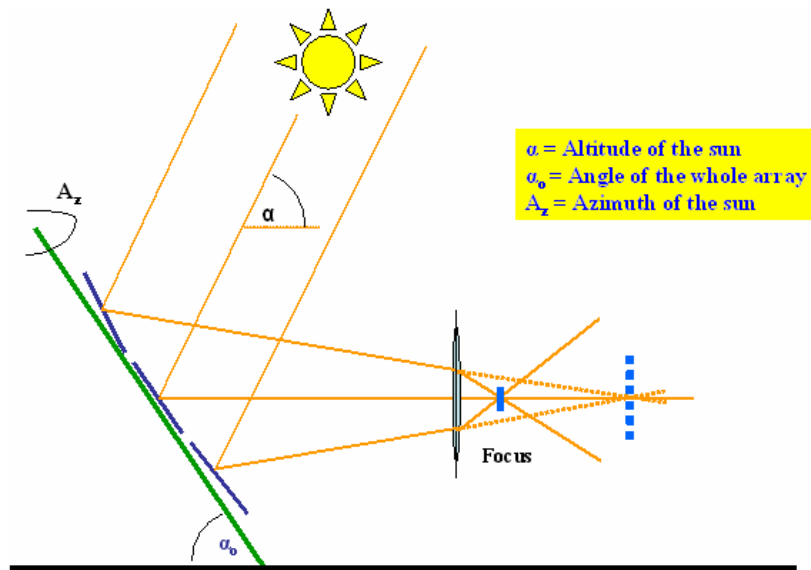
Fig. 5-31 A schematic representation of a mirror array with an additional Fresnel lens.

Fig. 5-32 The whole system of the mirror array in the laboratory.

Fig. 5-33 shows back of the system of mirror array where the motors with their screw sticks are shown, while Fig. 5-34 shows a photo of the electrical control unit built to control this system.

<div align="center">(a)   (b)</div>

Fig. 5-33 A view of the back of the system ((a) Motors with screw sticks. (b) Mirror bases and rotation system.).
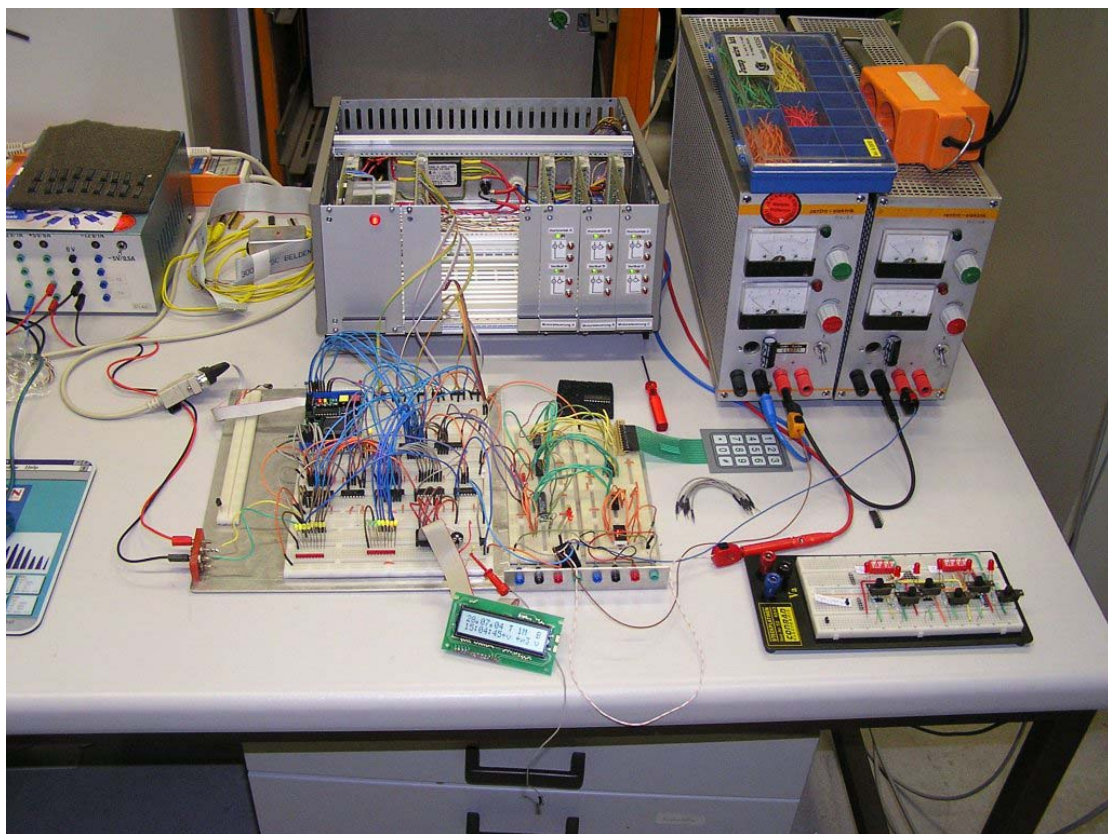
Fig. 5-34 The electrical control unit of the mirror array system.

The whole system was transported to the rooftop of the main building of the Technical University of Berlin to try it out under the outdoor conditions. Measurements and experiments were done during the two months, September and October 2004. Fig. 5-35 shows the whole mirror array system built in place, while Fig. 5-36 and Fig. 5-37 show the system while running.

After transporting the whole system, we adjusted it to face the real south direction. Then we determined the position of the focus to be 3 metres away from the intermediate row of the array.

Fig. 5-35 Mirror array set up on the rooftop of the main building of the Technical University of Berlin (Photo from front).

(a)

(b)

(c)

Fig. 5-36 Mirror array system focussing the solar radiation on a screen 3 m away.
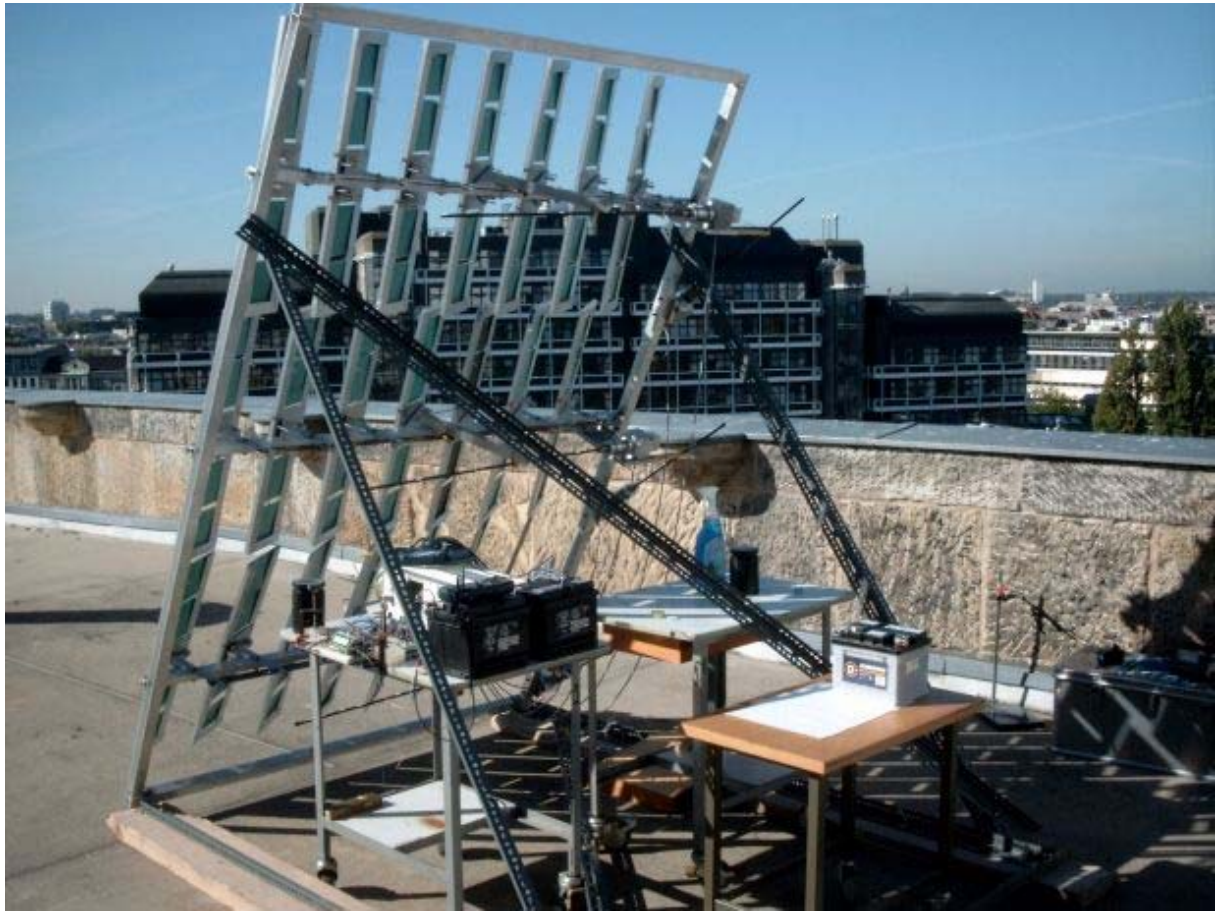
Fig. 5-37 Mirror array system on the rooftop of the main building of the Technical University of Berlin (Photo from behind). In the background is the new physics building.

We chose the focal length of our mirror array system to be 3 m. Because of the dimensions of each single mirror of the array and due to the subtended half-angle of the solar disc, one can expect the dimensions of the resulting image in the "Focal Plane" of the array to be about 20 cm × 20 cm. Due to the tolerance of the adjustment of such a system, those dimensions could be a bit more than the previous values. Practically, we succeeded to obtain image dimensions of 22 cm × 21 cm. There are two rim angles for the system; the horizontal one is 28°, and the vertical one is 30°.

An 8-Bit Basic-Processor (from Conrad Elektronik), synchronised with a radio clock, controls the 6 Motors every second, in order to get all of the mirrors tracking the sun during the day. The power supply used here is car batteries. One could possibly use solar cells instead of 12 V car batteries (accumulators) have been used as power supply to provide the whole energy of the system from the Sun.

Because the dimensions of our laser are smaller than the mentioned dimensions of the focus, the focus should be deceased. Moreover, we will have a higher concentration level if we diminish the image in the focus because the intensity will be decreased.

5.8 Using an additional Fresnel lens with the mirror array system

By using a Fresnel lens (SC 208) which has a diameter of 40 cm and focal length of 29.7 cm, we obtained smaller image dimensions (like 10 cm × 10 cm and 11 cm × 11 cm). But the system is still an imaging optical system. This lens from Fresnel Optics Inc. has a large chromatic aberration, but is corrected for parallel light [54, 55]. It is shown in Fig. 5-38.

5-38 The used additional Fresnel lens.

A relatively small dimensional image with high radiation intensity could damage the laser rod if we applied it to such a system. Fig. 5-39 shows the effect of using the additional Fresnel lens (SC 208).
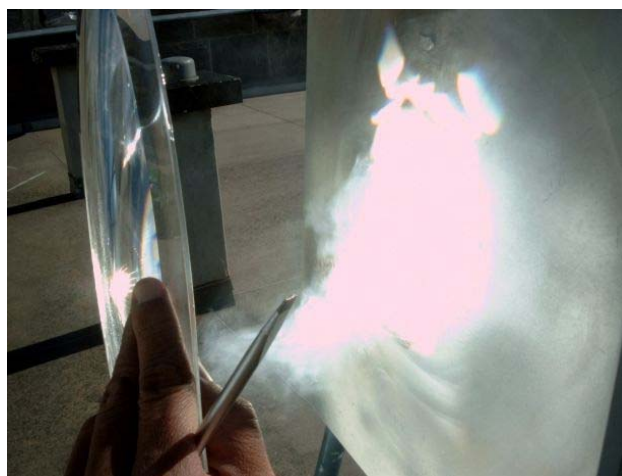
Fig. 5-39 Increasing the intensity of the focussed radiation using an additional Fresnel lens.

The Fresnel lens used to increase the concentration ratio of the mirror array system is made from PMMA and corrected for parallel monochromatic light. The Fresnel lens is transparent in the visible, the near U.V. and the near I.R. spectrum bands. Table 5-2 shows the technical data of this Fresnel lens (SC 208 of Fresnel Optics Inc.).

Technical Data	Value
Focal length	279.4 mm
Free Aperture	406.4 mm
Groove distance	0.508 mm

Table 5-2 Technical data of the used Fresnel lens.

5.9 Diffraction limited resolution of circular Fresnel lenses

Focussing a parallel beam of light at the focal point is limited by diffraction. The upper limit of the concentration ratio can be shown using the diffraction calculations. A first estimation of the area of the diffraction disc can be expected from the following equation that expresses the diffraction through a circular pinhole. The diameter of the diffraction disc is given by Equation (5-25).

$$d = 1.219\lambda\frac{f}{D} \tag{5-25}$$

where λ is the wavelength of the testing beam, D is the lens diameter and f is the focal length of the lens.

For a green light of 548 nm, we obtain a diffraction disc of 460 nm diameter which corresponds to a maximal concentration ratio for parallel light given by Equation (5-26).

$$C_{max} = \frac{d^2}{D^2} = 7.8 \times 10^{11} \tag{5-26}$$

We can get more accurate results if we considered the Fresnel lens as an overlap of many circular rings. The angular distribution of the intensity at the diffraction through a single ring of the radius a can be described through Equation (5-27).

$$\frac{J(\theta)}{J(0)} = \left[J_0\left(2\pi\theta a/\lambda\right)\right]^2 \tag{5-27}$$

where J_0 is the Bessel function of first type and zero order.

Equation (5-5) can be represented in the curve shown in Fig. 5-40.
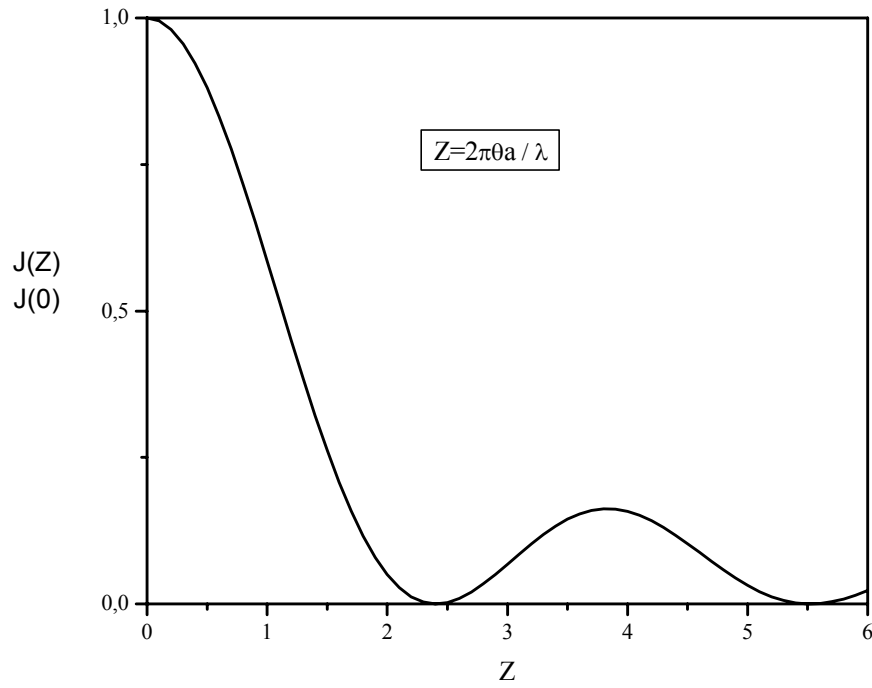
Fig. 5-40 Diffraction on the ring on the screen.

For every groove (total $D/2z = 400$ (z is the groove width)), there is such a distribution function g_i shown in the Equation (5-28).

$$g_i = \frac{8\pi a_i z}{\pi D^2}$$ (5-28)

The 400 functions are summed together weighted with the area of the lens rings through the total area of the lens. Accordingly, the diffraction behaviour of the Fresnel lens can be described according to the Equation (5-29).

$$\frac{J(\theta)}{J(0)} = \sum_{i=1}^{400} g_i \left[J_0 \left(2\pi\theta a_i / \lambda \right) \right]^2$$ (5-29)

which is represented by the curve shown in Fig. 5-41.
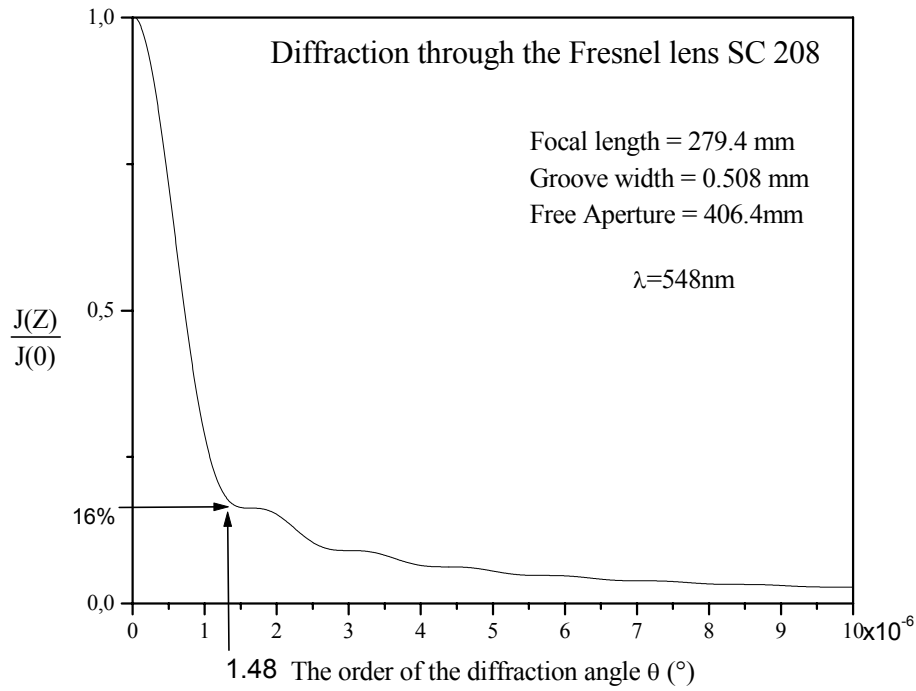
Fig. 5-41 The diffraction through the Fresnel lens SC 208.

The central maximum has a width (16 %) of $\Delta\theta_{diff} = 1.48 \times 10^{-6}$. This corresponds to a diffraction disc of a diameter $2\Delta\theta_{diff} f = 1.2$ µm, which corresponds to a maximal concentration ratio of $C_{max} = 1.1 \times 10^{11}$ for illumination with parallel light.

5.10 Measuring the concentration ratio of the Fresnel lens SC 208

5.10.1 The setup of the experiment

Because of the big lens area, standard optical methods can not be used to measure the concentration ratio of the Fresnel lens SC 208. Only a fraction from the lens itself can be illuminated instead of the whole lens. Fig. 5-42 shows the setup of the experiment for measuring the concentration ratio of the Fresnel lens.
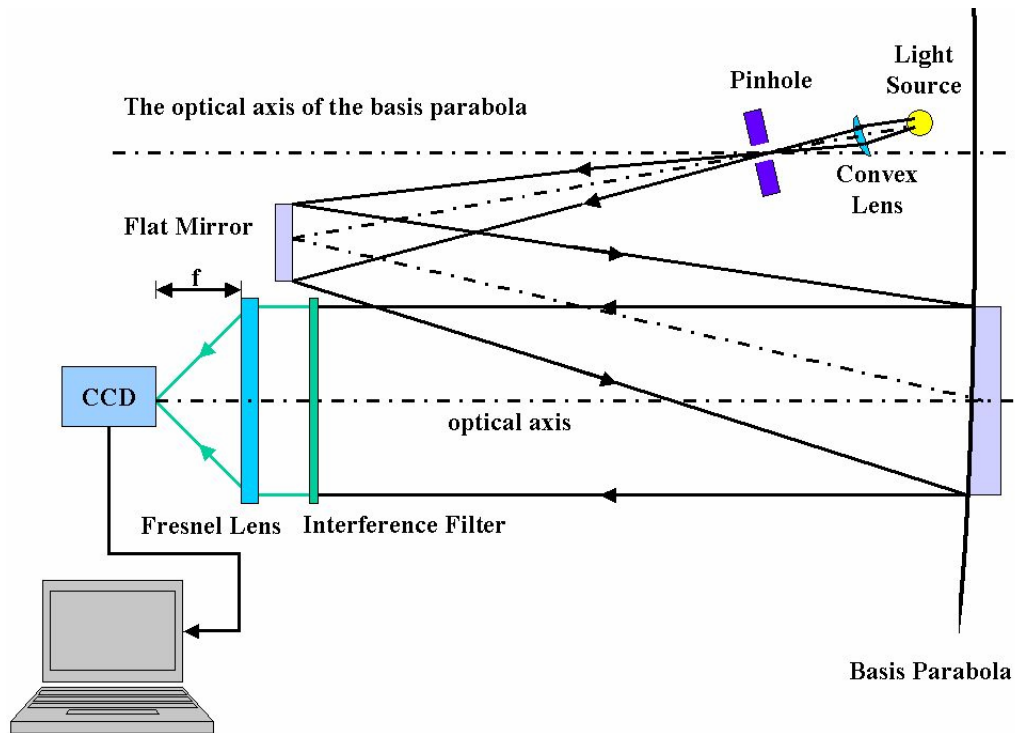
Fig. 5-42 Setup of the Fresnel lens concentration ratio measurement system.

A parallel light is produced with the help of a collimator from the objective measurement facility of the Optical Institute of the Technical University of Berlin. The light bundle is monochromized with an interference filter. This collimated beam bundle meets a plane mirror at an angle of 45°. This plane mirror lies transversly and is movable, on an optical bench at right angle to the direction of the lens. A CCD-Camera connected with a PC is put in the focal plane. The images have 8-bit greyscale with 512 × 512 Pixel. A pixel corresponds to 6.25 μm.

Three series of measurements were recorded with the wavelength at 548 nm for adjusting the camera in the focal plane. Thereby, the lens is illuminated with an elliptical spot that has a major axis of 2.5 cm and a minor axis of 1.5 cm (area = $\pi \times 2.5 \times 1.5$) axially and in 12 steps of 2.5 cm off-axially. Then, a series of measurements was recorded with the wavelengths 453 nm and 649 nm respectively. Images with wavelength of 548 nm were recorded at different tilt angles. Fig. 5-43 shows the images through illumination of the centre of Fresnel lens SC 208 at the wavelength 548 nm [56].
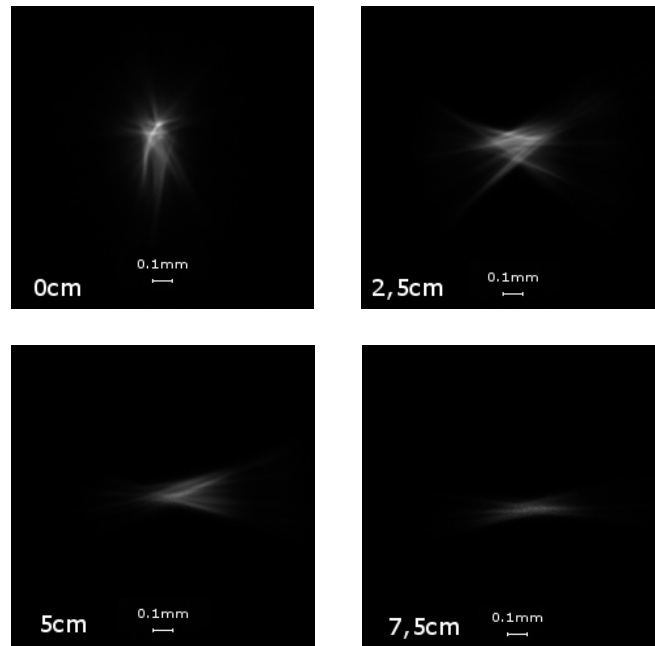
Fig. 5-43 Images at the wavelength 548 nm through illumination of the centre of Fresnel lens SC 208.

5.10.2 Data Analysis

Under the assumption that the Fresnel lens is rotationally symmetric, we can calculate the concentration ratio from knowing the radius of the image at the focus R measured from one side and the radius of the Fresnel lens itself (16.5 cm).

The images are overlaid with a computer graphic programme (GIMP) in 128 steps of 360°/128 weighted around a centre point. With the help of the computer programme (Origin), the radius of the circular image, which contains 68% of the total intensity, can be determined. Fig. 5-44 shows the intensity profile of the photos for the wavelength 649 nm. Fig. 5-45 shows the intensity profile of the photos for the wavelength 548 nm. Fig. 5-46 shows the intensity profile of the photos for the wavelength 453 nm. Accordingly, Table 5-3 shows the calculated concentration ratio of the Fresnel lens SC 208 as a function of the used wavelength [56].
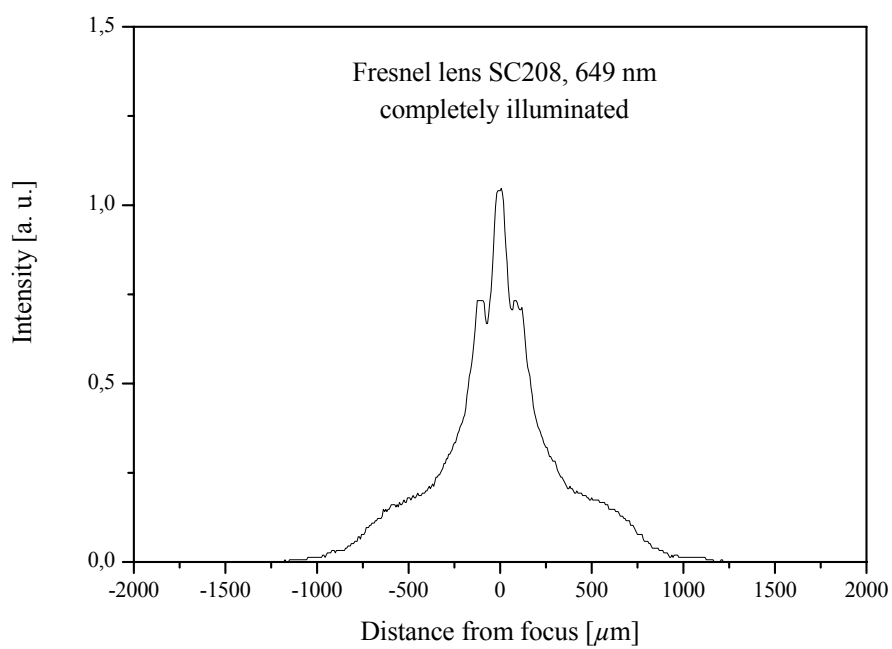
Fig. 5-44 Intensity profile of the photos for the wavelength 649 nm.
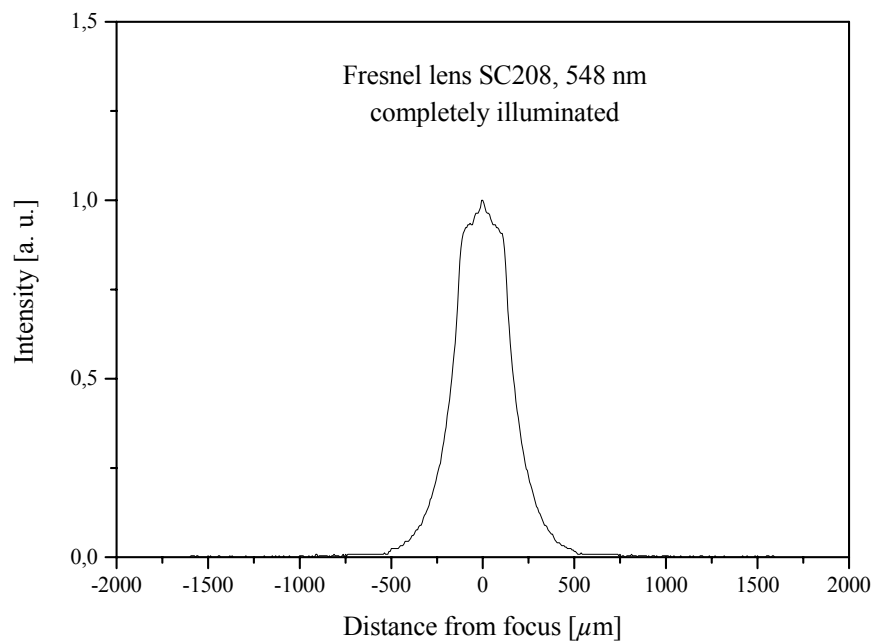
Fig. 5-45 Intensity profile of the photos for the wavelength 548 nm.
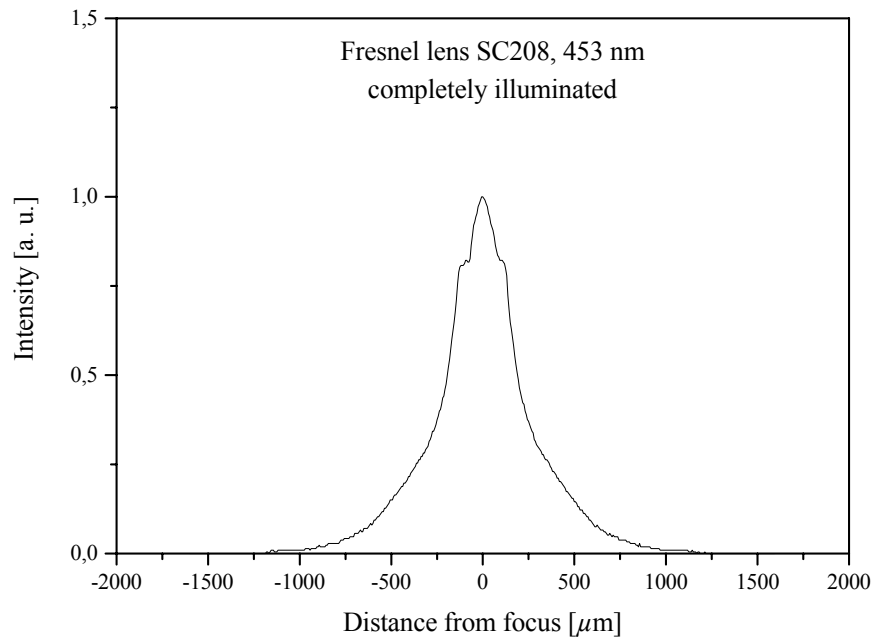
Fig. 5-46 Intensity profile of the photos for the wavelength 453 nm.

Wavelength λ [nm]	Radius of focus R [mm]	Concentration ratio C
548	0.30	12.1×10^5
453	0.52	4.05×10^5
649	0.63	2.79×10^5

Table 5-3 Concentration ratio of the Fresnel lens as a function of the used wavelength.

The determined concentration ratios are along way (about 16 %) from the upper limits which are given through the diffraction.

Using the programme (Origin), the integrals over the intensity of the photos, which recorded at different tilt angles to the normal plane, are formed. It appears that the intensity decreases inversely with the larger angles of tilt. Fig. 5-47 shows the photos at the focal plane for different tilt angles of the Fresnel lens SC 208, while Fig. 5-48 shows the representation of the intensity loss as a function of the tilt angle for the same Fresnel lens [56].
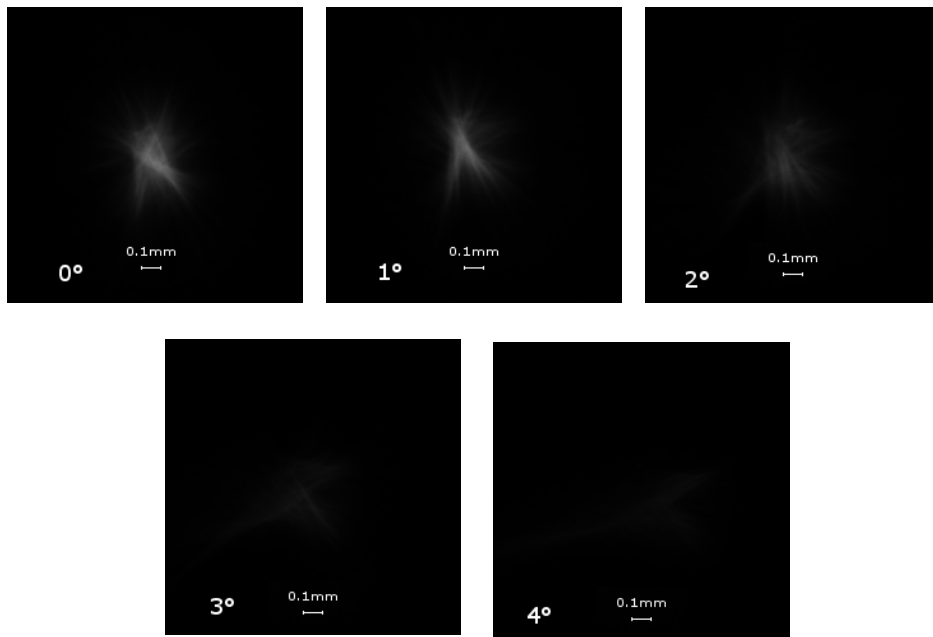
Fig. 5-47 Photos of the focal plane for different tilt angles of the Fresnel lens.
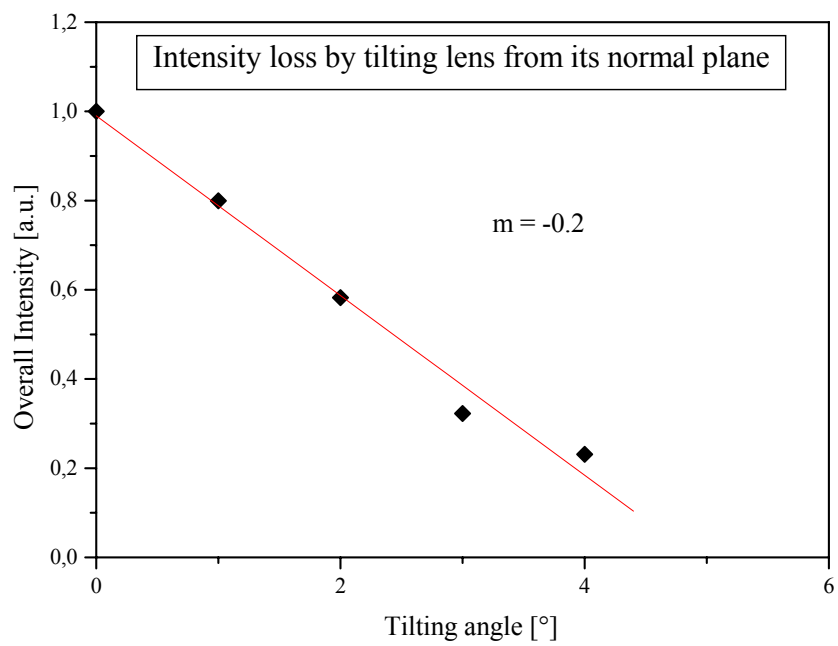
Fig. 5-48 Intensity loss through the tilting of the lens to the normal plane.

5.11 Measurements and results for the whole system of the Mirror array and Fresnel lens

After testing the Fresnel lens, we wanted to test the whole system under outdoor conditions. We selected a suitable and safe place on the rooftop of the main campus of the Technical University of Berlin to build our whole system.

During the two months of September and October 2004, we recorded with our system under all the possible conditions of weather. There were relatively sunny days especially in September, which can be considered as one of the best months for such measurements in Berlin in the year.

With the system of the mirror array alone, we could reach a power of more than 2 kW which is corresponding to an intensity value of 55 kW/m^2. After adding the Fresnel lens SC 208 as an additional concentrator, the values for the intensity increased to 110 kW/m^2. This represents a concentration ratio of about 110. A sample of our measurements is shown in Table 5-4.

Time	Solar radiation (w)	Solar radiation intensity on the sensor (w/m²)	Image area	Measured concentrated solar radiation on the sensor (w)	Concentrated solar radiation (w/m²)	Concentration ratio	Additional Fresnel lens (SC 208)			
							Concentrated solar radiation on the sensor (w)	Image area	Concentrated solar radiation intensity (w/m²)	Total concentration ratio
13:12	2.84	1.004×10^3	22 cm × 21 cm	157.41	5.567×10^4	55.426	302.4	11 cm × 11 cm	1.07×10^5	106.479
14:30	2.87	1.015×10^3	22 cm × 21 cm	162	5.73×10^4	56.446	310.5	11 cm × 11 cm	1.098×10^5	108.188
14:51	2.8	990.297	22 cm × 21 cm	148.5	5.252×10^4	53.036	297	11 cm × 11 cm	1.05×10^5	106.071

Table 5-4 Measurements of the mirror-array system with using the Fresnel lens SC 208.

We also used alternatively another Fresnel lens (SC 229) with the mirror array. This lens has a diameter of 39 cm and a focal length of 40 cm. The results of this lens were not better than the previous one (SC 208). Therefore, we decided to keep measuring with Fresnel lens (SC 208). A sample of our measurements with the Fresnel lens (SC 229) is shown in Table 5-5.

Time	Solar radiation (w)	Solar radiation intensity on the sensor (w/m^2)	Image area	Measured concentrated solar radiation on the sensor (w)	Concentrated solar radiation (w/m^2)	Concentration ratio	Additional Fresnel lens (SC 229)			
							Concentrated solar radiation on the sensor (w)	Image area	Concentrated solar radiation intensity (w/m^2)	Total concentration ratio
13:12	2.84	1.004×10^3	22 cm × 21 cm	157.41	5.567×10^4	55.426	221.4	13 cm × 13 cm	7.83×10^4	77.958
14:30	2.87	1.015×10^3	22 cm × 21 cm	162	5.73×10^4	56.446	224.1	13 cm × 13 cm	7.926×10^4	78.084
14:51	2.8	990.297	22 cm × 21 cm	148.5	5.252×10^4	53.036	216	13 cm × 13 cm	7.639×10^4	77.143

Table 5-5 Measurements of the mirror-array system with using the Fresnel lens SC 229.

218

Summary

To stimulate a high threshold level solid state laser, a light source of high optical stimulating power is needed. In the classical laser systems, pulsed or cw- flashlamps, while in the modern ones diode lasers are used. Although the latter are very efficient, they are expensive.

The use of the solar-pumped laser could be advantageous in the underdeveloped countries which have reliable intensive sun shine. The applications using the concentrated thermal solar radiation can reach a fraction of the sun surface temperature (< 6000 K). However, laser generation does not lie in the field of thermal application. In the solar laser field, the solar energy is converted into laser energy. With the well-established design of lasers, the beam quality, compared with a classical light source, has been significantly improved.

Directly pumped solar lasers are only able to be applied if the processes are not time-critical. These applications could be welding, soldering, cutting and hardening, especially in the field of the micro-mechanics or for light stimulated chemical conversion processes. Nevertheless, the solar radiation must be high enough to reach the threshold level.

These solar pumped lasers could be interesting in the following fields of application:

- **On earth:**

High power solar pumped lasers could be used for industrial applications (e.g. processing, laser welding, photochemistry etc.). This can be realized in a factory where one laser produces the radiation which is delivered via glass fibres to the application sites. Another possible terrestrial application could be the pollutant control and analysis of samples with a mobile measuring system.

- **In space:**

They could be used as an energy source for transmission of energy to other satellites, for space communication and for telemetric purposes.

The part of the solar spectrum that can not be used by the laser could be converted to electrical energy by means of photovoltaic systems or a thermal engine.

We can summarize our aim of this work in the following points:

4- Getting an alternative method for using solar energy.

5- Transformation of the solar energy directly to laser radiation without conversion to electrical energy.

6- Beginning of large scale projects for using the solar energy to generate the laser beam needed in different fields of recent technologies.

Simulation of a solid-state solar pumped laser systems using standard concentrators

As a beginning, one could use a concentration system consisting of a paraboloidal concentrator, as a primary concentrator, and a non-imaging concentrator like the compound parabolic concentrator (CPC) or the conical concentrator, as a secondary one. The calculations were made to optimize the dimensions for both concentrators.

Side pumping technique

The calculations of this model gave a laser output power of approximately 20 W corresponding to an intensity of 10^6 W/m^2 where the mean insolation level is 600 W/m^2.

Side pumping technique

The calculations of this model gave a laser output power of 0.54 W representing an intensity of 2.75×10^4 W/m^2 where the mean insolation level is 600 W/m^2. If the acceptance angle of the conical concentrator was increased to greater than 22°, we were unable to overcome the pumping threshold and hence no laser output was observed. Therefore, a conical concentrator as an easily manufactured concentrator is less useful as such an application

Therefore, the concentrators of the type three-dimensional compound parabolic concentrator (3D-CPC) are preferable in such a case because they can give suitable large acceptance angles with relatively small dimensions. The use of these types of concentrators therefore avoids the building of massive, large and expensive constructions.

The calculations of this model gave a laser output power of 0.75 W representing an intensity of 3.84×10^4 W/m^2 where the mean insolation level is 600 W/m^2.

Therefore, if we want to improve this large scale project of a solar pumped laser, we have to find new techniques which could realize two important goals needed. These two important goals are:

3- The simplicity of such a system, i.e. to construct such a system from portable components, which are easy to be controlled and repaired.

4- Lower costs for constructing and manufacturing such a system.

The Fresnel lens should be considered because on the one hand it has a relatively high level of optical concentration, and on the other hand it is relatively inexpensive. A practical solution would be to mount the Fresnel lens on an astronomical mount in order to track the sun. The high concentration level of the Fresnel lens is already known. The main disadvantage of such a system would be the relatively low obtainable concentration ratio which would be insufficient to overcome the lasing threshold one.

Another reasonable idea is the use of a mirror array concentrator (sometimes called Fresnel reflector). Such an array can work as a massive imaging parabolic concentrator if each single mirror has a certain angle in order to collect all of the reflected radiations into a certain place which we will call here the focus. If all of the mirrors have the same

dimensions, this focus will theoretically have the dimensions of a single mirror. The main disadvantage for such a system could be the difficulty to keep the resulted focus in the same place because of the apparent motion of the sun during the day.

Concentration system of Fresnel lenses as primary concentrators

We have investigated two large Fresnel lenses (named FLI and FLII). Each one was used as a primary concentrator for pumping the laser. Both of them have a rectangular form and are made from PMMA. They are held in a wooden frame fixed by aluminium arms onto an optical bench that is placed on an astronomical mount, tracking the sun by means of an electrical DC-motor. This mount EX6 is powered by 4 batteries of 1.5 Volts. The calculations showed that the maximum concentration ratio of the Fresnel lens FLI (59.5 cm $\times$ 58.5 cm) is 8.787×10^3, while that of the Fresnel lens FLII (103.5 cm $\times$ 79.5 cm) is 1.206×10^3. The lens FLI can theoretically form an image of the solar disc of a radius of 3.546 mm, while the radius of the solar disch formed by the lens FLII has a rdius of 4.66 mm.

The area of the focus of FLI was measured to be 38 mm^2 (diameter of 7 mm). For this Fresnel lens system, we have measured the incident solar radiation on a normal sunny day in Berlin which is sufficient to obtain laser action. According to the measured solar radiation, we reached an intensity of 510 W/m^2, which represents a power of 177.5 W. This was focused through the Fresnel lens onto the laser crystal of dimensions (28 mm $\times$25 mm $\times$ 7 mm). In the same manner we measured the diameter of the focus of FLII to be 12 mm.

We have investigated the properties of the two Fresnel lenses and their concentration ratios under out door conditions. Using a sensor of type Gentec PS-150 in connection with a power meter (type Gentec TPM-300), we recorded the power and the intensity of the concentrated solar radiation. The power measured by applying FLI was 230 W which represents an intensity of 2.6×10^6 W/m^2, while it was 440 W for FLII which represents 2.25×10^6 W/m^2.

We tested the both Fresnel lenses and found they have a chromatic aberration which has no effect on their concentration for generating the laser beam. We also found that the image quality of the Fresnel lens FLI is better than that of the Fresnel lens FLII.

We also tested the laser crystal of the type Nd:YAG in the laboratory and developed a model for generating the laser for it. The threshold pumping power was calculated to be 176.138 W.

After there, we used an additional collimating concentrator of the form of a lens to reduce the focusing area of the Fresnel lens and accordingly to increase the concentration level of the whole system till factor 4. This additional collimator lens was chosen to be a convex lens of diameter of 7.85 cm and with a focal length of 5 cm. A special holder was designed and constructed in the workshop to adapt it for the system.

We used another laser rod of the type Nd:YVO$_4$. Therefore, we designed a new secondary non-imaging concentrator of the type Compound Spherical Concentrator (CSC). Accordingly, we designed a new cavity to hold the laser rod with the secondary concentrator.

We tested the secondary concentrator in the laboratory and found that it can reach up to 4 times. Its dimensions allow using it within an interval of angle of incidence which lies

between –20º and +20º. Outside this range, the concentrator will not work any more. Moreover, it will attenuate the radiation needed to be concentrated.

The laser rod was tested and adjusted its cavity in the laboratory using a diode laser to see the effect of the CSC-Concentrator on the laser output. Therefore, two types of data were recorded; the output power without the concentrator and with it. Laser output of 10 mW has been obtained using an input power of 650 mW from a laser diode (808 nm).

Fixed mounted solar laser system using adaptive mirrors

Stationary mirror array system for the solar-pumped-laser system

We studied building a stationary system of mirror array to concentrate the solar radiation. During the day and because of the apparent motion of the sun, the focus of this concentration system can not be held in the same position. We calculated the divergences of the reflected radiations during one day in the vertical and the horizontal components. We found the the collection position (focus) of the reflected radiation moves during the day about one metre according to the vertical component of the apparent motion of the sun, while it moves about 16 metres according to the horizontal component of this apparent motion.

Adaptive mirror array system for the solar-pumped-laser system

We decided to use a group of 6 electro-mechanical motors in the system of the mirror array to let the system track the apparent motion of the sun. Accordingly we studied the variation of the angles of mirror units. Our system consisted of 105 flat mirrors divided into 3 rows. Each row has 7 panels. Each panel carries 5 mirrors. Three motors were responsible for tracking the apparent motion of the sun in its vertical component, while the other three motors were responsible for tracking the apparent motion of the sun in its horizontal component. We derived some forms to describe variation of the angles of the panels during the day as functions of the altitude and the azimuth of the sun. Accordingly, we calculated the variation of the setting angles of each panel during the day. Knowing these angles enabled us to calculate the number of electric pulses needed to be given to the motors in order to direct the panels according to these angles.

This system was considered as a geometrically easy but a relatively mechanically difficult system. This is because it is difficult to get the screw-nut fixed and easily moving through the day because the panel rotates around an axis in its centre line. To make it mechanically easier, we did a single modification, which is relatively easy. The panel must be higher than the main plane of rotation and the normal coupler of the holder itself rotates around an axis in the main plane. In this manner, we got a mechanically easier system although it could be geometrically difficult.

The new desktop-controlled adaptive mirror array system

After the decision of doing the last modification, we build the system of mirror array. We derived some forms to describe variation of the angles of the panels during the day as functions of the sltitude and the azimuth of the sun. Similarly as before, we calculated the

variation of the setting angles of each panel during the day. Knowing these angles enabled us to calculate the number of electric pulses needed to be given to the motors in order to direct the panels according to these angles.

We calculated the concentration behaviour of our mirror array system during the day. We found that the concentration ratio of the mirror array system varies during the day between 2071.24 and 2085.22. Moreover, the maximum values of this concentration ration is reached at the beginning and the end of the day, while the minimum value is reached at the noon.

We constructed this system, got it on the rooftop of the main campus of the Technical University of Berlin and made some measurements with it and with adding a circular small Fresnel lens of a focal length of 279.4 mm, 406.4 mm free aperture and 0.508 mm groove distance. Using 6 electro-mechanical motors controlled by a computer program, we could change the angles of each panel by giving a number of pulses (calculated according to the previous curves) to the motors in order to tip the panel over to hold the focus in a constant place during the time of the measurements.

With the system of the mirror array alone, we could reach a power of more than 2 kW which is corresponding to an intensity value of 55 kW/m^2. After adding the Fresnel lens SC 208 as an additional concentrator, the values for the intensity increased to 110 kW/m^2. This represents a concentration ratio of about 110.

We also used alternatively another Fresnel lens (SC 229) with the mirror array. This lens has a diameter of 39 cm and a focal length of 40 cm. The results of this lens were not better than the previous one (SC 208). Therefore, we decided to keep measuring with Fresnel lens (SC 208).

Conclusion

Solar directly-pumped laser of multi-stages optical concentrators for directly pumping solid state lasers have been constructed now using simple optical components and devices. Our study was dealing with two types of multi-stage systems; small- and medium-sized systems.

1- Small-sized directly solar-pumped laser system:

The first new achievement in our work was the substitution of the Fresnel lenses as primary concentrators instead of the large-dimensional paraboloidal mirrors. This system consisted of a Fresnel lens as a primary concentrator, a new secondary concentrator of the type of Compound Spherical Concentrator (CSC) and the laser cavity.

In the laser cavity, we used two types of laser crystals; a slab laser of the type of Nd:YAG and a laser rod of the type of Nd:YVO$_4$.

Two Fresnel lenses were used in our study. The First lens FLI has dimensions of 595 mm × 585 mm and focal length of 761 mm, while the second FII has dimensions of 1035 mm × 795 mm and focal length of 1000 mm. The measurement were recorded under the out-door conditions in Berlin (Germany).

The measurements taken with the Fresnel lens FLI showed a maximum concentrated solar radiation power of 230 W, which represents an intensity of 2.03 × 10^6 W/m^2. The measurements taken for the Fresnel lens FLII showed a maximum concentrated solar radiation power of 438 W, which represents an intensity of 2.9 × 10^6 W/m^2. As the two lenses were corrected for the lens errors, the lens spherical aberration played no role in lowering the concentrated solar radiation.

Using a secondary collimator lens to get a higher concentration ratio of the system proved that it was not a good idea because of the lens errors and the additional surface reflections which got the concentration ratio lower. Therefore, we could not reach the pumping threshold.

Using a simulation computer program, we developed a new type of secondary concentrator that matches the dimensions of the both the Fresnel lenses and the laser cavity. This secondary concentrator was of a new geometrical type. Because it was cut from a spherical convex lens (made from glass type of BK7), we called it Compound Spherical Concentrator (CSC). This concentrator got the concentration ratio of the system about 4 times higher together with a good distribution of the concentrated solar radiation.

As a continuous development for such a new concentrator, we developed similar concentrators again with making a hole for the laser rod. This can be a substitution of designing a separate cavity for the rod.

The laser output of such a system will be transferred using a flexible optical fibre. Therefore, such a system can be considered as an easily constructed, portable, low costing system.

2- Medium-sized directly solar-pumped laser system:

Because the output of the above mentioned solar laser system is low, it may be not able to be used in the large scale projects in which relatively higher output powers are needed. Therefore, we designed a new large solar directly-pumped laser system.

The idea of this new system is based on the partition of the primary concentrator to many flat mirrors which are directed in such a manner that each single mirror has its own angle in order to get the solar radiation reflected from each single mirror in one position. The system of such a mirror array consists of 105 mirrors distributed in three rows. Each row contains 7 panels. Finally, each panel carries 5 mirrors. A group of six electro-mechanical desktop-controlled motor was used to let the system track the sun during the day. Three of those motor were responsible for the tracking in the vertical (altitude) component, while the other tree motors were responsible for the tracking in the horizontal (azimuth) component. The measurements for this system were taken on the rooftop of the main campus of the Technical University of Berlin.

The measurements taken for this showed reaching the concentrated solar radiation power to 60 W, which represents an intensity of 5.73×10^4 W/m^2.

Using an additional circular Fresnel lens of 40 cm diameter and a focal length of 27.9 cm, we could increase the concentrated solar radiation power to 115 W, which represents an intensity of 1.098×10^5 W/m^2.

As a further development, one can use an additional non-imaging concentrator like that what we used before (CSC) for a further increasing of the concentrated solar radiation. The system will be a three-stages-concentrator system.

This system will be used in the medium scale solar laser projects where relatively high output power needed.

Such a system of concentrators can moreover be used in other applications and purposes like: lighting houses, heating, cooling in refrigerators and many other applications.

We have to say that both systems were tested in Berlin (Germany). If we used this system in a place of better solar radiation condition, better results could be readily obtained.

Solar pumped laser systems are recommended for the countries which receive high amounts of solar radiation during the year (e.g. Egypt). They are also recommended for the north countries (e.g. Germany) which have long summer days even if they have low amounts of solar radiation in the other seasons.

Appendix I: Earth-Sun Geometry

Earth Rotation and Revolution

The term Earth rotation refers to the spinning of the Earth on its axis. One rotation takes exactly twenty-four hours and is called a mean solar day. If you could look down at the Earth's North Pole from space you would notice that the direction of rotation is counterclockwise. The opposite is true if you viewed the Earth from the South Pole.

The orbit of the Earth around the sun is called Earth revolution. This celestial motion takes 365 1/4 days to complete one cycle. Further, the Earth's orbit around the sun is not circular, but elliptical as shown in Fig. AI-1. An elliptical orbit causes the Earth's distance from the sun to vary annually. However, this phenomenon does not cause the seasons. This annual variation in the distance from the sun does influence the amount of solar radiation intercepted by the Earth by approximately 6 %. On January 3rd, perihelion, the Earth is closest to the sun (147.5 million kilometers). The Earth is farthest from the sun on July 4th, or aphelion. The average distance of the Earth from the sun over a one year period is 150 million kilometers.
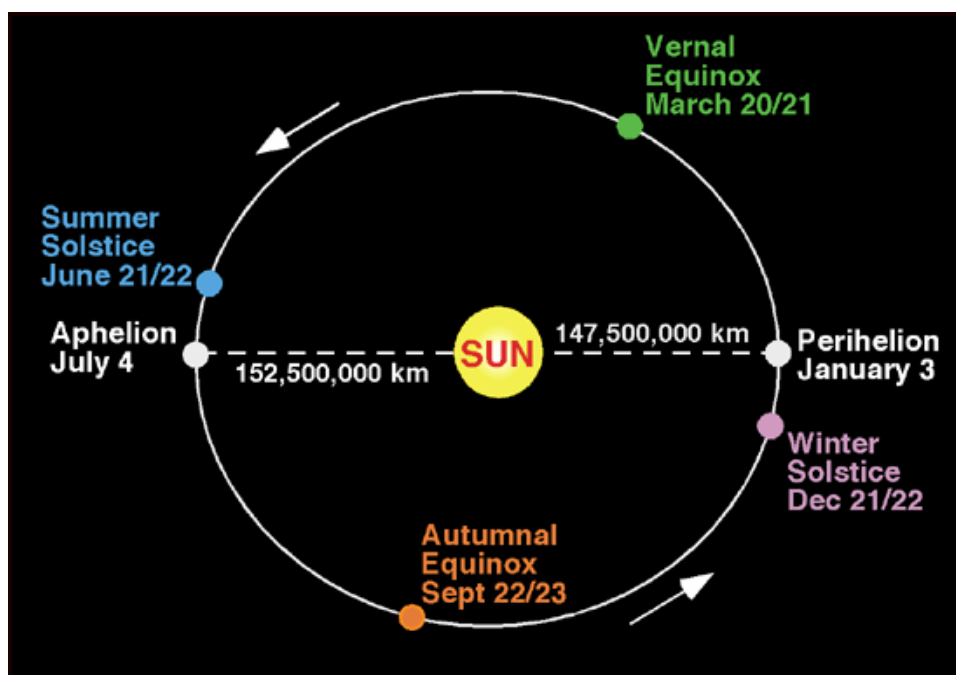
Fig. AI-1 Position of the equinoxes, solstices, aphelion, and perihelion on the Earth's orbit.

Tilt of the Earth's Axis

The Earth's axis is not perpendicular to the plane of the ecliptic, but inclined at a fixed angle of 23.45°. Moreover, the northern end of the Earth's axis always points to the same place in space (North Star). This circumstance is responsible for the annual changes in the

height of the sun above the horizon. It also causes the seasons, by controlling the intensity and duration of sunlight received by locations on the Earth.

On June 21 or 22, the Summer solstice, the Earth is positioned in its orbit so that the North Pole is leaning 23.45° toward the sun. During the Summer solstice, all locations North of the equator have day lengths greater than twelve hours, while all locations South of the equator have day lengths less than twelve hours as shown in Table A1-1. On December 21 or 22, the Winter solstice, the Earth is positioned so that the South Pole is leaning 23.45° toward the sun. During the Winter solstice, all locations North of the equator have day lengths less than twelve hours, while all locations South of the equator have day lengths greater than twelve hours as shown in Table AI-1.

Latitude	Winter Solstice	Equinoxes	Summer Solstice
90° N	0:00	Sun at Horizon	24:00
80° N	0:00	12:00	24:00
70° N	0:00	12:00	24:00
66.5° N	Sun at Horizon	12:00	24:00
60° N	5:33	12:00	18:27
50° N	7:42	12:00	16:18
40° N	9:08	12:00	14:52
30° N	10:04	12:00	13:56
20° N	10:48	12:00	13:12
10° N	11:25	12:00	12:35
Equator	12:00	12:00	12:00
10° S	12:35	12:00	11:25
20° S	13:12	12:00	10:48
30° S	13:56	12:00	10:04
40° S	14:52	12:00	9:08
50° S	16:18	12:00	7:42
60° S	18:27	12:00	5:33
66.5° S	24:00	12:00	Sun at Horizon
70° S	24:00	12:00	0:00
80° S	24:00	12:00	0:00
90° S	24:00	Sun at Horizon	0:00

Table AI-1 Day Lengths for selected latitudes (hours and minutes).
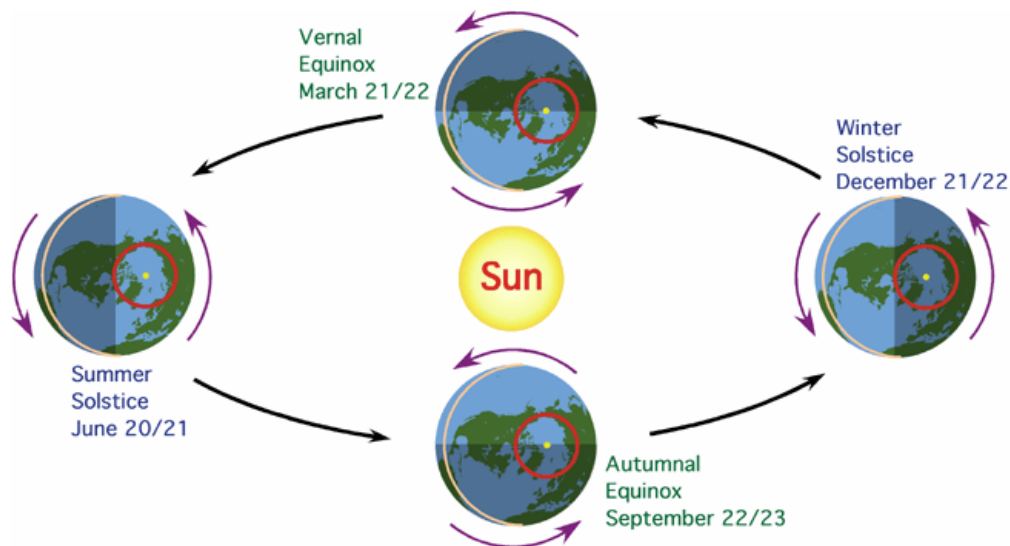
Fig. AI-2 Annual change in the position of the Earth in its revolution around the sun. In this graphic, we are viewing the Earth from a position in space that is above the North Pole (yellow dot) at the Summer solstice, the Winter solstice, and the two equinoxes. Note how the position of the North Pole on the Earth's surface does not change. However, its position relative to the sun does change and this shift is responsible for the seasons. The red circle on each of the Earths represents the Arctic Circle (66.5° N). During the Summer solstice, the area above the Arctic Circle is experiencing 24 hours of daylight because the North Pole is tilted 23.45° toward the sun. The Arctic Circle experiences 24 hours of night when the North Pole is tilted 23.45° away from the sun in the Winter solstice. During the two equinoxes, the circle of illumination cuts through the polar axis and all locations on the Earth experience 12 hours of day and night.

On September 22 or 23, the Autumnal equinox, neither pole is tilted toward the sun. March 20 or 21 marks the arrival of the Spring or Vernal equinox when once again the poles are not tilted toward the sun. Day lengths on both of these days, regardless of latitude, are exactly 12 hours.
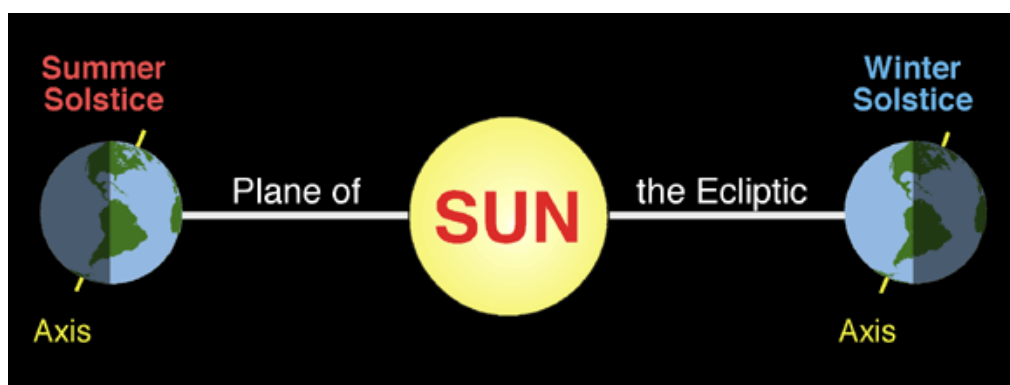
Fig. AI-3 During the Summer solstice the Earth's North Pole is tilted 23.45° towards the sun relative to the circle of illumination. This phenomenon keeps all places above a latitude of 66.5° N in 24 hours of sunlight, while locations below a latitude of 66.5° S are in darkness. The North Pole is tilted 23.45° away from the sun relative to the circle of illumination during the Winter solstice. On this date, all places above a latitude of 66.5° N are now in darkness, while locations below a latitude of 66.5° S receive 24 hours of daylight.
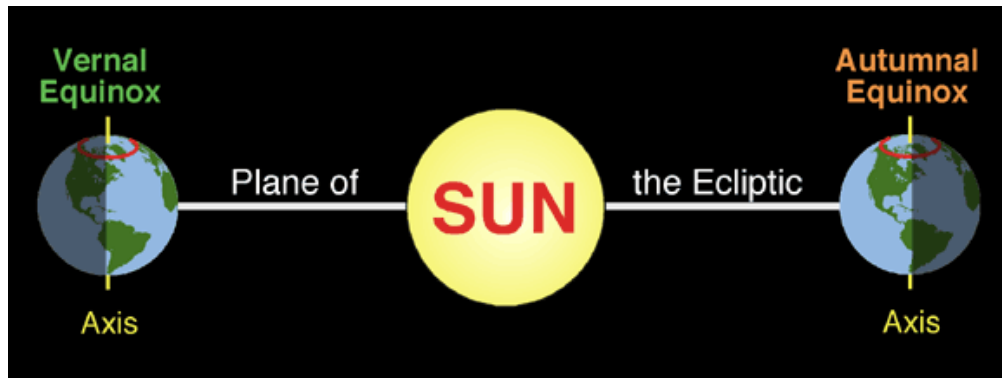
Fig. AI-4 During the equinoxes, the axis of the Earth is not tilted toward or away from the sun and the circle of illumination cuts through the poles. This situation does not suggest that the 23.45° tilt of the Earth no longer exists. The vantage point of this graphic shows that the Earth's axis is inclined 23.45° toward the viewer for both dates. The red circles shown in the graphic are the Arctic Circle.

Axis Tilt and Solar Altitude

The annual change in the relative position of the Earth's axis in relationship to the sun causes the height of the sun (solar altitude) to vary in our skies. The total variation in maximum solar altitude for any location on the Earth over a one year period is 47° (2 × 23.45 = 47). For example, at 50° North maximum solar altitude varies from 63.5° on the Summer solstice to 16.5° on the Winter solstice as shown in Fig. AI-5. Maximum solar height at the equator goes from 66.5° above the northern end of the horizon during the Summer solstice, to directly overhead on the fall equinox, and then down to 66.5° above the southern end of the horizon during the Summer solstice as shown in Fig. AI-6.
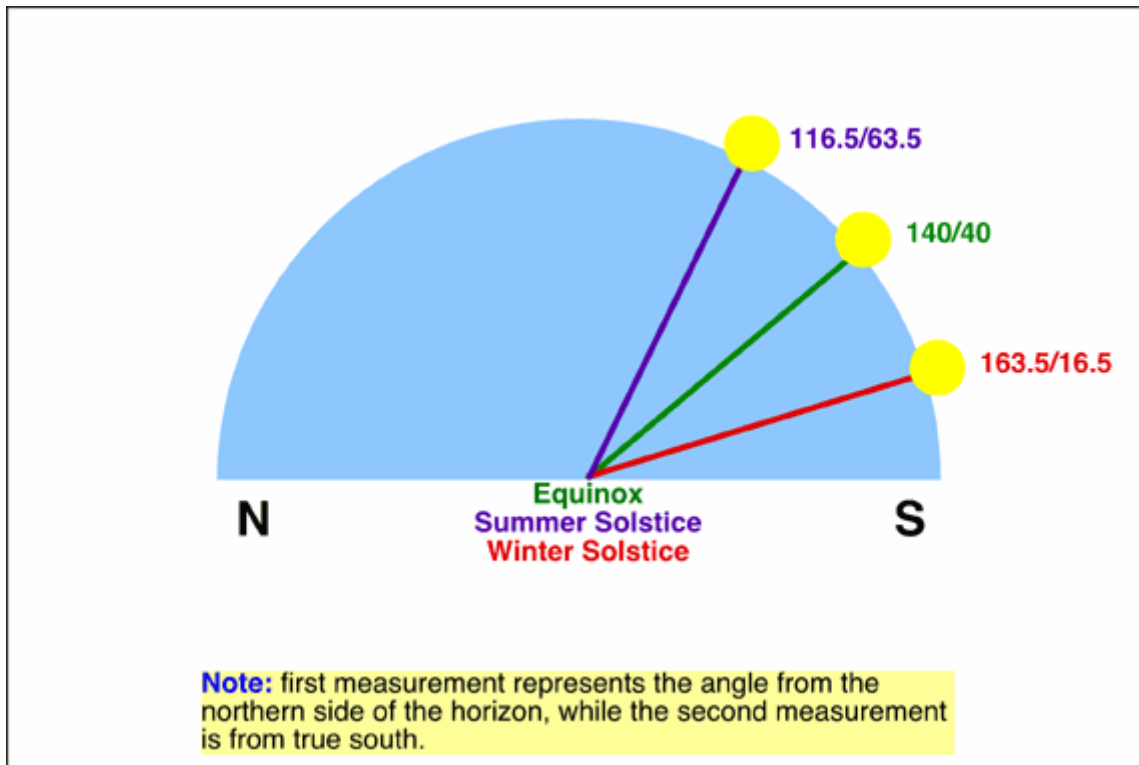
Fig. AI-5 Variations in solar altitude at solar noon for 50° North during the Summer solstice, equinox, and Winter solstice.
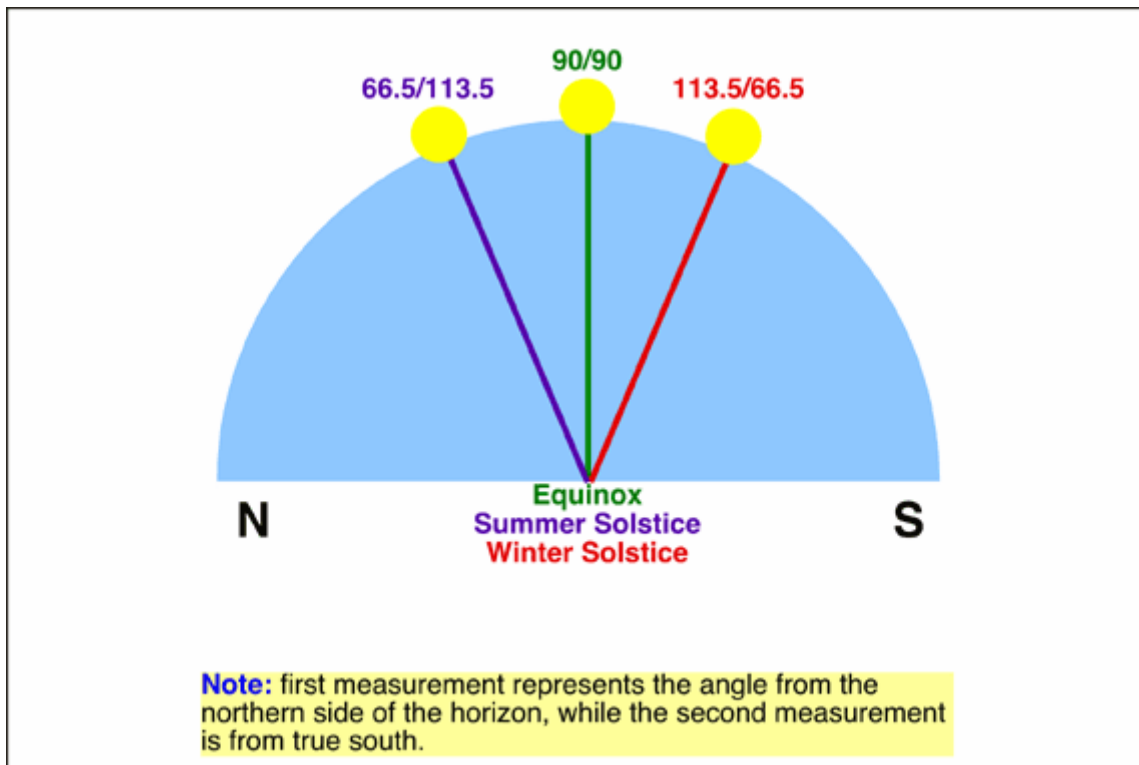
Fig. AI-6 Variations in solar altitude at solar noon for the equator during the Summer solstice, equinox, and Winter solstice.

The location on the Earth where the sun is directly overhead at solar noon is known as the subsolar point. The subsolar point occurs on the equator during the equinoxes as shown in Fig. AI-7 (a). During the Summer solstice, the subsolar point moves to the Tropic of Cancer because at this time the North Pole is tilted 23.45° toward the sun. The subsolar point is located at the Tropic of Capricorn on the Winter solstice. On this date, the South Pole is now tilted toward the sun as shown in Fig. AI-7 (b).

(a)   (b)
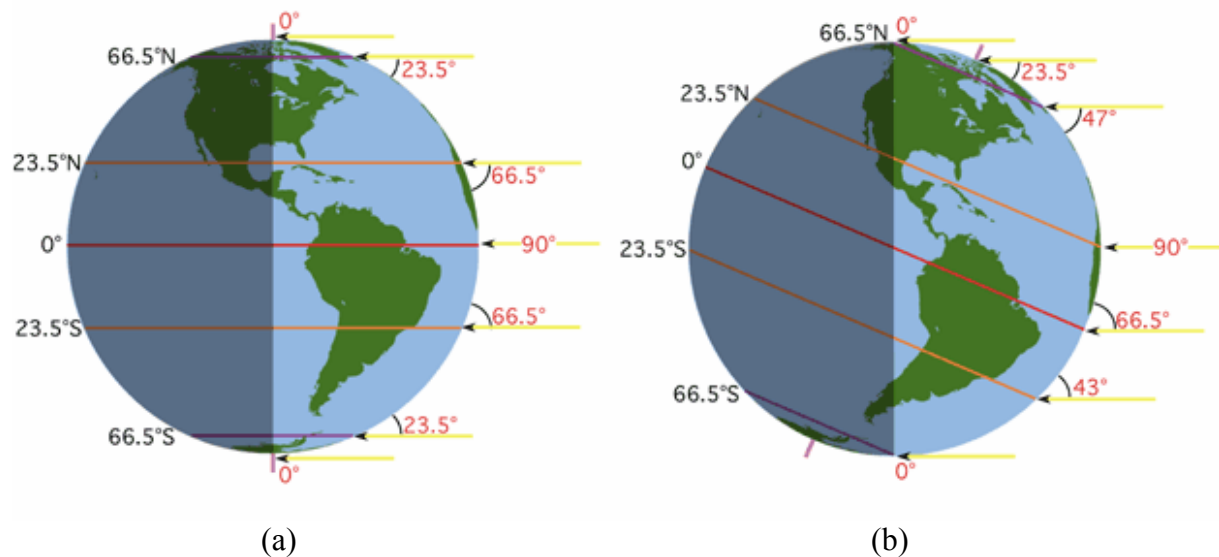
Fig. (AI-7) Relationship of maximum sun height to latitude for the equinox (left) and Summer solstice (right). The red values on the right of the globes are maximum solar altitudes at solar noon. Black numbers on the left indicate the location of the Equator, Tropic of Cancer (23.45° N), Tropic of Capricorn (23.45° S), Arctic Circle (66.5° N), and the Antarctic Circle (66.5° S). The location of the North and South Poles are also identified. During the equinox, the equator is the location on the Earth with a sun angle of 90° for solar noon. Note how maximum sun height declines with latitude as you move away from the Equator. For each degree of latitude travelled maximum sun height decreases by the same amount. At equinox, you can also calculate the noon angle by subtracting the location's latitude from 90. During the Summer solstice, the sun is now directly overhead at the Tropic of Cancer. All locations above this location have maximum sun heights that are 23.45° higher from the equinox situation. Places above the Arctic Circle are in 24 hours of daylight. Below the Tropic of Cancer the noon angle of the sun drops one degree in height for each degree of latitude travelled. At the Antarctic Circle, maximum sun height becomes 0° and locations south of this point on the Earth are in 24 hours of darkness.

Table AI-2 describes the changes in solar altitude at solar noon for the two solstices and equinoxes. All measurements are in degrees (horizon has 180° from True North to True South) and are measured from either True North or True South (whatever is closer).

Location's Latitude	Vernal Equinox March 21/22	Summer Solstice June 20/21	Autumnal Equinox September 22/23	Winter Solstice December 21/22
90° N	0°	23.45°	0°	- 23.45°
70° N	20°	43.5°	20°	-3.5°
66.5° N	23.45°	47°	23.45°	0°
60° N	30°	53.5°	30°	6.5°
50° N	40°	63.5°	40°	16.5°
23.45° N	66.5°	90°	66.5°	43°
0°	90°	66.5°	90°	66.5°
23.45° S	66.5°	43°	66.5°	90°
50° S	40°	16.5°	40°	63.5°
60° S	30°	6.5°	30°	53.5°
66.5° S	23.45°	0°	23.45°	47°
70° S	20°	-3.5°	20°	43.5°
90° S	0°	- 23.45°	0°	23.45°

Table AI-2 Maximum sun altitudes for selected latitudes during the two solstices and equinoxes.

Some astronomical definitions

Solar Altitude
> Height of the sun above the horizon from either True North or True South.

Solar Noon
> Point of time during the day when the sun is aligned with True North and True South.

True North
> Direction of the North Pole from an observer on the Earth.

True South
> Direction of the South Pole from an observer on the Earth.

North Pole
> Surface location defined by the intersection of the polar axis with Earth's surface in the Northern Hemisphere. This location has a latitude of 90° North.

South Pole
> Surface location defined by the intersection of the polar axis with Earth's surface in the Southern Hemisphere. This location has a latitude of 90° South.

Polar Axis
> Is a line drawn through the Earth around the planet rotates. The point at which the polar axis intercepts the Earth's surface in the Northern Hemisphere is called the North Pole. Likewise, the point at which the polar axis intercepts the Earth's surface in the Southern Hemisphere is called the South Pole.

Latitude

Latitude is a north-south measurement of position on the Earth. It is defined by the angle measured from a horizontal plane located at the Earth's center that is perpendicular to the polar axis. A line connecting all places of the same latitude is termed aparallel. Latitude is measured in degrees, minutes, and seconds. Measurements of latitude range from equator (0°) to 90° North and South from this point.

Longitude

Longitude is a west-east measurement of position on the Earth. It is defined by the angle measured from a vertical plane running through the polar axis and the prime meridian. A line connecting all places of the same longitude is termed a meridian. Longitude is measured in degrees, minutes, and seconds. Measurements of longitude range from prime meridian 0° to 180° West and East from this point.

Equator

Location on the Earth that has a latitude of 0°.

Meridian

A circular arc that meets at the poles and connects all places of the same lonitude.

Prime Meridian

The location from which meridians of longitude are measured.

It has the measure of 0° of longitude. The prime meridian was selected by international agreement to run through Greenwich, England.

Celestial equator

The outward projection of earth's equator.

Thus at earth's equator the celestial equator passes through the zenith and at the earth's pole the celestial equator lies along the horizon.

Celestial pole

A point on celestial sphere intersected by the earth's axis of rotation.

Declination

The angular distance on the celestial sphere above or below the celestial equator.

Right Ascension

The distance measured (in hours of time) eastward along the celestial equator starting at the location of the sun at vernal equinox.

Zenith

Directly overhead; altitude of 90 degrees.

Zenith sun refers to the situation of the sun crossing the zenith. The sun never crosses the zenith at Boulder. Only between the Tropic of Cancer (latitude +23.45 degrees) and Tropic of Capricorn (latitude -23.45 degrees) does the sun cross the zenith.

The yearly change in the position of the Earth's axis relative to the plane of the ecliptic also causes seasonal variations in day length to all locations outside of the equator. Longest days occur during the Summer Solstice for locations north of the equator and on the Winter Solstice for locations in the Southern Hemisphere. The equator experiences equal

day and night on every day of the year. Day and night is also of equal length for all Earth locations on the Autumnal and Vernal equinoxes. Fig. AI-8 describes the change in the length of day for locations at the equator, 10, 30, 50, 60, and 70° North over a one-year period. The illustration suggests that days are longer than nights in the Northern Hemisphere from the March equinox to the September equinox. Between the September to March equinox days are shorter than nights in the Northern Hemisphere. The opposite is true in the Southern Hemisphere. The graph also shows that the seasonal (Winter to Summer) variation in day length increases with increasing latitude.
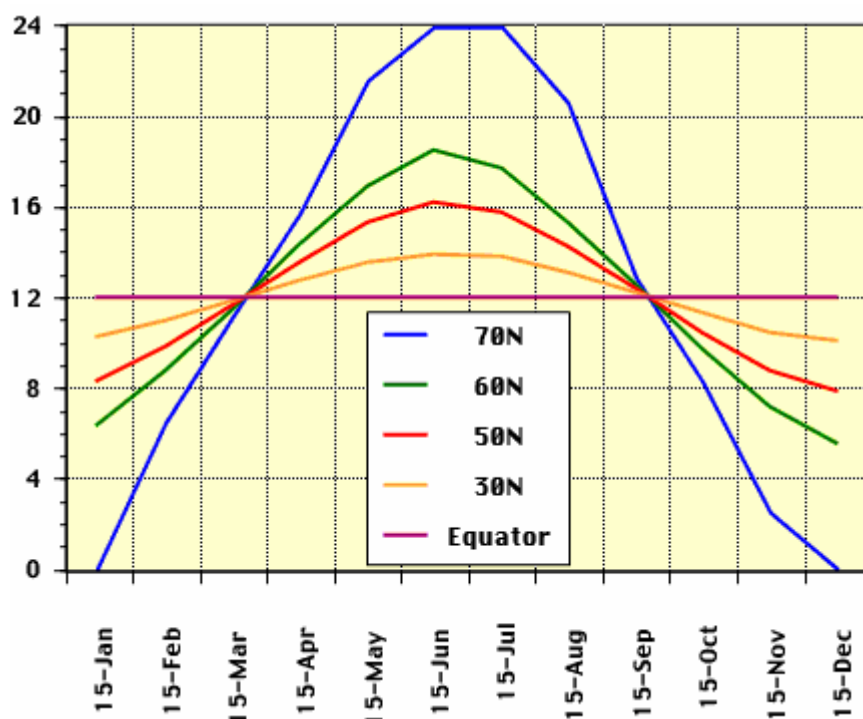
Fig. AI-8 Annual variations in day length for locations at the equator, 30, 50, 60, and 70° North latitude.

Variation of the recorded solar radiation due to the location on the earth

Fig. AI-9 describes the potential insolation available for the equator and several locations in the Northern Hemisphere over a one-year period. The values plotted on this graph take into account the combined effects of angle of incidence and day length durationas shown in Table AI-1. Locations at the equator show the least amount of variation in insolation over a one-year period. These slight changes in insolation result only from the annual changes in the altitude of the sun above the horizon, as the duration of daylight at the equator is always 12 hours. The peaks in insolation intensity correspond to the two equinoxes when the sun is directly overhead. The two annual minimums of insolation occur on the solstices when the maximum height of the sun above the horizon reaches an angle of 66.5°.

The most extreme variations in insolation received in the Northern Hemisphere occur at 90° North. During the Summer Solstice this location receives more potential incoming

solar radiation than any other location graphed. At this time the sun never sets. In fact, it remains at an altitude of 23.45° above the horizon for the whole day. From September 22 (Autumnal Equinox) to March 21, (Vernal Equinox) no insolation is received at 90° North. During this period the sun slips below the horizon as the northern axis of the Earth becomes tilted away from the sun.

The annual insolation curve for locations at 60° North best approximates the seasonal changes in solar radiation intensity perceived at our latitude. Maximum values of insolation are received at the Summer solstice when day length and angle of incidence are at their maximum as shown in Table AI-2. During the Summer Solstice day length is 18 hours and 27 minutes and the angle of the sun reaches a maximum value of 53.5° above the horizon. Minimum values of insolation are received at the Winter Solstice when day length and angle of incidence are at their minimum as shown in Table AI-2. During the Winter Solstice day length is only 5 hours and 33 minutes and the angle of the sun reaches a lowest value of 6.5° above the horizon.
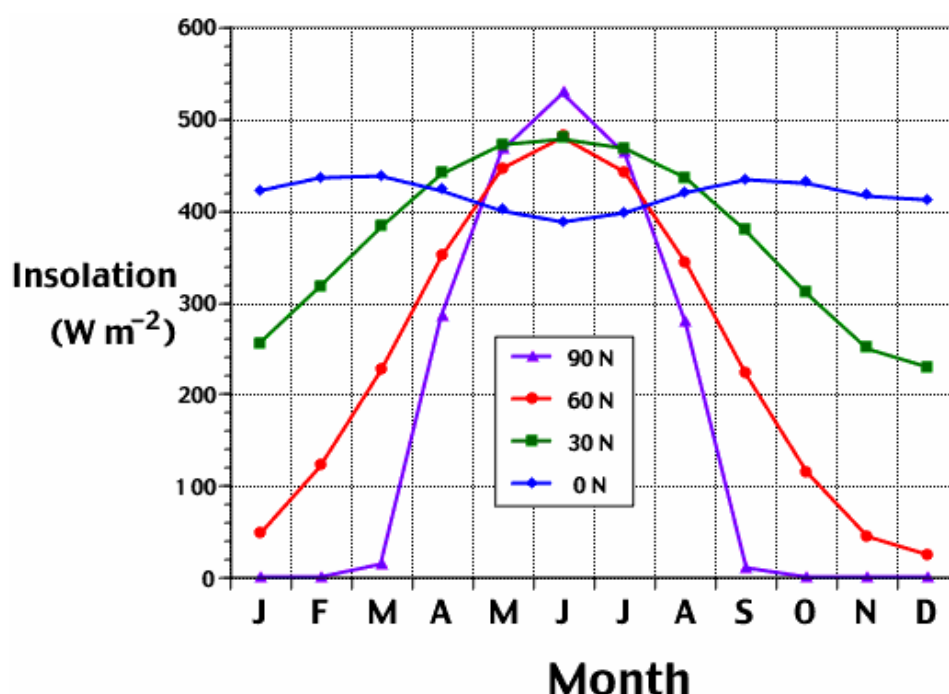
Fig. AI-9 Monthly values of available insolation for the equator, 30, 60, and 90° North.

Appendix II: Direction of beam radiation

The geometric relationships between a plane of any particular orientation relative to the earth at any time (whether that plane is fixed or moving relative to the earth) and the incoming beam solar radiation, that is, the position of the sun relative to that plane, can be described in terms of several angles. Some of the angles are indicated in Fig. AII-1. The angles are as follows:

φ **Latitude**, the angular location north or south of the equator, north positive; $-90° \leq \varphi \leq 90°$.

δ **Declination**, the angular position of the sun at solar noon (i.e., when the sun is on the local meridian) with respect to the plane of the equator, north positive; $-23.45° \leq \delta \leq 23.45°$.

β **Slope**, the angle between the plane of the surface in question and the horizontal; $0 \leq \beta \leq 180°$. *($\beta > 90°$ means that the surface has a downward facing component.)*

γ **Surface azimuth angle**, the deviation of the projection on a horizontal plane of the normal to the surface from the local meridian, with zero due south, east negative, and west positive; *$-180° \leq \gamma \leq 180°$.*

ω **Hour angle**, the angular displacement of the sun east or west of the local meridian due to rotation of the earth on its axis at 15° per hour, morning negative, afternoon positive.

θ **Angle of incidence**, the angle between the beam radiation on a surface and the normal to that surface.

Additional angles are defined that describe the position of the sun in the sky:

θ_z **Zenith angle**, the angle between the vertical and the line to the sun, i.e., the angle of incidence of beam radiation on a horizontal surface.

α_s **Solar altitude angle**, the angle between the horizontal and the line to the sun, i.e., the complement of the zenith angle.

γ_s **Solar azimuth angle**, the angular displacement from south of the projection of beam radiation on the horizontal plane, shown in Fig. AII-1. Displacements east of south are negative and west of south are positive.

The declination θ can be found from the equation:

$$\delta = 23.45 \sin(\frac{360}{365}(n+284)) \qquad \text{(AII-1)}$$

(a)   (b)
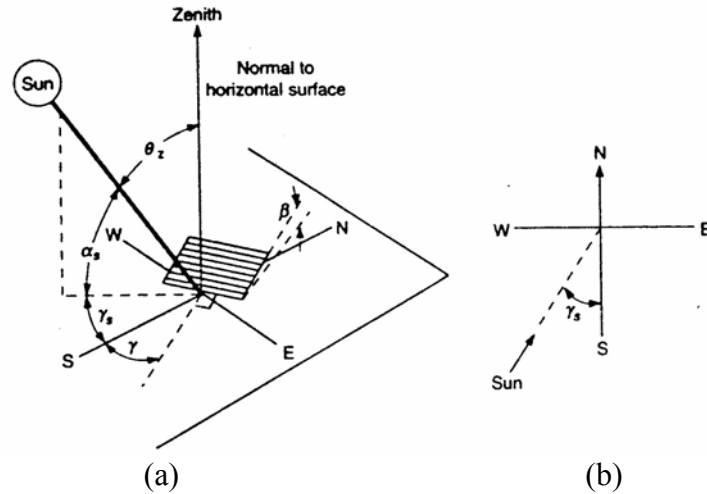
Fig. AII-1 (a) Zenith angle, slope, surface azimuth angle, and solar azimuth angle for a tilted surface. (b) Plane view showing solar azimuth angle.

The day of the year n can be conveniently obtained with the help of Table AII-1. Note that declination is a continuous function of time. The maximum rate of change of declination is at the equinoxes, when it is about 0.5°/day. For most engineering calculations, the assumption of an integer n to represent a day results in a satisfactory calculation of declination.

Month	n for ith Day of Month	For the average Day of the Month		
		Date	n, Day of Year	δ, Declination
January	i	17	17	-20.9
February	31 + i	16	47	-13.0
March	59 + i	16	75	-2.4
April	90 + i	15	105	9.4
May	120 + i	15	135	18.8
June	151 + i	11	162	23.1
July	181 + i	17	198	21.2
August	212 + i	16	228	13.5
September	243 + i	15	258	2.2
October	273 + i	15	288	-9.6
November	304 + i	14	318	-18.9
December	334 + i	10	344	-23.0

Table AII-1 Recommended average Days for Months and values of n by Months.

There is a set of useful relationships among these angles. Equations relating the angle of incidence of beam radiation on a surface θ to other angles are:

$$\cos(\theta) = \sin\delta\sin\phi\cos\beta - \sin\delta\cos\phi\sin\beta\cos\gamma + \cos\delta\cos\phi\cos\beta\cos\omega$$
$$+ \cos\delta\sin\phi\sin\beta\cos\gamma\cos\omega + \cos\delta\sin\beta\sin\gamma\sin\omega$$

(AII-2)

and

238

$$\cos\theta = \cos\theta_z \cos\beta + \sin\theta_z \sin\beta\cos(\gamma_s - \gamma) \qquad\text{(AII-3)}$$

There are several commonly occurring cases for which Equation (AII-3) is simplified. For fixed surfaces sloped toward the south or north, that is, with a surface azimuth angle γ of 0° or 180° (a very common situation for fixed flat-plate collectors), the last term drops out.

For vertical surfaces, $\beta = 90°$ and the equation becomes

$$\cos\theta = -\sin\delta\cos\phi\cos\gamma + \cos\delta\sin\phi\cos\gamma\cos\omega + \cos\delta\sin\gamma\sin\omega \qquad\text{(AII-4)}$$

For horizontal surfaces, the angle of incidence is the zenith angle of the sun, θ_z. Its value must be between 0° and 90° when the sun is above the horizon. For this situation, $\beta = 0$, and Equation (AII-3) becomes

$$\cos\theta_z = \cos\phi\cos\delta\cos\omega + \sin\phi\sin\delta \qquad\text{(AII-5)}$$

The solar azimuth angle γ_s can have values in the range of 180° to - 180°. For north or south latitudes between 23.45° and 66.45°, γ_s will be between 90° and -90° for days less than 12 hours long; for days with more than 12 hours between sunrise and sunset, γ_s will be greater than 90° or less than -90° early and late in the day when the sun is north of the east-west line in the northern hemisphere or south of the east-west line in the southern hemisphere. For tropical latitudes, γ_s can have any value when (δ - φ) is positive in the northern hemisphere or negative in the southern. e.g., at noon at $\varphi = 10°$ and $\delta = 200$, $\gamma_s = 180°$.

Thus, to calculate γ_s we must know in which quadrant the sun will be. This is determined by the relationship of the hour angle ω to the hour angle ω_{ew} when the sun is due west (or east). A general formulation for γ_s is conveniently written in terms of $\gamma_{s'}$ a pseudo surface azimuth angle in the first or fourth quadrant:

$$\gamma_s = C_1 C_2 \gamma_s^{'} + C_3 \left(\frac{1 - C_1 C_2}{2}\right)180 \qquad\text{(AII-6a)}$$

where
$$\sin\gamma_s^{'} = \frac{\sin\omega\cos\delta}{\sin\theta_z} \qquad\text{(AII-6b)}$$

or
$$\tan\gamma_s^{'} = \frac{\sin\omega}{\sin\delta\cos\omega - \cos\phi\tan\delta} \qquad\text{(AII-6c)}$$

$$C_1 = 1 \qquad \text{if } |\omega| \le \omega_{ew}$$
$$\text{(AII-6d)}$$
$$C_1 = -1 \qquad \text{if } |\omega| > \omega_{ew}$$

$$C_2 = 1 \qquad \text{if } (\varphi - \delta) \ge 0$$
$$\text{(AII-6e)}$$
$$C_2 = -1 \qquad \text{if } (\varphi - \delta) < 0$$

$$C_3 = 1 \qquad \text{if } \omega \geq 0$$

$$\text{(AII-6f)}$$

$$C_3 = -1 \qquad \text{if } \omega < 0$$

$$\cos \omega_{ew} = (\tan \delta) / (\tan \phi) \qquad \text{(AII-6g)}$$

Useful relationships for the angle of incidence of surfaces sloped due north or due south can be derived from the fact that surfaces with slope β to the north or south have the same angular relationship to beam radiation as a horizontal surface at an artificial latitude of $(\varphi - \delta)$. The relationship is shown in Fig. (AII-2) for the northern hemisphere. Modifying Equation (AII-5) yields

$$\cos \theta = \cos(\phi - \beta) \cos \delta \cos \omega + \sin(\phi - \beta) \sin \delta \qquad \text{(AII-7a)}$$

For the southern hemisphere modify the equation by replacing $(\varphi - \delta)$ by $(\varphi + \delta)$, consistent with the sign conventions on φ and δ:

$$\cos \theta = \cos(\phi + \beta) \cos \delta \cos \omega + \sin(\phi + \beta) \sin \delta \qquad \text{(AII-7b)}$$

For the special case of solar noon, for the south-facing sloped surface in the northern hemisphere,

$$\theta_{noon} = |\phi - \delta - \beta| \qquad \text{(AII-8a)}$$

and for the southern hemisphere:

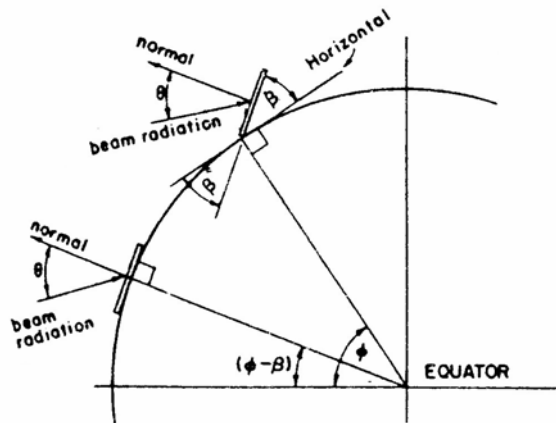$$\theta_{noon} = |-\phi + \delta - \beta| \qquad \text{(AII-8b)}$$

Fig. AII-2 Section of Earth showing β, θ, φ, and $(\varphi - \beta)$ for a south-facing surface.

where $\beta = 0$, the angle of incidence is the zenith angle, which for the northern hemisphere is:

$$\theta_{noon} = |\phi - \delta| \qquad\qquad\text{(AII-9a)}$$

and for the southern hemisphere:

$$\theta_{noon} = |-\phi + \delta| \qquad\qquad\text{(AII-9b)}$$

Equation (AII-5) can be solved for the sunset hour angle ω_s, when $\theta_z = 90°$:

$$\cos\omega_s = -\frac{\sin\phi\sin\delta}{\cos\phi\cos\delta} = -\tan\phi\tan\delta \qquad\qquad\text{(AII-10)}$$

It also follows that the number of daylight hours is given by:

$$N = \frac{2}{15}\cos^{-1}(-\tan\phi\tan\delta) \qquad\qquad\text{(AII-11)}$$

An additional angle of interest is the profile angle of beam radiation on a receiver plane R that has a surface azimuth angle of γ. It is the projection of the solar altitude angle on a vertical plane perpendicular to the plane in question. Expressed another way, it is the angle through which a plane that is initially horizontal must be rotated about an axis in the plane of the surface in question in order to include the sun. The solar altitude angle α_s (i.e., < BAC), and the profile angle α_p (i.e., < DEF), for the plane R are shown in Fig. AII-3. The plane AEDB includes the sun. Note that the solar altitude and profile angle are the same when the sun is in a plane perpendicular to the surface R (e.g., at solar noon for a surface with a surface azimuth angle of 0° or 180°). The profile angle is useful in calculating shading by overhangs. It can be calculated from:

$$\tan\alpha_p = \frac{\tan\alpha_s}{\cos(\gamma_s - \gamma)} \qquad\qquad\text{(AII-12)}$$
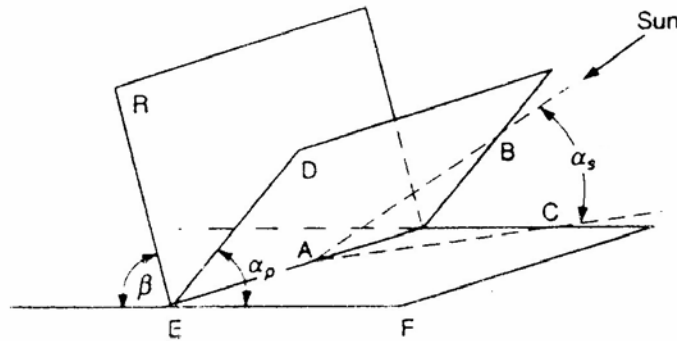

Fig. AII-3 The solar altitude angle α_s (< BAC), and the profile angle α_p (< DEF) for a surface R.

241

Angles for tracking surfaces

Some solar collectors "track" the sun by moving in prescribed ways to minimize the angle of incidence of beam radiation on their surfaces and thus maximize the incident beam radiation. The angles of incidence and the surface azimuth angles are needed for these collectors. The relationships in this section will be useful in radiation calculations for these moving surfaces.

Tracking systems are classified by their motions. Rotation can be about a single axis (which could have any orientation but which in practice is usually horizontal east-west, horizontal north-south, vertical, or parallel to the earth's axis) or it can be about two axes. The following sets of equations (except for Equations (AII-16)) are for surfaces that rotate on axes that are parallel to the surfaces.

For a plane rotated about a horizontal east-west axis with a single daily adjustment so that the beam radiation is normal to the surface at noon each day,

$$\cos\theta = \sin^2\delta + \cos^2\delta\cos\omega \qquad \text{(AII-13a)}$$

The slope of this surface will be fixed for each day and will be

$$\beta = |\phi - \delta| \qquad \text{(AII-13b)}$$

The surface azimuth angle for a day will be 0° or 180º depending on the latitude and declination:

$$\text{If } (\phi - \delta) > 0, \gamma = 0° \qquad \text{(AII-13c)}$$

$$\text{If } (\phi - \delta) < 0, \gamma = 180°$$

For a plane rotated about a horizontal east-west axis with continuous adjustment to minimize the angle of incidence,

$$\cos\theta = (1 - \cos^2\delta\sin^2\omega)^{1/2} \qquad \text{(AII-14a)}$$

The slope of this surface is given by

$$\tan\beta = \tan\theta_z |\cos\gamma_s| \qquad \text{(AII-14b)}$$

The surface azimuth angle for this mode of orientation will change between 0° and 180° if the solar azimuth angle passes through ± 90°. For either hemisphere,

$$\text{If } |\gamma_s| < 90, \gamma = 0° \qquad \text{(AII-14c)}$$
$$\text{If } |\gamma_s| > 90, \gamma = 180°$$

242

For a plane rotated about a horizontal north-south axis with continuous adjustment to minimize the angle of incidence,

$$\cos\theta = (\cos^2\theta_z - \cos^2\delta\sin^2\omega)^{1/2} \qquad\qquad \text{(AII-15a)}$$

The slope of this surface is given by

$$-\tan\beta = \tan\theta_z|\cos(\gamma - \gamma_s)| \qquad\qquad \text{(AII-15b)}$$

The surface azimuth angle for this mode of orientation will be 90° or -90° depending on the sign of the solar azimuth angle:

If $\gamma_s > 0$, $\gamma = 90°$
If $\gamma_s < 0$, $\gamma = -90°$

For a plane with a fixed slope rotated about a vertical axis, the angle of incidence is minimized when the surface azimuth and solar azimuth angles are equal. From Equation (AII-3), the angle of incidence is:

$$\cos\theta = \cos\theta_z\cos\beta + \sin\theta_z\sin\beta \qquad\qquad \text{(AII-16a)}$$

The slope is fixed, so

$$\beta = constant \qquad\qquad \text{(AII-16b)}$$

The surface azimuth angle is:

$$\gamma = \gamma_s \qquad\qquad \text{(AII-16c)}$$

For a plane rotated about a horizontal north-south axis parallel to the earth's axis with continuous adjustment to minimize θ,

$$\cos\theta = \cos\delta \qquad\qquad \text{(AII-17a)}$$

The slope varies continuously and is:

$$\tan\beta = \frac{\tan\phi}{\cos\gamma} \qquad\qquad \text{(AII-17b)}$$

The surface azimuth angle is:

$$\gamma = \tan^{-1}\frac{\sin\theta_z\sin\gamma_s}{\cos\theta'\sin\phi} + 180 C_1 C_2 \qquad\qquad \text{(AII-17c)}$$

where $\quad\quad \cos\theta' = \cos\theta_z\cos\phi + \sin\theta_z\sin\phi \qquad\qquad \text{(AII-17d)}$

$$C_1 = 0 \quad \text{if } (\tan^{-1}\frac{\sin\theta_z\sin\gamma_s}{\cos\theta'\sin\phi}) + \gamma_s = 0$$

243

$$C_1 = 1 \quad \text{otherwise} \tag{AII-17e}$$

$$C_2 = 1 \quad \text{if } \gamma_s \geq 0$$
$$C_2 = -1 \quad \text{if } \gamma_s < 0 \tag{AII-17f}$$

For a plane that is continuously tracking about two axes to minimize the angle of incidence,

$$\cos\theta = 1 \tag{AII-18a}$$

$$\beta = \alpha \tag{AII-18b}$$

$$\gamma = \gamma_s \tag{AII-18c}$$

Appendix III: Lens Errors

Aberrations

Lenses do not form perfect images, and there is always some degree of distortion or aberration introduced by the lens which causes the image to be an imperfect replica of the object. Careful design of the lens system for a particular application ensures that the aberration is minimised. There are several different types of aberration which can affect image quality.

Spherical aberration

Spherical aberration is caused because spherical surfaces are not the ideal shape with which to make a lens, but they are by far the simplest shape to which glass can be ground and polished and so are often used. Spherical aberration causes beams parallel to but away from the lens axis to be focused in a slightly different place than beams close to the axis. This manifests itself as a blurring of the image. Lenses in which closer-to-ideal, non-spherical surfaces are used are called Astigmatism aspheric lenses, which are complex to make and often extremely expensive. Spherical aberration can be minimised by careful choice of the curvature of the surfaces for a particular application: for instance, a plano-convex lens which is used to focus a collimated beam produces a sharper focal spot when used with the convex side towards the beam rather than with the plane side. A schematical representation of the spherical aberration is shown in Fig. AIII-1.
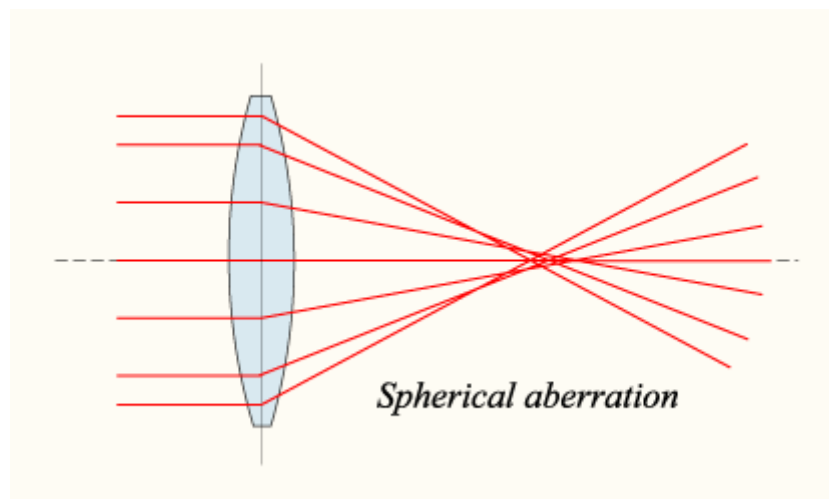

Fig. AIII-1. A schematical representation of the spherical aberration.

Coma

Another type of aberration is coma, which derives its name from the comet-like appearance of the aberrated image. Coma occurs when an object off the optical axis of the lens is imaged, where rays pass through the lens at an angle to the axis θ. Rays which pass through the centre of the lens of focal length f are focused at a point with distance f tan θ from the axis. Rays passing through the outer margins of the lens are focused at different points, either further from the axis (positive coma) or closer to the axis (negative coma). In general, a bundle of parallel rays passing through the lens at a fixed distance from the centre of the lens are focused to a ring-shaped image in the focal plane, known as a comatic circle. The sum of all these circles results in a V-shaped or comet-like flare. As with spherical aberration, coma can be minimised (and in some cases eliminated) by choosing the curvature of the two lens surfaces to match the application. Lenses in which both spherical aberration and coma are minimised are called bestform lenses. A schematical representation of the coma is shown in Fig. AIII-2.
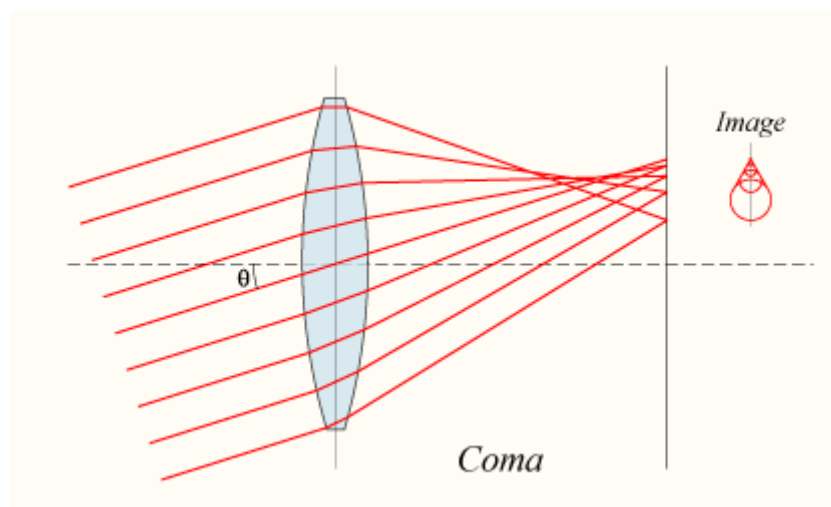
Fig. AIII-2 A schematical representation of the coma.

Chromatic aberration

Chromatic aberration is caused by the dispersion of the lens material, the variation of its refractive index n with the wavelength of light. Since the focal length f is dependent on the refractive index n according to Eq. (AIII-1), it follows that different wavelengths of light will be focused to different positions.

$$\frac{1}{f} = \left(\frac{n}{n'} - 1\right)\left[\frac{1}{R_1} + \frac{1}{R_2} + \frac{(n-1)d}{nR_1R_2}\right] \qquad \text{(AIII-1)}$$

where where *n* is the refractive index of the lens material, *n'* is the refractive index of the medium which the lens is in and d is the distance along the lens axis between the two surfaces (known as the thickness of the lens).

Chromatic aberration of a lens is seen as fringes of color around the image. It can be minimised by using an achromatic doublet (or achromat) in which two materials with differing dispersion are bonded together to form a single lens. This reduces the amount of chromatic aberration over a certain range of wavelengths, though it does not produce perfect correction. The use of achromats was an important step in the development of the optical microscope. An apochromat is a lens or lens system which minimizes both chromatic and spherical aberrations. A schematical representation of the chromatic and achromatic aberration is shown in Fig. AIII-3 (a), (b) respectively.
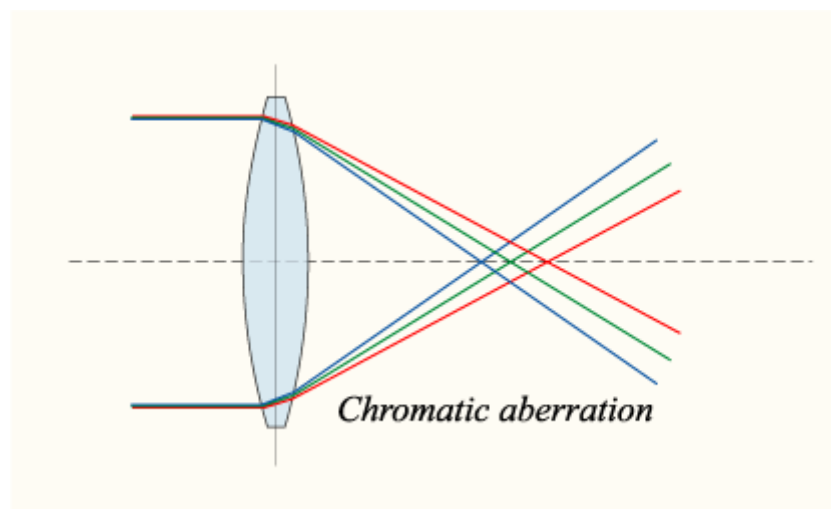
(a)
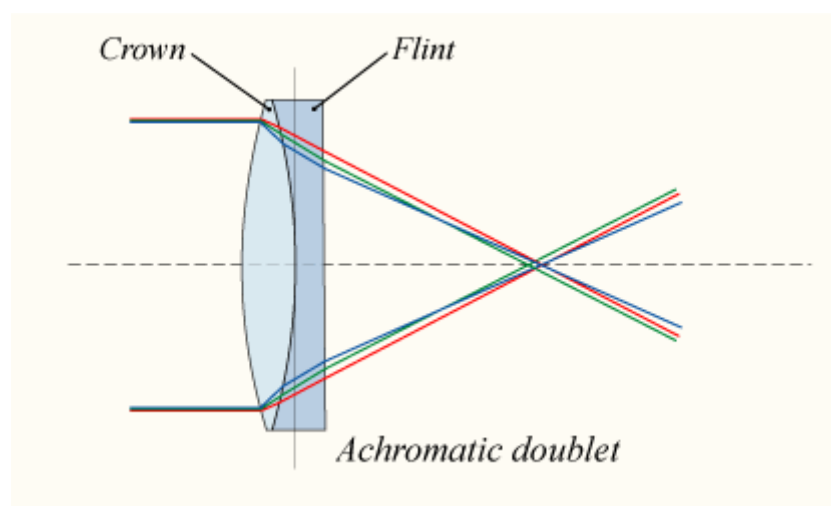
(b)

Fig. AIII-3 A schematical representation of the chromatic and achromatic aberration.

Barrel distortion

Barrel distortion is a divergence from the rectilinear projection in geometric optics where image magnification decreases with increasing distance from the optical axis. The visible effect is that lines that do not go through the centre of the image are bowed outwards, towards the edge of the image. A schematical representation of the barrel distortion is shown in Fig. AIII-4.

Fig. AIII-4 A schematical representation of the barrel distortion.

Pincushion distortion

Pincushion distortion is a divergence from the rectilinear projection in geometric optics where image magnification increases with increasing distance from the optical axis. The visible effect is that lines that do not go through the centre of the image are bowed inwards, towards the centre of the image. A schematical representation of the pincushion distortion is shown in Fig. AIII-5.
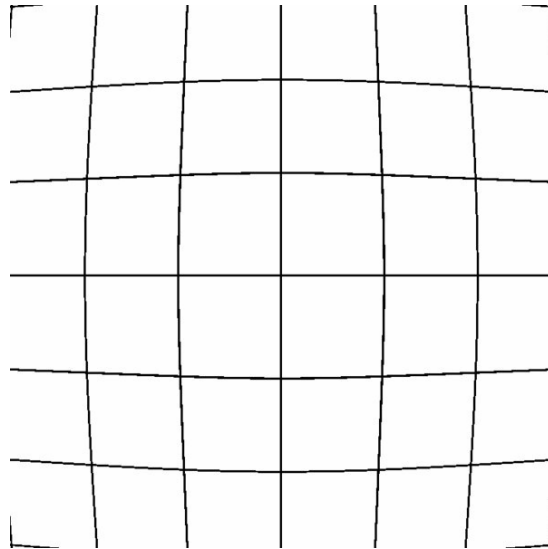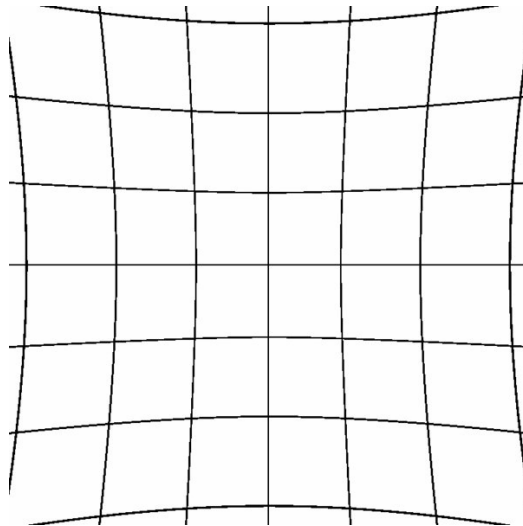
Fig. AIII-5 A schematical representation of the pincushion distortion.

Astigmatism

Astigmatism is a refraction error of the eye in which there is a difference in degree of refraction in different meridians. It is typically characterized by an aspherical cornea in which one axis of corneal steepness is greater than the perpendicular axis. Astigmatism causes difficulties in seeing fine detail, and can be often corrected by glasses with a cylindrical lens (i.e. a lens that has different radii of curvature in different planes), contact lenses, or refractive surgery.

Astigmatism occurs when either the cornea or the lens of the eye is not perfectly spherical. As a result, the eye has different focal points in different planes. For example, the image may be clearly focused on the retina in the horizontal plane, but in front of the retina in the vertical plane.

In some cases vertical lines i.e. walls, may appear to the patient to be leaning over like the tower of Pisa. A schematical representation of the astigmatism is shown in Fig. AIII-6.
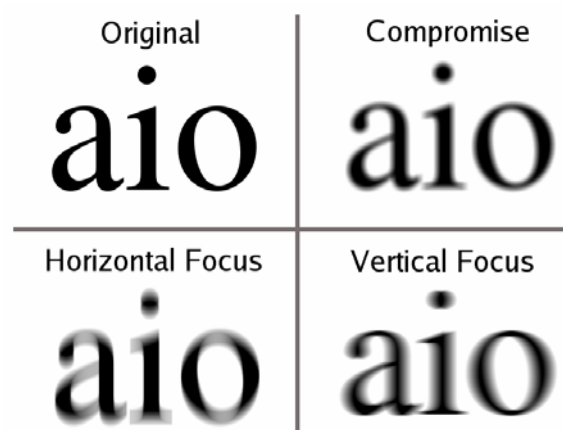
Fig. AIII-6 A schematical representation of the astigmatism

Appendix IV:Calculation of the concentration ratio of some types of optical concentrators

The concentration ratio and the optimum dimensions of any optical concentrator depend on the category of the concentrator (imaging or non-imaging concentrator) and its dimensional properties. Mathematical analysis can be done to derive formulas which express the concentration behaviour of the optical concentrator in the ideal conditions independent of the optical properties of its material. To find out the real values of the concentrator behaviour, the geometrically calculated values have to be multiplied with the efficiency of the concentrator resulted from knowing its optical properties.

Table AIV-1 gives a summary of some numerical and optimal values of two-dimensional (troughlike) parabolic concentrators and three-dimesional (dish) ones according to different types of absorber shapes [31].

Type / Absorber shape	CR	CR for $\theta_c =$			CR/CR$_{ideal}$	A_r/A_s
		¼°	½°	1°		
2D (trough)						
Tube	$\dfrac{\sin\phi}{\pi\sin\theta_c}$				$\dfrac{\sin\phi}{\pi}$	$\left[\dfrac{1}{\cos(\phi/2)} + \left(\cos\dfrac{\phi}{2}\right)\right.$
Flat	$\dfrac{\sin\phi\cos(\phi+\theta_c)}{\sin\theta_c} - 1$				$\sin\phi\cos(\phi+\theta_c) - \sin\theta_c$	$\left. \times \log_e \cos\left(\dfrac{\pi}{4} - \dfrac{\phi}{4}\right)\right]/2$
With optimal ϕ:						
Round tube $\phi_{opt} = \dfrac{\pi}{2}$	$\dfrac{1}{\pi\sin\theta_c}$	73	37	18	$\dfrac{1}{\pi}$	1.15
Flat $\phi_{opt} = \dfrac{1}{2}\left(\dfrac{\pi}{2} - \theta\right)$	$\dfrac{1}{2\sin\theta_c} - \dfrac{3}{2}$	113	56	27	$\dfrac{1}{2} - \dfrac{1}{2}\sin\theta_c$	1.03
3D (dish)						
Sphere	$\dfrac{\sin^2\phi}{4\sin^2\theta_c}$				$\dfrac{\sin^2\phi}{4}$	$\dfrac{2\,|1/\cos(\phi/2) - \cos^2(\phi/2)|}{3\sin^2(\phi/2)}$
Flat	$\dfrac{\sin^2\phi\cos^2(\phi+\theta_c)}{\sin^2\theta_c} - 1$				$\sin^2\phi\cos^2(\phi+\theta_c) - \sin^2\theta_c$	
With optimal ϕ:						
Sphere $\phi_{opt} = \dfrac{\pi}{2}$	$\dfrac{1}{4\sin^2\theta_c}$	13000	3300	820	¼	1.22
Flat $\phi_{opt} = \dfrac{1}{2}\left(\dfrac{\pi}{2} - \theta_c\right)$	$\dfrac{1}{4\sin^2\theta_c} - \dfrac{1}{2\sin\theta_c} - \dfrac{3}{4}$	13000	3200	790	$\dfrac{1}{4} - \dfrac{3}{4}\sin\theta_c - \dfrac{3}{4}\sin^2\theta_c$	1.04

Table AIV-1 Concentration ratio and Reflector/Aperture Area Ratio (A_r/A_a) as a function of rim angle ϕ_r and acceptance half-angle θ_c for parabolic reflectors. The flat absorber is one-sided; concentration for two-sided flat absorber can be obtained from (CR$_{2\text{-sided}}$ = 1/2 (CR$_{1\text{-sided}}$ + 1).

251

References

[1] "Numerical Simulation Model for the Optical Behaviour of the Compound Parabolic and Conical Solar Energy Concentrators for Laser Beam Generation", Y. A. Abdel-Hadi, M.Sc. thesis, Physics department, Faculty of Science, Ain Shams University, Cairo, Egypt, 1996.

[2] "Solar Engineering of Thermal Process", J. A. Duffie and W. A. Beckman, Chapter 7, edited by John Wiley & Sons, Inc. 1991.

[3] "Implementation of Renewable Energy Technologies – Opportunities and Barriers – Egypt Country Study", Report of the New and Renewable Energy Authority (NREA), Published by UNEP Collaboration Centre on Energy and Environment, Riso National Laboratory, Denmark, 2001, ISBN 87-550-3011-4.

[4] "Egyptian Solar Radiation Atlas", M. A. Mosalam Shaltout, managed by the New and Renewable Energy Authority (NREA), and the U.S. Agency for International Development (USAID), 1991.

[5] "Kompakter Nd-YAG Laser kleiner und mittlerer Leistung direkt gepumpt durch solarstralung", Y. A. Abdel-Hadi und A. Ding, Verhandlung der *Frühjahrstagung der deutschen physikalischen Gesellschaft (DPG)*, s. 115-116, März 4-8, 2002, Universität Osnabrück, Osnabrück, Deutschland (auf Deutsch).
("Compacted Nd:YAG laser of small and medium power pumped directly through the solar radiation", Y. A. Abdel-Hadi and A. Ding, Proc. of the *Spring Meeting of the German Society of Physics (DPG)*, pp. 115-116, March 4-8, 2002, University of Osnabrück, Osnabrück, Germany (in German language)).

[6] "Solargepumter Table-Top Nd:YAG-Laser", Y. A. Abdel-Hadi und A. Ding, Verhandlung der *Frühjahrstagung der deutschen physikalischen Gesellschaft (DPG)*, s. 116, März 24-28, 2003, Universität Hannover, Hannover, Deutschland (auf Deutsch).
("Solar pumped Table-Top Nd:YAG laser", Y. A. Abdel-Hadi and A. Ding, Proc. of the *Spring Meeting of the German Society of Physics (DPG)*, pp. 116, March 24-28, 2003, University of Hannover, Hannover, Germany (in German language)).

[7] "Hochleistunglaser für Raumfahrtaufgaben", U. Brauch, W. Schall und W. Wittwer, DLR-Nachrichten, Institut für Technische Physik, Deutsche Forschungsanstalt für Luft- und Raumfahrt (DLR), Stuttgart, Heft 65, November 1991.
("High Power Laser for Space Duties", U. Brauch, W. Schall und W. Wittwer, DLR-Nachrichten, Institute of Technical Physics, German Research Institute of Space and Aeronautics (DLR), Stuttgart, Vol. 65, November 1991).

[8] "Solar Furnaces for Materials Processing in Space", R. A. Hobday, B. Norton, and S. D. Probert, A Feasibility Study, Final Report, For the Science and Engineering Research Council, Swidon, U.K., 31st December 1987.

[9] "Design of Nonimaging Concentrators as a Second Stage in Tandem with Image-Forming First-Stage Concentrators", R. Winston and W. T. Welford, Applied Optics, Vol. 19, No. 3, pp. 347 - 351, February 1980.

[10] "Solar-Pumped Solid-State Lasers", M. Weksler and J. Schwartz, IEEE Journal of Quantum Electronics, Vol. 24, No. 6, pp. 1222 - 1228, June 1988.

[11] "Comparison of Solar Pumped Nd:YAG and Nd:Cr:GSGG Lasers at Liquid Nitrogen and Room Temperature" U. Brauch, J. Muckenschnabel, A. Yogev, R. Benmair, Y. Noter, M. Oron, and A. Brauch, Research Report of the German Research Institute of Space and Aeronautics (Deutsche Forschungsanstalt für Luft- und Raumfahrt (DLR)), Stuttgart, ISBN 0171-1342, July 1989.

[12] "Solar-Pumped Er, Tm, Ho:YAG Laser", R. M. J. Benmair, J. Kagan, Y. Kalisky, Y. Noter, M.Oron, Y. Shimony, and A. Yogev, Optics Letters, Vol. 15, No. 1, pp. 36–38, January 1990.

[13] "Thermal Effects on Cavity Stability of Chromium- and Neodymium-doped Gadolinium Scandium Gallium Garnet Laser under Solar-Simulator Pumping", Kyong H. Kim, Demtius D. Venable, and Lamarr A. Brown, Journal of Applied Physics, Vol. 69, No. 5, pp. 2841–2848, 1st March 1991.

[14] "Efficiency and Threshold Pump Intensity of CW Solar-Pumped Solid-State Lasers", I. H. Hwang and J. H. Lee, IEEE Journal of Quantum Electronics, Vol. 27, No. 9, pp. 2129–2134, September 1991.

[15] "Solar-pumped Solid State Lasers for Space to Space Power Transmission", U. Brauch, J. Muckennschnabel, H. Opower, and W. Wittwer, Space Power, Resources, Manufacturing and Development, Vol. 10, No. 3-4, pp. 285-294, 1991.

[16] "Influence of Operating Temperature on the Power, Divergence, and Stress-Induced Birefringence in Solar-Pumped Solid State Lasers", U. Brauch, J. Muckennschnabel, G. A. Thomson, H. Bernstein, A. Yogev, A. Reich, and M. Oron, Optical Engineering, Vol. 31, No. 5, pp. 1072 – 1078, May 1992.

[17] "Power Transmission Using Solar Pumped Laser", N. Naftali, I. Pe'er, and A. Yogev, SPIE, Vol. 3139, pp. 259 – 265, 1997.

[18] "Visible Solar-Pumped Lasers", M. Lando, Y. Shimony, R. M. J Benmair, D. Abramovich, V. Krupkin and A. Yogev, Optical Materials, Vol. 13, Issue 1, pp. 111 – 115, October 1999.

[19] "Passive Q Switching of A Solar-Pumped Nd:YAG Laser", M. Lando, Y. Shimony, Y. Noter, R. M. J. Benmair and A. Yogev, Applied Optics, Vol. 39, No. 12, 20th April 2000.

[20] "A solar-pumped Nd:YAG laser in the high collection efficiency regime", M. Lando, J. Kagan, B. Linyekin, V. Dobrusin, Optics Communications, 222, pp. 371-381, 23 May 2003.

[21] "A Sun-Pumped cw One-Watt Laser", C.G. Young, Applied Optics, Vol. 5, No. 6, pp 993-997, June 1966.

[22] "Achievement of Ultrahigh Solar Concentration with Potential for Efficient Laser Pumping", P. Gleckman, Applied Optics, Vol. 27, No. 21, pp. 4385-4391, November 1988.

[23] "Ultra-High Solar Flux and Applications to Laser Pumping", Roland Winston, Dave Cooke. Philip Gleckman and Joseph J. O'Gallagher, Proc. Of Proc. of Renewable Technology and the Environment, the Second World Renewable Energy Congress, Vol. 1, Edited by A. A. M. Sayigh, Pergamon Press, Reading, U.K., September, 1992.

[24] "Sonnengepumpter, gütegeschalteter Nd-Laser", G. Phillipps, Report of the Institute of Optics, technical University of Berlin, Berlin, Germany, December 1993.

[25] "Broadband Laser Amplifier Based on Gas-Phase Dimer Molecules Pumped by The Sun", I. Pe'er, I. Vishnevitsky, N. Naftali and A. Yogev., Optics Letters, Vol. 26, No. 17, pp. 1332-1334, 1st September 2001.

[26] "Optoelectronics, An Introduction", J. Wilson, J. F. B. Hawkes, Prentice Hall International Inc., London, 1983.

[27] "Solid-State Laser Engineering", W. Koechner, Springer Series in Optical Science, Vol. 1, 3rd edition, Springer Verlag, 1992.

[28] "Thermal and Laser Properties of Nd:YVO$_4$ Crystal", H. J. Zhang, L. Zhu, X. L. Meng, Z. H. Yang, C. Q. Wang, W. T. Yu, Y. T. Chow, M. K. Lu, Crystal Research Technology, Vol. 34, No. 8, pp. 1011-1016, 1999.

[29] "Solar Furnaces for Materials Processing in Space", A Feasibility Study, Final Report, For the Science and Engineering Research Council, R. A. Hobday, B. Norton, and S. D. Probert, Swidon, U.K., 31st December 1987.

[30] "Solar Energy, Principles of Thermal Collection and Storage", S. P. Sukhatme, Chapter 6, edited by McGraw-Hill 1982.

[31] "Solar Energy Handbook", J. F. Kreider and F. Kreith, Chapter 8, edited by McGraw-Hill 1981.

[32] "Design of Nonimaging Concentrators as a Second Stage in Tandem with Image-Forming First-Stage Concentrators", R. Winston and W. T. Welford, Applied Optics, Vol. 19, No. 3, pp. 347-351, February 1980.

[33] "Optical and Thermal Properties of Compound Parabolic Concentrators", A. Rabl, Solar Energy, Vol. 18, pp. 497-511, 1976.

[34] "Effects of Tracking Errors on the Performance of Point Focusing Solar Collectors", O. Hughes Robert, Solar Energy, Vol. 24, pp. 83-92, 1980.

[35] "Energy Balance on A Parabolic Cylinder Solar Reflector", G. O. G. Lof, D. A. Fester, and J. A. Duffie, Trans. ASME, Journal of Engineering for Power, Vol. 84A, pp.24, 1962.

[36] "Optimization of Focusing Solar-Collectors Design", G. O. G. Lof and J. A. Duffie, Trans. ASME, Journal of Engineering for Power, Vol. 85A, pp. 221, 1963.

[37] "Incidence-Angle Modifier and Average Optical Efficiency of Parabolic Trough Collectors", H. Gual and A. Rabl, Trans. ASME, Journal of Solar Energy Engineering, Vol. 102, pp. 16, 1980.

[38] "On the Performance of Cylindrical Parabolic Solar Concentrators with Flat Absorber", D. L. Evans, Solar Energy, Vol. 19, pp. 379, 1977.

[39] "The Flux Distribution Through the Focal Spot of Solar Furnace", P. D. Lose, Solar Energy, Vol. 1, No. 23, 1957.

[40] "The Sun", G. Abetti, edited by Van Nostrand Co., Princeton, NJ, 1938.

[41] "Active Solar Collectors and their Applications", A. Rabl, Oxford University Press and Oxford, 1985.

[42] "Optics of Parabolic-Trough, Solar-Energy Collectors, Possessing Small Concentration Ratios", D. E. Prapas, B. Norton and S. D. Probert, Solar Energy, Vol. 39, No. 6, pp. 541-550, 1987.

[43] "Principles of Solar Concentrators of A Novel Design", R. Winston, Solar Energy, Vol. 16, pp. 89-95, 1974.

[44] "Optical and Thermal Properties of Compound Parabolic Concentrators", A. Rabl, Solar Energy, Vol. 18, pp. 497-511, 1976.

[45] "Detailed Parametric Analyses of Heat Transfer in CPC Solar Energy Collectors", P. C. Eames and B. Norton, Solar Energy, Vol. 50, No. 4, pp. 321-338, 1993.

[46] "Validated, Unified Model for Optics and Heat Transfer in Line-Axis Concentrating Solar EnergyCollectors", P. C. Eames and B. Norton, Solar Energy, Vol. 50, No. 4, pp. 339-355, 1993.

[47] "New Reflector Design Which Avoids Losses Through Gaps Between Tubular Absorber and Reflectors", W. R. McIntire, Solar Energy, Vol. 25 pp. 215-220, 1980.

[48] "Model for Solar Concentrators to Increase Photovoltaic Performance", M. A. Mosalam Shaltout, M. Medhat, and Y. A. Hadi, Proc. of Fourth World Congress on Renewable Energy, Denver, Clorado, U.S.A., 15-21 June 1996, edit by A. Sayigh.

[49] "Model for Solar Concentrators to Increase Photovoltaic Performance at Cairo, Egypt", M. A. Mosalam Shaltout and Y. A. Hadi, Proc. of Renewable Energy Conference and Workshop ASRE'96, April 14-18, 1996, Cairo, Egypt, Under Publishing.

[50] "Development of Compound Parabolic Concentrators for Solar Energy", J. J. O'Gallagher and R. Winston, International Journal of Ambient Energy, Vol. 4, No. 4, pp. 171-186, October 1983.

[51] "High Collection Nonimaging Optics", W. T. Welford and R. Winston, Academic Press, ISBN 0-12-742885-2, 1989.

[52] "Solar Power Plants, Fundamentals, Technology, Systems, Economics", C. J. Winter, R. L. Sizmann, and L. L. Vant-Hull (Eds), Chapter 3, edited by Springer-Verlag, 1990.

[53] "Guardians of the Golden Gate: Lighthouses and Lifeboat Stations of San Francisco Bay", Ralph Shanks and Lisa Woo Shanks, editor. 1995, Costano Books, ISBN: 0-930268-08-3.

[54] "Unconventional Optical Concentration Devices for Solar-pumped Solid State Lasers", Y. A. Abdel-Hadi und A. Ding, submitted to *Solar Energy* (under publishing).

[55] "Optische Konzentratoren für solargepumpte Table-Top-Laser", Y. A. Abdel-Hadi und A. Ding, Verhandlung der *Frühjahrstagung der deutschen physikalischen Gesellschaft (DPG)*, Teil. 3, s. 160, März 4-9, 2005, Technische Universität Berlin, Deutschland (auf Deutsch).
("Optical Concentrators for Solar Pumped Table-Top Laser", Y. A. Abdel-Hadi und A. Ding, Proc. of the *Spring Meeting of the German Society of Physics (DPG)*, Vol. 3, pp. 160, March 4-9, 2005, Technical University of Berlin, Germany (in German language)).

[56] "Focal Properties of Large Fresnel Lenses", Y. A. Abdel-Hadi, A. Ding, N. Nüsse und P. Erichsen, Verhandlung der *Frühjahrstagung der deutschen physikalischen Gesellschaft (DPG)*, Teil. 3, s. 160, März 4-9, 2005, Technische Universität Berlin, Deutschland (auf Englisch).
("Focal Properties of Large Fresnel Lenses", Y. A. Abdel-Hadi, A. Ding, Nils Nüsse und Patrick Erichsen, Proc. of the *Spring Meeting of the German Society of Physics (DPG)*, Vol. 3, pp. 160, March 4-9, 2005, Technical University of Berlin, Germany (in English language)).

[57] "Non-Imaging, Focusing Heliostat", Y. T. Chen, K. K. Chong, T. P. Bligh, J. Yunus, K. S. Kannan, B. H. Lim, M. A. Alias, N. Bidin, O. Aliman, S. Salehan, Shk. Abd. Rezan S. A. H., C. M. Tam and K. K. Tan, Solar Energy, Vol. 71, No. 3, pp. 155 − 164, March 2001.

Curriculum Vitae

Personal Data

Family name: Abdel-Hadi
First name: Yasser
Sex: Male
Place of birth: Cairo, Egypt
Date of birth: 07.06.1969
Nationality: Egyptian
Marital Status: Single

Educational Background

09.1974 – 05.1980	Primary School Cairo, Egypt and in Riyadh, Saudi Arabia.
09.1980 – 05.1983	Middle School in Riyadh, Saudi Arabia.
09.1983 – 05.1986	Secondary School in Riyadh, Saudi Arabia.
09.1986 - 05.1990	Studying Physics at Ain Shams University in Cairo (Egypt), getting B.Sc. degree. Title: "Nuclear Magnetic Moments"
10.1990 - 12.1991	Military service.
09.1991 - 10.1996	Studying M.Sc. in Physics at Ain Shams University in Cairo (Egypt). Title of the thesis: "Numerical Simulation Model for the Optical Behaviour of the Compound Parabolic and Conical Solar Energy Concentrators for Laser Beam Generation".
02.1999 – 04.1999	Attending an intensive German course in Regional Centre for Adults Education (ISFEC) in Sirs El-Layyan (Egypt) as a DAAD-Scholarship holder.
10.1999 – 03.2000	Attending an intensive German course in Goethe Institute of Göttingen (Germany) as a DAAD-Scholarship holder - Success in DSH Examination.
04.2000 – Now	Doctoral student at Physics in the Technical University of Berlin (Germany). Field of the thesis: „Research on Solar Pumped Laser".

Employment Records

06.1991 - 01.1997	Reader in the National Research Institute of Astronomy and Geophysics, Helwan, Cairo, Egypt.
01.1997 - 09.1999	Assistant Lecturer in the National Research Institute of Astronomy and Geophysics, Helwan, Cairo, Egypt.
04.2000 – Now	Ph.D.-Scholarship holder in the Technical University of Berlin (Institute of Optics) granted by the DAAD.

Further Education

Courses at: *the Academy of Scientific Research and Technology, the Scientific Instruments Centre, the Central Agency for Organisation and Administration, the American University in Cairo (AUC), the Regional Centre for Adults Education (ISFEC), the Goethe Institute of Göttingen (Germany), the Technical University of Berlin (Germany)*, in different fields like: *New Technologies in the Information Field, English Language, Techniques of Writing Abstracts, The Uses of Laser Systems, Basic Knowleges of Planning with (Access) Programme, Basic Knowledges of (Visual Basic), German Language, (Management of International Economical and Scientifical Cooperation Projects), (Intensive Application Trainings for Foreign Students and Graduated of the TU-Berlin 2005), (Career Planning and Preparation for the Profession), (Team Training and Conflict Management), (How to Start a Business) and (International Marketing, Innovation Mangement).*

Scientific Publications

13 Reseaches (reports, papers, articles and thesis) were published in international journals and conferences.

Acknowledgment

Praise be to God, the Lord of the worlds, who helped me to complete this work.

Abstract in Arabic

.

:

(Fresnel Lens)

.

.

(Nd:YAG)   :

)(Nd:YVO$_4$)   .

.(

(Compound Spherical Concentrator (CSC)) (   )

.

(15 cm × 15 cm)   105

.

.

.   (Fresnel Lens)

.

.

A

A

2005